THE RESEARCH AND OPTIMISATION OF EFFICIENT, LOW COST, ULTRA HIGH SPEED PM MACHINES

A Thesis Submitted to Newcastle University

for the Degree of Doctor of Philosophy

In the Faculty of Science, Agriculture and Engineering

2017

Mingzhe Hu

109155041

SCHOOL OF ELECTRICAL AND ELECTRONIC ENGINEERING

NEWCASTLE UNIVERSITY

SCHOOL OF ELECTRICAL AND ELECTRONIC ENGINEERING

I, Mingzhe Hu, confirm that this report and the work presented in it are my own achievement.

I have read and understand the penalties associated with plagiarism.

Signed: .....

Date: 07/08/2017

Abstract

Manufacturers of electric motors for industrial products are often able to lead the market by placing a focus on high speed, compact, low weight and low cost designs which maintain a high motor efficiency. The current generation of battery powered electric drives for domestic products consists of a power-dense high-speed permanent magnet brushless DC motor which is controlled by a high efficiency digital drive to spin the rotor at over 100,000rpm.

The purpose of this project is to pursue a new type of mains powered high-speed (150,000rpm) highly efficient (>85%) motor, from development of fundamental theory and modelling to a carefully designed prototype, matched to a given requirement, and practically validated as a fully built prototype tested in excess of the designed speed. The targeted motor input power is 750W.

A thorough literature review is conducted to view all possible motor types. A permanent magnet brushless DC motor is preferred due to its advantages of high power density, compact size and reliable high speed operation. A hybrid simulation approach which combines the advantages of both analytical simulation and finite element simulation is utilised. Precise loss estimation is investigated to support the creation of an analytical simulation model. The accuracy of the constructed analytical simulation model is validated by 3-dimensional finite element modelling.

This project puts particular focus on motor per unit material cost with design for mass-production in mind. The elimination of high performance but costly motor raw materials, such as high residual flux density rare-earth permanent magnets, low loss density amorphous steels and stranded wires, while still keeping the same level of motor performance in ultra-high speed applications, becomes the biggest challenge in this project.

Table of Contents

List of Figures

List of Tables

Acknowledgments

Firstly, I would like to express the deepest appreciation to my academic supervisor Prof. Barrie Mecrow for the continuous support of my Ph.D study and other life commitments, for his efforts, inspiration, and immense knowledge. His guidance and advice helped me throughout these years of researching. I am truly grateful to have him as my mentor.

Besides, I would like to say a big thank you to Dr. Daniel J Smith, for his continuous help and support through the years and patient prove reading as well as comments about this thesis plus tireless correction. I also would like to thank the rest of my Ph.D supervisors: Dr. Glynn Atkinson, Dr. Chris Bateman, Dr. Tuncay Celik, Dr. Neil Hodgins for their insightful suggestions and encouragements which make this research more completed and in-depth.

Moreover, my sincere thanks also go to Dr. Mark Leaver, and Sam Hinchliffe, who provided me an opportunity to join Motors & PS Team, and provide me the time to finish this work.

Last but not the least, I would like to thank my parents and my wife, Xiaoxi, for supporting me enormously throughout my study and my life.

List of symbols

The following information presents a list of the symbols commonly used throughout this thesis. Motor speed is given in revolutions per minute (rpm).

A_c Cross-sectional area of rotating cylinder parallel to the applied force vector

$\vec{a}$ Acceleration of cylinder

d_c Outer diameter of cylinder

F_c Centrifugal force in a solid cylinder

F A constant force

f_{elec} Electrical frequency of machine

f_{mech} Mechanical frequency of cylinder

g Gravitational acceleration

m_c Mass of cylinder

n Rotational speed in rpm

P Machine's rated power

p Number of pole pairs

P_{out} Machine's output power

R_{out} Outer radius of rotor

R_{in} Inner radius of rotor

r Radius of rotor

B_{hot} Magnet residual flux density at operational temperature

r_c Radius of cylinder

s Displacement of force

T_{out} Machine's output torque

T_c Time of one rotating cycle

t Per unit time

v Poisson's ratio

v Circumferential speed

W Motor generated work

ω Angular velocity speed

δ Weight per unit volume

σ_{r1}, σ_{r2} Radial tensile stress

σ_{t1}, σ_{t2} Tangential tensile stress

ρ_c Mass density of cylinder

T_{opm} Magnet operational temperature

T_{cold} Nominal ambient temperature

$\vec{M}$ Magnet magentisation vector

φ Magnetic potential

M_{rn} Magnetisation of radial component

$M_{\theta n}$ Magnetisation of angular component

ρ_{hot} Coil hot resistivity

R_{hot} Coil hot resistance

R_0 Coil cold resistance

α_p Magnet pole are to rotor pole pitch ratio

C_{T_f} Magnet Temp-demag coefficient

T_f Magnet Temp-demag factor

C_{crr} Coil resistivity rise coefficient

T_{opc} Coil operational temperature

Chapter 1 : Introduction

This PhD project has been sponsored by a leading domestic appliance manufacturer which is constantly in search of innovation to drive its competitive advantage. The electric motors designed by the company enable their products to lead the market by placing a focus on high speed, compact, low weight and cost designs which maintain a decent level of motor efficiency. The simple structure, highly efficient and remarkably reliable electric drive systems developed by the company are one of the most significant technologies in their battery powered products to implement the world leading performance.

The current generation of battery powered electric drives manufactured by the company consists of a power-dense high-speed permanent magnet brushless DC motor which is controlled by a high efficiency digital drive to spin the rotor at over 100,000rpm. This high speed system allows them to be much lighter and smaller in comparison to conventional brushed DC motors, and hence improved power dense.

The target of this sponsored PhD project is to pursue a new type of mains powered high-speed highly efficient motor, from development of the fundamental theory and modelling of the system to a carefully designed prototype matched to a given requirement, and practically validated as a fully built prototype tested in excess of the designed speed. The detailed design specifications and the research procedures will be shown on the following chapters.

1.1 Thesis overview

This thesis demonstrates the research of a potential next generation mains powered high-speed power-dense electric motor for the sponsoring company, which provides improved motor performance as well as reduced weight and size compared to their current machines. The whole thesis is structured as follows:

- Chapter one introduces the machine concept and the design requirements of target motor. The major design challenges and novelties are discussed.
- Chapter two presents a detailed discussion about previous research in the field of power-dense high-speed electric machines. With the required design specifications as the judging metrics, the advantages and disadvantages of different machine types are analysed.
- Chapter three to chapter six demonstrate the analytical research, design, finite-element validation and system simulation of the potential motors. The design optimization is affected by the interaction of constraints from the following five aspects: electromagnetic, mechanical, thermal, manufacturing complexity and motor cost. Particular attention is given to the analysis of various motor topologies and the estimation of each loss element.
- Chapter seven illustrates the detailed assembly procedures of the built prototype.
- Chapter eight shows the carried out validation tests of the fully assembled prototype.
- Chapter nine gives an overall set of conclusions for the whole project and plans for further work.

1.2 Project concept and specifications

The top motivation for this project is to design and build a power-dense high-speed electric motor which can be utilised in a mains powered domestic home appliance. Typical products in the same category are normally driven by the conventional brushed universal motors, resulting in a cheap solution for the drive system but the one with a number of shortcomings, such as heavy weight, big volume, high maintenance current commutator devices, restricted maximum spinning speed and relatively low system efficiency.

Getting the inspiration from portable battery powered products, a compact, high speed, low weight and cost brushless DC motor is considered for use in the targeted mains powered consumer goods. With the utilisation of high-residual flux density neodymium-iron-boron (NdFeB) permanent magnets and bespoke power electronics, the current generation of battery powered electric motor can accelerate to over 100,000 rpm operating speed in less than one second, and features a high electrical to mechanical system efficiency with over $20 kW/L$ power density. It is desired to apply such technology to conventional mains powered electric drive system to acquire the same benefits compared to predecessors. Enhanced performance on at least one of the following aspects is required while the other fields need to have the same level of performance:

- Motor efficiency
- Motor cost
- Motor size
- Motor weight
- Motor noise

Apart from the aforementioned design requirements, the constraints from motor packaging, mass production difficulty and final product casing deliver extra limitations on the motor overall dimensions as well as the size of drive system. The detailed design specifications are demonstrated as follows:

Design aspects:	Limitations:
System input power	750W
Motor power supply voltage	230V
Rated speed	150,000rpm
System efficiency	85%
Motor overall outer diameter	<30mm
Motor overall axial length	<30mm
Motor overall mass	<200 $grams$
Motor per-unit cost of used materials	<3 dollars
DC-link capacitance	<10μF

Table 1-1: Design specifications for the aimed high-speed motor

Table 1-1 demonstrates that the aimed motor is powered by the UK/EU mains supply (230V±10V), and features an ability to rotate at a rated speed of 150,000 revolutions per minute with 750 watts input power.

According to the required minimum 85% system efficiency, it considers not only the electromagnetic losses such as copper loss and iron loss, but also the drive losses including rectifier diode loss, input inductor loss, dc-link capacitor loss, switching and conduction loss, etc. The rotating wind-friction loss is regarded as a significant component of the total losses as well.

Moreover, the received material prices in this project from the industrial suppliers includes not only the cost of the raw material itself, but also the manufacturing cost which could be as high as approximately 60% of the overall fee in some cases. Due to the strong concern over the motor packaging and the expense and reliability of the applied electronics, the dc-link capacitance has to be kept to the minimum yet allowing the machine with an ability to operate with close to 100% ripple on the dc-link voltage.

Additionally, the cost of assembling and manufacturing procedures of the motor in mass-production are taken into account as well. Although it is temporarily regarded as a secondary factor in the design at current stage, the expenses on both the manufacturing equipment and the

establishment of automatic assembling line can be significantly decreased by way of introducing the simpler winding approach and the larger manufacturing tolerances as well as the reduced assembly steps.

1.3 Project challenges and novelties

The design of a power-dense high-speed electrical motor tends to be a systematic task, demanding a multidisciplinary analysis that considers the effects of electromagnetic and mechanical as well as thermal aspects. The significant challenges in all three design domains push the capabilities of the materials and the system to their maximum to achieve the required performance.

Specifically speaking, due to the conducted high-speed operation, the induced rotational forces on the rotor are essentially large, leading to dangerously high level of motor stress which can result in rotor deformation or even catastrophic failure of the spinning rotor. Besides, rotor resonance is another potential risk in high-speed motors. If the frequency of rotor rotation or excitation torques matches a natural frequency of vibration, it can cause, excessive noise, unnecessary bearing loss, increased bearing heat or failure of complete rotor system due to the shaft deformation. When designing high-speed electric machines, accurate prediction of the stress and natural frequencies of the rotor is therefore critical.

The thermal challenge in the design lies in staying below the maximum operating temperatures in each motor component. In all types of motors, overheating of the phase windings beyond the rated temperature limit can cause severely accelerated degradation of motor insulation, resulting in the risks of short circuits or even fire. Excessive winding temperatures additionally raise the winding resistance, leading to a drop of the motor efficiency.

Regarding the machines fitted with permanent magnets, a temperature rise in the utilised magnets can result in an increased risk of demagnetisation. With the increase of the magnet temperature, the residual flux density is gradually reduced proportionally to the temperature growth on magnets, offering comparatively lower flux density in the machine’s effective air-gap. Consequently, a higher electrical loading becomes necessary to maintain the same level of output torque. This compensation lead to additional copper loss on motor phase coils which lowers down the achieved efficiency.

Although the temporary demagnetisation effects on magnet is reversible, and can be recovered by cooling magnet temperature back to nominal level, the increased risk of irreversible demagnetization at elevated temperatures due to demagnetising armature flux is a serious concern for the performance of the motor and could lead to scrapping of the product if it has not been accounted for in the design stage.

Motor loss density is controlled by the ratio of generated motor total losses to machine's active volume. In electrical motors, the produced output torque is significantly impacted by the coupling between magnetic loading and electrical loading.

$$P_{out} = E * I = T_{out} \times \omega \qquad (1-1)$$

From Equation 1-1, it shows that a rise of machine's operating speed contributes to the reduction of motor's required output torque for a target power. Given that torque scales with rotor volume in typical PMSM machines this in turn results in the choice of a decrease in the machine's overall dimensions or a reduction in the electrical and magnetic loading to improve motor efficiency.

As discussed in previous paragraphs, the rise in the machine's operational speed brings tighter restrictions in size due to the limits of mechanical strength as well as an increase in frequency dependent losses such as iron loss and proximity and skin effect losses. These increased difficulties for high-speed machines force the designer to apply the appropriate weighting factors in each design domain, to push the motor performance to an acceptable boundary through an iterative process.

The previous defined limits on motor size and weight as well as the material costs bring about additional challenges in this project. As the designed motor is targeted to be adopted in a potential portable consumer product, it is essential to keep its overall weight and volume, as well as production cost, to a minimum. Typically, in order to achieve the best electromagnetic performance and satisfy both mechanical and thermal requirements of an aimed specification, most prior articles utilise high-performance, high-strength but costly materials in any prototype to maximise the machine efficiency whilst keeping both the machine size and weight small. In previous research, the commonly utilised but comparatively expensive materials include amorphous steels for stator, multi-stranded wires for winding coil and high-residual flux density rare-earth magnets for rotor as well as high strength low weight sleeves for mechanical containment [1-17].

In contrast to the previous studies, this project features a unique demand of designing with the minimised motor cost in mind from the very beginning. Starting from the preliminary design on the machine topology, the optimised structure aims to deliver a reduced motor per-unit cost via eliminating the use of costly materials whilst achieving the design requirements on both motor weight and size. At the same time, the balance between machine cost and efficiency is investigated by simulation of the losses under various raw materials and manufacturing processes. The detailed discussion about the target machine in this project will be discussed in the following chapter two.

The topology of the designed machine can contribute to its competitive advantage through a simple winding process as well as demonstrating a low sensitivity to the manufacturing tolerances, thus saving in the associated costs of high precision manufacturing procedures.

1.4 Conclusion

To summarise, this chapter demonstrates the major motivation for this research and the particular project specifications to design a highly efficient, high-speed, low cost mains powered electric that is both light weight and low cost. It is accepted that replacing the old brushed low-speed electric motor with the new power-dense, high-speed electric drive can provide such advantage improved motor efficiency, decreased motor per-unit raw material cost, reduced machine size and simplified mass-production procedures.

The motor specification targets a 25% increase in motor operating speed over pervious commercial designs, which is expected to deliver a compromise solution between greater power density and increased efficiency.

In addition to the contents stated above, the key challenges in this project lie in the various design constraints are also demonstrated in this chapter. The concerns over the motor per-unit cost are highlighted as significant as the traditional design aspects, such as electromagnetic, mechanical and thermal limits. A key aspect is that from the initiation of the design process, the influence on machine structure of the cost minimisation strategy is taken into consideration; not just in terms of raw material costs only but also manufacturing processes and the benefits of making it competitive for mass-production.

Chapter 2 : Literature Review

2.1 Introduction

During the past decade, high-speed electric machines have attracted increasing attention due to their potentials for increased power density, improved system efficiency, decreased overall weight and size, etc. The large number of published scientific papers related to this field can be categorised into various groups focussing on the following stated areas:

1. Improved analytical calculations of machine loss elements, output torque and power, as well as the distribution of generated magnetic fields. [18-27].
2. Optimizations of machine topologies according to the specific design constraints using multiphysics mathematical models and finite-element simulations [4, 13, 14, 28-39].
3. Development of drive power electronics with a particular focus on the reduction of electronic losses, printed circuit board (PCB) size and the elimination of insignificant electronic components. [40-45].
4. Mechanical analysis on the rotor dynamics and the vibration modes at varied operating speeds [5, 46-49].
5. Thermal modelling and management based on different machine topologies and various cooling techniques [50-53].
6. Implementation of automatic error detection, fault isolation and fault tolerance capability in electric drive system [54-59].

As this project is mainly focused on the design in the electromagnetic, mechanical and thermal domains, particular attention is paid to the papers associated with those, and covered in point one, two, four and five.

2.2 Definition of high-speed

The definition of the term "high-speed" tends to be quite ambiguous on some occasions. Commonly, it can be claimed without argument that a 100W electric motor with over 500,000rpm operating speed [2] can be categorised in the high-speed range due to its high absolute speed. Nevertheless, an electrical machine which operates at a much lower rotating speed whilst delivering much higher output power, for instance, can also be considered as high speed. For instance, a machine spinning at only 10,000 revolutions per minute (rpm) with up to 12,000kW shaft power [60] has its electromagnetic, mechanical and thermal capabilities all pushed to their boundaries, presenting the same level of design difficulties as the machine with absolutely high operational speed.

In general, when the rotating speed in a machine becomes as close as possible to its theoretical maximum value as defined by restrictions from the electromagnetic, mechanical and thermal domains, it is reasonable to claim that this machine is high speed even if the absolute value of its rated speed is relatively low. Consequently, the classification of high-speed machines is not simply performed using their absolute speed value, but depends on all the interacting factors including power level, rated speed and rotor dimensions. In industry and academia, there are two different approaches to define the term "high-speed".

2.2.1 Categorization of high-speed machines in industry

The first classification method which is commonly applied to define the term "high-speed" for electrical machines in industry was initially derived and broadly used by a commercial company, Torquemeters [60], linking both a machine's rated power and operational speed. A introduced coefficient '$n\sqrt{P}$' is introduced as the empirical metric for comparison, where n refers to the rotating speed in rpm and P presents the machine's rated power in kilowatts (kW). The calculated values from different machines help to give a quick and direct comparison to illustrate the level of design difficulties and the categorised speed range of each machine.

According to the evaluation criterion from the company [60], electrical machines with $n\sqrt{P}$ value over 1,000,000 are classified in the super-high-speed range, which proves to be truly challenging to achieve in industry for commercial products under the existing material and manufacturing technology. Machines with between 500,000 to 1,000,000 coefficient values are

categorised as the high-speed applications while those featuring lower values of less than 500,000 are considered as the normal speed due to their moderate manufacturing difficulties as well as the use of cheaper, less capable materials. As this approach is closely related to the machine's power rate, it can also be regarded as the classification method for high-speed high-power machines.

On the other hand, this classification approach becomes limited once the absolute value of machines' rated speed turns to be extremely high. Specifically speaking, when the machine's operating speed is at an absolutely high level, the induced iron loss and proximity loss are both significantly larger than those in a low-speed situation due to high frequency of motor rotating magnetic field. These losses increase more than linearly with frequency, and can quickly become dominant at frequencies greater than several thousand hertz. Figure 2-1 below shows the loss density for different stator core-back materials under varied core flux frequencies. The graph indicates that, with the rise of core flux frequency, the loss density values for all kinds of materials are dramatically increased. Amorphous steels feature the lowest loss density in both low and high frequency ranges, but has the highest per unit price due to complex manufacturing procedures.

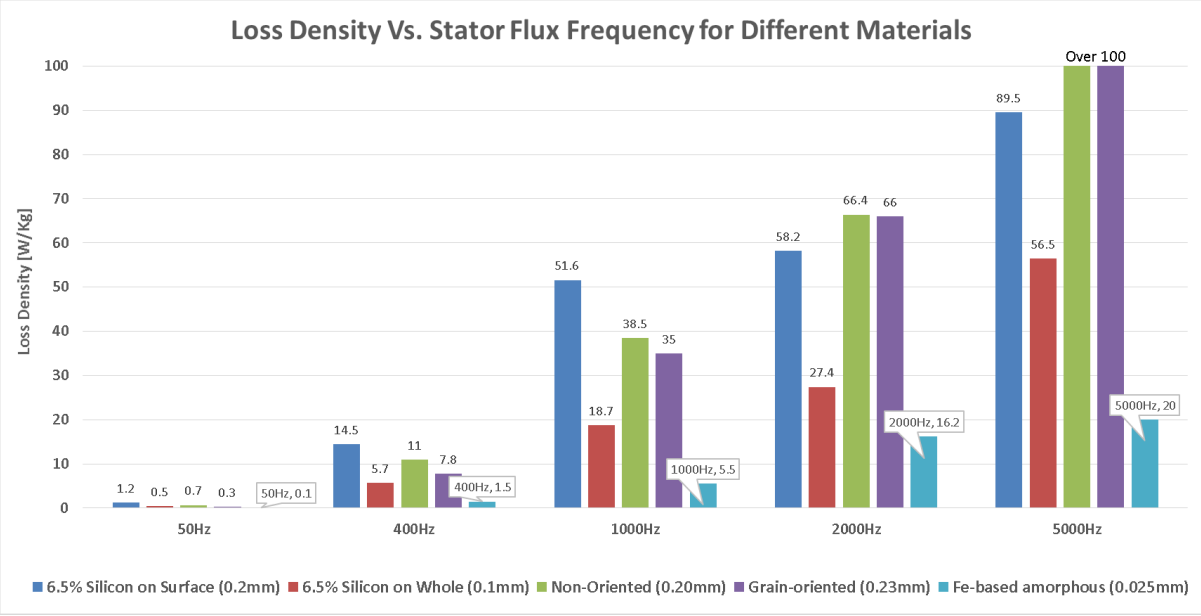

Figure 2-1: Loss density for different stator core-back materials under varied core flux frequencies

Due to the high rotor velocity, the generated wind-friction loss on the rotor surface also dramatically increases, becoming another dominant loss component compared to the traditional hysteresis and joule losses on a low speed machine. Therefore, machines with absolutely high operational speed can have a high working temperatures due to the higher losses presented above, coupled with their reduced size (due to their typically lower torques and mechanical limitations on their rotor volume), leading to them having high loss densities. This presents a thermal limit based on the capabilities of the utilised materials in the machine, which forces a reduction of machines' electric and magnetic loadings to ensure both the total losses and the generated heat are within the given boundaries. It then results in a less torque and hence lower power-dense design for the machine.

In addition, under the same motor cooling conditions, to avoid the undesirable winding overheat, the copper diameter of wire has to be increased to reduce the effective current density, resulting in the reduced number of turns in the given winding space for high speed designs of the same winding filling factor. This outcome leads to the reduced motor phase inductance, which for inverter-fed electric drives leads to a larger variation on the phase current during a switching period. This causes a relatively larger current ripple which can worsen the effective total losses that were intended to be decreased by the loading reduction and further reduce the achieved machine power density.

According to the aforementioned reasons, most of the electrical machines with enormously high speed actually have relatively lower value of the coefficient $n\sqrt{P}$, showing the limitation of this categorization approach as illustrated in [61].

2.2.2 Categorization of high-speed machines in academia

In academia, another classification theory is raised by A. Binder and T. Schneider to categorise the range of high-speed machines through consideration of the rotor's size and speed [61]. Theoretically, a cylinder rotating about its centroid can bring about an undesirable mechanical stress due to the induced centrifugal force, which is proportional to the square of velocity as well as the square of radius.

According to the research in [5], an empirical standard of the high-speed classification is given that machines within the 100 to 250m/s circumferential speed range can be categorised as the high-speed applications.

2.3 Comparison of different motor types

Generally speaking, all electrical machines can be defined as either alternating current or direct current machines, based upon the nature of their armature currents. Figure 2-2 below demonstrates a classification of the most commonly used types of electrical machines in both industry and academia via a node tree diagram. Each type of machine has its own advantages over the others, which are appropriate for use of certain applications. The following several paragraphs discuss those kinds of machines that are suitable for high-speed applications. The attractiveness and restrictions for those machine structures are discussed. At the end of this section, a summary of the chosen type of electrical machines is concluded in consideration of the stated project specifications in chapter one.

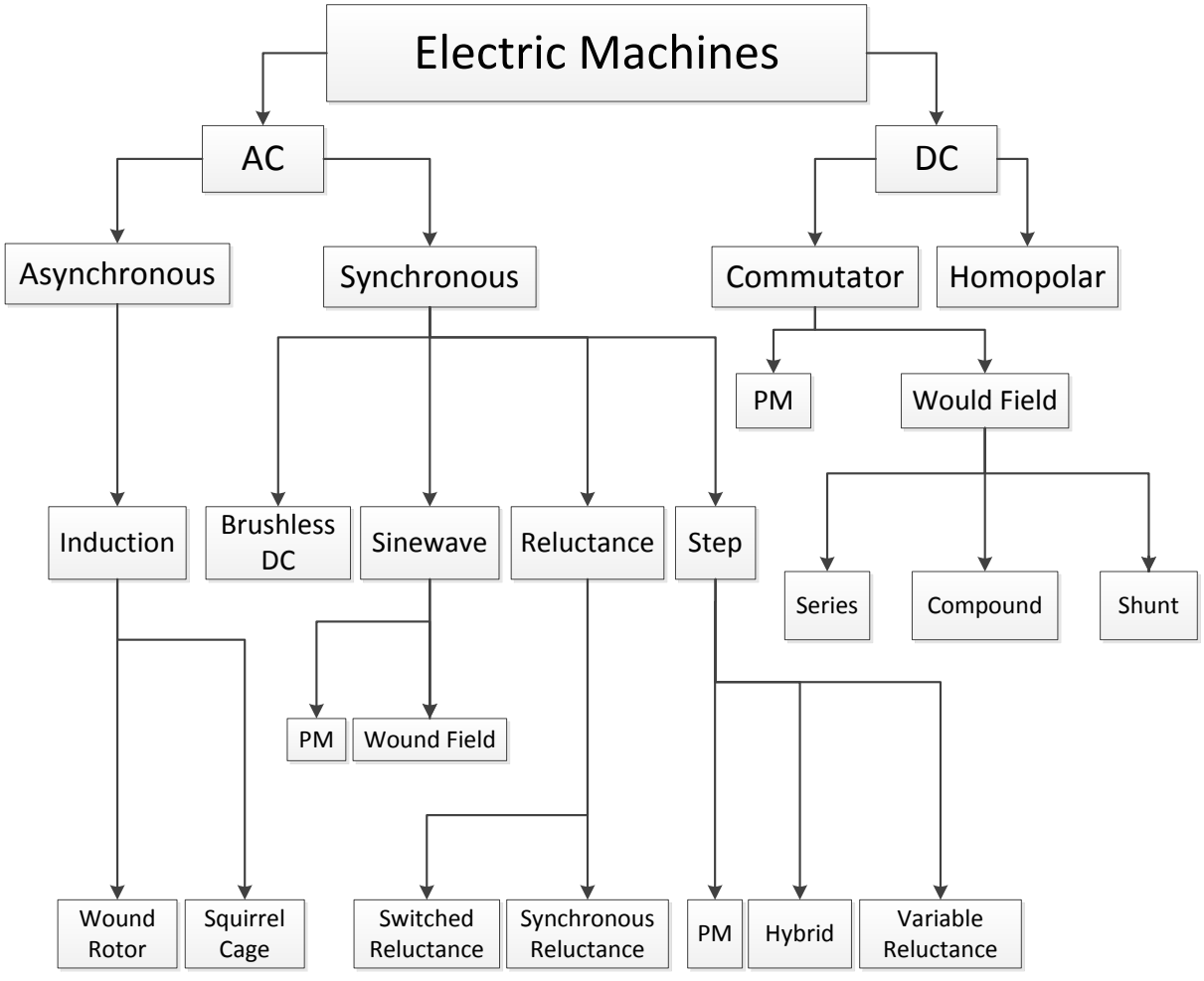

Figure 2-2: Node tree diagram of different electrical machine types

2.3.1 Brushed DC machine

Brushed DC machines are a class of mechanically commutated electrical machines which have been widely utilised in commercial and industrial products to drive mechanical loads via electric power during the past 100 years. This type of machine features the advantages such as a straightforward structure, low cost and simple control circuitry. However, due to the large volume of copper made armature windings, vulnerable brushes and commutator ring, relatively low system efficiency and high maintenance, brushed DC machines prove not to be an appropriate option for the high-speed applications, especially those machines demanding absolutely high values of the rated speed.

2.3.2 Induction machine

Induction machines transfer power to the rotor by means of electromagnetic induction with no mechanical commutator, in order to construct the rotor magnetic field for torque generation. Due to the merits of the naturally high mechanical strength of the rotor, low manufacturing difficulties and high reliability, this kind of machines has been broadly investigated and applied in high speed high power applications in different fields. For instance, in paper [10], it illustrates a systematic research work of design , analysis and testing of an induction motor which delivers 120kW shaft power with 45,000rpm maximum rotating speed. By way of utilising a simple solid rotor structure (squirrel cage structure), it pushes the boundaries of mechanical strength outlined in the previous section to achieve over 200m/s circumferential speed. Similarly, paper [9] presents a design for a high-speed high-power-density induction machine with laminated rotor structure. By changing the rotor topology from the conventionally used round-shape bar design to a pear-shape bar design, it can generate a great level of rated power density of $28kW/L$ and higher than 200m/s peripheral speed. In [35], a multi-domain design of a high-speed induction machine is described, involving with all impacts from electromagnetic, mechanical and thermal aspects. With the optimised split ratio of the rotor diameter to the total motor diameter, the rotor surface speed of the machine can reach the value of over 200 meter per second, pushing the electromagnetic and mechanical as well as thermal performance to their limits. Other investigated high-speed induction machines with either over 100m/s circumferential speed or over 500,000 value of the coefficient $n\sqrt{P}$ are demonstrated in [62-65] for the applications of electric vehicle, electric pump and centrifugal compressor.

However, this does not mean that induction machines are appropriate for all types of high speed applications. From the reviewed literatures [9, 10, 35, 62-66], it indicates that the high-speed applications which employ induction machines as electric drive system generally have a comparatively large overall machine size and high level of output power. For small power machines, the generated losses associated with inducing the rotor magnetic field result in both power density and motor efficiency to be poor compared to those machines using permanent magnets to construct the rotor field. This disadvantage limits the practicability of induction machines in use of low power-level, small size domestic and portable appliances, despite their low relative cost.

2.3.3 Reluctance machine

In reluctance machines, the output torque is generated by using the variance of stored magnetic energy due to the change of reluctance at different rotor positions. There are two main types of reluctance machines: switched reluctance machines and synchronous reluctance machines. Due to those attractive advantages such as simple rotor structure, high rotor mechanical stiffness, low rotor inertia, low machine material cost and decent reliability, this type of machine has drawn a great deal of attention in research of high speed applications, and is popular in a wide range to replace low efficiency induction machines [67] with the same overall size. It also competes with rare-earth permanent magnet machines [68] with only a little compromise on the machine efficiency in comparison to a significant cost saving by removing the need of magnets.

With the help of composite materials and novel doubly salient rotor structure, an experimental switched reluctance motor with 200,000rpm rated speed and 1kW shaft power was designed and produced in [40] to illustrate the feasibility of this type of machine in absolutely high speed applications. In Ref. [68], as the price of high-residual flux density rare earth magnets has been significantly boosted since 2008 and hit the peak at 2011, a small size switched reluctance motor with over 100m/s peripheral speed is utilised to replace traditional permanent magnet motors for an engine supercharger application. Even in early 2017, the cost of Neodymium-Iron-Boron magnets is still 10 times higher compared to the normal ferrite magnets with the price of over $40 per kilogram [69]. Compared to the machines equipped with rare-earth magnets, the switched reluctance motor benefits from the elimination of expensive magnets, a robust laminated rotor and improved reliability in high temperature working environments. The

authors of [41] illustrate a promising alternative to induction motors to drive a pure electric vehicle or hybrid car. Two switched reluctance motors in the medium-speed range and high-speed range are designed, optimised and compared to each other to study the influence of high operational speed on the machine's performance of power density, motor efficiency and acoustics.

However, similar to induction machines, reluctance machines also feature several limits for some typical applications. Because of the machines being highly dependent on the variation of magnetic reluctance around the rotor periphery, the thickness of machine's effective air-gap has to be maintained as small as possible to minimise its contribution to the reluctance paths, and so decrease the phase current for the required toque. On the other hand, the minimised motor air-gap increases the accuracy of required manufacturing tolerances, adding extra difficulties as well as cost in mass-production, especially for small size applications. Moreover, without the use of high-residual flux density permanent magnets to generate the rotor magnetic field, reluctance machines have naturally lower torque density and larger overall size compared to the same torque level permanent magnet machines. This outcome makes it an unattractive choice for relatively small-size but power-dense high-speed applications. The enhanced rotor mechanical robustness cannot compensate the disadvantage of reduced power density in compact, high speed designs.

Additionally, it is well known that the operating torque ripple in reluctance machines is naturally high, which along with the high radial magnet forces on the stator teeth, can cause unattractive acoustic noise and rotor vibration which are critical in a consumer goods application.

2.3.4 Brushless permanent magnet machine

In comparison with brushed DC machines, electronic commutation equipment is utilised in brushless permanent magnet machines to replace the traditional mechanical commutator to apply the direct current at the appropriate time in each phase. Permanent magnets are introduced and fitted on the rotor to set up a rotating magnetic field, coupling with the armature field to generate the output torque. With the further development of fast switching speed and low switching loss power electronic devices as well as high-residual flux density and high temperature resistive permanent magnets; the rated speed, size, weight, power density and

efficiency of brushless permanent magnet machines have been knowingly enhanced in relation to competing machine types. These factors make this sort of machine appealing to both academic and industrial researchers for varied high-speed and super-high-speed applications with compact overall size.

Ref. [4] and [13] demonstrate a series of research where all the essential design features of stator topology, rotor structure, winding approach and bearing system are investigated to achieve a high-speed permanent magnet generator which is driven by a micro turbine. The machine's maximum operating speed can exceed 100,000 revolutions per minute along with over 100m/s circumferential speed. In paper [12], a high-speed permanent magnet synchronous motor for an air blower cooling fuel cells has been designed, manufactured and tested, delivering about 215m/s peripheral speed. Although this motor requires 15kW shaft power, the overall outer diameter of the rotor is only 34mm when the total stack length of machine is within 50mm. Moreover, in paper [2], a three-phase, 1kW, 500,000rpm permanent magnet motor is designed as the direct drive for the turbo-compressor system. With the help of titanium made rotor sleeve and high-residual flux density permanent magnets, the designed motor achieves over 250m/s rotor surface velocity speed with high power density of over $65kW/L$. The overall motor outer diameter is only 25mm. Figure 2-3 below displays a direct comparison of manufactured motor components to a single match, highlighting the small scale on which such an ultra-high speed motor are built on with 30mm axial length only. Likewise, The authors of [1] show an fully assembled ultra-high speed miniature electrically driven turbo-compressor with up to 600,000rpm maximum operating speed. All design domains of electromagnetic, thermal, aerodynamic, drive inverter topology and control scheme have been taken into consideration. The dimension of the outer diameter of the integral system is limited to only 35 mm and the whole compressor length is just less than 80mm.

Figure 2-3: Comparison of manufactured motor components to a match [2]

For small size home appliances, as early as 1987, a permanent magnet motor has already been researched and utilised as direct drive to power a 10W, 150,000rpm handheld drilling tool in [11]. This 2-pole motor uses surface mounted samarium-cobalt permanent magnet rotor with small dimensions of just 7mm axial length and 3mm outer diameter to generate magnetic field. In [14], a permanent magnet synchronous motor featuring an output power of 2kW at 200,000rpm operational speed is designed and tested at room temperature to drive a centrifugal compressor. Compared to typical permanent magnet motors, it requires extra attention during the design to allow it to work properly at a cryogenic temperature of 77K only. With only 21mm motor active length and 35mm total stator outer diameter, this permanent magnet motor gives above $90kW/L$ power density. Paper [70] describes the conducted fluid field simulation of two ventilation systems to estimate the induced air friction loss on an inner rotor, high speed PM motor. It summarises an empirical equation for the calculation of rotor air friction loss based upon motor operational speed.

To summarise the reviewed literatures above, there is a clear trend that brushless permanent magnet machines are the preferred choice for high speed mini-size applications, offering highest power density and machine efficiency.

Nevertheless, this type of machine has its own shortcomings too. Firstly, both sintered and bonded magnets have lower mechanical strength compared to electrical steel [71-73], which in turn limits both the shape and size of the utilised rare-earth magnets in high-speed applications, adding extra challenging to the aimed motor design. Besides, the employed magnets are also

required to be fitted on the rotor using either an adhesive or a retaining sleeve, or else by being inserted inside the rotor structure. This outcome brings not only manufacturing difficulties, but also increased rotor failure modes in high-speed operation. Furthermore, the utilised conductive magnet materials can induce the unwanted eddy current loss on the rotor due to stator MMF and slotting effect, increasing the risk of demagnetisation during motor operation.

In addition, the price of high-residual flux density rare-earth permanent magnet is continuously fluctuating during the past couple of years. Due to the cost of magnet being a dominant factor in the total cost of this type of machine, the profitability of consumer good applications using this technology can be very sensitive to these fluctuations.

2.3.5 Permanent magnet claw pole machines using soft magnetic composite materials

In recent decades, claw pole motor topology has been considered for high-speed applications as well. In [74], the authors summarise the existing high-speed electrical machines in academia, where some typical high-speed claw pole motors and generators operate in a speed range from 80,000rpm to 100,000rpm, covering a power range of 25 to 50kW. In the same manner as the reviewed high-speed brushless permanent magnet machines in previous section, these machines utilise a small size rotor fitted with high-residual flux density permanent magnets to create rotor magnetic field, in contrast to the wound field rotor of traditional claw pole machines, delivering a high power density but lower mechanical stress under high-speed operation.

In contrast to a traditional laminated stator with only 2-dimensional (2-D) flux paths, claw pole machines use Soft Magnetic Composite (SMC) materials to form a complex 3-dimensional (3-D) shaped stator providing 3-D flux routes. The 3-dimensional stator made by SMC powders is manufactured through a complex sintering process, whose advantages and disadvantages for mass production are discussed in [75]. Reference [76] demonstrates a three-phase axial flux permanent magnet motor with SMC made stator core to reduce iron losses and cost, showing that it can generate 28% more torque compared to the sample motor with 2-D laminated electrical steel stator. In [77], it presents an improved data optimisation of targeted permanent magnet claw pole design with SMC cores, maximising the merit of magnetic flux concentrating.

The use of SMC materials allows a 3-D stator topology with isotropic magnetic properties. This therefore allows the researchers to place the stator materials where they can so as to achieve the maximum utilisation of generated flux from the adopted permanent magnets and coil volumes. Furthermore, the insulation layer on the surface of SMC particles helps to significantly narrow the potential eddy current loops inside the stator, which in turn minimizes the generated eddy current loss at high speeds, making SMC made machine an attractive proposition in high speed machine design.

On the other hand, the first main drawback of SMC made stator comes from mechanical side. The utilised sintering process in manufacturing limits the achieved maximum mechanical strength which turns to be considerably lower compared to electrical steel, requiring more mass for the same dynamic loads or placing limitation on acceptable vibrations and loads. Secondly, the insulation layers between particles dramatically reduce relative permeability compared to laminated silicon steel, which limits the achievable torque density because of the limited flux carrying capacity of the material. Furthermore, in comparison to most electrical silicon steel laminations, iron based soft magnetic composite materials have a larger hysteresis loop, leading to higher hysteresis loss during the operation. This can then cancel out the benefit of reduced eddy current losses at higher speeds. Evaluation of the benefits of SMC materials over silicon steel laminations must be performed on an application and frequency specific basis.

2.3.6 Summary of the chosen type of machine

To summarise, this section gives an overall review of all possible types of electrical machines for high-speed applications. Merits and drawbacks of each kind have been analysed, focusing on their key benefits and challenges for high-speed, power-dense and small size designs.

In line with the previous discussions, there is no benefit to be gained from pursuing brushed DC machines or inductance machines for the targeted application, owing to the root causes of weight, size, efficiency and mechanical robustness (brushed DC machines).

Considering the required absolutely high rated speed of 150,000rpm, reluctance machines and brushless permanent magnet machines as well as permanent magnet claw pole machines are all attractive. In a direct comparison between reluctance machines and brushless permanent magnet machines for designs with an absolute high speed [2, 6, 7, 40], the latter provides the capabilities of either relatively smaller overall size for a fixed power-level or better power

density for a given operational speed. Moreover, the acoustic noise and the operating vibration caused by the relatively higher torque ripple in switched reluctance machines also weaken the attractiveness of this type of machines for some high-speed applications, particularly in consumer good applications.

With regards to SMC materials, the low saturation flux density in stator requires a comparatively thicker stator to avoid flux saturation which increases both the overall volume and weight of machine as well as the induced iron losses. In addition, the lower mechanical strength of the SMC made machine poses a risk of damage during shipping, handling and product dropping test which prevents it being considered for this application.

In conclusion, a brushless permanent magnet machine has been selected in this project to be the best candidate for achieving the target operating speed of 150,000rpm and high power densities and efficiencies required by the project specifications.

2.4 Motor cost of the chosen type of machine

2.4.1 Review of motor cost in prior research

In recent decades, with the general use of expensive high residual flux density rare-earth permanent magnets and low loss density lamination steels in brushless permanent magnet machines to provide better system performance, the motor per-unit cost can be significant as it is sensitive to the price of these employed materials. Therefore, this kind of machine requires direct design effort to minimise the motor per-unit cost given that the intended application is a price sensitive consumer good.

Without changing the fundamental machine type, there has been little research focusing on minimising the motor material cost on high-speed power-dense permanent magnet machines. The influence of the use of low-cost ferrite magnets in an outer rotor permanent magnet synchronous motor is investigated in [78]. It indicates that a permanent magnet motor with ferrite magnets to generate a rotating magnetic field can deliver better machine efficiency as well as improved power density with the same level of motor cost compared to an induction motor, giving a promising option for small-size high-performance blower applications. Similarly, in [79], cheap ferrite magnets are inserted in the rotor for a permanent magnet synchronous motor design to eliminate the use of costly high-residual rare-earth permanent magnets in a flux concentrating arrangement which can improves their contribution to air-gap flux density and their mechanical resistance against centrifugal force.

The authors of [80] discuss that a direct comparison among bonded magnets, ferrites magnets and hybrid magnets (60% neodymium-iron-boron and 40% ferrites) in a three-phase fan motor application using both finite-element analysis and prototype tests. According to the simulated results, it indicates that the design using ferrite magnets offers the lowest machine cost for the same electromagnetic performance compared to the other two designs, but the dimensions of the built ferrite magnet motor with respect to the overall stack length and the outer diameter are comparatively larger accompanied by the increased total motor mass.

For absolutely high speed applications, where power density is also one of the key factors for portability, in order to achieve the better electromagnetic performance whilst keeping both the machine weight and size to the minimum, it is still beneficial to stick with high-residual flux

density but rather expensive materials. Designs where the rotors are fitted with costly high flux density permanent magnets and the titanium or carbon fibre made rotor sleeves are illustrated in [1-6, 12-16] for absolutely high speed permanent magnet machines. In order to minimise the induced iron loss under high-speed operation, amorphous steel is utilised in [1-3, 6]. For slot-less designs, stranded wires are introduced to limit the generated proximity loss [2, 17]. Both these options can enabled smaller, lighter and more efficient designs but at an increased material cost.

2.4.2 Motor cost analysis for the aimed motor

In this project, the considered motor per-unit cost of the utilised materials consists of the three major components: laminated stator, copper windings and rotor without shaft. The cost of motor drive system as well as the mass-production line cost are not considered at the current stage. According to information received from industrial suppliers, Table 2-1 below demonstrates the types of the available materials and the estimated purchasing prices for different motor components.

Material Types:	Price:
Solid Wire	$10/kg
Stranded (Litz) Wire	$40/kg
Non-oriented, 0.2mm Thickness Electrical Steel	$10/kg
6.5% Silicon, 0.2mm Thickness Electrical Steel	$40/kg
0.65-0.9T Br Bonded Magnet	$55/kg
0.95-1.05T Br Bonded Magnet	$70/kg
1.1-1.35T Br Sintered Magnet	$135/kg
A Pre-Formed Carbon Fibre Rotor Sleeve	≥ $1 per motor

Table 2-1: Comparative price list for different motor components

The prices listed in Table 2-1 of permanent magnets and rotor sleeve include both the cost of raw material and the manufacturing processes to achieve the expected shapes specifically

required for this research. Depending on different manufacturing requirements, the latter part of cost is varied and can be as much as approximately 60% of the total price.

Typical thin gauge, non-oriented electrical steels utilised in this project have a thickness of 0.2mm with a silicon content around 3.5% which are available from a wide range of industrial suppliers with reasonably price. The 6.5% high silicon grade electrical steels have the same thickness as the non-oriented one of 0.2mm, but features a comparatively lower loss density when core-back flux frequency is higher than 2000Hz (shown in Figure 2-1), making it competitive for high speed applications. However, it features a four times higher price and a much more niche property that is brittle and difficult to work with due to high (6%+) silicon content. Therefore, it delivers a great advantage for high speed applications by decreasing the eddy current losses, but at a significant cost rise.

From Table 2-1, it can tell that the expense of the rare-earth permanent magnets can be a dominant factor of the motor total cost due to their highest price per unit weight. It is significant to note that low-loss materials, such as the stranded wire and high silicon laminations, both have knowingly higher marked prices in comparison to the normally selected alternatives. Additionally, the cost of utilising a pre-formed carbon fibre rotor sleeve would represent a significant portion of the total allowable price. Considering the targeted three-dollar maximum motor per-unit cost of the utilised raw materials, there is significant cost pressure in avoiding the use of these expensive materials and significant design innovation must be employed to ensure they are not required to achieve the performance specification, at the risk of the cost specification.

Consequently, the investigated motor designs in the following chapters will eliminate the utilisation of expensive motor components as well as costly optional materials, for instance, carbon fibre rotor sleeve, stranded wire and high silicon lamination steel, to minimise the motor per-unit cost whilst keeping the achieved motor efficiency within the acceptable range.

2.5 Conclusion

This chapter has delivered a systematic review of the existing research for high-speed electrical machines in both industry and academia. It has also analysed the advantages and disadvantages of different types of machines, focusing on the special benefits for high-speed, power-dense and highly efficient as well as light weight applications. Depending on the previous discussions in this chapter, brushless permanent magnet motors are selected as the fundamental machine type to be utilised to achieve 150,000rpm, 750W high-speed motor to drive the aimed domestic home appliance. Due to the reason that the motor per-unit cost of the utilised raw materials is regarded as one of the significant constraints, the normally employed high-quality, high-performance and high-price raw materials for different motor components are strictly restricted in use during the design procedures.

Next four chapters will demonstrate an investigation of various motor topologies for brushless permanent magnet motors. The following design features including rotor structure, stator construction, magnetization patterns, pole and phase numbers, phase connection methods and winding approaches will all be specifically discussed in the individual sections.

Chapter 3 : Design of Motor Topology

3.1 Introduction

This chapter presents an organised study of various motor topologies for brushless permanent magnet motors, stating the advantages and disadvantages of each machine structure under consideration, based upon the aimed machine characteristics of high operational speed, high power density and small overall size as well as low cost. The selected machine construction features the capabilities to achieve the targeted machine electromagnetic performance whilst satisfying the constraints from the other essential design factors of rotor dynamics, operating temperature and motor per-unit material cost.

In the following sections, particular attention is given to the below listed six aspects of motor construction to determine the most appropriate design in the project:

I. The rotor structure;
II. The stator construction;
III. Magnet magnetization patterns;
IV. Number of poles;
V. Number of phases;
VI. Winding approaches;

3.2 The rotor structure

3.2.1 Radial flux or axial flux

For permanent magnet motors, the selected rotor structure sets the magnetic flux direction of the created excitation field. Commonly, there are two types of the distributed flux patterns in the machines, classified by the direction of the effective magnetic flux travelling from rotor permanent magnets to the stator core.

Concerning most conventional, cylindrical permanent magnet motors, the direction of the magnetic flux flowing from the rotor to the stator have the same orientation as the radius of the shaft, which results in these motors being regarded as radially distributed flux electrical machines (RFM). For those machines whose magnetic fields travel through the motor air-gap to the stator in a direction parallel with the axis of the rotating shaft, the term ‘axially distributed flux electrical machines (AFM)’ is utilised. Figure 3-1 shows the basic structures of permanent magnet motors with radially and axially distributed flux patterns. On the left, it is the topology of an inner rotor, radial flux motor, whilst on the right is the geometry of a single sided, axial flux, permanent magnet motor.

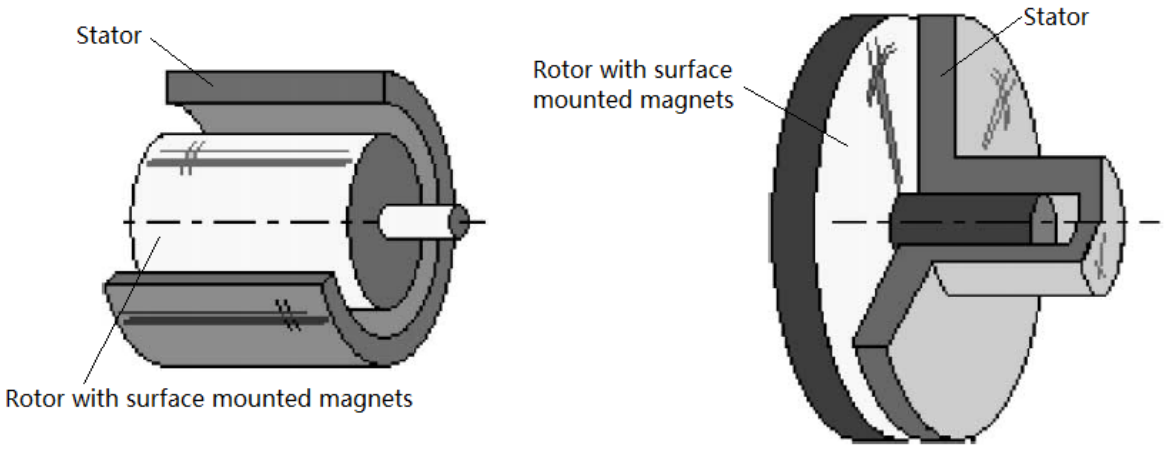

1. Structure of a typical radial flux motor.
2. Structure of a typical axial flux motor.

Figure 3-1: Basic structures of different flux pattern permanent magnet motors [81]

Although radial flux machines are dominantly utilised in a wide range of fields for both industrial and domestic applications, the first practically built permanent magnet electrical machine was actually an axial flux machine made by Michael Faraday in 1831 [82]. Owing to

the pancake shape of both rotor and stator, this class of axial flux permanent magnet machines is also known as a disc-type electrical machine, due to a relatively small axial length and large overall outer diameter, compared to radial flux machines with the same level of output power.

The unique flat shape of axial flux electrical machines gives the capability to make full use of the cross section space perpendicular to the axis of the rotor shaft to generate comparatively more power and torque for a given overall volume. The effective air-gap in axial flux permanent magnet machines is controlled by the actual distance between the rotor and stator along the direction of the shaft axis. By increasing the air-gap via axially separating the rotor and stator, the induced air-gap flux density can be reduced to implement field weakening.

Because of the high torque density and compact construction, axial flux electrical machines are competitive candidates for a range of industrial applications including the powertrains of hybrid electric vehicles, integrated in-wheel electric drive systems, overhead hoists and wind turbine generators. The unique pancake shape results in a comparatively large overall outer diameter which contributes to a high moment of inertia, which can be beneficial for the flywheel energy-storage systems. But of course, axial flux permanent magnet machines are not appropriate for all applications. Their natural disadvantages hinder the general use of them at those applications with high absolute speed.

One disadvantage of axial flux motor is the large magnetic force between rotor and stator for single sided machines. Radial flux electrical machines have symmetrically located magnets on the rotor so that the effective total magnetic force is zero in no load condition. Figure 3-2 below illustrates the cross-section views of two-pole, four-pole and six-pole radial flux permanent magnet motors, showing the direction of the induced magnetic forces on the stator. The graph demonstrates how there is always a pair of magnetic forces of equal value but in opposing directions in radial flux machines. Consequently, the resultant magnetic force is zero.

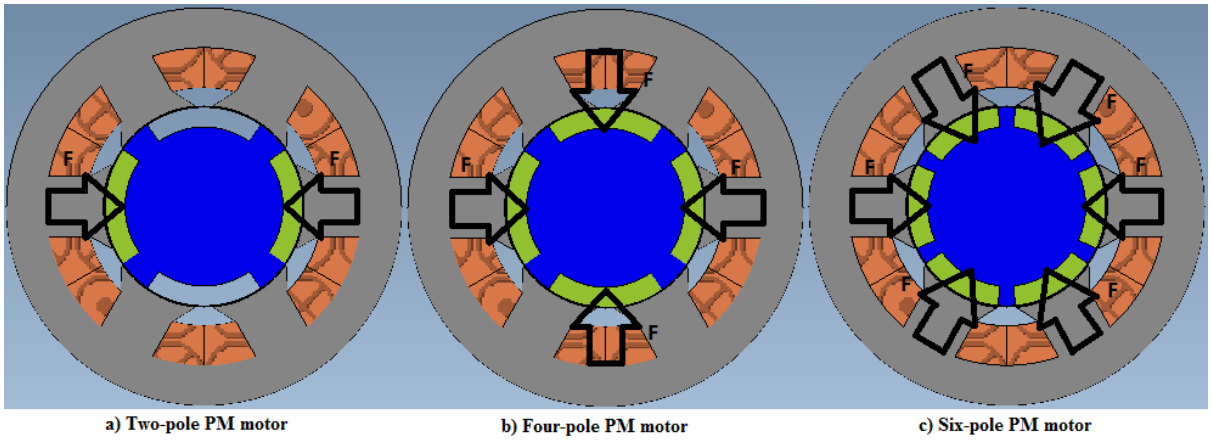

a) Two-pole PM motor b) Four-pole PM motor c) Six-pole PM motor

Figure 3-2: Induced magnetic forces of PM motors with different number of poles

Figure 3-3 below presents the cross-section view of a single sided axial flux permanent magnet motor, indicating the induced magnetic forces. The resultant magnetic force is no longer zero and is along the axial direction. To maintain the operational stability and the required performance, it is essential to maintain mechanical strength of the shaft, which in turn may increase the material cost. In industry and academia, multi-stage structure of axial flux machine is used to eliminate the impact of resultant axially magnetic force. Figure 3-4 illustrates a three-stage axial flux permanent magnet motor [83]. The arrows indicate that the net magnetic force on the stator is zero.

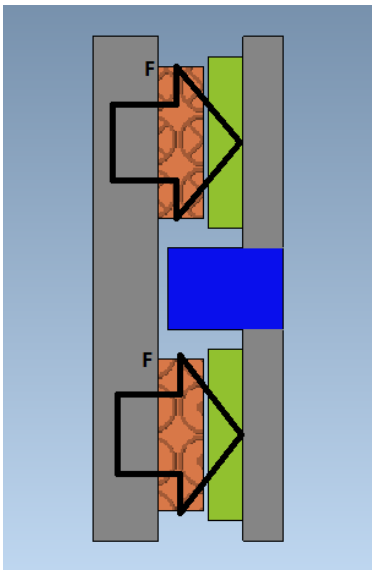

Figure 3-3: Induced magnetic force for the single sided axial flux machine

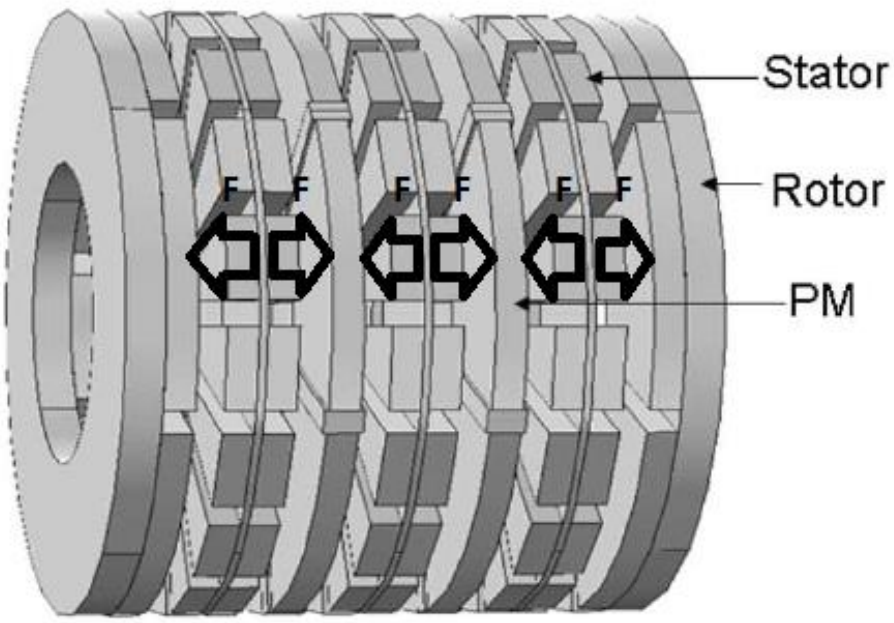

Figure 3-4: Three-stage axial flux permanent magnet motor [83]

The authors of [83] discuss the design of a targeted motor for downhole applications at high operational temperature. Three candidates are considered: a conventional radial flux motor, a multi-stage axial flux motor and a transverse flux motor. A direct comparison of output power, torque density and motor efficiency is given for the same overall outer diameter, current density, electrical loading and rated speed. The efficiency of the multi-stage axial flux motor proves to be the lowest, owing to the comparatively large amount of the end-windings. By increasing the number of poles, the effective motor efficiency is improved because of the reduction of the overall end-winding length. Nevertheless, the increased pole number requires a higher electrical frequency, giving increased iron losses and higher switching losses in the control power electronics.

Another shortcoming of axial flux permanent magnet machines results from mechanical limits which restrict their use in the aimed high speed applications. Chapter one discusses that there are two mechanical limitations on the spinning rotor: one is the generated rotor stresses which limit the rotor radius; the other is caused by rotor resonance, which can dramatically affect the maximum feasible axial length of rotor. The first of these two mechanical constraints is the dominant limiting factor for practical high-speed axial flux permanent magnet motors.

Because of the large overall outer diameter and comparatively short axial length, the rotor core in the axial flux motor core-back can be assumed as a homogenous solid disc with the overall outer radius R_{out}. Meanwhile, the fitted permanent magnets on the rotor can be considered to be a uniform annular disc of outer radius R_{out} with a central hole of radius R_{in}. Figure 3-5 below illustrates the graphs of the equivalent homogenous solid disc and annular disc for axial flux motor core-back and adopted magnet respectively with labelled dimensions.

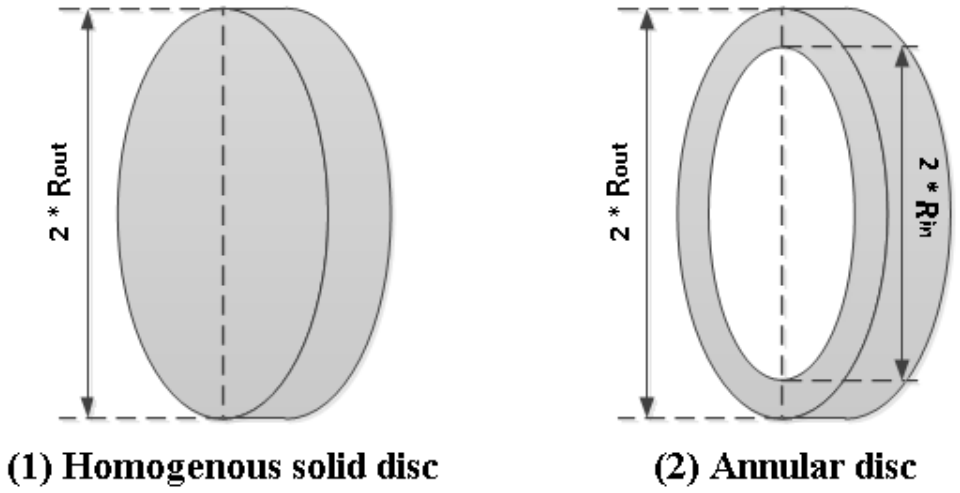

Figure 3-5: The equivalent homogenous solid disc and annular disc for axial flux motor and its adopted magnet respectively with labelled dimensions

As stated in [84], the generated tensile stresses on both the motor core-back and the adopted permanent magnets for the two-dimensional analysis is shown as the following set of Equations 3-1, 3-2, 3-3 and 3-4 [84].

$$\sigma_{r1} = \frac{1}{8}\frac{\delta\omega^2}{g}[(3 + \mathrm{v})(\mathrm{R}_{out}^2 - \mathrm{r}^2)] \qquad (3-1)$$

$$\sigma_{r2} = \frac{3 + \mathrm{v}}{8}\frac{\delta\omega^2}{g}\left(\mathrm{R}_{out}^2 + R_{in}^2 - \frac{R_{out}^2 R_{in}^2}{r^2} - \mathrm{r}^2\right) \qquad (3-2)$$

$$\sigma_{t1} = \frac{1}{8}\frac{\delta\omega^2}{g}[(3 + \mathrm{v})\mathrm{R}_{out}^2 - (1 + 3\mathrm{v})r^2] \qquad (3-3)$$

$$\sigma_{t2} = \frac{1}{8}\frac{\delta\omega^2}{g}[(3 + \mathrm{v})(\mathrm{R}_{out}^2 + R_{in}^2 + \frac{R_{out}^2 R_{in}^2}{r^2}) - (1 + 3\mathrm{v})\mathrm{r}^2] \qquad (3-4)$$

From the above shown series of equations, the Equation 3-1 and 3-3 calculate the generated radial tensile stress σ_{r1} and the tangential tensile stress σ_{t1} respectively on the assumed homogenous solid disc shape motor core-back. In these equations, v is introduced to stand for Poisson's ratio of the chosen materials and δ shows their density; ω is the rotor's angular velocity, g is the gravitational acceleration and r is the radius of stress measurement point.

The induced tensile stress is proportional to the square of the machine's rotating speed. The following two diagrams Figure 3-6 and Figure 3-7 demonstrate the trend of the maximum tensile stress along with varied overall outer diameter at a fixed operating speed. The overall outer diameters of both two components are varied from 8mm to 20mm while the annular disc shape permanent magnets have a centre hole of two-millimetre radius. Figure 3-6 indicates that there is a growth in the generated radial tensile stress on both the motor core-back and the magnets when their overall outer diameters are increased. Likewise, from Figure 3-7, it can be seen that the rise in outer diameter is accompanied by an increased tangential tensile stress. The two graphs together demonstrate that the induced tangential tensile stress becomes dominant on the simplified annular disc shape permanent magnets. According to the data received from industrial suppliers [71-73], rare-earth permanent magnets have much lower tensile strength than electrical steel. For sintered ring-shape magnet, the maximum endurable tensile strength is about 130MPa; while for bonded one, this limit is significantly dropped by around 60% to 54MPa.

Consequently, the induced high tensile stresses on the brittle rare-earth permanent magnets in axial flux motors significantly limits its overall outer diameter in high speed applications. This outcome makes this type of motor an inappropriate option for the targeted high speed products.

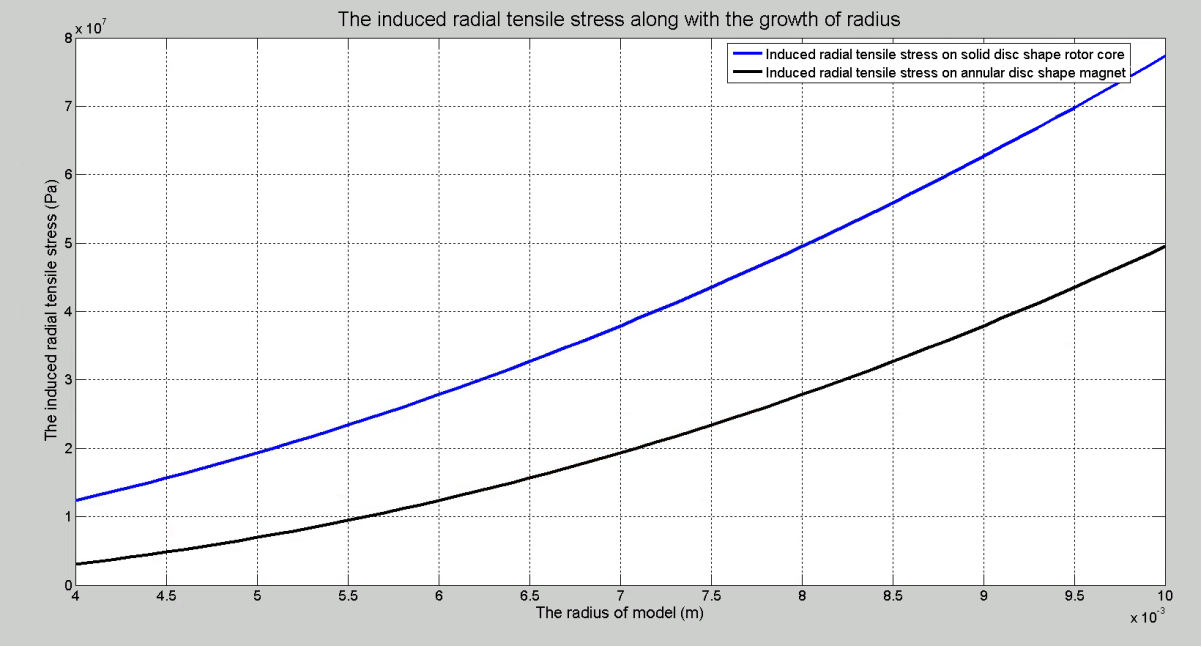

Figure 3-6: Induced radial tensile stress along with the growth of radius

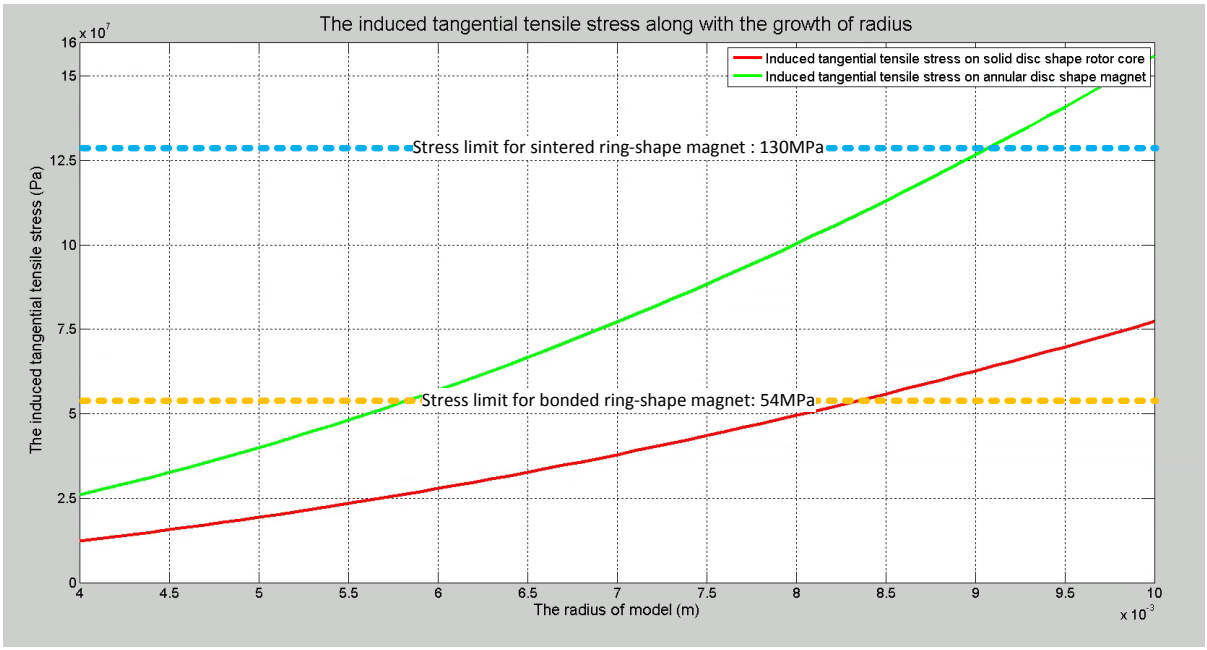

Figure 3-7: Induced tangential stress along with the growth of radius

A third disadvantage of axial flux permanent magnet machines is from the manufacturing point of view, which adds extra difficulties in production with the decreased manufacturing tolerances, making motor production more costly. Any axial offset of the rotor position can impact the effective air-gap thickness and uniformity as well as the designed motor performance; also the unbalanced axial magnetic force must be resisted by the utilised bearings.

In consequence of the aforementioned weaknesses of the axial flux permanent magnet motors, conventional radial flux machines prove to be a more practical choice for the aimed motor specifications.

3.2.2 Rotor position: inner rotor or outer rotor?

Within the category of radial flux permanent magnet machines, there are two major types of rotor arrangements: inner rotor and outer rotor, as shown in below Figure 3-8.

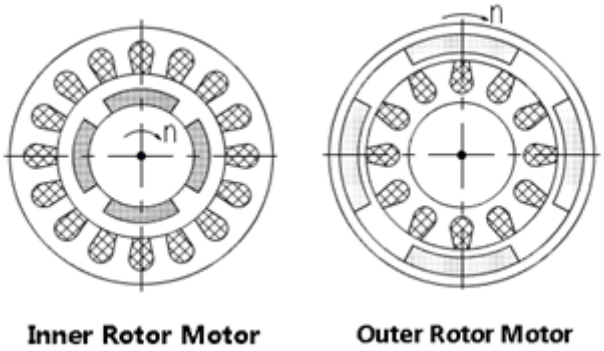

Figure 3-8: Arrangements of inner rotor and outer rotor radial flux motors

With the same overall outer diameter, due to the larger rotor radius in outer rotor machines, it can provide a higher torque compared to the inner rotor one. Nevertheless, the outer rotor machines suffer the higher compressive stress on the low strength permanent magnets, which limits their implementation in ultra-high speed applications. In this project, an inner rotor structure design is the preferred.

3.3 Stator structure: slotted or slot-less?

This section discusses two different stator topologies for the design of inner rotor structure radial flux permanent magnet motor, as shown in Figure 3-9. The graph illustrates the 2-dimensianl cross-section views of both slotted stator motor and slot-less stator motor.

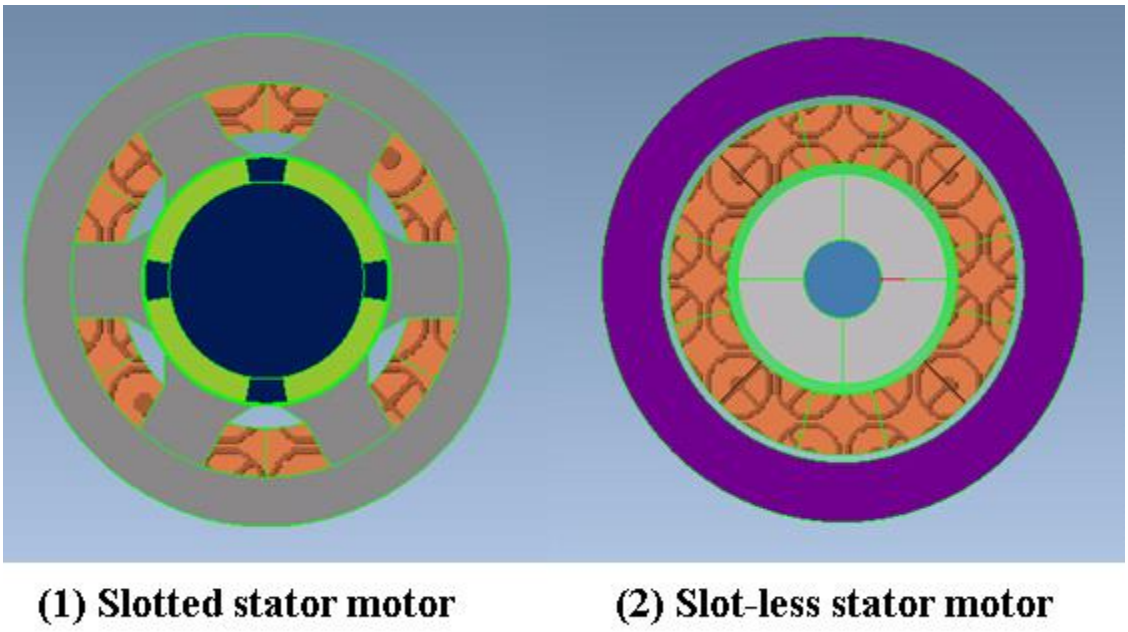

Figure 3-9: The cross-section views of slotted stator motor and slot-less stator motor

In recent decades, the conventional slotted permanent magnet brushless DC motors have attracted a great deal of attention in high speed applications [1-3, 6, 11, 14, 16, 78, 79]. There is a clear trend that this kind of motor is preferred for high-speed power-dense small-size applications, offering highest power density and machine efficiency. Meanwhile, permanent magnet BLDC motors with slot-less stator structure also become increasingly popular in use of high speed range as presented in [17, 27, 29, 33, 85-87].

It is true that slotted permanent magnet motors feature relatively higher power-conversion efficiency in comparison with slot-less structure machines because of the minimised air-gap flux leakage. Nevertheless, the introduced stator teeth bring the nature of stator slot opening, causing undesirable operating noise due to the induced cogging torque and additional magnet loss owing to the resultant slotting effect. All these drawbacks can be overcome by the employed slot-less stator structure.

Furthermore, as a consequence of slot-less topology, the resultant motor armature reaction under load condition become reasonably small compared to the slotted motors. The induced rotor eddy current loss is hence minimised so that the risk of magnet demagnetisation is mostly limited in slot-less machines. When the real chopped current is injected into motor phase coils, the effective iron loss caused by the high-order time harmonics in actual stator core-back flux is also minimised. Also, as the effective air-gap thickness in slot-less motors is inherently larger than slotted ones, stator core-back flux density is hence comparatively smaller than slotted designs, resulting in less used lamination materials. This outcome helps to lower down the induced iron loss and stator weight as well as lamination cost.

From a mass-production point of view, because of comparatively large effective air-gap thickness in slot-less stator designs, both motor phase inductance and induced back-EMF become less sensitive to the variation of actual clearance gap between rotor outer surface and winding coils compared to slotted machines. Besides, manufacturing challenge for the simple ring-shape slot-less stator is significantly lower than producing the complex toothed stator lamination. These features contribute to the achievement of more relaxed manufacturing tolerance, reducing the cost of potential manufacturing line.

In addition, the author in [88] states that the slot-less stator structure may be the only available choice for ultra-high speed miniature motors as the induced iron losses greatly limit the motor performance. With the growth of motor operational speed, the split ratio of stator inner diameter to overall outer diameter has to be decreased. Thanks to the removed stator teeth, the slot-less structure motors feature the larger split ratio compared to the slotted ones under the same overall outer diameter.

After considering the aforementioned pros and cons of each stator structure, slot-less stator topology was selected for this project to exploit its advantages.

3.4 Number of Poles

In synchronous permanent magnet machines, the rotating speed is based on the frequency of machine supply voltage and number of poles, as expressed in Equation 3-5. n is the machine rotating speed; p is the number of pole pairs; f_{elec} is the electrical frequency of the supply voltage.

$$n = \frac{f_{elec}}{p} \qquad (3-5)$$

Based upon above equation, it indicates that the more number of poles a motor has, the slower it runs at a given input frequency. For very high speed operation, the electrical frequency of the supply voltage is also required to be high in a design with fixed pole pairs. At the given operating speed, the required switching frequency increases with the rise of number of pole pairs.

Consequently, for very high speed applications, a low number of pole pairs is necessary for practical designs to minimise stator iron loss, winding proximity loss and motor drive loss which are directly impacted by motor electrical frequency. In addition, the actual motor pole number influences the effective air-gap flux distribution and resultant flux leakage in slot-less inner rotor radial flux machines. The details will be systematically analysed on the following section.

3.5 Choice of Magnetisation Patterns

Two common magnetisation patterns can be utilised in permanent magnet motors: parallel magnetisation and radial magnetisation, as shown in Figure 3-10. The following Figure 3-11 illustrates the magnetic flux distribution with parallel magnetisation in two, four and eight-pole permanent magnet motors with air-gap windings. The residual flux density of the permanent magnet, the magnet outer diameter, the inner diameter, the axial length, and the air-gap radial length is identical in each motor.

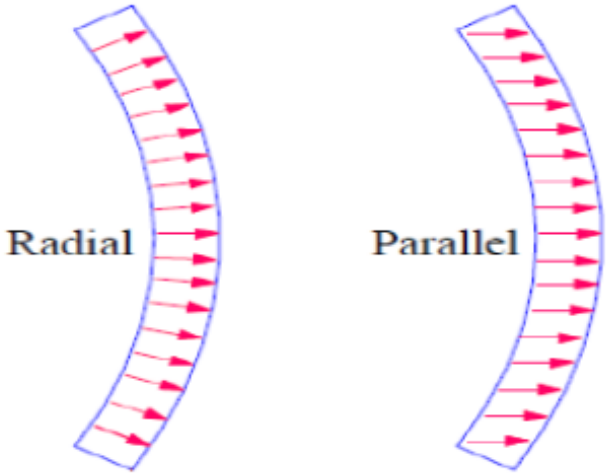

Figure 3-10: Parallel and radial magnetisation patterns

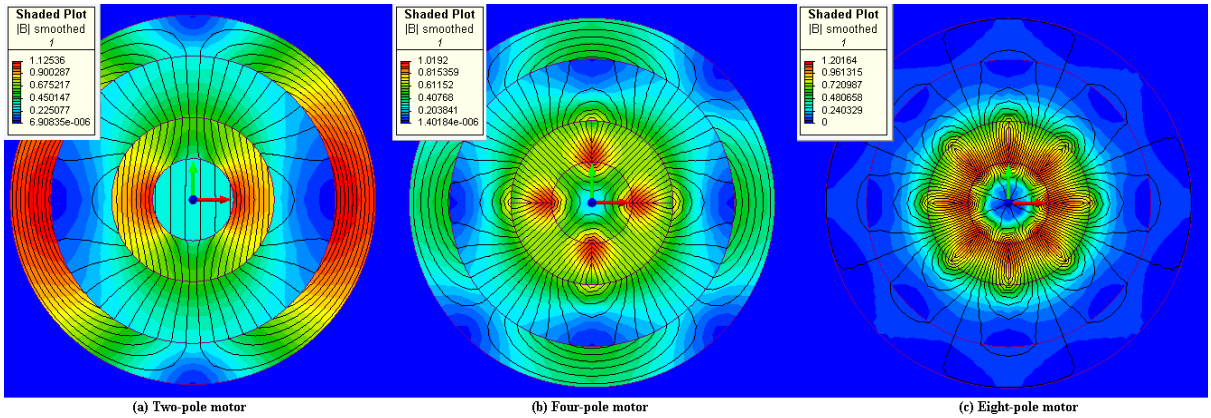

Figure 3-11: Comparison of the air-gap flux distribution in two, four, eight-pole parallel magnetised motors

Figure 3-11 above demonstrates how the rotor magnet generated magnetic flux distributed in the motor, and in particular the air-gap flux leakage increases considerably with increased pole number. Owing to the effectively large motor air-gap, the resultant high air-gap magnetic reluctance forces some flux to directly flow back to the south pole, rather than flow to the laminated stator, leading to the major flux leakage in the machine as shown in Figure 3-11.

Figure 3-12 displays the measured radial air-gap flux density in the middle of the air-gap in two, four and eight-pole parallel magnetised motors. The graph clearly illustrates that the maximum value of the magnetic flux density in the middle of the air-gap decreases with an increase of the motor number of poles. The peak air-gap flux density in the 4 pole motor is approximately 0.057T lower than that in the 2-pole motor, which produces 14% reduced magnetic loading. When increasing the pole number to 8, the reduction is almost 63% of that in the 2-pole motor.

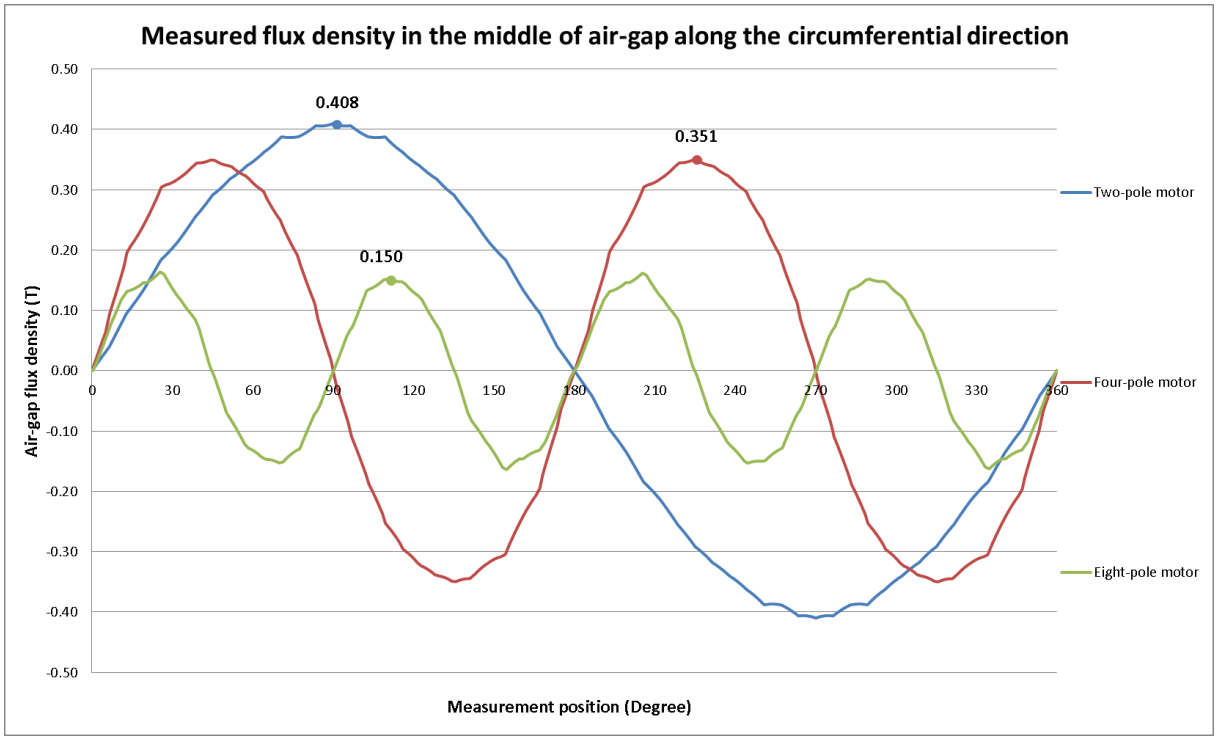

Figure 3-12: Measured air-gap flux density in the middle of the air-gap along the circumferential direction for 2, 4 and 8-pole parallel magnetised motors

Figure 3-13 below shows the maximum air-gap flux density variation along the air-gap radial length, starting from the outer surface of the rotor permanent magnet and ending at the inner surface of the stator in two, four and eight-pole simulation models. All three simulated motors

have the same magnet residual flux density, the same magnet outer and inner diameters, and the same magnet axial length. From the labelled values in the start, middle and end points on the plotted flux density curves shown in Figure 3-13, the flux density in the middle of the effective air-gap in two-pole motor is 32% less than the maximum value at the outer surface of magnet. What is worse, the flux density value drops to almost half of the peak value at the inner surface of the stator. In terms of the four-pole motor, these two reduction values will increase to 41.5% and 58% respectively, while the worst case is occurred in eight-pole machine which features more than 69% reduction of the maximum flux density in the middle of air-gap and only has approximately 17% of the effective magnetic flux density remaining at the stator inner surface.

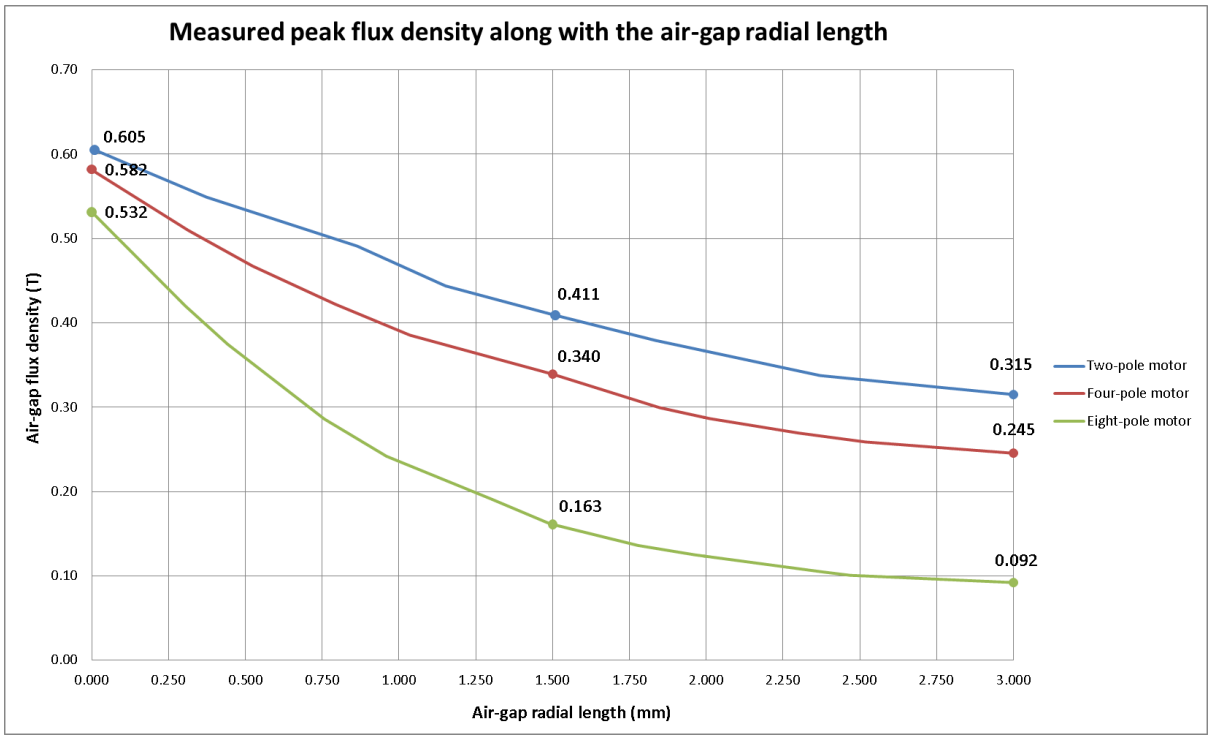

Figure 3-13: Measured peak air-gap flux density along the air-gap radial length for parallel magnetised motor

When considering use of radially magnetised permanent magnets and comparing with the parallel magnetised designs, similar conclusions can be achieved. Figure 3-14 below demonstrates the finite element simulated magnetic flux distribution in two, four and eight-pole radially magnetised magnet motors with the same residual flux density of the utilised permanent magnet, the same magnet outer and inner dimensions as well as the axial length of the drawn models plus the same air-gap radial thickness of the simulated motors.

The following Figure 3-15 demonstrates the simulated air-gap flux density in two, four and eight-pole slot-less stator structure motors with the radially magnetised permanent magnets. As earlier, all the plotted flux density graphs are attained in the middle of the effective air-gap along the rotor circumferential direction. Finally, Figure 3-16 shows the variation of flux density in radial direction of the effective air-gap. Once again, the achieved flux density value drops rapidly and dramatically with both an increase of magnet pole number and radial location in the effective air-gap.

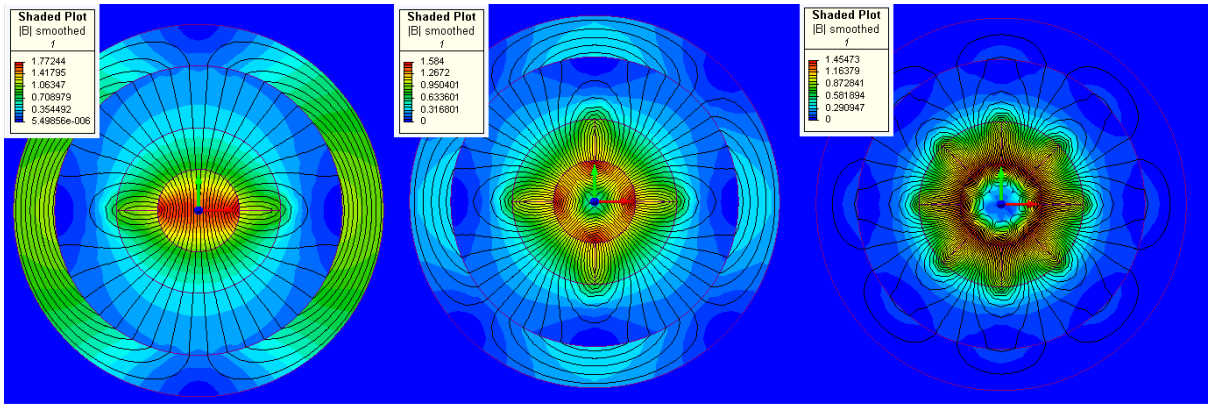

Figure 3-14: Comparison of the air-gap flux distribution in two, four, eight-pole radially magnetised motors

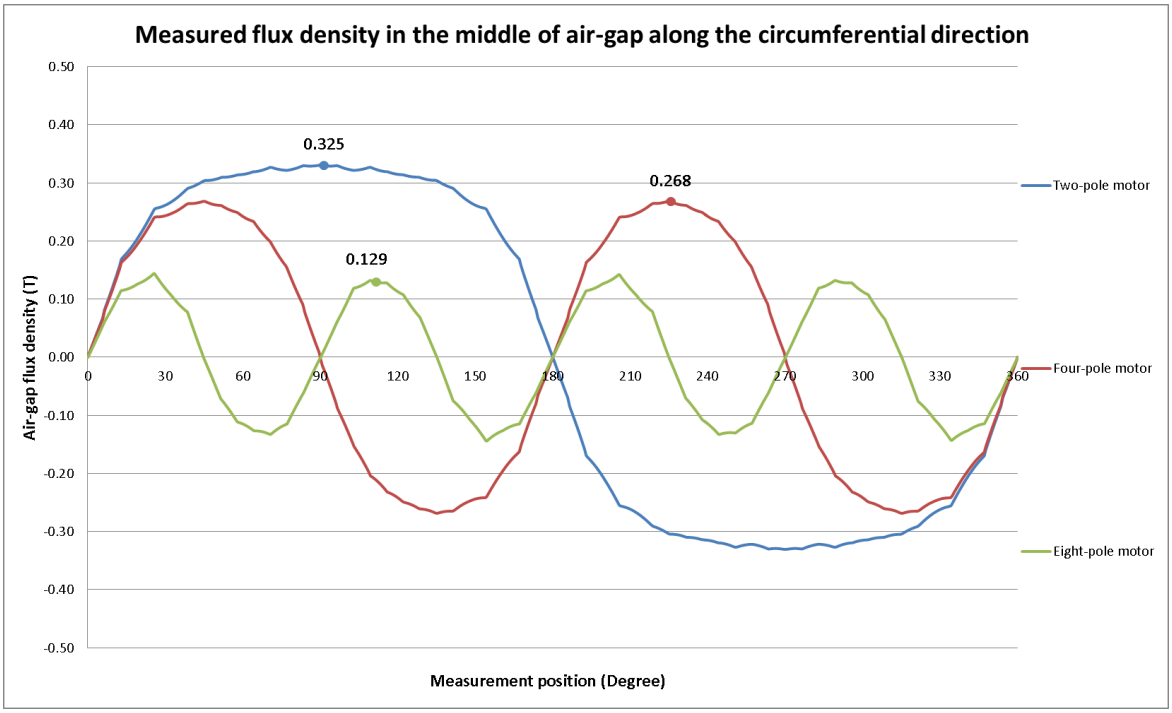

Figure 3-15: Measured air-gap flux density in the middle of the air-gap along the circumferential direction for 2, 4 and 8-pole radially magnetised motors

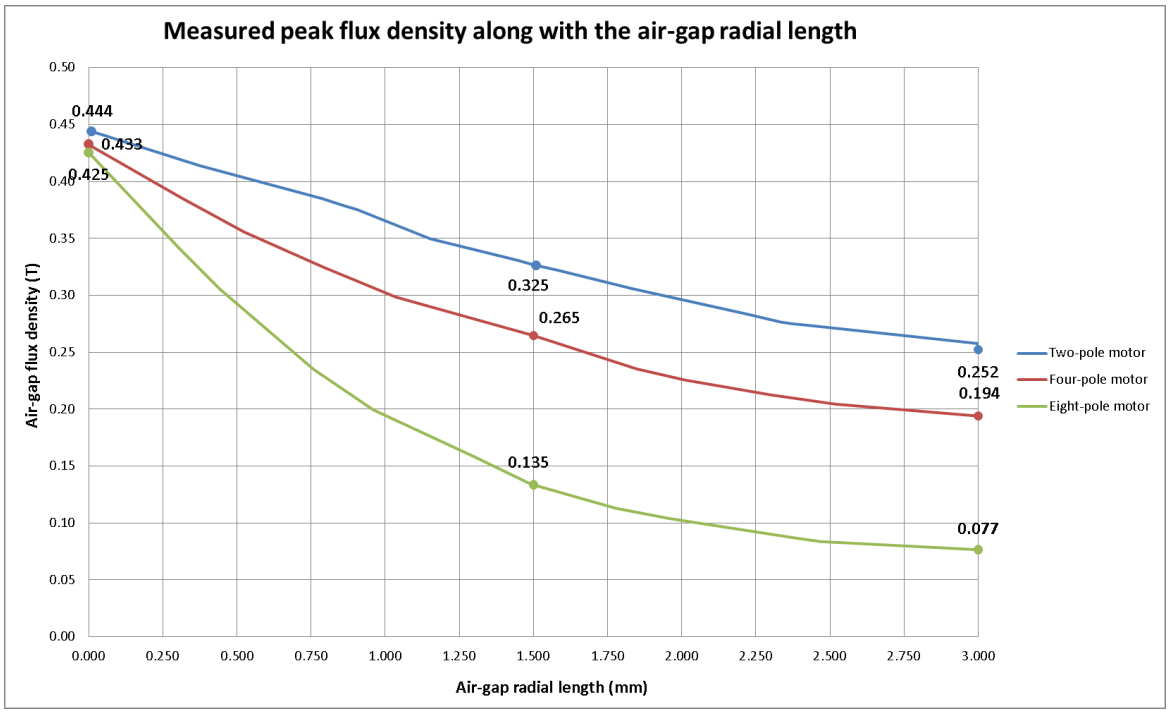

Figure 3-16: Measured peak air-gap flux density along with the air-gap radial length for 2, 4 and 8-pole radially magnetised motors

Comparing the parallel and radially magnetised magnet motors, the parallel magnetisation pattern has higher magnetic flux than the radial magnetised motors for the slot-less inner rotor radial flux designs.

Figure 3-17 below compares the motor flux functions in the 2-pole and 4-pole slot-less inner rotor motors. For each simulated motor shown in the figure, there are forty magnetic flux lines drawn in total. Consequently, the more plotted magnetic flux lines in one area indicates the higher flux density it actually features. Based upon the graph, it shows that for both 2-pole and 4-pole parallel magnetised motors, the air-gap magnetic flux per pole is both greater in total than that in the radially magnetised machines and has a smaller component of leakage flux. It has to be noted that the 8 pole machines are not included in this comparison because Figure 3-11 and Figure 3-14 above have already shown their poor perform under both magnetisation patterns.

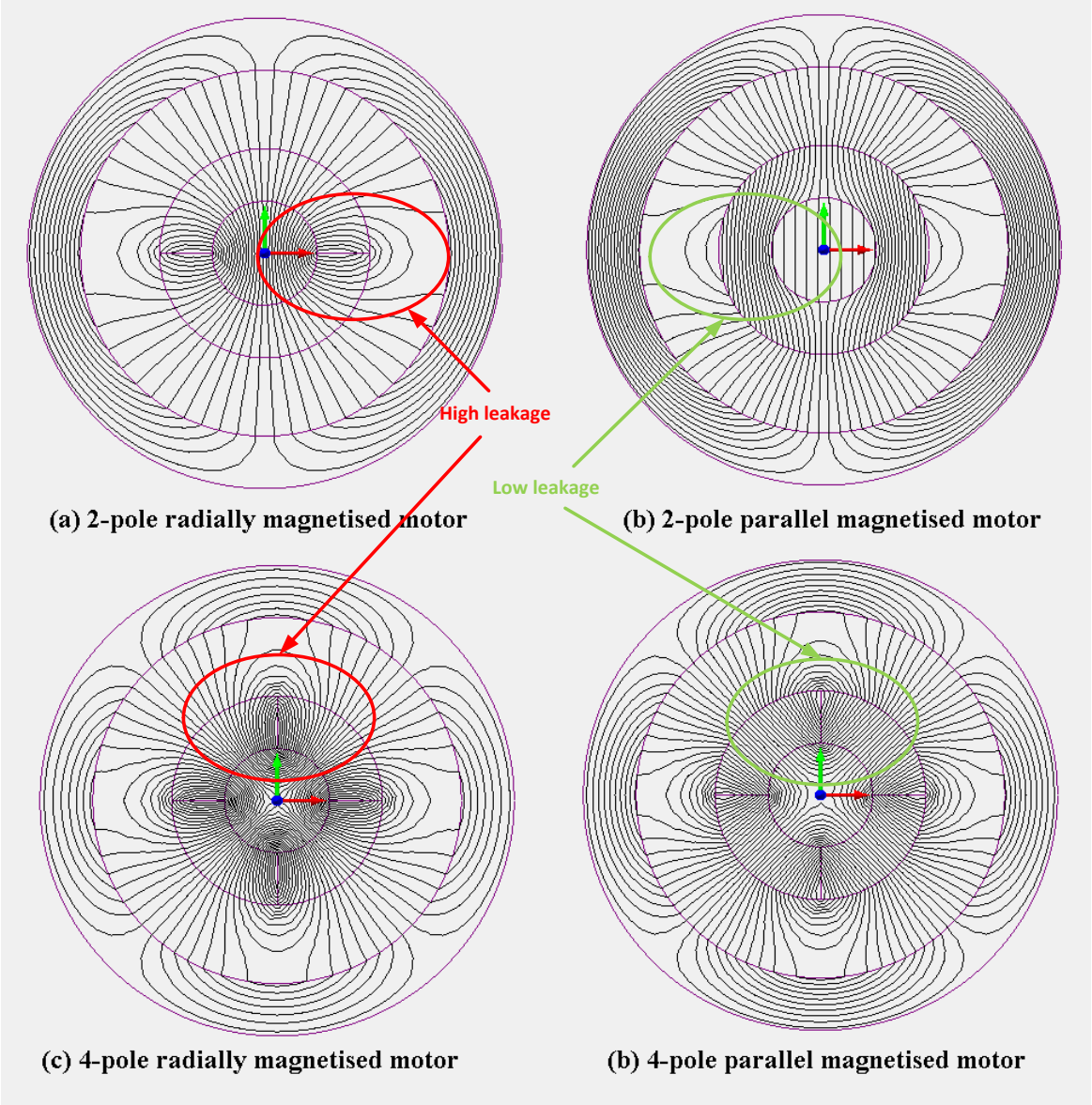

Figure 3-17: Comparison of the plotted magnetic flux functions in the two-pole and four-pole slot-less motors with both radial and parallel magnetisation patterns

Figure 3-18 below demonstrates the magnified magnet pole edge areas of the simulated motors with the plotted magnetic flux functions and the arrows of the flux direction. Both the radial and the parallel magnetisation patterns are shown to demonstrate the specific flux leakage patterns in each type of the magnet. The red-coloured circles highlight the regions where the motor flux leakage is most likely to occur.

With the radial magnetisation pattern, the leakage of the motor magnetic flux normally appears in the areas near the magnet outer surface at the pole edges. Large amount of the generated

motor magnetic flux prefers to flow from the north pole of the magnet straight back to the adjacent magnet south pole through the limited pole edge regions beneath the magnet outer surface rather than the designed flux loop which contains the entire air-gap and the laminated stator. This type of flux leakage pattern, therefore, delivers high leakage of magnet generated magnetic flux near the outer surface of the utilised magnets, resulting in the comparatively low air-gap flux density in the slot-less inner rotor structure designs.

On the other hand, for the simulated motors with the parallel magnetisation pattern, the magnet regions near the inner surface of the magnets at the pole edges are preferred to provide the shortest flux path between the poles with the lowest magnetic reluctance to allow the flux to travel through.

To summarise, regarding of the selected slot-less stator inner rotor structure for the targeted high speed design, a parallel magnetisation pattern is preferable to a radial one because it produces higher air-gap flux densities with the same volume of permanent magnets.

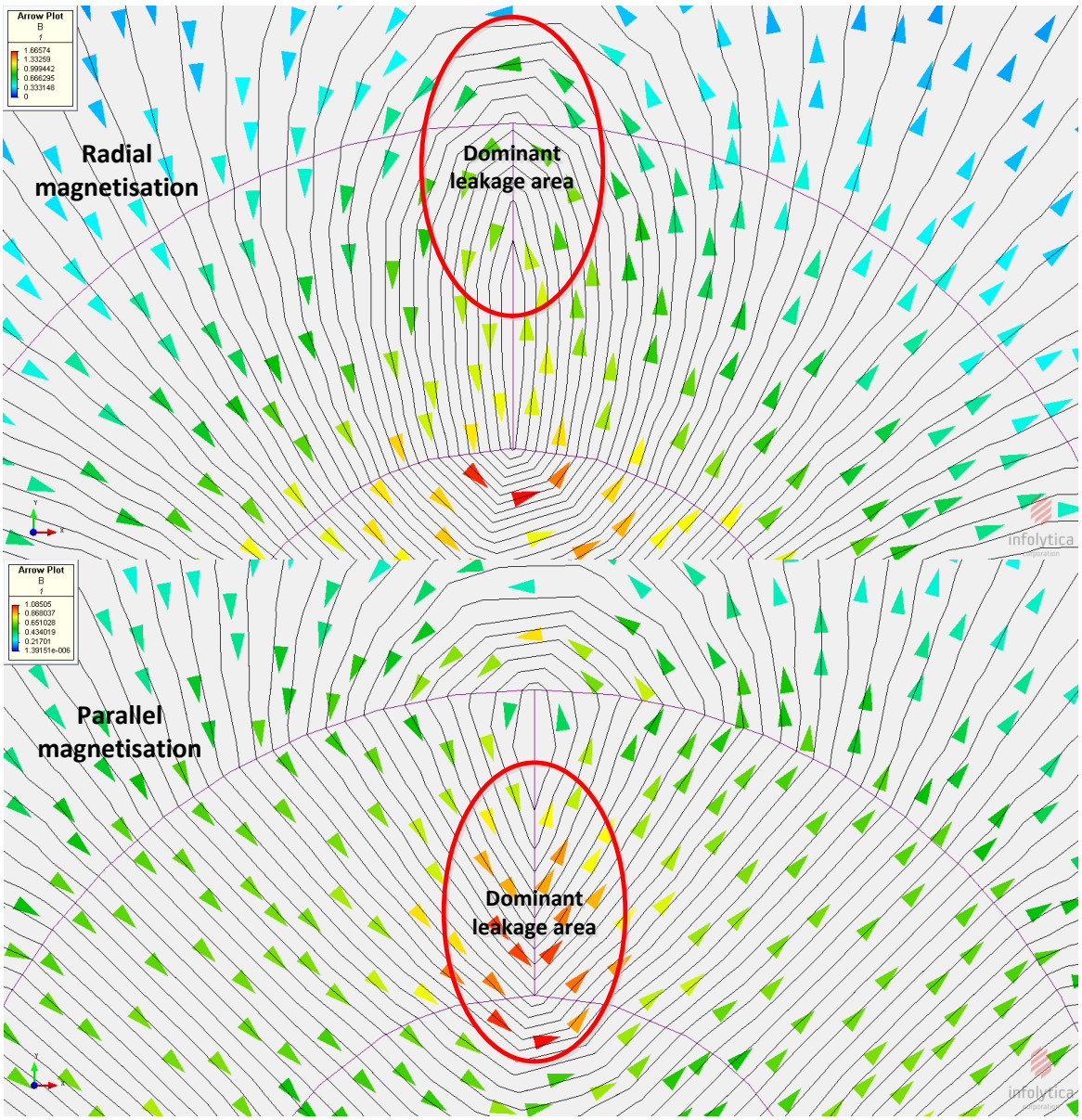

Figure 3-18: Comparison of the magnified magnet pole edge regions on both radial and parallel magnetised motors

In addition to the two common magnetisation patterns discussed above, there is a third magnetisation pattern, named Halbach magnetisation, which is also widely used in permanent magnet machines. Halbach magnets can be categorised into two groups: Halbach arrays and Halbach cylinder. The former was initially proposed in [89] by K. Halbach from U.S. Lawrence Berkeley National Laboratory in 1980s. In his article, the Halbach array is defined as a group of specially oriented permanent magnets which can enhance the generated magnetic field on one side, whilst weakening the field to almost zero on the other side, as shown in Figure 3-19

below. In terms of the Halbach cylinder, as described in [90], a strong homogeneous magnetic field is generated in the confined space of a precisely magnetised cylinder with very weak magnetic field elsewhere. The following Figure 3-20 displays the basic structure and the designed flux path of the utilised cylinder shape permanent magnet with the Halbach magnetisation pattern in an outer rotor structure motor presented in [90].

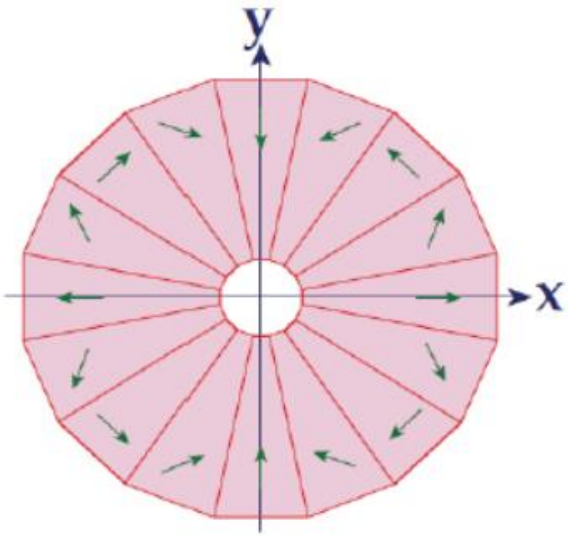

Figure 3-19: Cross section of 16-piece Halbach array [89]

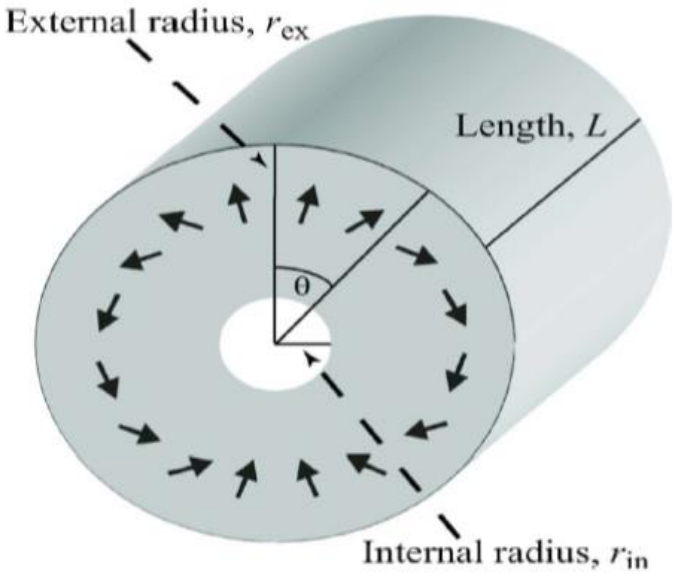

Figure 3-20: A drawn Halbach cylinder with the marked internal and external radius, length and direction of residual magnetic flux [90]

Figure 3-21 below presents the simulated motor magnetic flux distribution in 2-pole, 4-pole and 8-pole inner rotor structure motors with a Halbach magnetisation pattern. The plotted image illustrates that the Halbach magnetised magnets can deliver minimal motor flux leakage compared to the radial and the parallel magnetised magnets, featuring higher utilisation rate of the same volume of permanent magnets. Noted that two pole Halbach magnetised magnet is much easier to be manufactured than those with higher number of poles. In fact, considering the effective flux paths inside and outside permanent magnet, 2-pole parallel magnetised magnet can be regarded as 2-pole Halbach magnet.

For Halbach magnetised permanent magnets in slot-less stator inner rotor structure machines, there is almost no generated magnetic flux that will cross the inner surface of the magnets into the rotor yoke and the assembled rotor shaft. Consequently, both the rotor core-back and the rotor shaft can, if it is desired, be replaced by non-magnetic materials, such as a ceramic to change rotor mechanical properties, such as shaft stiffness, rotor inertia and rotor heat dissipation.

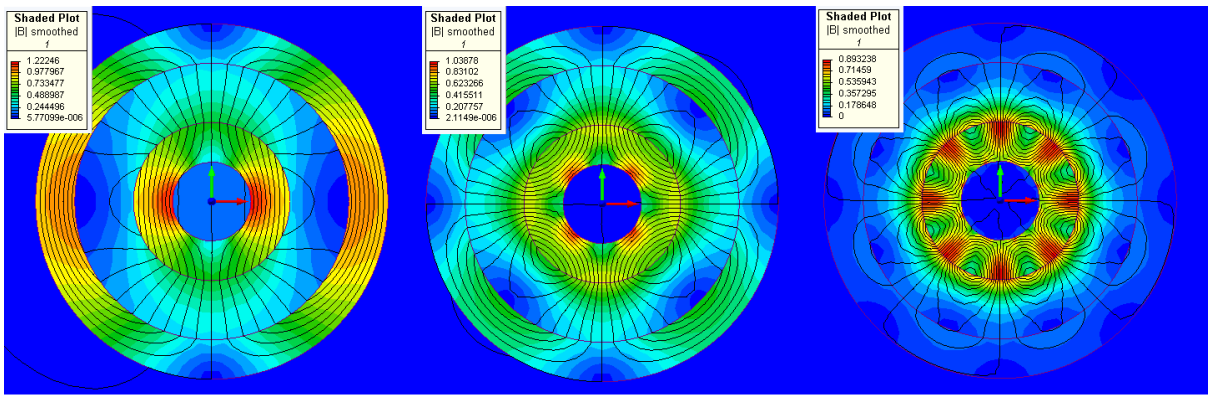

(a) Two-pole motor (b) Four-pole motor (c) Eight-pole motor

Figure 3-21: Comparison of the air-gap flux distribution in two, four, eight-pole Halbach magnetised motors

Figure 3-22 demonstrates the simulated air-gap flux density in two, four and eight-pole permanent magnet motors with the Halbach magnetisation pattern. As earlier, all the data points on the flux density curves are obtained from the location of the middle of the effective air-gap along the circumferential direction. The maximum air-gap flux density value in the middle of the air-gap is approximately 0.4T in the 2-pole motor, and for the 4-pole motor, this is only slightly reduced by about 5% to 0.38T. Similar to the motors with the radial and the parallel magnetisation patterns, when the motor pole numbers are further increased to 8, the value of

the maximum air-gap flux density dramatically drops to 0.213T, which becomes more than 45% lower than that in the 2-pole and 4-pole motors.

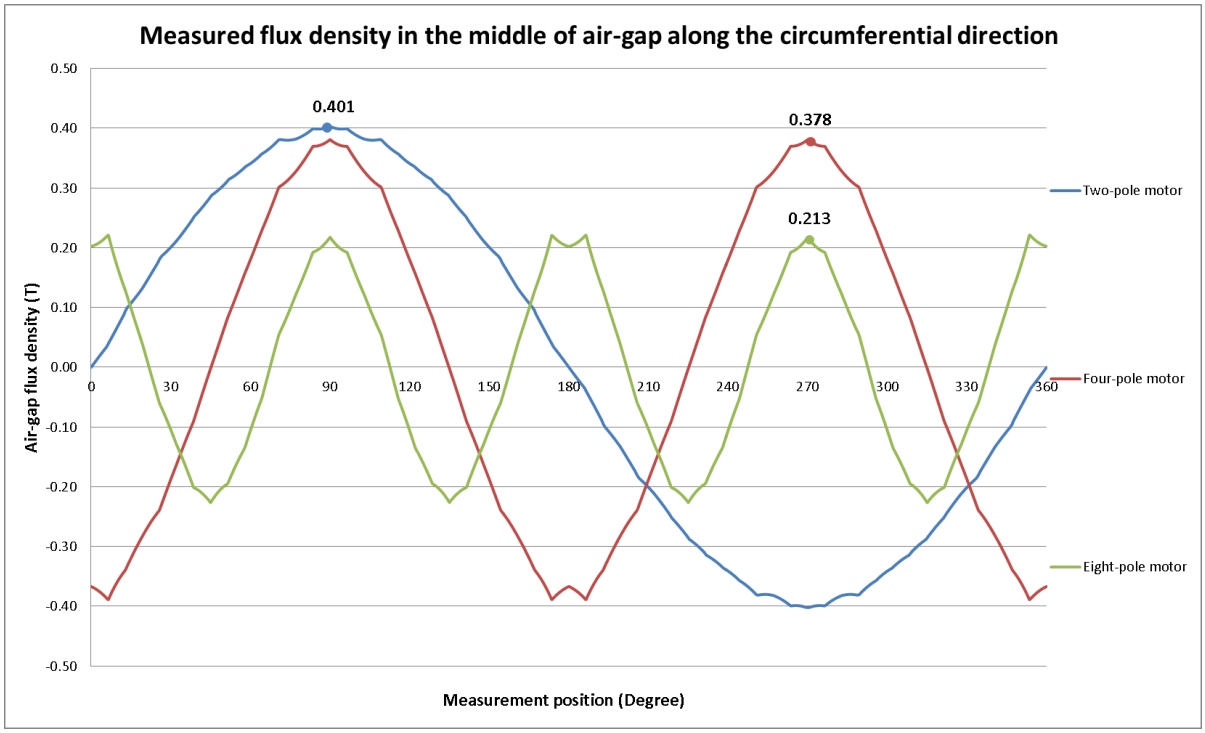

Figure 3-22: Measured air-gap flux density in the middle of the air-gap along the circumferential direction for 2, 4 and 8-pole Halbach magnetised motors

Follow up the above analysis, maximum air-gap flux density variation with radial position in the motor effective air-gap is shown in Figure 3-23. For the 2-pole motor, the air-gap flux density in the middle of the air-gap is 32.5% lower than that at the outer surface of the magnet.

It has to be noted that there are substantially different trends of air-gap flux density variation under different magnet poles in the Halbach magnet motors in comparison to the parallel and radial magnetisation motors, when considering the air-gap flux density at the outer surface of the magnet. The obtained flux density value reduces with magnet pole number growth for the radial and parallel cases, but increases with the Halbach magnetisation pattern.

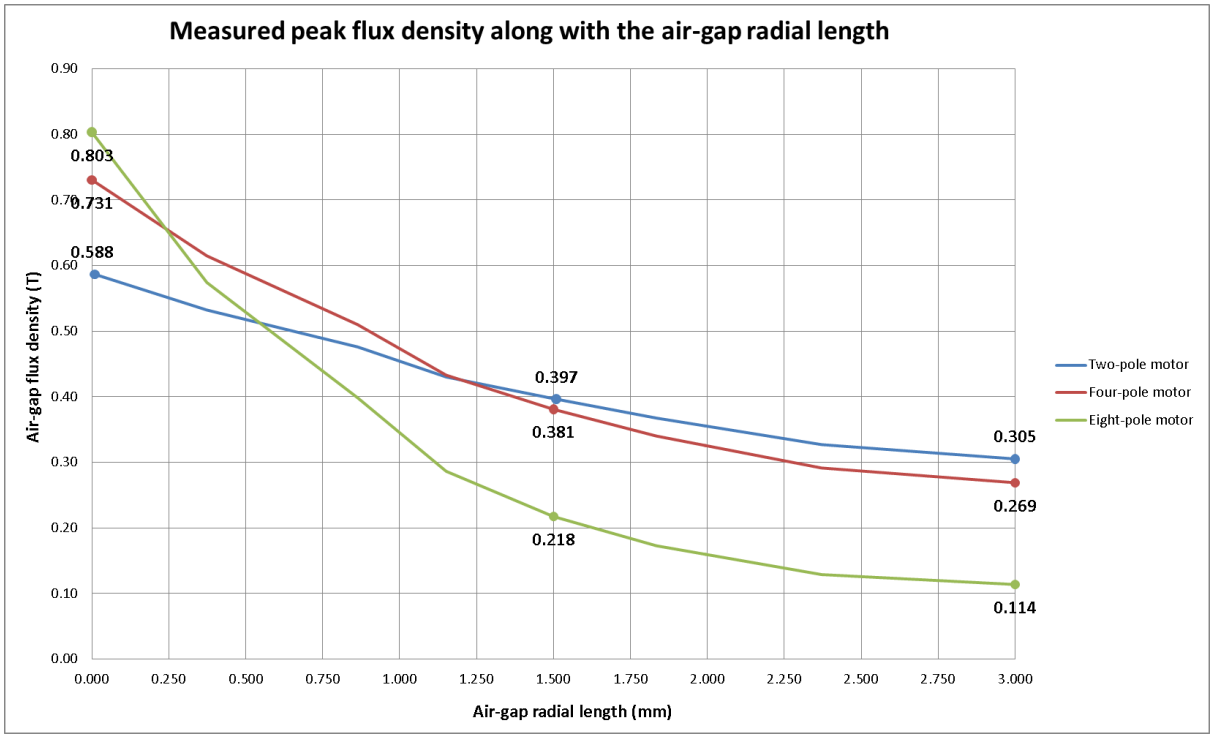

Figure 3-23: Measured peak flux density along with the air-gap radial length for 2, 4 and 8-pole Halbach magnetised motors

The flux variation trend in radial and parallel magnet motors under different pole numbers is mainly due to the increasingly higher flux leakage between the two poles inside the magnet shown earlier in

Figure **3-18**. The different dominant flux leakage regions in Halbach magnetised magnet motor bring about the observed different flux variation trend.

On one hand, the Halbach magnetised motors minimise flux leakage between the poles as all the generated flux follows the designed flux routes inside and outside the magnets. Nevertheless, there is still crucial flux leakage on the areas of magnet poles in slot-less stator inner rotor design. Figure 3-24 below shows the magnified magnetic flux plot for the 2-pole motor with the Halbach magnetised magnet. The undesirable flux leakage mostly occurs along the magnet pole arc towards to the magnet pole edge. The wider the magnet pole arc a motor has, the higher the flux leakage it features, and the lower flux density it delivers at the pole centre near the magnet outer surface.

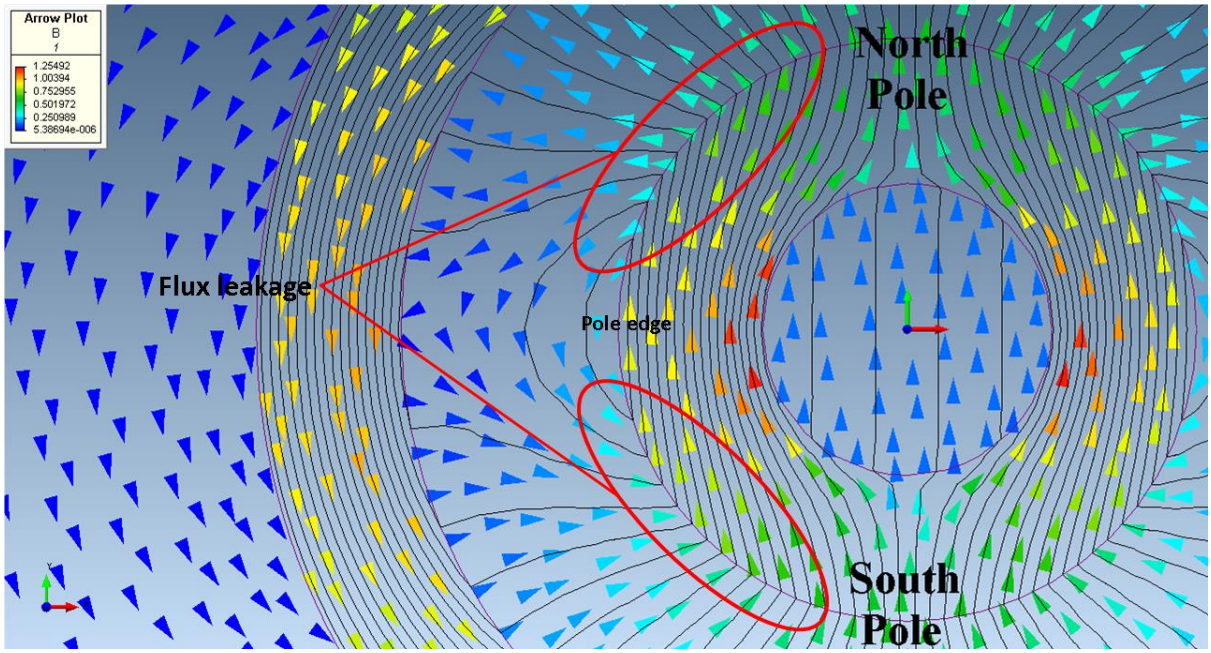

Figure 3-24: Plotted flux functions and arrows of the flux direction in the 2-pole Halbach magnetised motor with the highlighted flux leakage

Consequently, for the 4-pole and the 8-pole Halbach magnetised magnet motors, the naturally shorter magnet pole arc results in more concentrated magnetic flux in the centre of pole, leading to higher flux density values close to the outer surface of the utilised permanent magnets. Figure 3-25 below demonstrates captured magnetic flux plots in both 4-pole and 8-pole motors with the Halbach magnetisation patterns. The graph shows that the unexpected flux leakage along the magnet pole arc is limited by the relatively shorter pole arc length, forcing most of the generated flux to be restricted at the region of the magnet pole centre, travel through the magnet outer surface and then flow to the motor air-gap. This consequence contributes to the higher maximum air-gap flux density values adjacent to the outer surface of Halbach magnet at the pole centre regions, as shown in Figure 3-23 above. Compared to the 2-pole machine, the attained peak flux density values in 4-pole and 8-pole motors are 24.3% and 36.6% higher respectively.

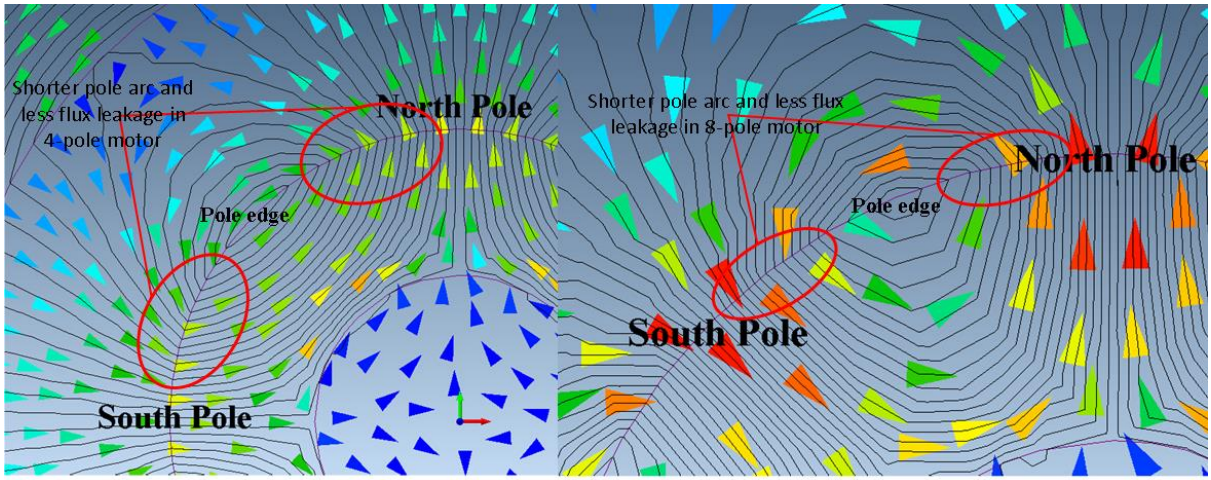

Figure 3-25: Plotted flux functions and flux direction arrows in 4-pole and 8-pole Halbach motors

On the other hand, the Halbach magnetised motors with higher magnet pole numbers still cannot overcome the weakness of major flux leakage issue occurring in the large effective motor air-gap in slot-less stator inner rotor structure design. Similar to the radial and the parallel magnetised magnet motors, a large proportion of the generated magnetic flux flows straight back to the next pole through the motor air-gap, instead of travelling to the targeted laminated stator as shown in Figure 3-21 above. This effect is magnified for motors with higher pole number.

Referring to Figure 3-23, by the middle of the motor effective air-gap, both the 4-pole and 8-pole magnetic fields have fallen to below that of the 2-pole field. With the 2-pole Halbach array, the flux density decays by almost 50% at the stator core back inner surface, whilst this reduction rises to 63% with the 4-pole and 85% with the 8-pole array.

Comparing the air-gap flux density values achieved with parallel and Halbach magnetisation patterns, as shown in Figure 3-13 and Figure 3-23, for the 2-pole permanent magnet motors, the maximum air-gap flux density values are within 3% difference. In 4-pole motors, the Halbach arrangement has a higher peak flux density value by 25%; and with 8-pole magnet, the difference increases: the Halbach array gives 35% more. As a consequence, the motors with the Halbach magnetisation pattern are shown to be a more competitive choice than the parallel magnetised one with respect to the slot-less stator inner rotor structure designs.

3.6 Summary

The following points summarise what has been found in this chapter:

1. Slot-less, inner rotor topology with radial flux distribution has been selected for the targeted high-speed power-dense small-size motor design.
2. Small magnet pole numbers are preferred due to reduced motor air-gap leakage flux, resulting in the greater air-gap radial flux density.
3. For slot-less design, although 2-pole motors can provide comparatively higher air-gap flux density compared to 4-pole machines, larger stator core-back are required to avoid undesirable magnetic saturation, leading to a larger motor overall outer diameter.
4. The generated motor electromagnetic torque is proportional to the total flux linkage and the rotor number of poles. Therefore, 4-pole motors always feature higher torque capability compared to 2-pole machines when same amount of permanent magnet is utilised as the flux linkage drop is less than 50% in 4-pole slot-less design.
5. Halbach arrays are found to outperform both radial and parallel magnetisation patterns.

Chapter 4 : Motor Design Procedures

4.1 Introduction

This chapter discusses the detailed design procedures utilised in the targeted slot-less stator, inner rotor, radial flux, permanent magnet brushless DC motor.

Potential design approaches will firstly be discussed, illustrating their advantages and disadvantages, and then enabling selection of the most appropriate method. Design variables and constraints are presented afterwards, along with the creation of analytical design models. Generated motor losses are considered, including the calculation of such dominant motor loss elements as copper Ohmic loss, proximity loss, iron loss and rotor loss. Operating temperature and 3-dimensional effects are both taken into consideration. Using material prices provided by commercial suppliers, the per-unit material cost of the motors is also evaluated during the motor design process.

By the end of this chapter, the essential machine properties, including dimensions, efficiency, mass and cost can be accurately predicted.

4.2 The motor design approaches

4.2.1 Equivalent magnetic circuit

This section discusses the use of equivalent magnetic circuits in the design of a permanent magnet brushless DC motor. In simple terms, the magnetic circuit can be split into a number of components as magneto-motive force (MMF), magnetic reluctance and magnetic flux. The generated magnetic flux is equal to the ratio of the created total MMF in the circuit to the effective circuit reluctance.

Permanent magnets with a residual flux density B_r, thickness l_m and relative permeability μ_r, can be represented by an MMF, calculated by the equation of $\frac{B_r l_m}{\mu_0 \mu_r}$, in series with the magnetic reluctance. The reluctance of any one component is dependent upon the flux path length l_{flux}, the flux path cross-section area A_{flux}, and the flux path permeability μ. The value of the magnetic reluctance $S = \frac{l_{flux}}{\mu * A_{flux}}$. It has to be noted that, the permeability of air is not equal to zero. Hence, it is very likely that the generated magnetic flux can leak through the unexpected air paths, rather than flowing through the intended magnetic circuit.

The major benefit of such a simple, lumped design approach is the rapid estimation of motor performances, including but not limited to the generated magnetic flux, the induced back-EMF, the motor losses and the delivered shaft power. Design variables such as magnet dimensions, air-gap radial thickness and stator cross-section area can all be easily changed to determine their effect upon motor performances.

On the other hand, this design method has one major disadvantage: it is extremely challenging to accurately include every leakage path in the machine. Consequently, for those motors with high leakage flux, such as slot-less a stator structure permanent magnet motor with a radial or parallel magnetisation pattern, the use of an equivalent magnetic circuit in the motor design is not recommended.

4.2.2 More sophisticated analytical simulation

This section considers the use of a more sophisticated analytical simulation approach in the targeted motor design, which is appropriate to model relatively simple geometries in an

accurate manner. Air-gap winding machines generally consist of a set of concentric rings of core back, windings, air-gap and magnet. If the winding end effects are ignored, a two dimensional geometry can be modelled analytically including the in-plane flux leakage fields. However, such models are for a linear system which cannot deal with the case of magnetic saturation.

This type of analytical modelling has the clear advantage of fast computation, making it relatively straight forward to optimise a parameterised geometry. Furthermore, it can also be embedded into computer aid analysis software, such as Microsoft Excel or Matlab, using their functions of data calculation and post-processing to accelerate the analytical simulation process. Fast calculation of the motor performance, including the induced back-EMF, the motor losses and the shaft power as well as the motor per-unit cost and mass, can be carried out for a vast number of potential designs in one multi-run simulation.

4.2.3 Finite element simulation

This section discusses the use of finite element (FE) simulation in complex 2-dimensional and 3-dimensional motor design. Because of the utilised linear calculation equations and approximate treatment to some system variables, there is inevitable error in the conducted analytical simulations. Hence, a finite element simulation is generally used owing to its capability to incorporate complex geometries and nonlinearity into the simulation models.

This section will firstly discuss the basic principle of the finite element analysis, and then highlight the advantages and disadvantages of this approach in the targeted permanent magnet motor design. It has to be noted that finite element models remain a numerical approximation to the exact solution, whose accuracy dependents on the size of the defined finite elements.

Figure 4-1 illustrates the simplified design procedures of a standard finite element analysis. The first step is to transfer the real engineering problem to a solid model with appropriate boundary conditions. Afterwards, each component in the constructed model is discretised into a large number of elements with the defined properties of the utilised materials. The principal differential equations are then posed in integral form, and numerically integrated to produce a set of simultaneous equations representing the potential at each “node” in the solution space. In first order elements, these nodes correspond to the corners of each element. Following

solution of the simultaneous equations, the final approximate solution of the entire solid model can be achieved by way of the integration of the individual potentials.

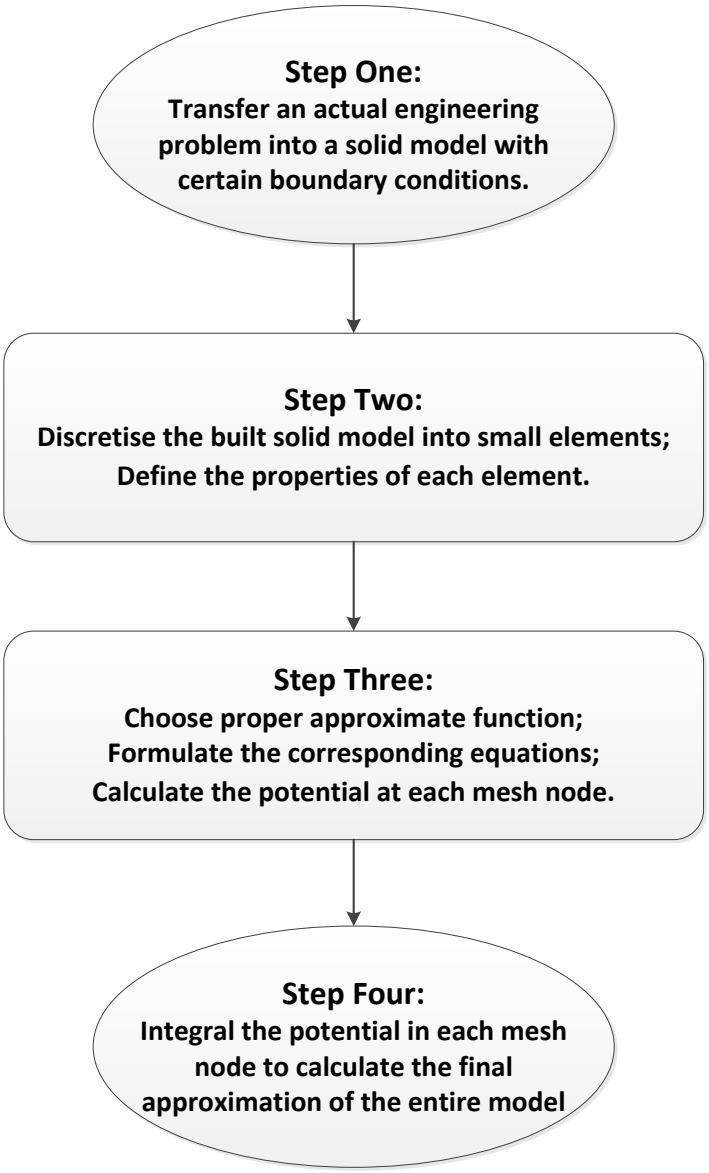

Figure 4-1: Simplified design procedures of the standardised finite element analysis

According to the number of dimensions of the defined meshed models, the motor finite element simulation can be categorised as 2-dimensional or 3-dimensional simulation. Three-dimensional simulation permits inclusion of all three dimensional effects, but are much more time consuming to undertake.

Finite element solutions can be categorised into the following four groups: static simulation, time-harmonic simulation, transient simulation and transient with motion simulation. Static

finite element simulation can simulate the generated static magnetic fields and the corresponding magnetic flux at a given rotor position in a permanent magnet motor. To obtain the motor flux distribution over a complete electrical cycle, a set of static solutions must be determined over a range of rotor positions. From these, the essential motor properties, such as the generated motor phase flux linkage, the induced motor back-EMF and the corresponding stator core-back flux density, can all be precisely simulated to predict the motor performances. It has to be noted that the static solver can only estimate the static magnetic fields generated by either the permanent magnets or the source currents in conductors. Effects due to changing magnetic fields, such as induced eddy currents, cannot be incorporated into the static solutions.

Simulation of magnetic fields that are generated by sinusoidal alternating currents and the resulting associated eddy currents can be achieved by way of using a time-harmonic solver. Analysis is at a single frequency in the complex domain with both the real and the imaginary parts, and makes the use of the phasors to represent the field quantities.

However, time-harmonic FE simulation is not suitable for analysis of magnetic fields created by permanent magnets. Where both rotor magnets and induced currents are presented, it is necessary to use a transient solver as an alternative. Transient solver in finite element simulation utilises a time stepping process in which the field is calculated at a series of discrete times, with the changing fields linking to each discrete solution.

Three properties are required to be set before the start of the transient finite element simulation: starting time, ending time and time step. The time stepping routine utilises second order time stepping with two solutions per time iteration. The second solution which is obtained at the end of the set time step is utilised as the initial condition for the next time instant. The smaller length of the time interval it has, the more accurate the approximation of the solution it delivers.

When the rotor movement is taken into consideration in the targeted finite element simulation, a fourth solver type, i.e. a transient with motion solver, is introduced to include rotor rotation in the simulation. This solver can predict the induced currents in different motor components due to motional effects.

Among all four simulation solvers mentioned above, the transient with motion solver is the most powerful one and can include the complete functions of all the other three types. However, this type of finite element simulation method is very computationally intensive and should only be adopted when the other types are unsuitable.

To summarise, the following statements can be concluded for the method of finite element modelling:

1. The accuracy of finite element simulation is generally higher than that of equivalent magnetic circuit and analytical simulation;
2. Major features, such as motor magnetic flux distribution, motor output torque and induced loss elements can be precisely estimated;
3. The precision of the achieved finite element simulated results depends on the number and the size of the defined model elements in the constructed finite element models.
4. Complex 3-dimensional motor structures and boundaries as well as non-linear operating conditions can be accurately modelled.
5. Motor parameters in the built simulation models can be freely adjusted by way of updating the geometrical models during the simulation process, delivering the predicted motor performances for a range of design variables.

On the other hand, the shortcomings of finite element analysis are also fairly clear:

1. The finite element simulation is computationally intensive. For instance, the required simulation time was commonly found to exceed 72 hours in a transient with motion simulation for a completely drawn 3-dimensional model with 0.1mm mesh size.
2. The capital cost can be high due to the utilised computer aided finite element simulation software.

4.2.4 Hybrid simulation

In order to combine the speed advantage of an analytical simulation approach with the accuracy of finite element analysis, a hybrid motor design method is introduced. This approach combines the merits of both the fast global calculation from the analytical simulation to rapidly estimate the related motor performance in a huge range of designs, with the high accuracy of the simulated results from the finite element simulation.

Figure 4-2 below demonstrates the design procedures of the hybrid simulation method. The sophisticated analytical simulation is first used to carry out the complete theoretical electromagnetic analysis globally and quickly, followed up with the more precise finite element simulation for the result approval and re-optimisation.

Specifically speaking, the hybrid simulation approach starts with all the design variables to be considered, contributing to the creation of an analytical simulation model which is utilised to predict the motor magnetic flux distribution, torque and power consumption across all the motor design variables. Simultaneously, a 2-dimensional finite element simulation model is utilised to carry out the relatively quick FE simulations with random values of the motor variables. Afterwards, a direct comparison between analytical results and finite element simulated results is conducted across a few specific sets of design variables. If the two sets of results are matched to each other within acceptable error ranges, the hybrid simulation can be moved to the next step; otherwise the created analytical model must be improved to provide more accurate prediction of the motor behaviours. Once the accuracy of the created analytical model is satisfied, the global analytical simulation of the motor is carried out across a wide ranges of motor variables. Later, the achieved analytical results are post processed to obtain the optimal design within the given project specifications.

With the motor dimensions from the selected optimal design, a 3-dimensional finite element simulation model can be constructed, producing high precision results including previously ignored 3-dimensional effects. These values are then compared back with the earlier analytical simulation results to re-validate the accuracy of the selected optimal design. If the error exceeds an acceptable tolerance, it is necessary to carry out a further improvement of the analytical model.

Once the required accuracy of the updated analytical simulation is achieved, another global analytical simulation is conducted with a small range of motor variables. Hence, an updated optimised design can be chosen from the new analytical results, which in turn are applied in the 3-dimensional finite element simulation model to finalise the design variables and the corresponding motor performance.

In conclusion, in comparison with traditional design methods, the hybrid simulation approach features two advantages during the design process.

1. The capability of rapid global scanning of all the considered design variables in a wide ranges within a limited time using the analytical model;
2. High accuracy of the final results with respect to the estimated motor performance due to the merit of the complex 3-dimensional finite element simulation model.

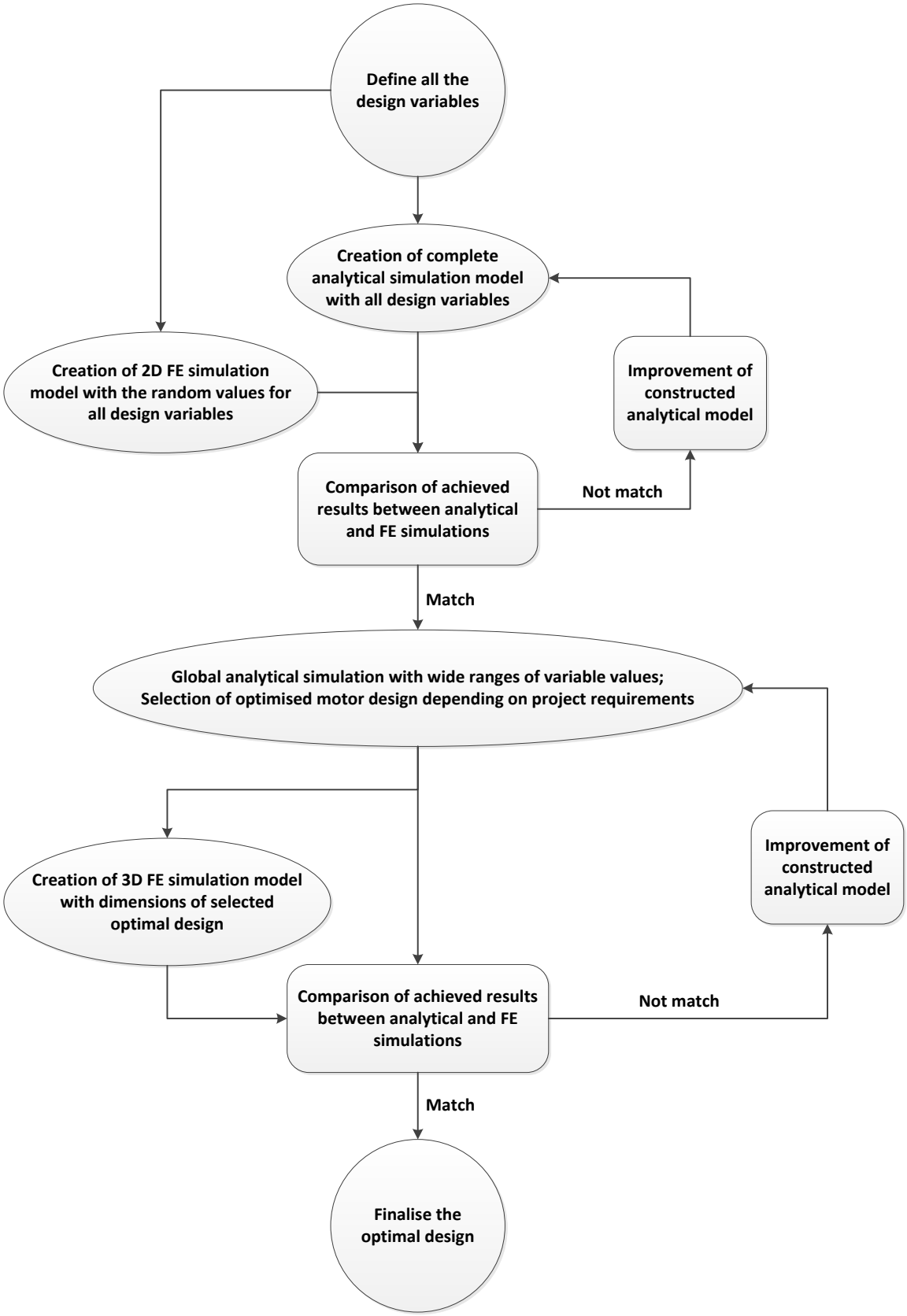

Figure 4-2: Design procedures of the hybrid simulation for the motor design

4.3 Motor variables and design constraints

This section discusses the principal motor design variables and the design constraints.

4.3.1 Motor design variables

Figure 4-3 illustrates the standard slot-less stator, inner rotor, radial flux, permanent magnet motor with the major motor variables indicated.

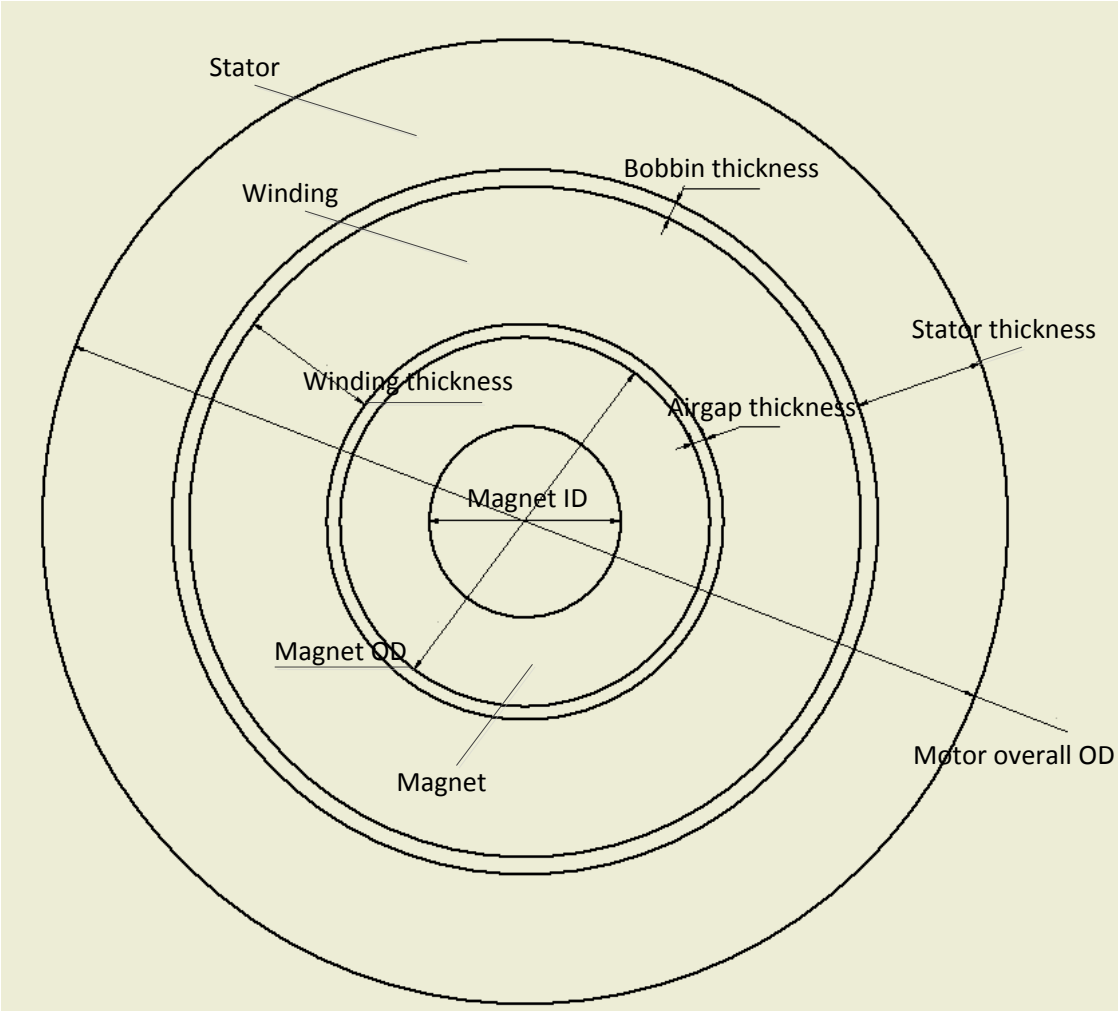

Figure 4-3: The drawing of standard slot-less structure permanent magnet motor with marked major motor variables from cross-section view

Among complete design variables, there are three to be considered first due to their significance in the design procedures: magnet outer diameter, magnet inner diameter and magnet axial

length. Adding the other motor variables of magnet residual flux density, magnet relative permeability and radial thickness of the motor air-gap as well as radial depth of the air-gap winding, both the total magnet magneto-motive force and the effective air-gap flux distribution can be estimated by way of using analytical and finite element simulation models. Afterwards, the stator core-back radial thickness and the stack length of the stator laminations can be optimised to avoid magnetic saturation in the stator core, and to decrease the induced iron loss as well as to minimise both the motor overall outer diameter and mass.

Other design variables including the motor number of turns per phase, the phase RMS current and the wire diameter can be therefore regarded as the design outputs which can be achieved based upon the calculation of the design inputs discussed in the previous paragraph, along with the motor specifications of the motor input power, the motor nominal speed and the motor efficiency. Motor loss elements, such as the winding copper loss, the proximity and skin effect loss and the phase current density as well as the thermal capability can obtained simultaneously.

Table 4-1 below lists all the motor variables in the created analytical simulation model. It has to be noted that some of the variables can be represented by functions of others, only the independent motor design variables are considered for optimisation. The material properties, such as the mass density, the magnet temperature rise demagnetisation coefficient, the lamination loss coefficients and the coil conductivity as well as the conductor temperature rise resistivity growth rate, are all treated as design inputs in the analytical simulation model, using data received from industrial material suppliers.

Motor Design Variables	
Magnet inner diameter	Motor outer diameter
Magnet outer diameter	Motor axial length
Magnet axial length	Stator core-back radial thickness
Magnet residual flux density	Stator axial length
Number of turns	Stator flux saturation point
Air-gap radial thickness	Bobbin thickness
Winding area radial thickness	Wire nominal diameter
Winding span arc	

Table 4-1: Considered motor design variables in the constructed analytical simulation model.

4.3.2 Motor design constraints

The optimised design in this project should feature significant improvements of motor performance in at least one of the following aspects, while the performance in the fields of thermal and mechanical is still within the limit.

- Efficiency
- Material cost
- Overall size
- Total mass
- Acoustic behaviour

In this work, system efficiency, motor dimensions and per-unit material cost are ranked as the top three design constraints during the optimisation.

4.4 Creation of motor analytical simulation model

This section discusses the creation of a sophisticated analytical simulation model of the slot-less stator structure, inner rotor, radial flux, permanent magnet brushless DC motor. As discussed in the previous section, once the fundamental design variables are defined, along with their permissible ranges, the rest of the design variables can be calculated.

4.4.1 Theoretical basis for no-load magnetic field analytical calculation

For the first step, it is required to construct an analytical simulation model of a surface mounted, permanent magnet motor, to determine the no-load magnetic field. An improved analytical calculation, developed from reference [19] is employed using polar coordinates. This analytical method can be utilised for both slotted and slot-less topologies with either the radial or parallel magnetisation patterns. Figure 4-4 below shows the drawn motor topology for slot-less stator, inner rotor, radial flux, permanent magnet machine. R_r is the radius to the magnet inner surface; R_m is the radius to the magnet outer surface; R_s is the radius to the stator inner surface; $\vec{M}$ is the amplitude of the magnetisation vector generated by magnet; and R_a is the air-gap magnetic flux measurement radius.

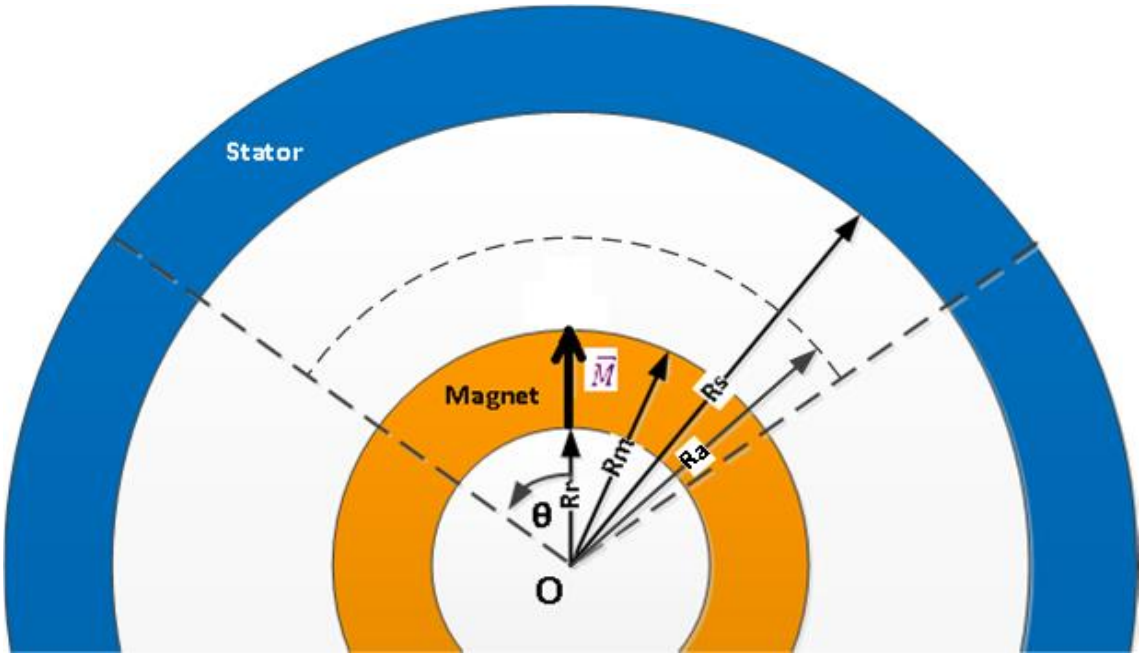

Figure 4-4: Motor topology for slot-less stator, inner rotor, radial flux, permanent magnet machine

In polar coordinates, the amplitude of the magnetisation vector can be expressed as Equation 4-1. The radial coordinate component M_r and the angular coordinate component M_θ can be expressed as Fourier series as Equation 4-2 and 4-3. p is the number of pole pairs.

$$\vec{M} = M_r\vec{r} + M_\theta\vec{\theta} \qquad (4-1)$$

$$M_r = \sum_{n=1,3,5\ldots}^{\infty} M_{rn}\cos(np\theta) \qquad (4-2)$$

$$M_\theta = \sum_{n=1,3,5\ldots}^{\infty} M_{\theta n}\sin(np\theta) \qquad (4-3)$$

As specified in [19], the effective magnetisation can be achieved through the following simultaneous equations [19]. α_p is the ratio of magnet pole arc in comparison to motor pole pitch.

$$M_n = M_{rn} + npM_{\theta n} \qquad (4-4)$$

For radial magnetisation,

$$M_{rn} = 2\frac{B_r}{\mu_0}\alpha_p \frac{sin\frac{n\pi\alpha_p}{2}}{\frac{n\pi\alpha_p}{2}} \quad (4-5a)$$

$$M_{\theta n} = 0 \quad (4-5b)$$

For parallel magnetisation,

$$M_{rn} = \frac{B_r}{\mu_0}\alpha_p(A_{1n} + A_{2n}) \quad (4-6a)$$

$$M_{\theta n} = \frac{B_r}{\mu_0}\alpha_p(A_{1n} - A_{2n}) \quad (4-6b)$$

$$A_{1n} = \frac{\sin\left[(np+1)\alpha_p\frac{\pi}{2p}\right]}{(np+1)\alpha_p\frac{\pi}{2p}} \quad (4-6c)$$

$$A_{2n} = \frac{\sin[(np-1)\alpha_p\frac{\pi}{2p}]}{(np-1)\alpha_p\frac{\pi}{2p}}\ for\ np \neq 1 \quad (4-6d)$$

$$A_{2n} = 1\ for\ np = 1 \quad (4-6c)$$

With the support of calculated effective magnetisation, the air-gap flux distribution can be deduced from general solution of Laplacian equations for air-gap scalar magnetic potential as Equation 4-7 [19].

$$B_r(r,\theta) = \sum_{n=1,3,5\ldots}^{\infty} K_B(n) * f_{B_r}(r) * \cos(np\theta) \quad (4-7a)$$

$$B_\theta(r,\theta) = \sum_{n=1,3,5\ldots}^{\infty} K_B(n) * f_{B_\theta}(r) * \sin(np\theta) \quad (4-7a)$$

For a permanent magnet motor design with defined motor dimensions and given magnet properties, $K_B(n)$ is the constant part in the solution which depends on the value of M_n, R_r, R_s, R_m, p and magnet permeability μ_r, whilst $f_{B_r}(r)$ is varied with value of air-gap magnetic flux measurement radius R_a. It has to be noted that the simulated permanent magnet

is assumed to have a linear demagnetisation characteristic, and is fully magnetised in the direction of magnetisation.

To simulate the motors with Halbach magnetisation patterns, a group of equations based upon reference [24] are introduced using polar coordinates. As with radial and parallel magnetisation patterns, the targeted Halbach flux distribution in both the air-gap and permanent magnets can also be described by scalar magnetic potential as shown below Equation 4-8a and 4-8b [24].

$$\nabla^2\varphi_1 = \frac{\partial^2\varphi_1}{\partial r^2} + \frac{1}{r}\frac{\partial\varphi_1}{\partial r} + \frac{1}{r^2}\frac{\partial^2\varphi_1}{\partial\theta^2} = 0 \qquad (4-8a)$$

φ_1 is magnetic potential in air-gap.

$$\nabla^2\varphi_2 = \frac{\partial^2\varphi_2}{\partial r^2} + \frac{1}{r}\frac{\partial\varphi_2}{\partial r} + \frac{1}{r^2}\frac{\partial^2\varphi_2}{\partial\theta^2} = \frac{div\vec{M}}{\mu_r} \qquad (4-8b)$$

φ_2 is magnetic potential in permanent magnet.

The radial component of air-gap flux density can be derived from general solution of set governing equations under the defined boundary conditions as shown Equation 4-9a and 4-9b [24]. The achieved simulated air-gap flux density value is decided by M_n, R_r, R_s, R_m, p, μ_r and R_a.

$$B_{air-gap} = -\frac{4B_r p}{D_0(1+p)}\left[1-\left(\frac{R_r}{R_m}\right)^{p+1}\right] * \left[\left(\frac{R_a}{R_s}\right)^{p-1}\left(\frac{R_m}{R_s}\right)^{p+1} + \left(\frac{R_m}{R_a}\right)^{p+1}\right] cosp\theta \qquad (4-9a)$$

$$D_0 = 2[\left(\frac{R_r}{R_m}\right)^{2p}\left[(1-\mu_r)+(1+\mu_r)\left(\frac{R_m}{R_s}\right)^{2p}\right] - \left[(1+\mu_r)+(1-\mu_r)\left(\frac{R_m}{R_s}\right)^{2p}\right]] \qquad (4-9a)$$

It has to be noted that the Halbach air-gap flux density calculation equations in this section are only suitable for iron-cored, inner rotor design. The simulated magnet is fully magnetised in the direction of oriented magnetisation whilst the axial length is regarded as infinitely long.

To summarise, based upon the aforementioned theoretical calculations and the utilised computational software (Matlab in this project), an analytical simulation model can be created

with the reasonably accurate determination of motor no-load magnetic field for all three magnetisation patterns. Magnet inner and outer diameters, radius to stator inner surface and magnet axial length are regarded as the fundamental design variables.

4.4.2 Layered effective air-gap space in the built analytical simulation model

To minimise the potential errors in the simulated no-load magnetic field in a slot-less stator, inner rotor structure machine due to the effectively large air-gap flux leakage, the total effective air-gap space (including pure air-gap space and air-gap winding space) is divided into ten layers of identical radial thickness compared to each other at different radii from the rotor centre. Figure 4-5 below illustrates the layered effective air-gap space in the slot-less motor. The air-gap magnetic field is calculated within each air-gap layer.

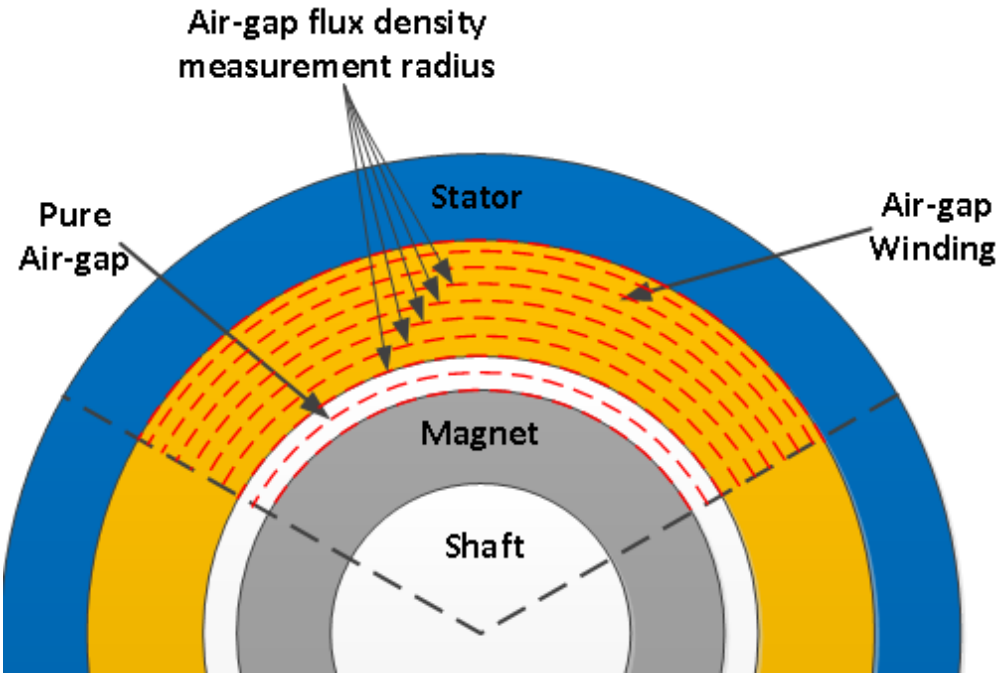

Figure 4-5: Slot-less stator structure motor with layered effective air-gap space

Figure 4-6 below shows the simulated air-gap flux densities with different air-gap radii in two electrical cycles. From air-gap Radius 1 to Radius 10, the simulated air-gap radial thickness increases in 0.2mm steps. The maximum flux density values in the defined air-gap layers with the smallest and the largest radii indicate that, in a slot-less structure motor, the actual air-gap

flux density varies significantly with the effective air-gap radius from the rotor centre. A 2mm radius increase can lead to almost 50% air-gap flux density drop.

Consequently, the commonly utilised mean or median values of estimated air-gap flux density in a slotted motor design are not acceptable in a slot-less stator structure design. It is compulsory to layer the effective air-gap space in the analytical simulation model to precisely determine the air-gap flux distribution layer by layer, so as to correctly calculate the coil flux linkage and the induced electro-motive forces in the air-gap windings. The more number of layers it defines, the more accurate results it delivers. As mentioned at the beginning of this section, there are 10 layers defined in the constructed analytical simulation model in this project.

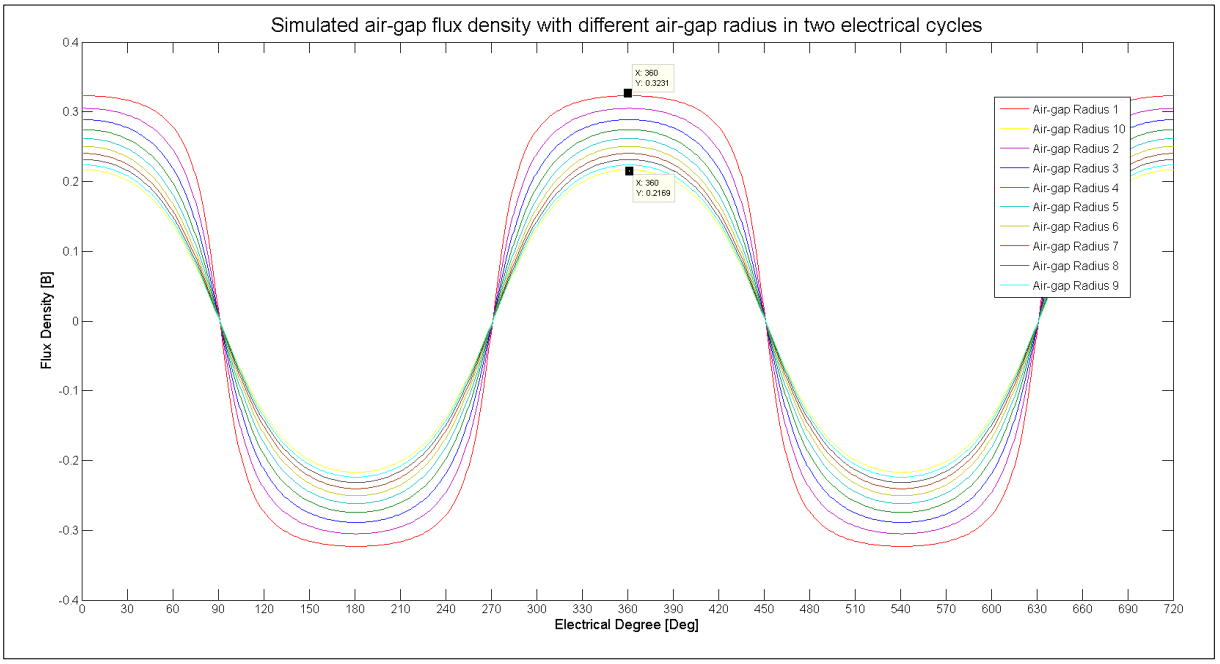

Figure 4-6: Simulated air-gap flux densities with different radial air-gap radii in two electrical cycles

4.4.3 Analytical simulation of motor performance

Based upon the analytically determined motor no-load flux distribution, the flux linkage in one stator coil can be predicted along with the induced motor back-EMF. It has to be noted that, when calculating the amplitude of the generated motor back-EMF, the motor winding factor must be taken into account. The calculation of motor winding factors for slotted and slot-less motors are discussed in the following section. From the calculated back-EMF in one coil, the

required number of turns per phase and the phase rated current can be determined to meet the aimed motor design specifications.

Once the air-gap magnetic field, the number of turns per phase and the phase rated current of the motor are calculated, the next stage is to finalise the motor geometrical details such as the effective winding area, the conductor size of the phase wire and the motor volume, along with calculations of current density in the phase wire, iron loss in the stator core-back, Ohmic loss in the windings and proximity loss in the coils. Motor loss estimation is discussed in the following section.

Lastly, using the volumes of each motor component and the given mass density, the weight for each component is obtained as well as the material cost.

4.4.4 Thermal effect on magnet residual flux density

It is known that the phenomenon of reversible temporary demagnetisation can occur in rare-earth permanent magnets with the growth of magnet temperature. In an operating permanent magnet motor, the induced motor total losses generate undesirable heat in the system, leading to the increased magnet temperature. Due to the drop in magnet residual flux density, the resultant motor performance, including the phase back-EMF, the motor output torque and the output power are all unavoidably reduced. Consequently, it is necessary to include the magnet thermal effect in the analytical simulation to compensate for the magnet demagnetisation caused motor power drop. For most electric motors, the operating temperature is higher than 20°C nominal ambient temperature.

Figure 4-7 below demonstrates the demagnetisation curves under different magnet temperatures for rare-earth permanent magnets with varied residual flux densities. The shown demagnetisation in the graph is purely due to the magnet temperature change, and no external demagnetising flux is applied. All plotted data is achieved from industrial supplier. The graph indicates that all eight sorts of NdFeB permanent magnets feature the same tendency of reduced magnet residual flux density with rise of magnet temperature. The temperature range of typical motor operation is highlighted by red slash lines in the graph. According to the curves, the demagnetisation of rare-earth permanent magnets changes linearly in the normal motor operational temperature range of domestic applications, i.e. 0°C ~ 100°C.

Consequently, a linear relationship between residual flux density drop and magnet temperature rise can be expected, and a corresponding compensation scheme can be introduced in the analytical simulation model.

The following equations represent the magnet thermal compensation method in the constructed analytical simulation model. B_{hot} is the magnet residual flux density at operational temperature; T_f is the magnet temperature based demagnetisation factor; C_{T_f} is the magnet temperature based demagnetisation coefficient. ΔT_{rise} is the temperature rise between the magnet operational temperature T_{opm} and the nominal ambient temperature T_{cold}.

$$B_{hot} = B_r * T_f \quad (4-10)$$

$$T_f = 1 - (C_{T_f} * \Delta T_{rise}) \quad (4-11)$$

$$\Delta T_{rise} = T_{opm} - T_{cold} \quad (4-12)$$

The value of C_{T_f} is achieved from curve-fitting of the plotted magnet demagnetisation curves. In the analytical simulation model, this value is set as 0.11% Tesla per degree Celsius.

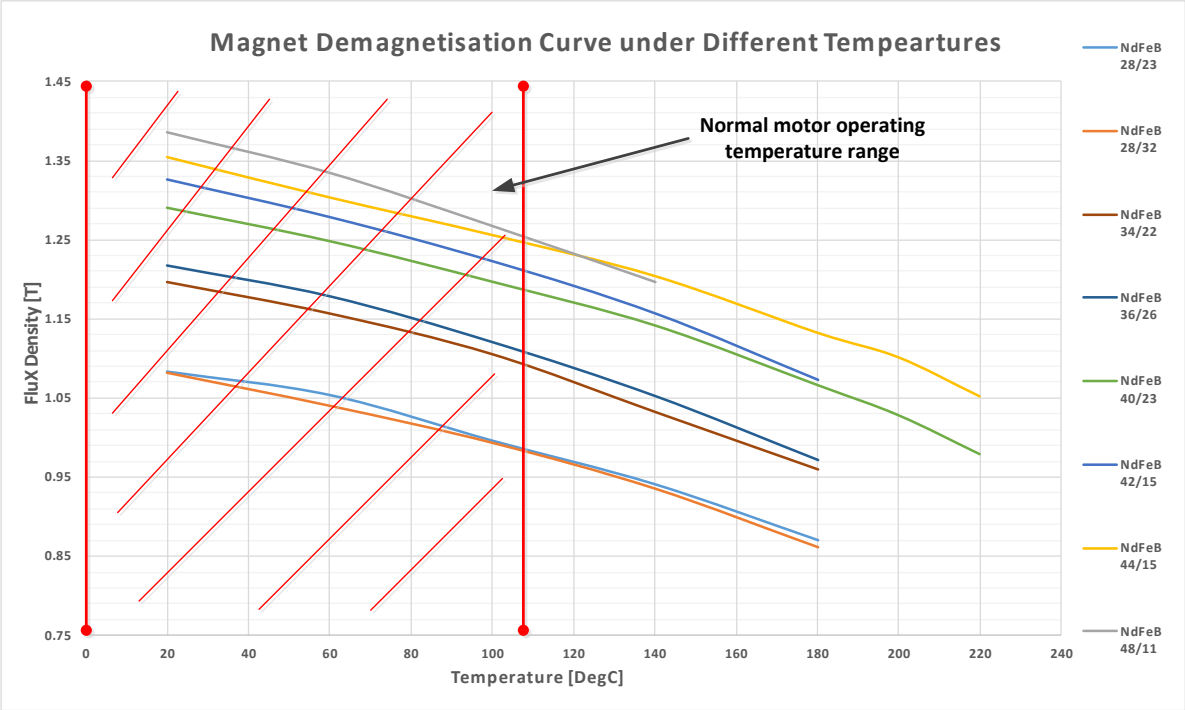

Figure 4-7: Magnet demagnetisation curves under different magnet temperatures

4.4.5 Thermal effect on wire resistance

Contrary to the magnet residual flux density, the resistance of copper wire is increased along with a rise of coil temperature due to increased resistivity. The increased coil resistance results in greater motor Ohmic loss, lowering the motor operating efficiency, and bringing the risk of coil overheating. Therefore, the resistance thermal effect must be taken into account at the motor preliminary design stage.

As earlier, the coil resistivity rise coefficient C_{crr} is introduced to estimate copper resistivity rise per degree Celsius. The hot copper resistivity in the analytical simulation model is expressed as Equation 4-13. T_{opc} is the coil operation temperature.

$$\rho_{hot} = 1 + (T_{opc} - T_{cold}) * C_{crr} \qquad (4-13)$$

The effective operational wire resistance can be expressed as in Equation 4-14.

$$R_{hot} = R_0 * \rho_{hot} \qquad (4-14)$$

Using the same curve-fitting approach as above, the coil resistivity rise coefficient C_{crr} is calculated to be 0.00393 in the analytical simulation model, as shown in Figure 4-8. The plotted points are achieved based upon experimental data of a wire-wound resistor with known resistance value. The high precision milliohm meter is utilised.

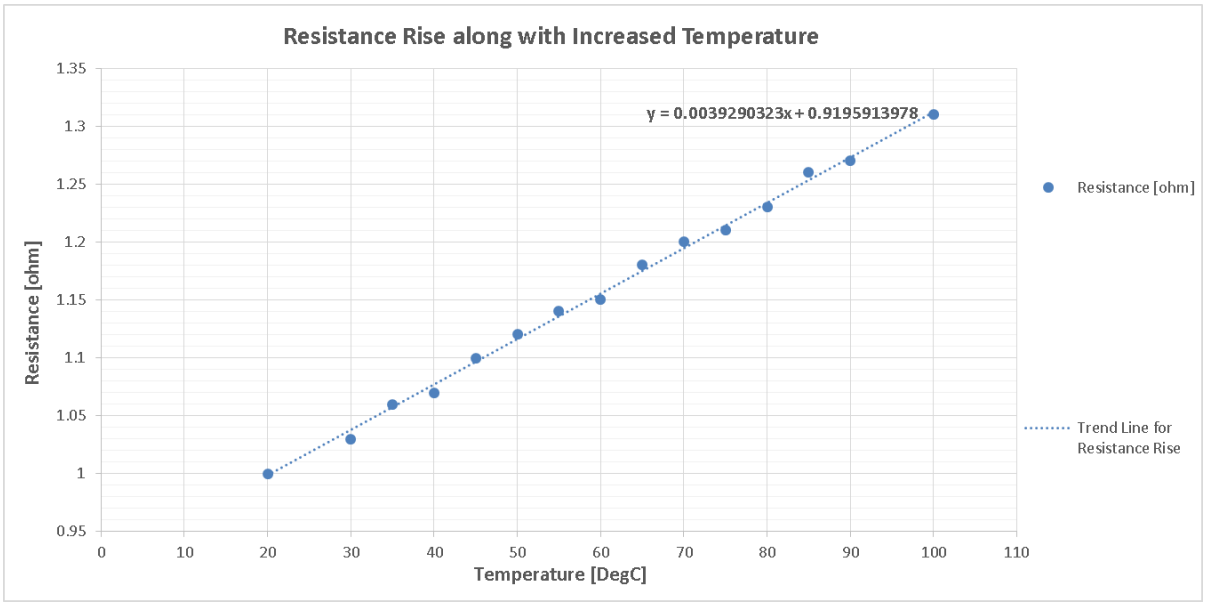

Figure 4-8: Increased resistance value along with temperature rise with plotted trend line and curve fitting equation

4.5 Motor loss estimation

Due to the high speed, power-dense nature of the designed motor, there are several significant sources of motor losses. This section considers the major loss elements in slot-less structure machine, including DC copper loss, iron loss, AC copper loss and rotor loss. The calculations of each loss element will be included in the constructed analytical simulation model.

4.5.1 DC copper loss

When passing a direct current through a coil, it produces heat due to the resistance of the conductor, resulting in DC copper loss. Based upon Joule's Law, this is illustrated in Equation 4-15.

$$P_{dc} = I^2 R \qquad (4-15)$$

Because of the large effective air-gap and high flux leakage in air-gap winding machines, the motor electrical loading is required to be higher than that in slotted designs to compensate for the drop of motor magnetic loading. Therefore, the operating current density can be higher in slot-less motors, leading to increased DC copper loss and reduced motor efficiency.

Consequently, for slot-less stator designs, it is more critical to include phase end-winding effects at the preliminary design stage, which helps to evaluate the worst case scenario. Figure 4-9 below demonstrates a half sized air-gap winding with labelled paths of overall winding length and end-winding length. The graph shows that overall winding length is calculated along the loop in the middle of the winding coils. The end-winding length for a complete air-gap winding is considered as Equation (4-16). As shown in the graph, l_w is the coil width; l_p is the size of pole pitch.

$$End - winding\ length = 2 * \left(2 * l_w + l_p\right) \qquad (4-16)$$

Equation 4-16 is then introduced in the analytical simulation model to minimise error in the DC copper loss estimation.

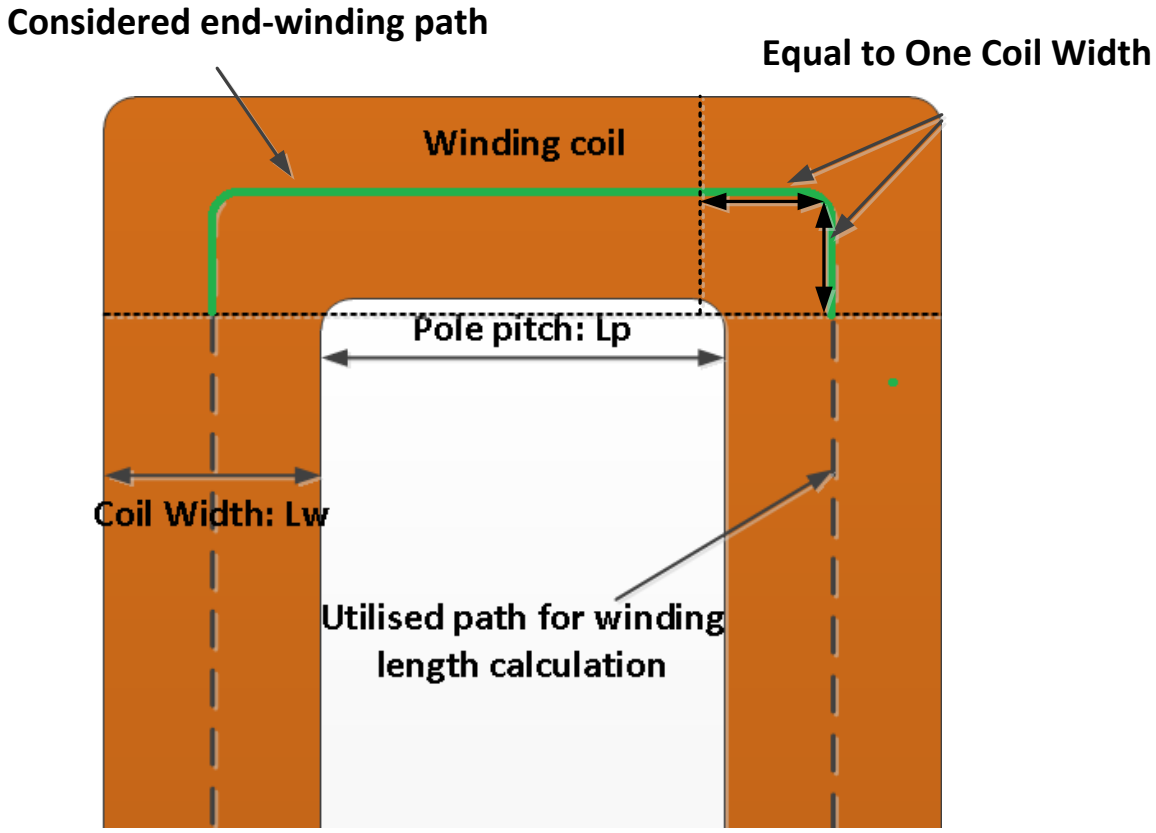

Figure 4-9: Illustrated paths for overall winding length and end-winding length calculations in half-sized air-gap winding

4.5.2 Iron loss

The high residual flux density permanent magnets utilised in high-speed, power-dense, brushless DC motors contribute to significant iron loss induced in the stator core-back.

As stated in [91, 92] and [93], iron loss consists of three components: eddy current loss, hysteresis loss and anomalous loss as shown in Equation 4-17.

$$Iron\ loss = P_e + P_h + P_a = K_e f^2 B^2 + K_h f B^{\alpha} + K_a f^{1.5} B^{1.5} \qquad (4-17)$$

The constants of K_e, K_h, K_a are coefficients for eddy current loss, hysteresis loss and anomalous loss respectively, which are determined by the properties of the lamination materials. f is the electrical frequency of the stator magnetic flux; B is the flux density in stator core-back.

On the other hand, Equation 4-17 only concerns the ideal case which iron loss is only due to the fundamental flux in the stator core-back. With high frequency chopping currents, the resultant armature reaction produces ripples in the stator magnetic flux, introducing high order time harmonics in the stator core-back flux density. Each flux harmonic contributes to the effective iron loss, hence, the resultant iron loss must be calculated for each harmonic component, based upon the flux frequency and its peak value. There are two common approaches to calculate the improved iron loss.

1. Use a Fast Fourier Transform Algorithm to calculate the amplitude of each core-back time harmonic component; and then calculate the corresponding eddy current loss, hysteresis loss and anomalous loss in each harmonic.
2. Using Finite Element Analysis Software to simulate the iron loss with simulated or captured real phase currents [94], employing their own calculation methods.

Method one needs plenty of computational calculation for each harmonic component, whilst method two demands extremely fine mesh size in the simulation model and long simulation times.

For slot-less topology designs, the impact of high order time harmonics of core-back flux on stator iron loss is limited. Removing the stator teeth can significantly reduce the phase inductance, and hence the armature reaction. The amplitudes of the resultant high order harmonics are therefore comparatively low. Figure 4-10 below demonstrates the 3-phase, slot-less stator structure, finite element simulation model for iron loss analysis. The model features a 25mm outer diameter and a 25mm axial length. The stator lamination steel is 0.2mm non-oriented electrical steel. In the simulation, the motor operates at 150,000rpm with a chopped phase current of 5000Hz fundamental electrical frequency to deliver fixed 640W output power. The following Figure 4-11 illustrates the waveform of applied chopped current in two mechanical cycles.

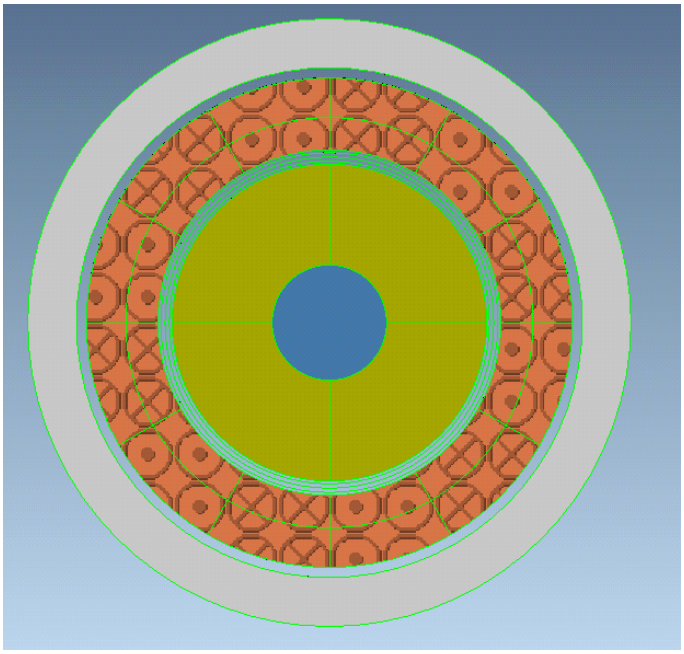

Figure 4-10: Created 3-phase slot-less structure FE simulation model for iron loss analysis with chopped phase current

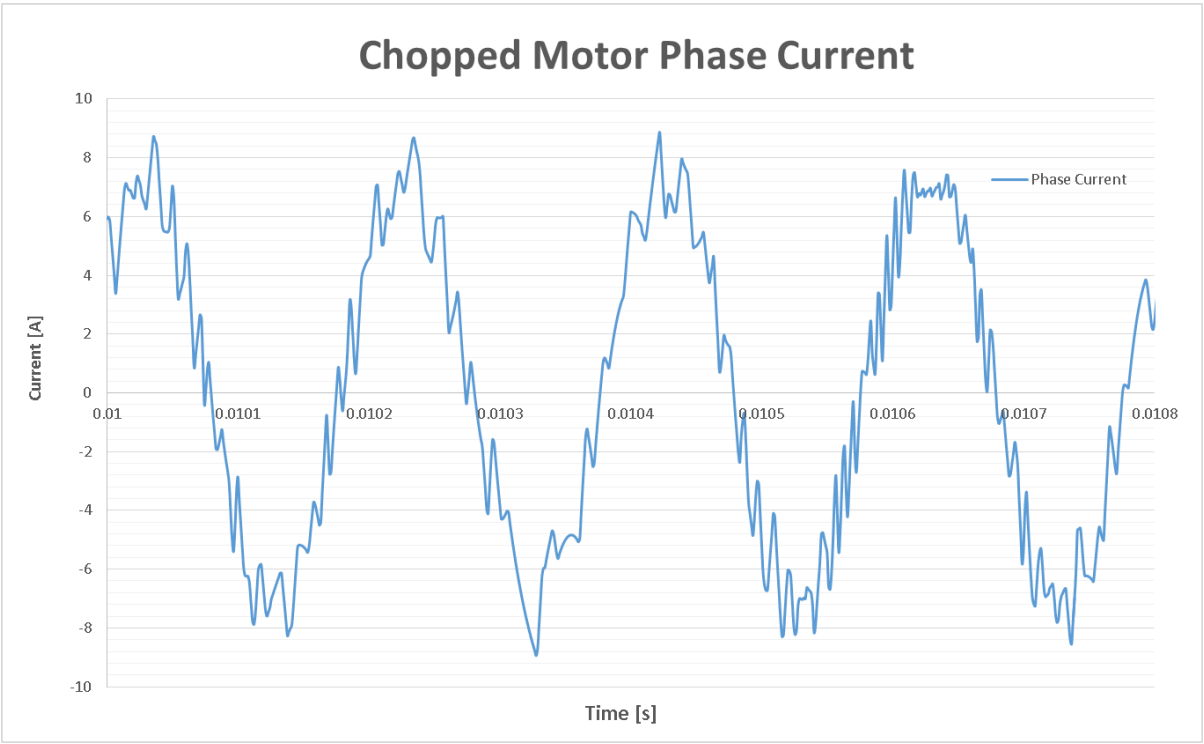

Figure 4-11: Applied simulated chopped phase current with 5000Hz fundamental electrical frequency

The analytically calculated iron loss with ideal currents is calculated using Equation 4-17. Another FE simulation model is constructed, identical to that of Figure 4-10, but fed with ideal sinusoidal phase current to repeat the same iron loss simulation. Comparing the three sets of results, the highest iron loss is achieved when using the chopped phase current, although the difference is only 0.8W, which is a 12.5% loss increase.

Figure 4-12 below demonstrates the spectrum plot of the simulated stator magnetic flux at a point 0.2mm away from the stator inner surface, within stator core-back laminations over a mechanical cycle. The graph shows that, the 3rd and the 5th order time harmonics have a relatively higher amplitude in comparison with the other harmonics, which are around 6% and 10% larger respectively compared to the fundamental harmonic. In a slotted stator permanent magnet motor, this ratio could be as high as 20% [95].

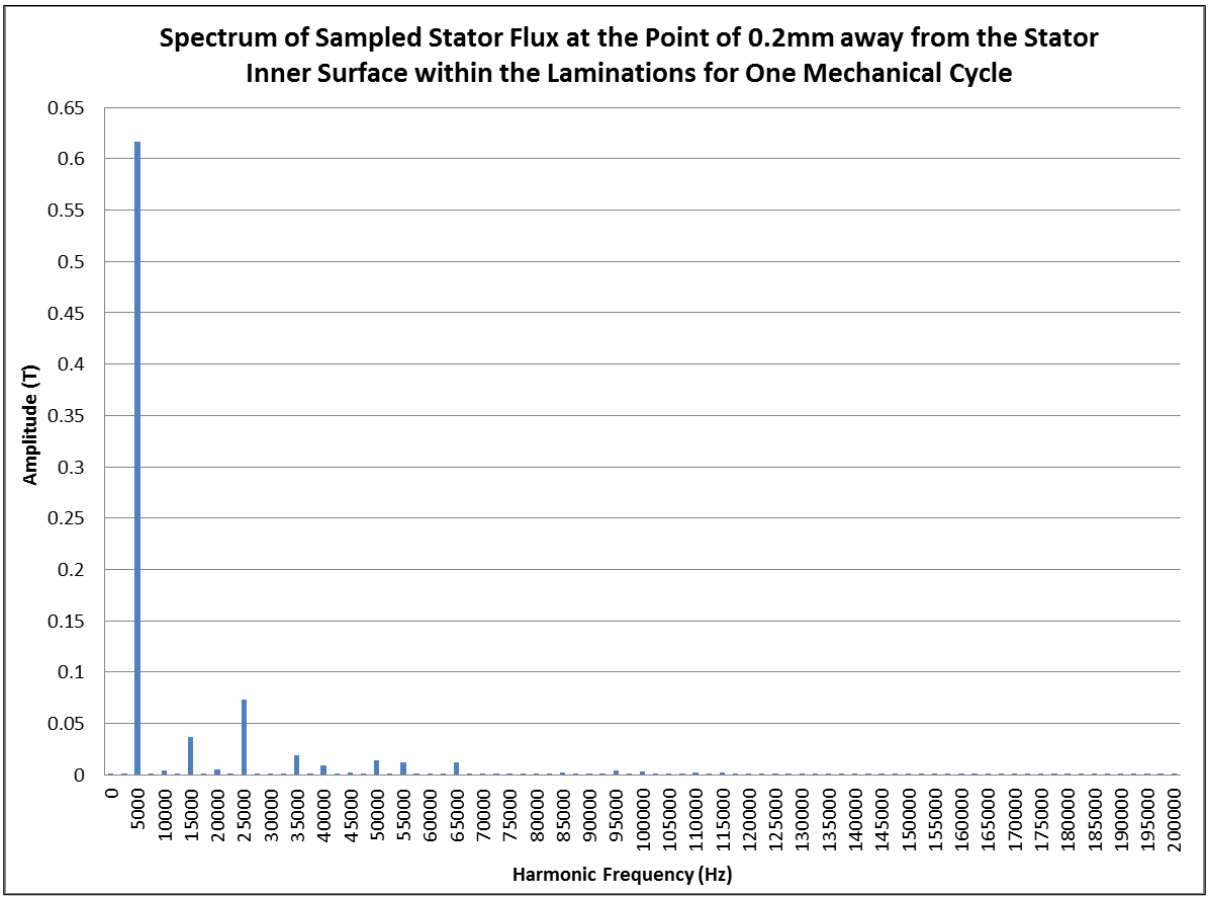

Figure 4-12: Spectrum of sampled stator core-back flux at point of 0.2mm away from stator inner surface within stator core-back lamination in one mechanical cycle

To summarise, thanks to the large effective air-gap, the core-back flux density in air-gap winding motors is much lower than that in slotted designs, which helps to reduce the total lamination loss. Removing stator teeth also contributes to such advantages as reduced lamination volume and weight. Consequently, the iron loss is much lower in slot-less stator structure designs in comparison with the other loss elements. Furthermore, finite element simulation suggests that the increase in iron loss due to high order current harmonics is actually low. Consequently, it is reasonable to simply use Equation 4-17 in the analytical simulation model to estimate the iron loss. The resultant error will be extremely small (<0.15%) when compared to the overall 750W input power.

4.5.3 Magnet eddy current loss

In permanent magnet synchronous motor, there is no eddy current loss induced in the rotor magnets, as the magnet rotates synchronously with the armature field. Nevertheless, in real cases, voltages can be induced in conductive permanent magnets due to asynchronously rotating air-gap magnetic field components. These asynchronous magnetic fields come from time harmonics, caused by high frequency chopping phase currents, tooth ripple harmonics due to slotting effects, harmonics of the winding MMF or any other combined interaction from these three factors.

As the induced eddy current loss can cause undesirable heat, it causes temporary demagnetisation along a reduced phase back-EMF and reduced motor output power. More importantly, there may be demagnetising armature flux, resulting in irreversible demagnetisation of the rotor permanent magnets. Furthermore, the repeated and rapid temperature change of the magnet can weaken its mechanical strength, making it more brittle than it should be. In recent years, there has been a lot of work on estimating and minimising magnet eddy current loss [15, 20, 25, 26].

When considering magnet eddy current loss in a slot-less stator structure motor, the induced eddy currents in the rotor magnet tend to be comparatively low. To be specific, slotting effects are eliminated as the stator permeance is constant in the circumferential direction of air-gap. Space harmonics of the stator armature field are also minimized due to the distributed nature of the air gap winding. In addition, the armature reaction per unit flux is also low due to the

high reluctance of the armature magnetic circuit. The large air gap on the motor effectively minimises the influence of any asynchronous air-gap harmonics on the rotor.

As earlier, a 2-dimensional 3-phase slot-less structure finite element simulation model is created with chopped current to deliver 640W output power at 150,000rpm. Both shaft and magnet are defined with conductivity values extracted from material datasheets to simulate the resultant eddy current loss. Figure 4-13 demonstrates the distribution of induced eddy current inside the simulated permanent magnet under the rated load conditions. The unit of J is Ampere per meter square. The following Figure 4-14 shows the simulated Ohmic loss values in the rotor magnet over a period of one mechanical cycle. The simulated rotor magnet has 4 poles with parallel magnetisation pattern. Noted that, though the manufacturer can produce the ring shape magnet with parallel magnetisation, in the conducted finite element simulation, the rotor magnet is segmented so as to easily define the required magnetisation. The edge between two magnet segments is defined with infinite permeability. The loss curves indicate that the potential rotor loss can be ignored for a slot-less stator structure motor. In the analytical simulation model, no rotor loss estimation function is implemented. It is only validated in the finite element simulation stage.

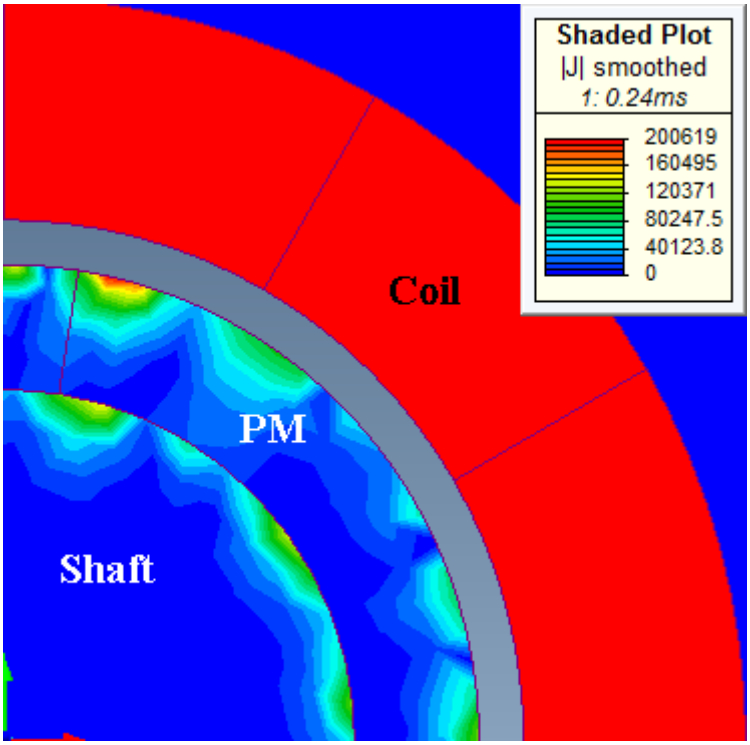

Figure 4-13: Eddy current distribution within the magnet under the rated load condition

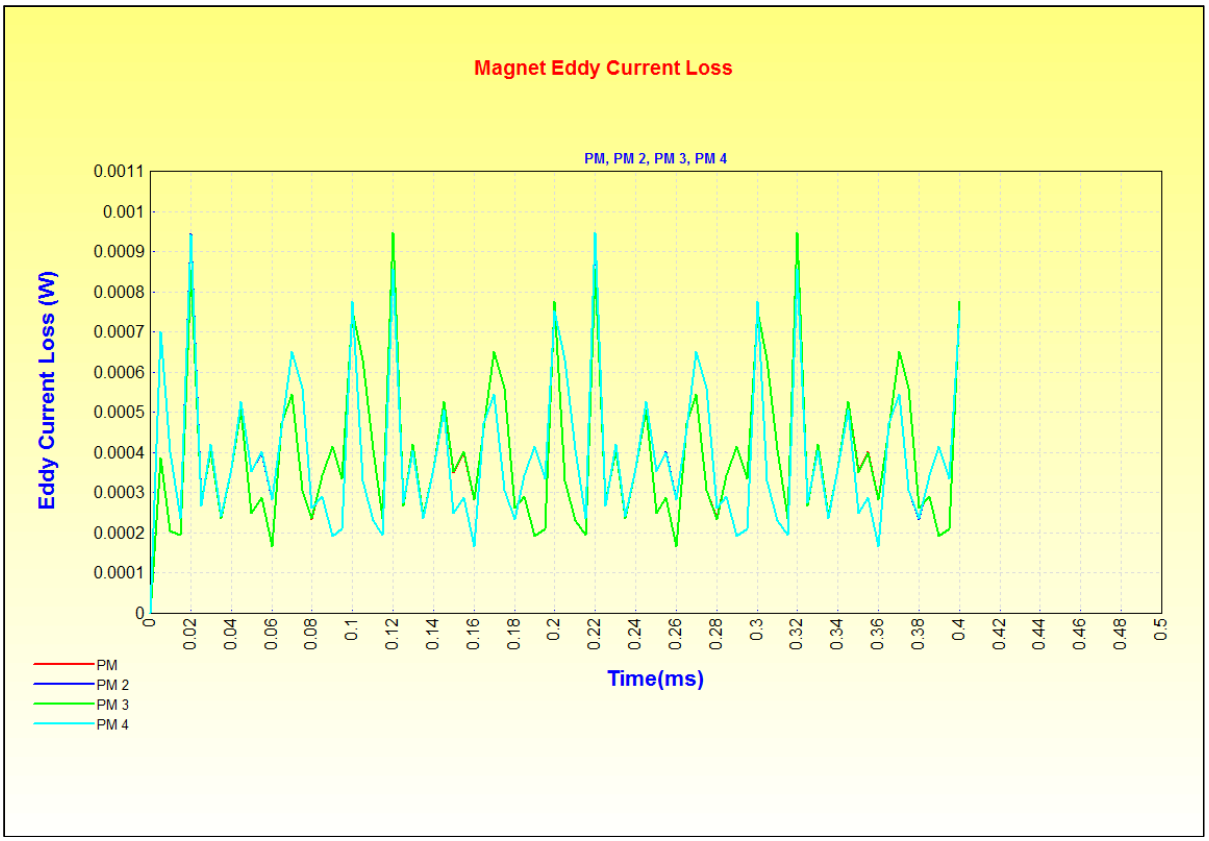

Figure 4-14: Magnet eddy current loss in a time period of one mechanical cycle

4.5.4 AC copper loss

When passing a direct current through a coil, it only produces DC copper loss. Nevertheless, when 5000Hz alternating current is injected into the coil, the effective copper loss is significantly higher due to AC effects. This section discusses the major causes of AC copper loss in permanent magnet motors including their impacts on the constructed analytical simulation model.

4.5.4.1 Skin effect

When a high frequency alternating current flows through a conductor, the induced time varying magnetic field inside the conductor induces eddy currents with opposite direction of the carrying current, which cancels the main current in the centre of conductor but enhances it at the conductor surface. This outcome forces the current to be re-distributed from evenly across the conductor to flowing at the conductor surface, as shown in Figure 4-15. This then increases the effective resistance value of the conductor, decreasing the current transmission efficiency.

The depth of conductor surface where the current is forced to pass through is termed as the "skin depth", which can be determined via Equation 4-18 [96]. δ is the skin depth; μ is material permeability, which equal to the product of the relative permeability μ_r and Vacuum permeability μ_o; ω is angular velocity.

$$\delta = \sqrt{\frac{2}{\sigma * \omega * \mu}} \qquad (4-18)$$

For the targeted 4-pole motor at a speed of 150,000rpm, the skin depth of copper wire is 0.92mm. If the final selected wire diameter is significantly less than 1.8mm, the skin effect can be ignored.

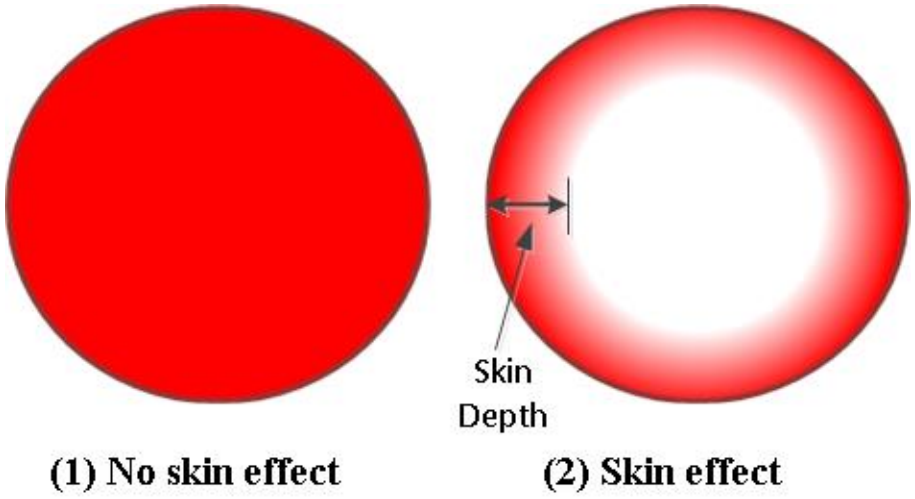

Figure 4-15: Comparison of two conductors with and without skin effect

4.5.4.2 Proximity loss

When a high frequency alternating current flows through a conductor, the induced internal time varying magnetic field causes the skin effect, whilst the created external time varying magnetic field results in the proximity effect.

When two conductors are close to each other and carry high frequency alternating current, each one will be influenced by the other's generated external magnetic field. When both conductors carrying the same frequency and same direction of current, induced eddy currents will cancel the main current on the adjacent side of each conductor. When two conductors carrying the same frequency but opposing directions of current, the current flowing through the remote side

of each conductor will be eliminated. Figure 4-16 below demonstrates the flux distribution fields of two adjacent conductors illustrating proximity effect. The next Figure 4-17 shows the resultant current distribution inside the conductors.

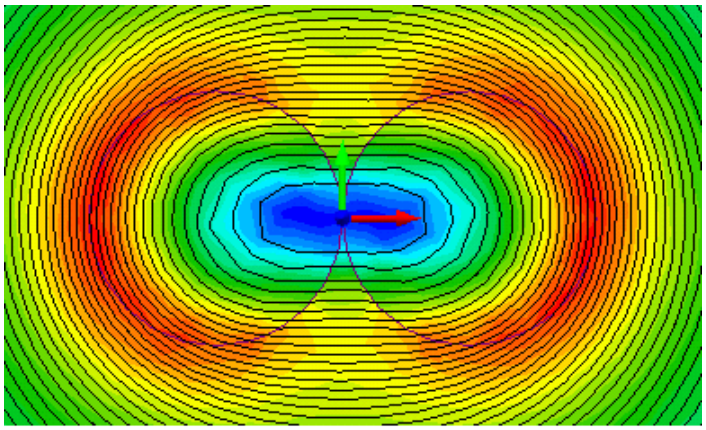

(1) Current Flow in Same Direction

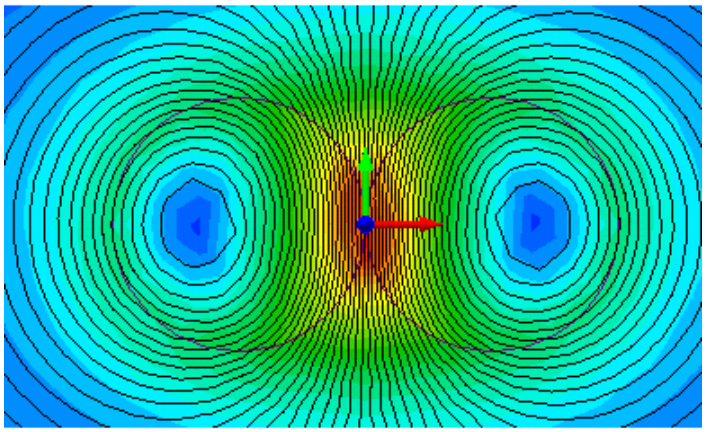

(2) Current Flow in Opposing Direction

Figure 4-16: Plotted flux distribution fields of two adjacent conductors illustrating proximity effect.

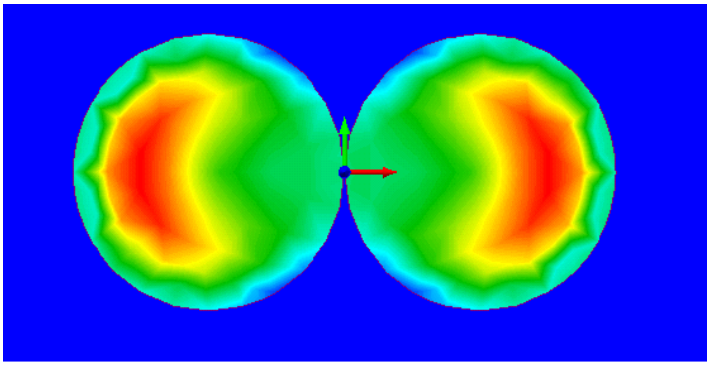

(1) Current Flow in Same Direction

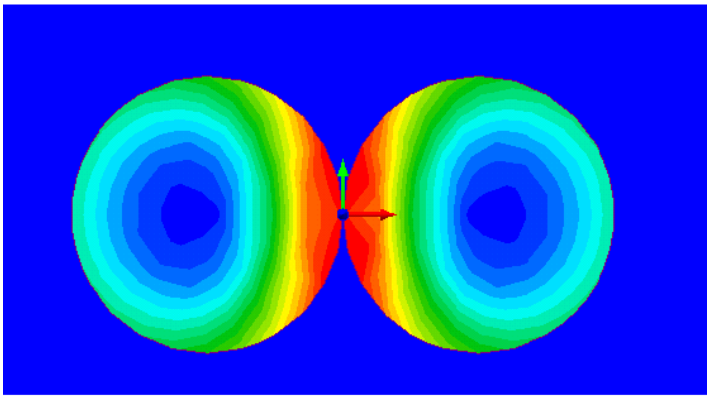

(2) Current Flow in Opposing Direction

Figure 4-17: The resultant current distribution inside two adjacent conductors illustrating proximity effect.

In a slot-less structure motor, there are more than two conductors adjacent to each other per phase winding. If these conductors are connected in parallel, then due to combined proximity effect, it can be predicted that the current flowing in the conductors located at the centre of the winding coil has been significantly cancelled out; whilst the currents in the rest of the coils are forced to pass through the remote side of the conductor. Similar to the skin effect, the effective resistance of each conductor is increased due to forced uneven current distribution. Figure 4-18 below demonstrates the flux distribution fields of a group of conductors illustrating proximity effect. The next Figure 4-19 shows the resultant current distribution inside the conductors.

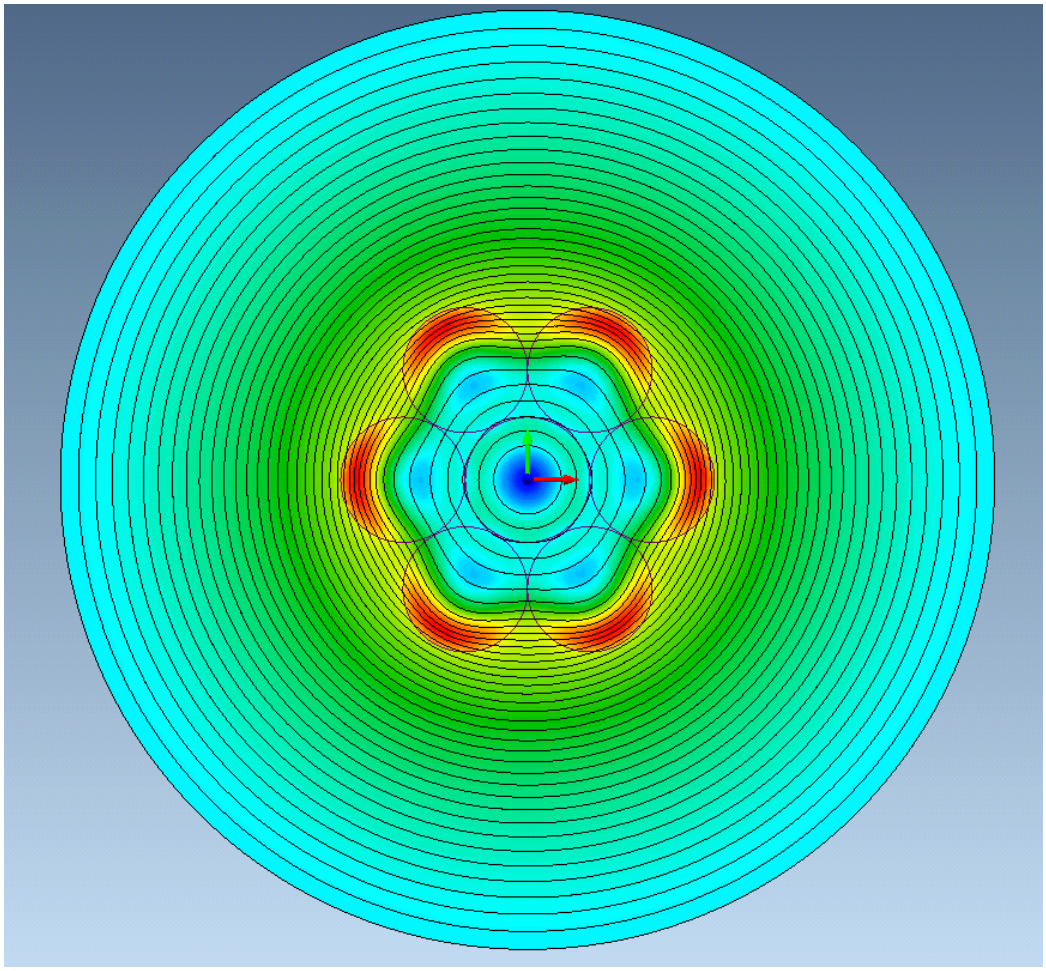

Figure 4-18: Plotted flux distribution fields of a group of conductors illustrating proximity effect.

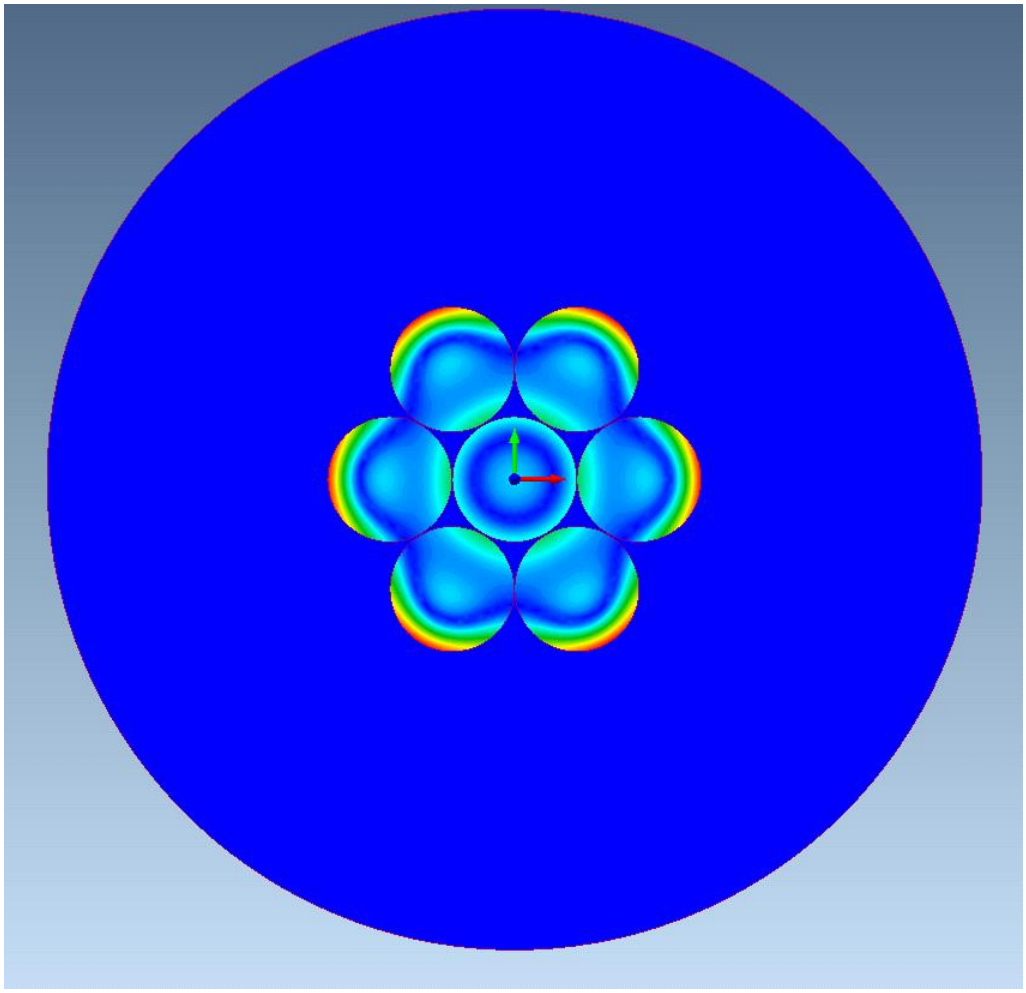

Figure 4-19: The resultant current distribution inside a group of conductors illustrating proximity effect.

More importantly, due to the air-gap winding structure, magnetic flux generated by the rotor permanent magnets flows through the stator phase windings, as shown in Figure 4-20. Therefore, even under no-load condition, the winding coils suffer from the undesirable proximity effect. The unevenly distributed eddy currents inside the coils are demonstrated in Figure 4-21.

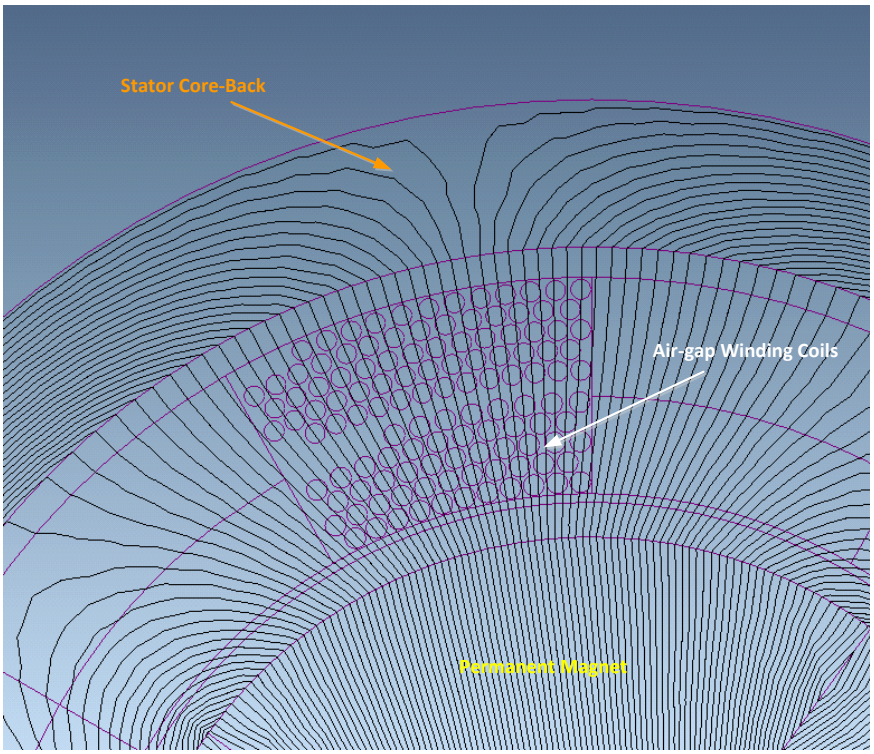

Figure 4-20: Flux plot for air-gap winding coils

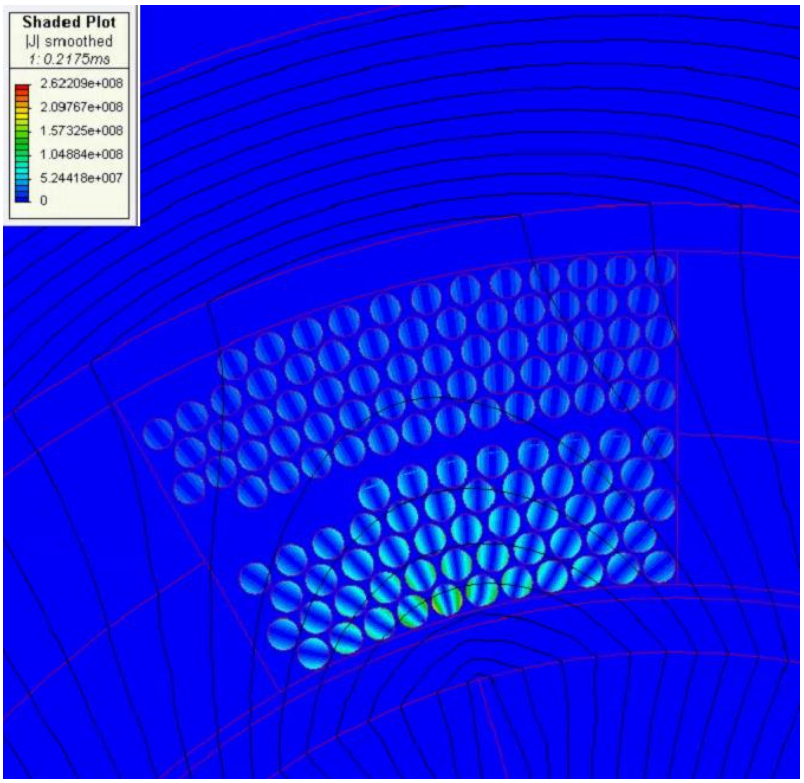

Figure 4-21: Distributed current in winding coils due to proximity effect

Reference [97] discusses an investigation of the proximity effect on the conductor, and illustrates a method for prediction of the associated AC copper loss, as given in Equation 4-19. l is the conductor length; ρ_c is the conductor resistivity; d_c is the conductor diameter. From the equation, it shows that proximity loss in a single conductor is proportional to the 4th power of conductor diameter, and so rises quickly with growth of wire diameter.

$$P_{AC}(t) = \frac{\pi l d_c^4}{64\rho_c}\left(\frac{dB}{dt}\right)^2 \qquad (4-19)$$

The motor DC copper loss, given in Equation 4-20, indicates that Ohmic loss is inversely proportional to the square of conductor diameter, and so falls rapidly with growth of wire diameter.

$$P_{DC} = I^2R = I^2\rho_c\frac{l}{\pi\left(\frac{d_c}{2}\right)^2} = \frac{4\rho_c I^2 l}{\pi {d_c}^2} \qquad (4-20)$$

As a consequence, adjusting the wire diameter can create opposing impacts on the resultant copper loss. It is necessary to find a balance between the two loss elements. Figure 4-22 below illustrates the trend of the total copper loss with reduced wire OD for a varied ratio of proximity loss to Ohmic loss. Note that these curves are achieved based upon theoretical calculation under the assumptions of fixed conductor axial length, fixed conductor resistivity, fixed RMS value of injected current and fixed AC current fundamental frequency. The DC copper loss induced under the original wire OD is defined as 1 p.u. The green line demonstrates the total copper loss with the increasing proximity loss. The other lines show the new trend lines of the total copper loss under the reduced wire ODs.

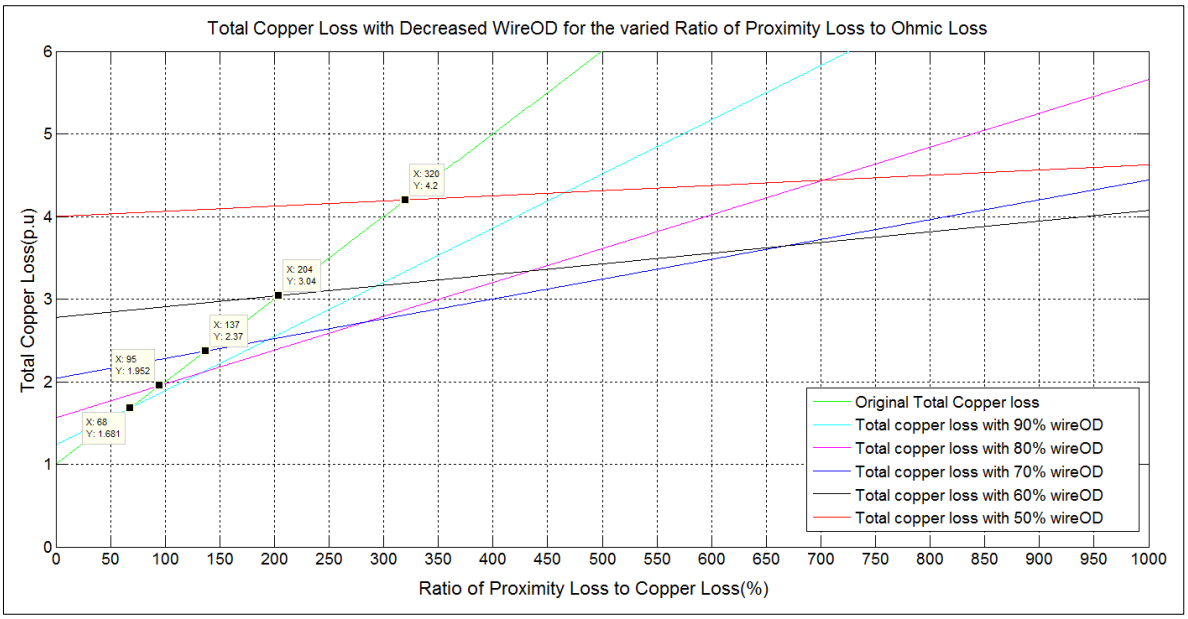

Figure 4-22: Total copper loss with decreased wire OD under varied ratio of proximity loss to Ohmic loss.

Figure 4-22 illustrates that the change of total copper loss depends on both the ratio of proximity loss to Ohmic loss, and the ratio of reduced conductor size to the original size. The marked positions on the graph represent the balancing design points, at which the new total copper loss under the use of decreased wire size is equal to the original values of total copper loss. When the ratios of proximity loss to Ohmic loss in the original designs have higher values than those at these points, it is better to reduce the wire diameter to reduce the combined loss under the constraint of fixed mean coil current density. When this loss element ratio is lower than the value on the balancing point, the opposite result occurs. It has to be highlighted that the above conclusion is available when the proximity loss is only caused by the used permanent magnet generated field. The effect of armature reaction on proximity loss has not been considered yet.

To summarise, due to unavoidable proximity loss generated in an air-gap winding motor, the estimation of this AC loss must be taken into consideration in the analytical simulation model, with the support of Equation 4-19.

4.6 Analysis of the motor winding factor

The winding factor for a given winding can be defined as the ratio of the actual voltage induced in that winding in comparison to the maximum voltage which can be generated in a single-layer fully pitched winding with the same number of turns and only a single slot of each phase. The effective winding factor can be expressed as the product of the motor pitch factor, k_p, and the distribution factor, k_d, i.e. $k_w = k_p * k_d$. Note that, as there is no cogging torque in slot-less stator structure motors, the magnet skewing factor is treated as 1 and not taken into consideration in this project.

For a fully pitched winding coil, the phase angle between the two coil sides is 180° electrical. Consequently, the resultant back-EMF of this coil is simply equal to the numerical sum of the back-EMFs induced in both coil sides. In this case, as there is no phase angle between the two sides of the coil, the numerical sum of the induced back-EMFs is equivalent to the value of its vector sum.

When the value of actual phase angle between the two opposite coil sides becomes less than 180° electrical, this type of the winding coil is termed short pitched. The induced back-EMFs from the two sides of the coil are required to be vectorically added together to obtain the resultant coil back-EMF. The pitch factor, therefore, is referred to the ratio of the resultant back-EMF in a short pitched winding coil compared to the resultant back-EMF in a fully pitched winding coil with the same active length and the same number of turns. As Figure 4-23 shows, the calculation of the motor pitch factor can be expressed as Equation 4-21 below. The symbol "α" refers to the phase angle between the generated back-EMFs in two opposite coil sides. It has to be noted that this calculation approach is only applied for the fundamental component of the resultant back-EMF. Regarding the higher order harmonics in the generated back-EMF, the corresponding pitch factor can be achieved via Equation 4-22, where the symbol "r" in the equation represents the calculated r^{th} order harmonics.

$$k_p = \frac{Resultant\ back-EMF\ of\ a\ short\ pitched\ coil}{Resultant\ back-EMF\ of\ a\ fully\ pitched\ coil} = cos\frac{\alpha}{2} \qquad (4-21)$$

$$k_{pr} = cos\frac{r\alpha}{2} \qquad (4-22)$$

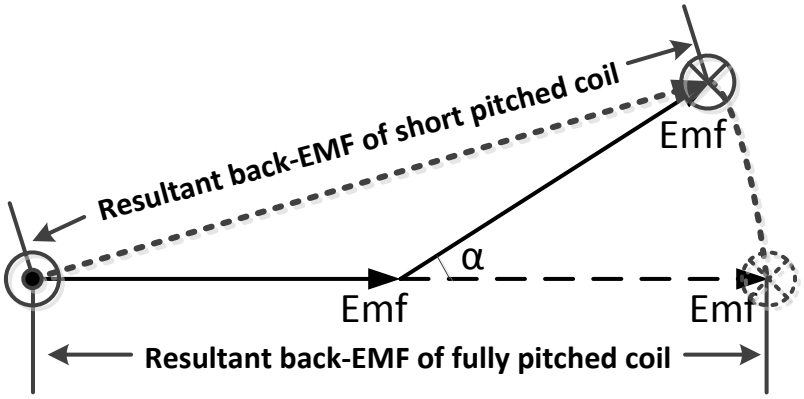

Figure 4-23: Pitch factor calculation

The winding distribution factor reflects the fact that the winding coils are distributed in a number of slots per phase per pole, rather than bunched in a single slot. Windings which feature concentrated coils in one slot per phase per pole are termed concentrated windings with unity distribution factor. As there is no phase angle between each coil, the resultant back-EMF of the phase winding can be achieved via the numerical sum of the induced back-EMF in each coil and equals to the value of its vector sum.

With a distributed winding structure, the winding coils of each phase are distributed in a number of slots with a non-zero phase angle between the coils. Accordingly, the resultant back-EMF value of the phase winding can only be achieved through the vector sum of the induced back-EMFs in all coils in each slot.

Accordingly, the value of the winding distribution factor is defined as the ratio of the resultant back-EMF of a distributed winding in comparison to the back-EMF induced in a concentrated winding. As stated in Figure 4-24, the motor pitch factor can be expressed as Equation 4-23. The symbol "n" equals to the number of the total slots per phase, and the symbol "β" represents the phase angle of the back-EMFs induced in the coils located in two adjacent slots in the same phase. As with the pitch factor, the calculation of the motor distribution factor is only appropriate for the fundamental component of the resultant back-EMF. For higher order harmonics in the generated back-EMF, the corresponding distribution factor is shown in Equation 4-24, where the symbol "r" in the equation represents the targeted r^{th} order harmonics.

$$k_p = \frac{Back-EMF\ induced\ in\ distributed\ winding}{Back-EMF\ induced\ in\ concentrated\ winding}$$

$$= \frac{Vector\ sum\ of\ EMFs\ induced\ in\ each\ slot\ per\ phase}{Numerical\ sum\ of\ EMFs\ induced\ in\ each\ slot\ per\ phase}$$

$$= \frac{\sin(\frac{n\beta}{2})}{nsin(\frac{\beta}{2})} \qquad (4-23)$$

$$k_{pr} = \frac{\sin(\frac{rn\beta}{2})}{nsin(\frac{r\beta}{2})} \qquad (4-24)$$

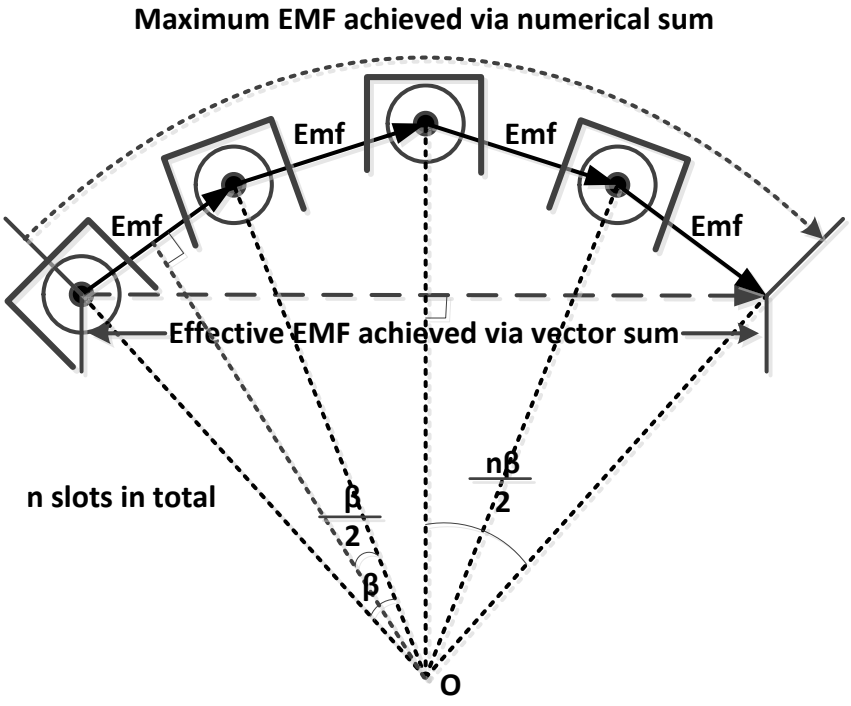

Figure 4-24: Distribution factor calculation

When evaluating the motor distribution factor in an electrical machine with a slot-less stator topology, the equations discussed above must be modified.

Considering a single-layer, fully spanned phase winding with N turns of winding coils distributed along the stator arc to cover the entire pole arc range of 180 electrical degree, the generated back-EMF in the first turn of the winding coils features the inevitable phase difference compared to the back-EMF induced in the last turn coil of the same winding, as

shown in Figure 4-25 below. Figure 4-25 indicates that the resultant back-EMF generated by the slot-less winding in the motor is not simply equal to the value of the numerical sum of the induced back-EMFs in each turn of the winding coils. In a slot-less stator structure motor, the effective motor distribution factor is determined by the effective phase angle in electrical degree between the first turn and the last turn of the motor winding, i.e. the winding span arc of the machine.

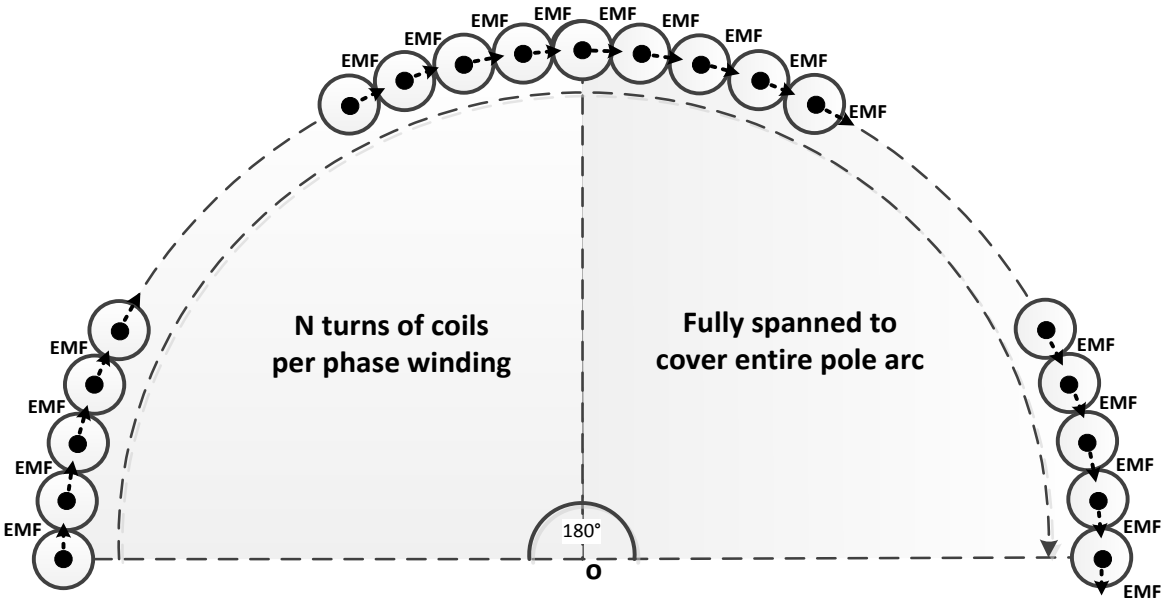

Figure 4-25: Single-layer fully spanned (covering complete pole arc of 180° electrical) winding coils in slot-less structure motor

The equivalent phasor diagram of the winding distribution factor for the air-gap windings is shown as Figure 4-26 below. The symbol "β" refers to the actual winding span arc in electrical degrees for the designed slot-less topology windings. The corresponding mathematical calculation of the distribution factor is illustrated in Equation 4-25 for the fundamental component and Equation 4-26 for r^{th} order harmonics. Both equations are utilised in the created analytical simulation model to predict the induced back-EMF per phase per pole.

$$k_p = \frac{Vector\ sum\ of\ EMFs\ induced\ in\ all\ turns\ per\ phase}{Numerical\ sum\ of\ EMFs\ induced\ in\ all\ turns\ per\ phase}$$

$$= \frac{2 * \sin(\frac{\beta}{2})}{\beta} \qquad (4-25)$$

$$k_{pr} = \frac{2 * \sin(\frac{r\beta}{2})}{r\beta} \qquad (4-26)$$

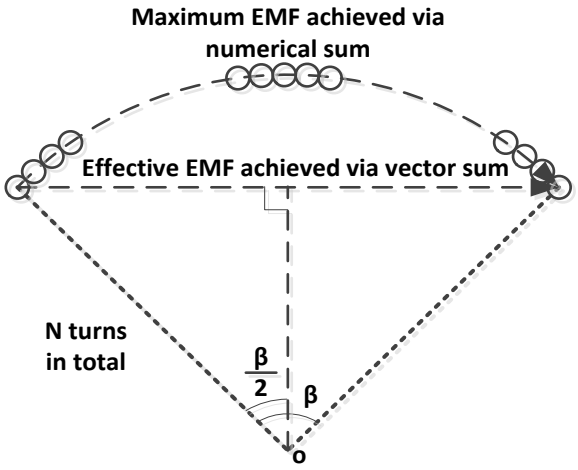

Figure 4-26: The equivalent phasor diagram of winding distribution factor calculation for a slot-less winding

4.6 Summary

This chapter describes an analytical simulation model utilised in the selected hybrid simulation motor design approach.

With the accurately determined no-load magnetic field, the rest of motor geometries can be achieved with the precise estimation of such dominant motor loss elements as copper Ohmic loss, proximity loss and iron loss. Operating temperature, 3-dimensional effects, winding temperature, motor per-unit cost and overall volume all have to be considered in the constructed analytical simulation model.

The next chapter will discuss the detailed single phase slot-less stator, inner rotor, radial flux, permanent magnet design.

Chapter 5 : Design of a Single Phase Slot-less Permanent Magnet Motor

5.1 Introduction

This chapter examines motor performance in the single phase, radial flux, slot-less stator, inner rotor with permanent magnet design, based upon the analytical simulation model discussed in Chapter 4. The selection of the optimised motor design is dependent on the multi-disciplinary constraints illustrated in the first Chapter, including motor electromagnetic efficiency, mechanical stiffness, product packaging and machine per-unit material cost. In this research, the first critical design constraint is the total motor electromagnetic losses, which consist of Ohmic loss in the windings, iron loss in the laminations and proximity loss in the coils. The calculation of each loss element has been systematically discussed in Chapter 4.

Figure 5-1 below demonstrates the drawing of single phase slot-less PM motor with labelled motor variables in 2-D cross-sectional view. The other design variables which are not labelled in the graph are listed as follows.

- Magnet residual flux density;
- Stator axial length;
- Stator core-back magnetic flux operating point;
- Phase current density;
- Number of turns;
- Wire overall outer diameter;
- Winding filling factor.

In the design of single phase slot-less motor, due to manufacturing limits, four motor variables are defined as the fixed values.

i. Bobbin thickness = 0.35mm;
ii. Air-gap clearance = 0.5mm;
iii. Magnet inner diameter = 4mm;
iv. Winding filling factor = 70%.

In the conducted analytical simulation, the following six motor variables are treated as the independent design inputs, while the rest of motor variables are calculated based upon them. Note that all designs are targeted to deliver the average torque of 0.04297Nm at 150,000rpm rated speed. The injected phase current features the pure sinusoidal waveform, which is in phase with the generated motor back-EMF. In real motor cases, the rotor position and the induced back-EMF are usually monitored by the utilised position sensor.

1. Magnet radial thickness;
2. Winding span in electrical degree;
3. Motor overall outer diameter;
4. Magnet residual flux density;
5. Stator magnetic flux operating point;
6. Current density.

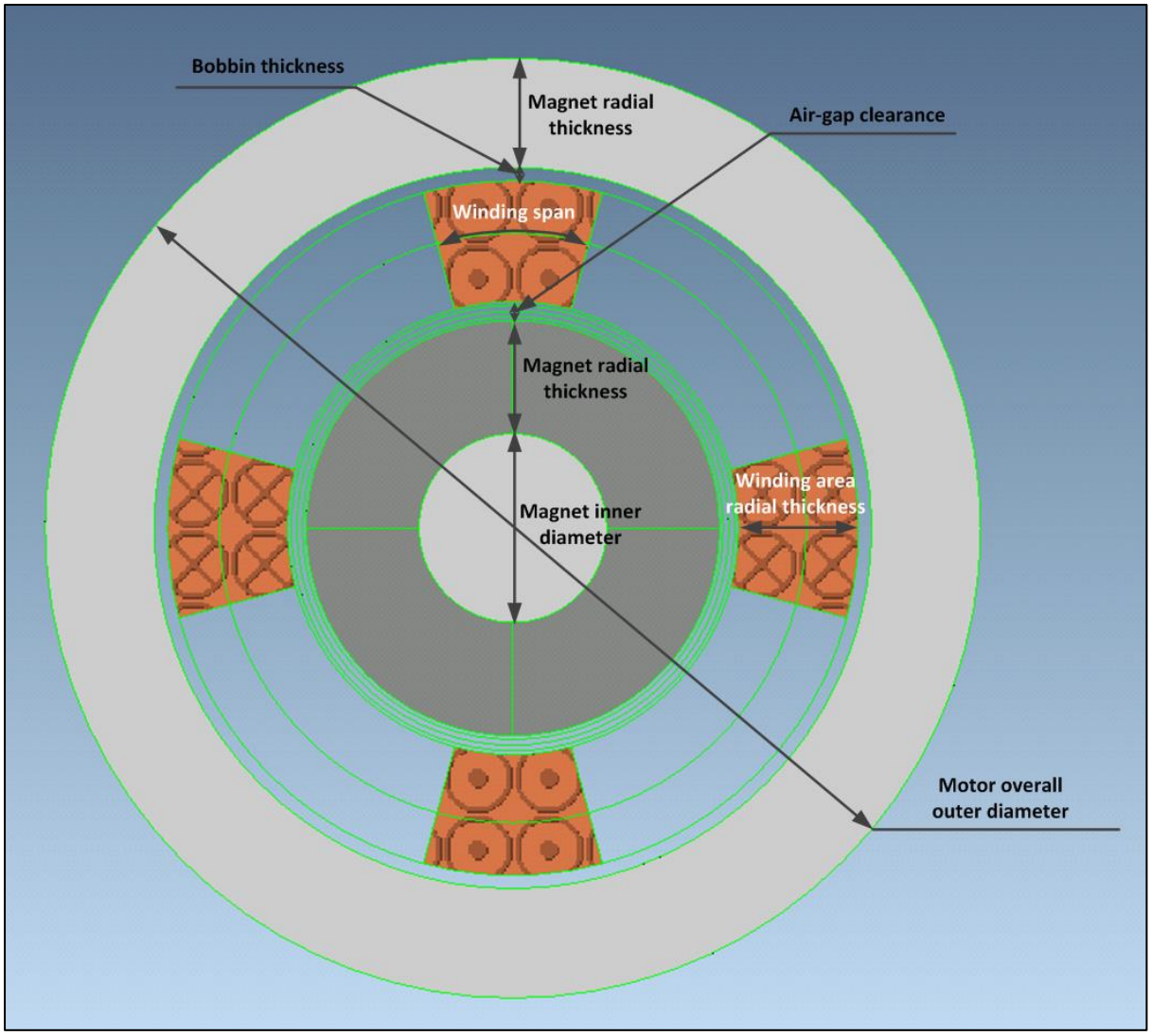

Figure 5-1: Schematic drawing of single phase slot-less PM motor with labelled motor variables in 2-D cross-sectional view

5.2 Design with varied magnet thickness

To start with, the five design inputs, i.e. the winding span arc, the motor overall outer diameter, the magnet residual flux density, the stator magnetic flux operating point and the phase current density, are all fixed, only with the variation of the magnet radial thickness. This aims to investigate the influence of the magnet radial depth on the total motor electromagnetic losses. The stator core-back thickness, the radial thickness of the effective winding area, the minimum motor axial length and the number of turns as well as the wire overall outer diameter are all calculated based on the selected magnet radial thickness. The value of magnet radial depth ranges from 1mm to 5mm in 0.1mm steps. Table 5-1 below lists the values of fixed five design inputs and the targeted output torque.

	Value	Unit
Winding span arc	30	Mechanical Degree
Motor overall outer diameter	29	mm
Magnet residual flux density	1.1	T
Stator magnetic flux operating point	0.8	T
Current density.	25	A/mm^2
Output torque	0.04297	Nm

Table 5-1: Defined values of fixed five design inputs and targeted output torque

Figure 5-2 below illustrates the variation of the total motor losses with the increase of the magnet radial depth. All the data points on the trend line deliver the same output torque with the minimum motor volume. The graph indicates that the total motor losses initially decrease with the growth of magnet thickness until reaching the minimum loss point, then bounce back to a higher value. The following Figure 5-3 shows the trends of each loss element under the varied magnet thickness. In the graph, the blue line illustrates the DC copper loss; the red line shows the iron loss; and the green line reflects the proximity loss. According to the plotted trend lines, the DC copper loss is the leading loss component among the three loss elements when the magnet thickness is relatively small.

Moreover, the DC copper loss can be dramatically decreased by increasing the magnet radial thickness. This is due to the higher magnetic flux provided by the thicker magnet, giving a higher amplitude of induced back-EMF per unit length per turn. Hence, the same level of the

motor shaft power can be achieved with fewer turns and a shorter axial length with the same electrical loading.

Nevertheless, the higher magnetic flux provided by the thicker magnet flowing through the air-gap and the stator laminations will also travel through the winding conductors, resulting in the boosted proximity loss. In order to maintain the fixed core-back operating flux density, the radial thickness of the stator core-back has to be increased simultaneously, which in turn pushes the iron loss up. Consequently, the total motor losses increase once the proximity loss and the iron loss become the dominant loss elements of the total motor losses.

Moreover, under the limits of the fixed motor overall outer diameter and the larger magnet OD as well as the thicker stator core-back, the radial thickness of the effective winding area thus becomes increasingly small. In order to satisfy the set values of the fixed phase current density and the limited winding filling factor, the total number of turns per phase needs to be further reduced while the motor axial length has to be increased again to maintain the targeted back-EMF value. Figure 5-4 demonstrates the minimum total motor volumes for the designs with a varied magnet thickness. As the motor overall outer diameter is fixed in the designs, the volume curve reflects the variation of the motor axial length, which is similar to the trend of the total motor losses.

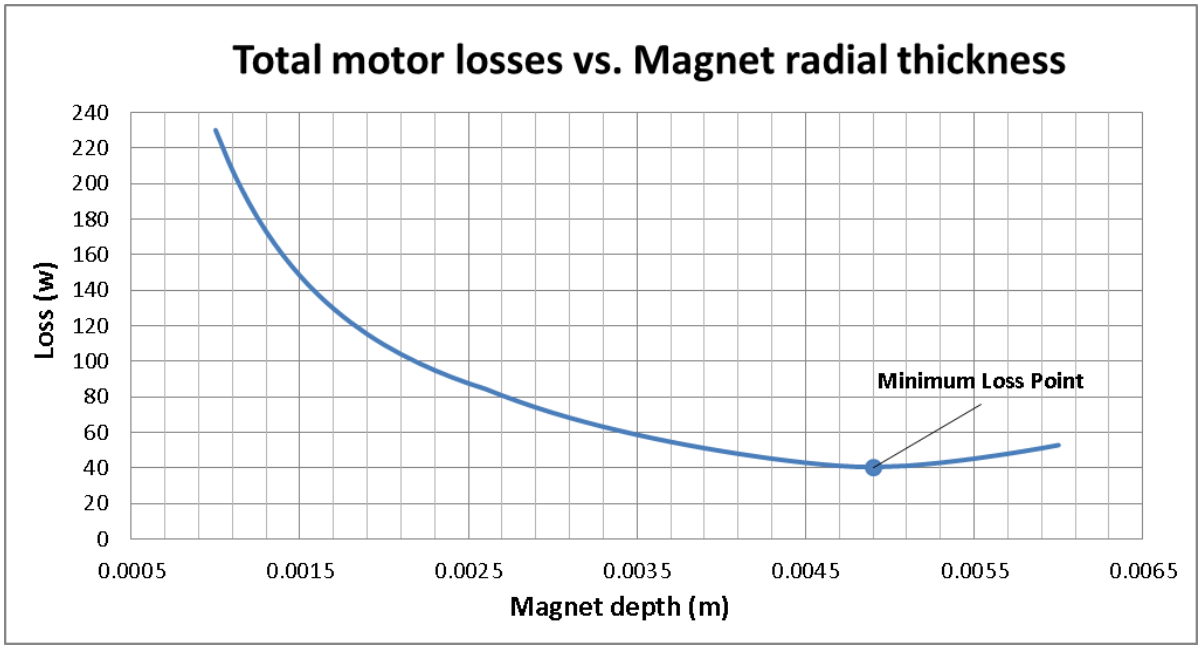

Figure 5-2: The trend of the motor total losses with the varied magnet radial thickness

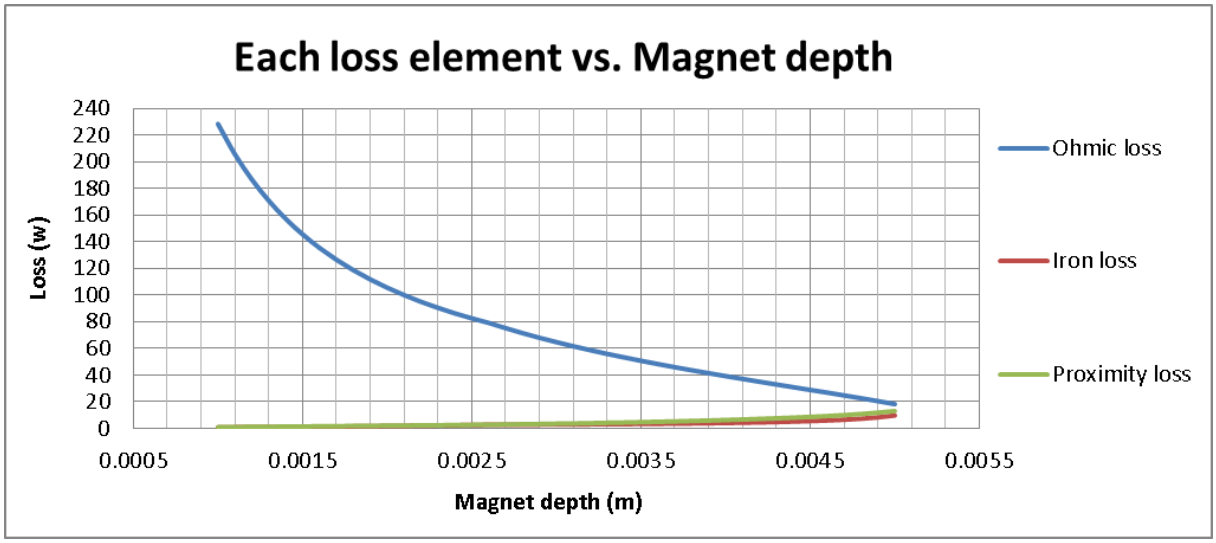

Figure 5-3: The trends of each loss element with varied magnet radial thickness

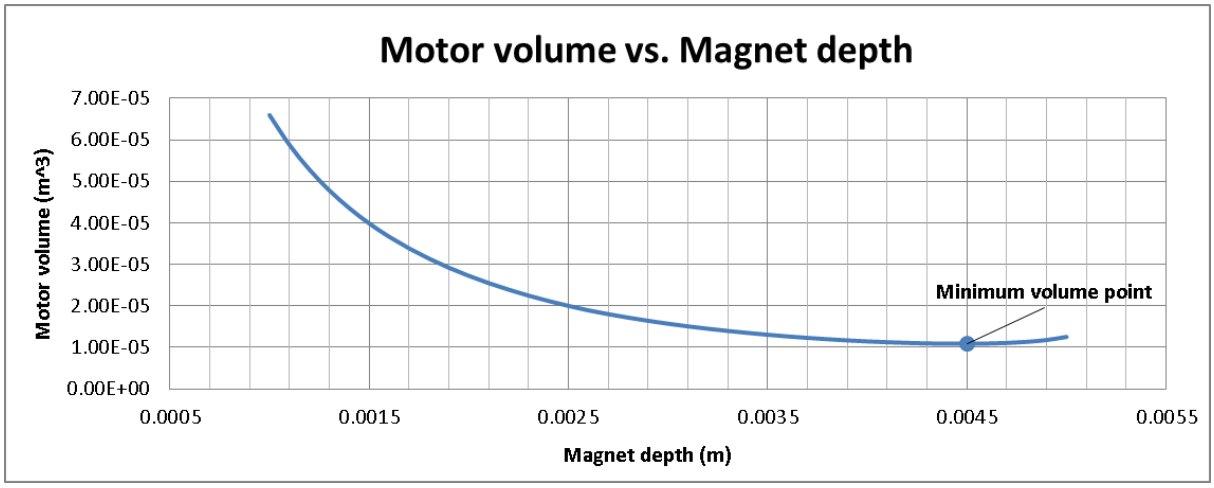

Figure 5-4: The trend of the motor total volume with varied magnet radial thickness

5.3 Design with a varied magnet residual flux density

This section discusses the use of the magnet residual flux density as a unique design variable, so as to investigate its impact on the motor performance. As earlier, the other five design variables are all fixed to a pre-set value, while the rest of the motor dimensions can be correspondingly calculated based upon the chosen flux density value. Table 5-2 below lists the values of fixed five design inputs and the targeted output torque. The considered magnet residual flux density ranges from a bonded magnet of 0.7T to a 1.4T sintered one in 0.1T steps. Figure 5-5 below demonstrates the variation of the motor total losses as a function of the magnet residual flux density. The trend line indicates that an increased residual flux density contributes to a direct drop in the overall motor losses, which is mainly due to a drop in DC copper loss. With the higher residual flux density, significantly more flux can be provided by the magnet so that a higher back-EMF is induced per-unit length of conductor. Therefore, the total number of turns and the active winding axial length can be reduced with the same level of delivered output torque for a given electrical loading.

	Value	Unit
Winding span arc	30	Mechanical Degree
Motor overall outer diameter	29	mm
Magnet radial thickness	4.9	mm
Stator magnetic flux operating point	0.8	T
Current density.	25	A/mm^2
Output torque	0.04297	Nm

Table 5-2: Defined values of fixed five design inputs and targeted output torque

Similar to the case of increased magnet radial thickness, the higher magnet residual flux density also means that there is the increased magnetic flux flowing through the air-gap and the stator laminations as well as the winding conductors, which in turn increases both the proximity loss and the iron loss. Therefore, the total motor losses will increase once more after reaching a minimum loss point where the Ohmic loss ceases to be the dominant loss element. The following Figure 5-6 displays the trends of each loss element with increased magnet residual

flux density. The variation of each loss element with magnet residual flux density is almost identical to that with variation of magnet radial thickness.

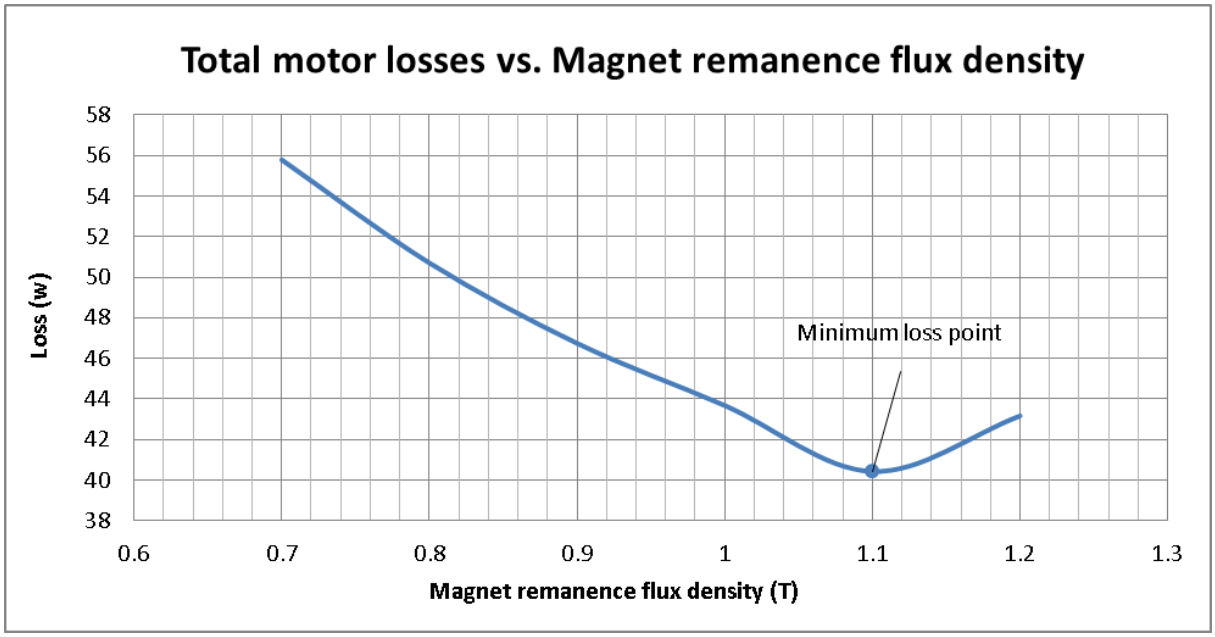

Figure 5-5: The trend of motor total losses with varied magnet residual flux density

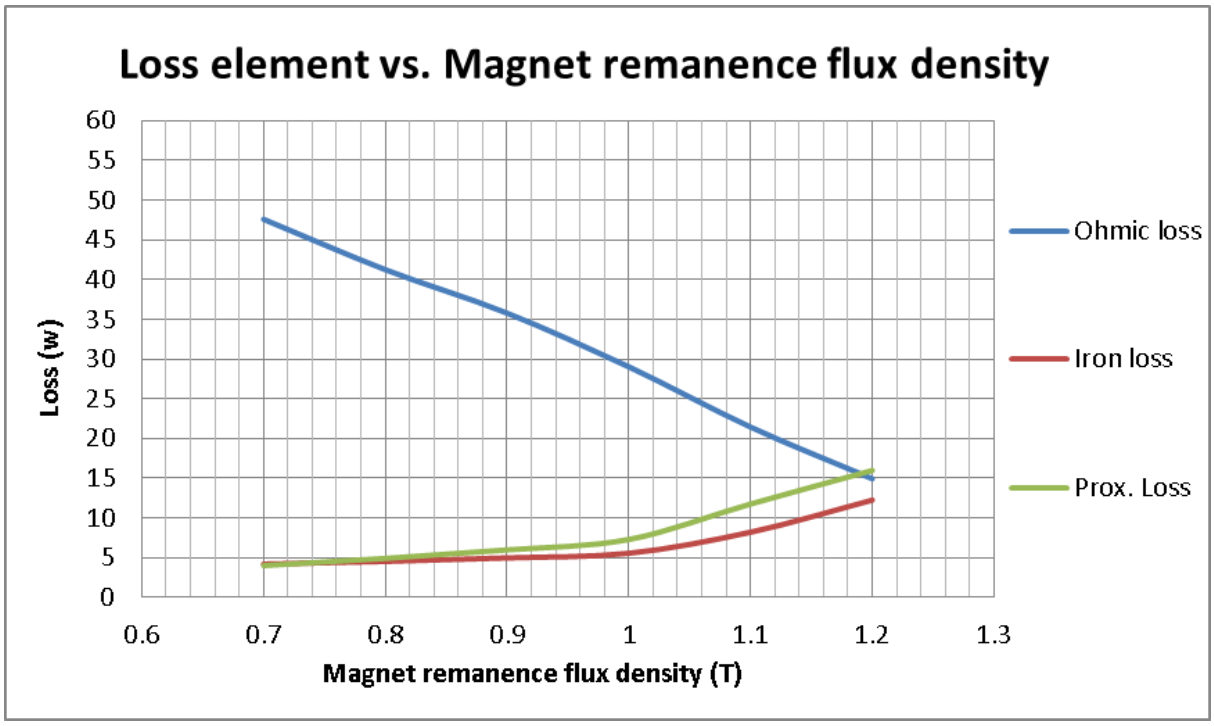

Figure 5-6: The trends of each loss element with varied magnet residual flux density

5.4 Design with varied magnet residual flux density, magnet thickness and motor outer diameter

This section initially considers both magnet residual flux density and magnet thickness as the adjustable design inputs, whilst other four variables are still kept fixed. Table 5-3 below lists the values of fixed four design inputs and the targeted output torque. The magnet residual flux density ranges from 0.7T to 1.4T in 0.1T steps; the magnet radial depth is varied from 2mm to 6.5mm in 0.1mm steps. Figure 5-7 below illustrates the variation of total motor losses with different magnet radial thickness and different residual flux densities. All the points on the trend lines deliver the same shaft power with the minimum motor volume. The curves indicate that the minimum loss points generally occur in the region of large magnet radial thickness. Note that there is very limited loss reduction in this region with the increased magnet residual flux density.

	Value	Unit
Winding span arc	30	Mechanical Degree
Motor overall outer diameter	29	mm
Stator magnetic flux operating point	0.8	T
Current density.	25	A/mm^2
Output torque	0.04297	Nm

Table 5-3: Defined values of fixed four design inputs and targeted output torque

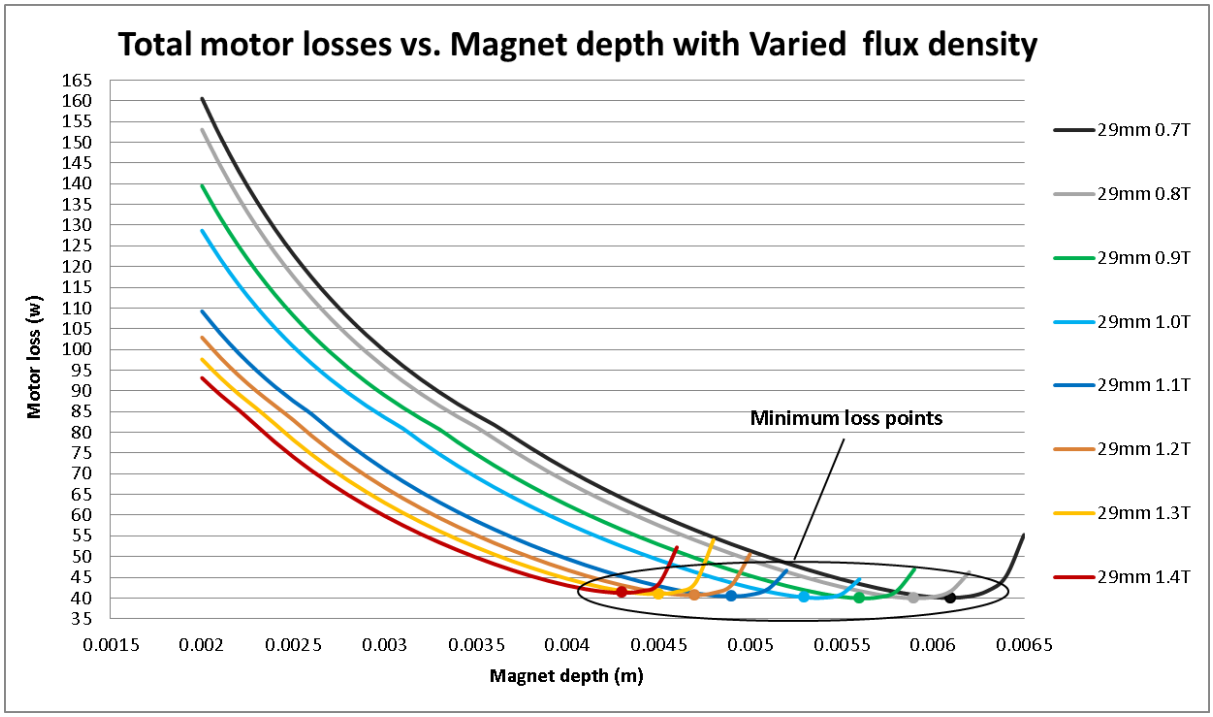

Figure 5-7: The trend of motor total losses with varied magnet depth and varied residual flux density

To reduce the amount of costly permanent magnet in the motor, the overall outer diameter is now utilised as the third design variable to investigate the effect on total motor losses. The magnet overall outer diameter ranges from 22mm to 30mm in 2mm steps. With the growth of the motor overall outer diameter, there is more space provided to allow a larger winding area. Consequently, a higher number of turns can be adopted with a shorter motor axial length to generate the same back-EMF.

However, the larger effective winding area also brings larger effective air-gap thickness, which then reduces the magnetic loading. With further growth of motor overall outer diameter, the axial length then needs to be increased again to achieve the required torque. Figure 5-8 illustrates the trends of total motor losses under the conditions of varied magnet radial thickness, varied magnet residual flux density and varied motor overall outer diameter. The other three design variables of winding span arc, phase current density and stator flux saturation point are all fixed to a given value as shown in Table 5-4 and the motor shaft power is maintained constant.

	Value	Unit
Winding span arc	30	Mechanical Degree
Stator magnetic flux operating point	0.8	T
Current density.	25	A/mm^2
Output torque	0.04297	Nm

Table 5-4: Defined values of fixed three design inputs and targeted output torque

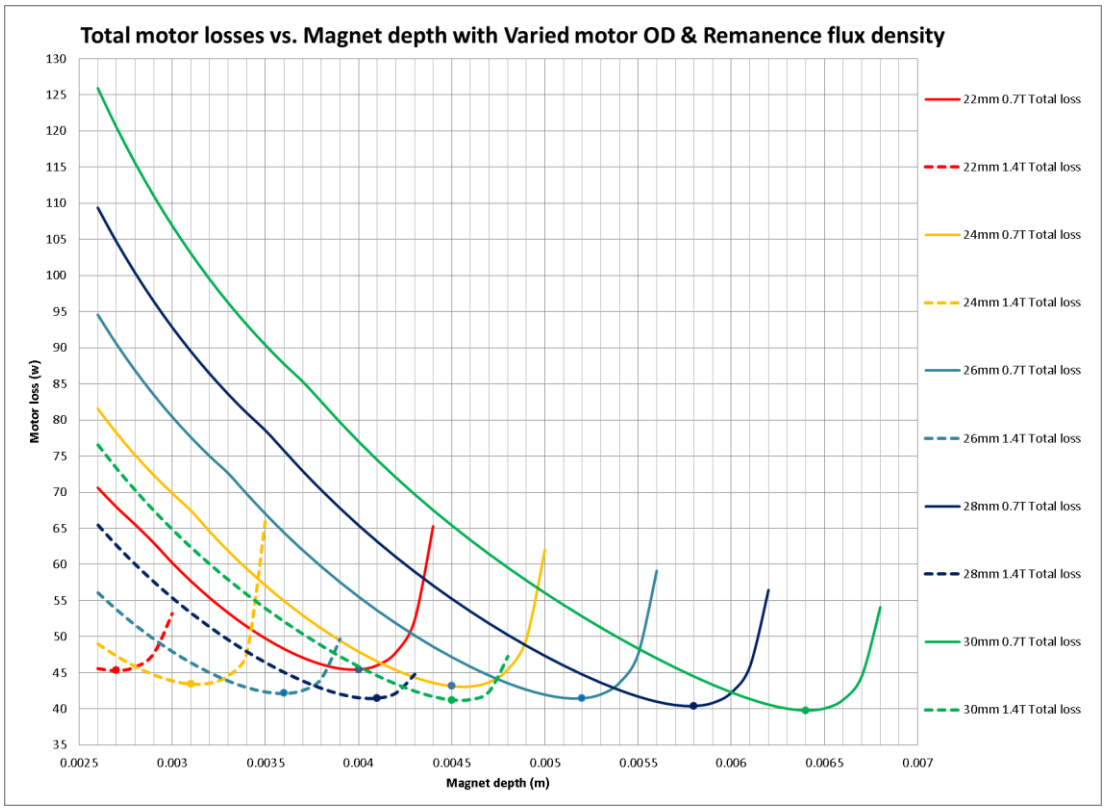

Figure 5-8: The trends of total motor losses with varied magnet depth, varied magnet residual flux density and varied motor outer diameter

Above Figure 5-8 shows the curves of motor total losses against magnet radial depth for a series of outer diameters and residual flux densities. The dashed lines refer to a sintered magnet with 1.4T residual flux density while the solid lines represent a bonded magnet with 0.7T flux density. The curves indicates that the minimum motor total losses are slightly reduced with an increase of motor overall outer diameter.

To be specific, an 8mm increase in motor overall outer diameter from 22mm to 30mm can contribute to an approximately 5W loss drop in the total losses with both kinds of the magnets. The loss reduction is about 11% of the minimum total losses in a 22mm OD design. However, this amount of loss reduction requires a significant growth of the radial thickness of the utilised permanent magnet by around 1.8mm (66.7%) in the sintered magnet design and around 2.4mm (60%) in the bonded magnet design.

It has to be noted that the range of magnet thickness in the designs with sintered magnet is much narrow compared to the bonded magnet designs for a fixed motor outer diameter. This limit is because a larger stator core-back is required due to the higher magnetic flux provided by the sintered magnet, leading to a limited effective winding space. In order to maintain the generated output torque, the motor axial length has to be increased again to compensate for the reduction of the overall outer diameter as shown in Figure 5-9. The graph illustrates the minimum motor axial length with varied magnet radial depth, magnet residual flux density and outer diameter. Note that all points on the curves are for the same motor shaft power. Those curves with the same colours represent the designs with the same overall outer diameter. Dashed lines in the graph are for the designs with 1.4T sintered magnets, while solid curves refer to 0.7T bonded magnet designs. Figure 5-9 demonstrates how an increased outer diameter can always bring a reduction in motor axial length for a fixed magnet depth and residual flux density.

The next Figure 5-10 demonstrates the variation of motor overall volume for a varied magnet depth, residual flux density and outer diameter. As in Figure 5-9, Figure 5-10 has different colours for different motor ODs; and different line styles refer to different magnet residual flux densities. The graph indicates that, with a thin permanent magnet, the total motor volume for the larger outer diameter designs is bigger than for those with a small outer diameter. The reduction of the motor axial length cannot compensate for the rise of the motor outer diameter.

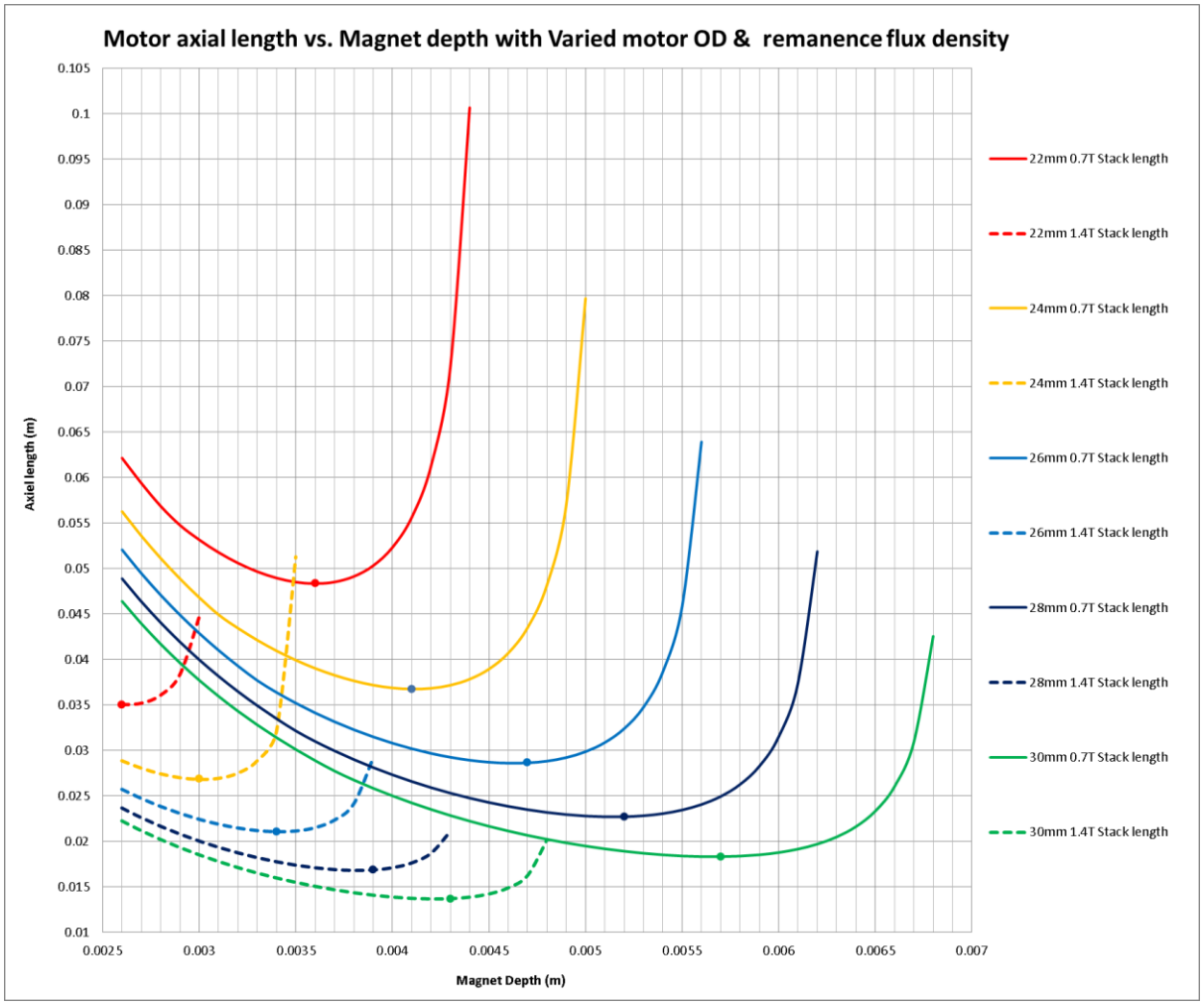

Figure 5-9: The trend of motor axial length with varied magnet radial thickness, varied magnet residual flux density and varied motor overall outer diameter

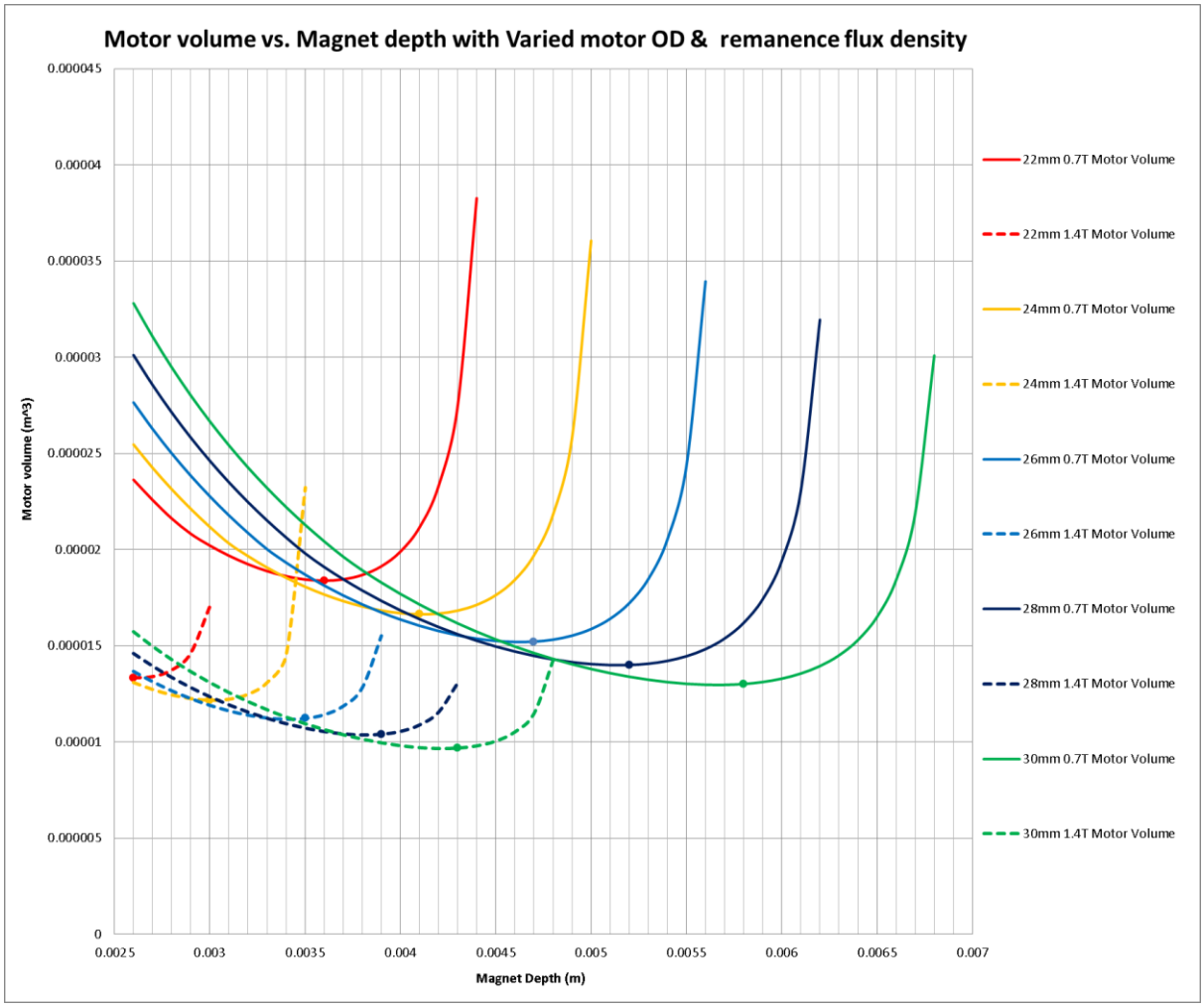

Figure 5-10: The trends of motor volume with varied magnet radial thickness, varied magnet residual flux density and varied motor overall outer diameter

5.5 Design with varied winding span arc

This section takes winding span arc into investigation as the only design variable. As earlier, only the winding span arc is varied whilst all the other five design inputs are fixed. Table 5-5 below lists the values of fixed five design inputs and the targeted output torque. As shown in Chapter 4, with increased angles of winding span, the winding distribution factor is decreased, leading to a lower back-EMF per unit length. Therefore, the required number of turns for the targeted back-EMF value is increased with a rise of the winding span angle. On the other hand, the enlarged winding span arc expands the winding area to provide space for additional turns. With a fixed current density and shaft power, the larger winding span enables a reduced motor axial length.

	Value	Unit
Motor overall outer diameter	29	mm
Stator magnetic flux operating point	0.8	T
Current density.	25	A/mm^2
Magnet residual flux density	1.1	T
Magnet radial thickness	4.9	mm
Output torque	0.04297	Nm

Table 5-5: Defined values of fixed five design inputs and targeted output torque

Figure 5-11 below demonstrates the variation of total motor losses with a changing winding span from 30 mechanical degree to 90 mechanical degree. As there are four poles, the corresponding electrical degree is varied from 60 degrees to 180 degrees. Noted that, when the winding span is further decreased to be less than 30 mechanical degree, due to the limited available winding space, the minimum motor axial length turns to be longer than 29mm with 4mm thickness permanent magnet adopted to deliver the targeted power under the fixed current density (25A/mm^2) and winding filling factor (70%) as well as overall outer diameter (29mm). Therefore, the winding span of 30 mechanical degree is selected as the limit in this project. From Figure 5-11, it indicates that the total motor losses rise with a growth of the winding span. This outcome is because there is higher DC copper loss caused by the significantly increased total number of turns.

The following Figure 5-12 demonstrates each loss element with growing angles of motor winding span. The Ohmic loss is dominant among the three and doubles its value when the coils are fully spanned. The iron loss and the AC copper loss are both less than half of the Ohmic loss, especially when a large winding span is applied. As discussed above, the iron loss is gradually reduced owing to a slightly reduced motor axial length. Conversely, as the iron loss has a minor impact on the total losses, the overall motor losses still grow when the winding span arc is increased.

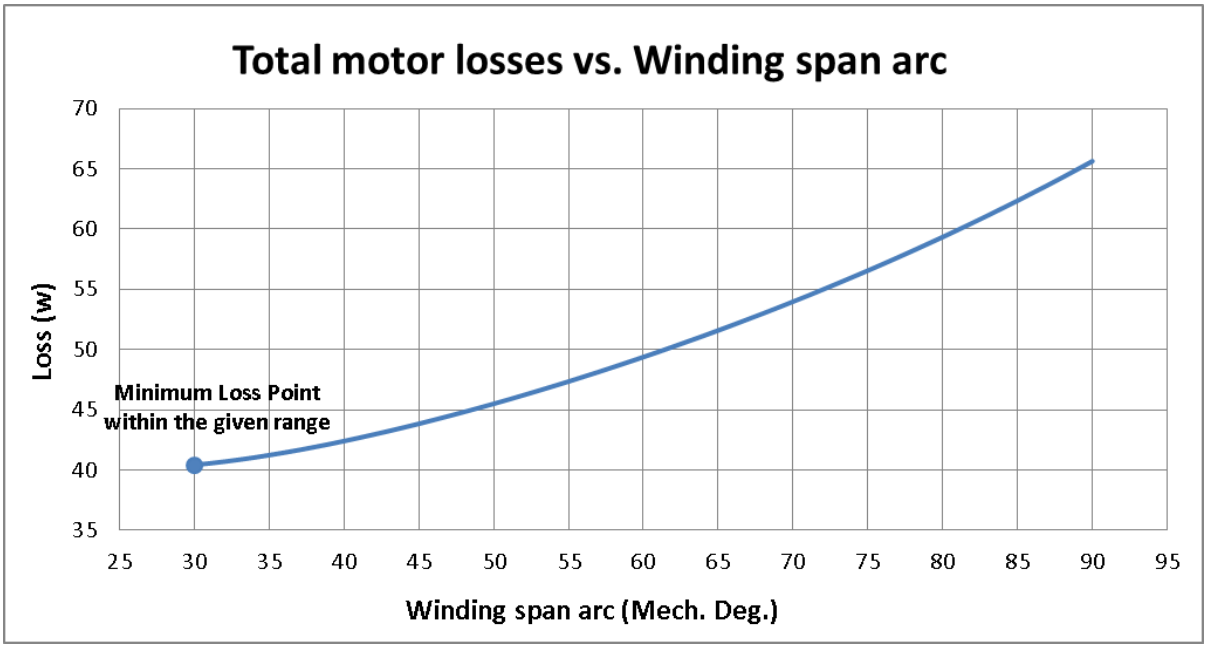

Figure 5-11: The trend of total motor losses with varied winding span arc

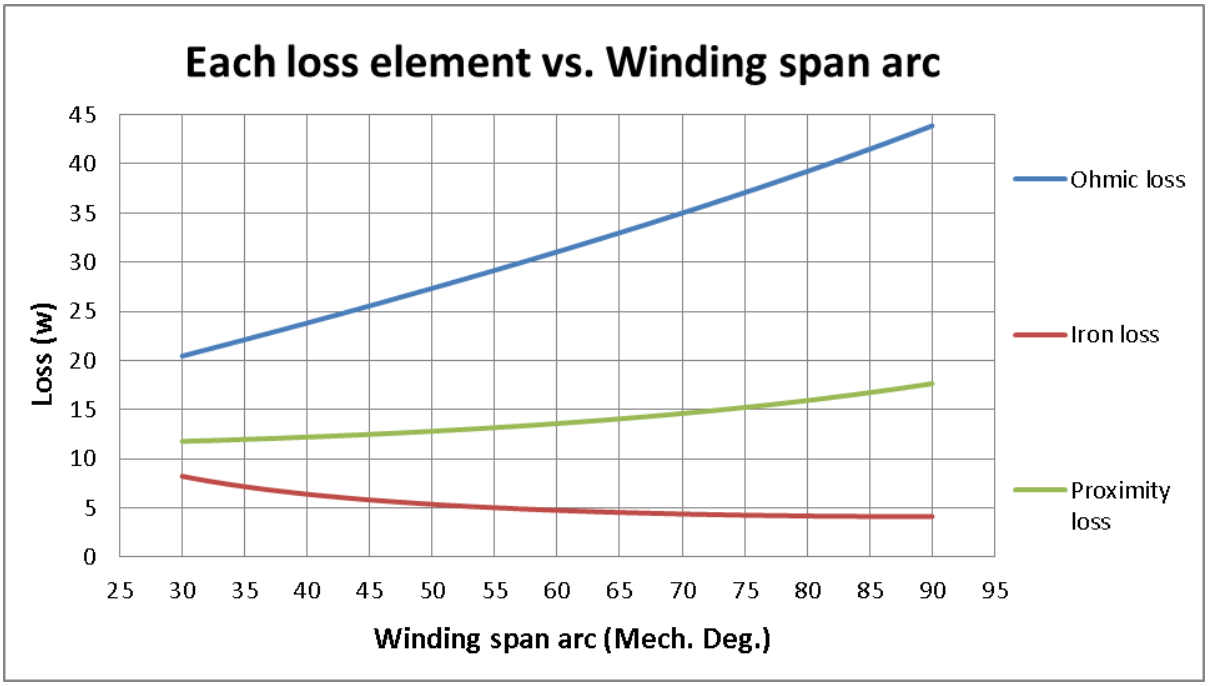

Figure 5-12: The trends of each loss element with varied winding span arc

5.6 Design with varied stator magnetic flux operating point

This section discusses the impact of varying magnetic flux operating point in the stator core-back on motor efficiency. Motor output torque, phase current density, winding span arc, motor outer diameter and magnet radial thickness as well as magnet residual flux density are all fixed as shown in Table 5-6. The stator core-back flux density ranges from 0.5T to 1.5T in 0.1T steps. The radial thicknesses of the winding area, the stator core-back, the minimum motor axial length, the required total number of turns and the wire outer diameter are correspondingly calculated.

	Value	Unit
Motor overall outer diameter	29	mm
Winding span arc	30	Mechanical Degree
Current density.	25	A/mm^2
Magnet residual flux density	1.1	T
Magnet radial thickness	4.9	mm
Output torque	0.04297	Nm

Table 5-6: Defined values of fixed five design inputs and targeted output torque

Figure 5-13 below shows the losses at various stator core-back operating points. The graph indicates that the total motor losses are increased along with growth of the core-back operating flux density. The following Figure 5-14 illustrates the trends of each loss element with the growing lamination flux density operating points, indicating that Ohmic loss is dominant among the three loss elements especially when high core-back operating flux density is chosen.

A rise in operating flux density within the stator core-back reduces the required cross-sectional area of stator core. With a fixed outer diameter, the radial thickness of the winding area must then be increased, leading to the further decreased air-gap flux density. Consequently, the required number of turns is boosted up for a given fixed phase current density to deliver the same level of shaft power. Although there is a reduction of AC copper loss, it remains insignificant compared to the Ohmic loss.

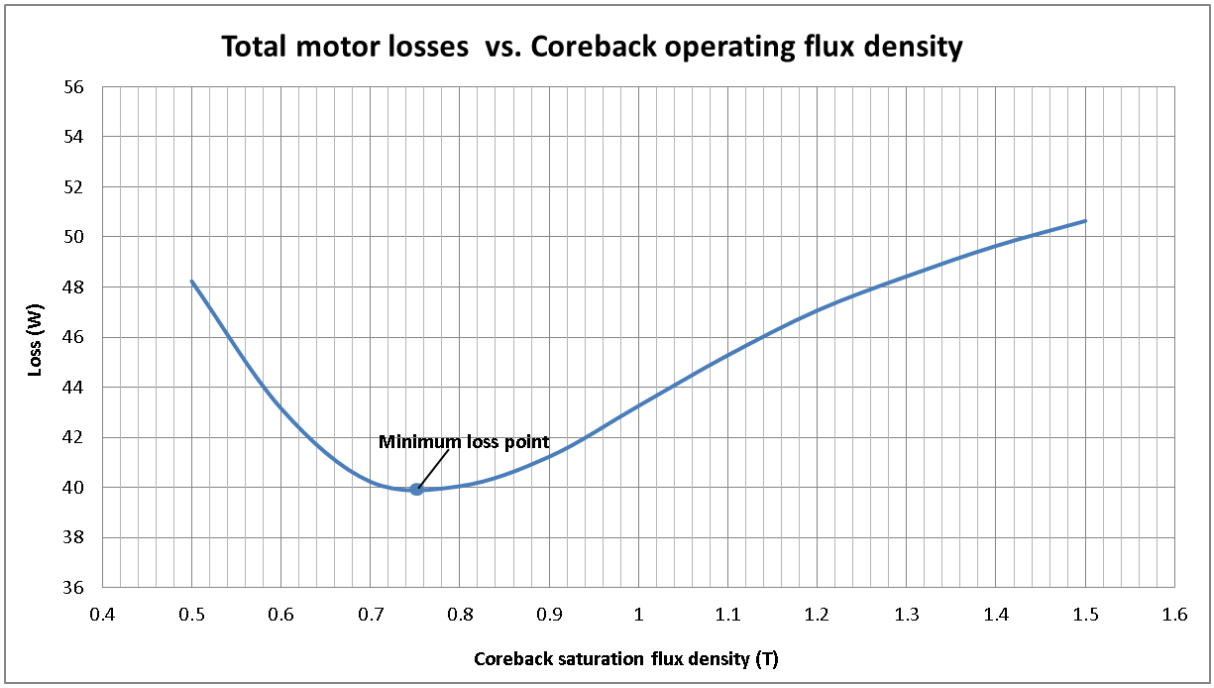

Figure 5-13: The trend of total motor losses under varied stator core-back operating flux density

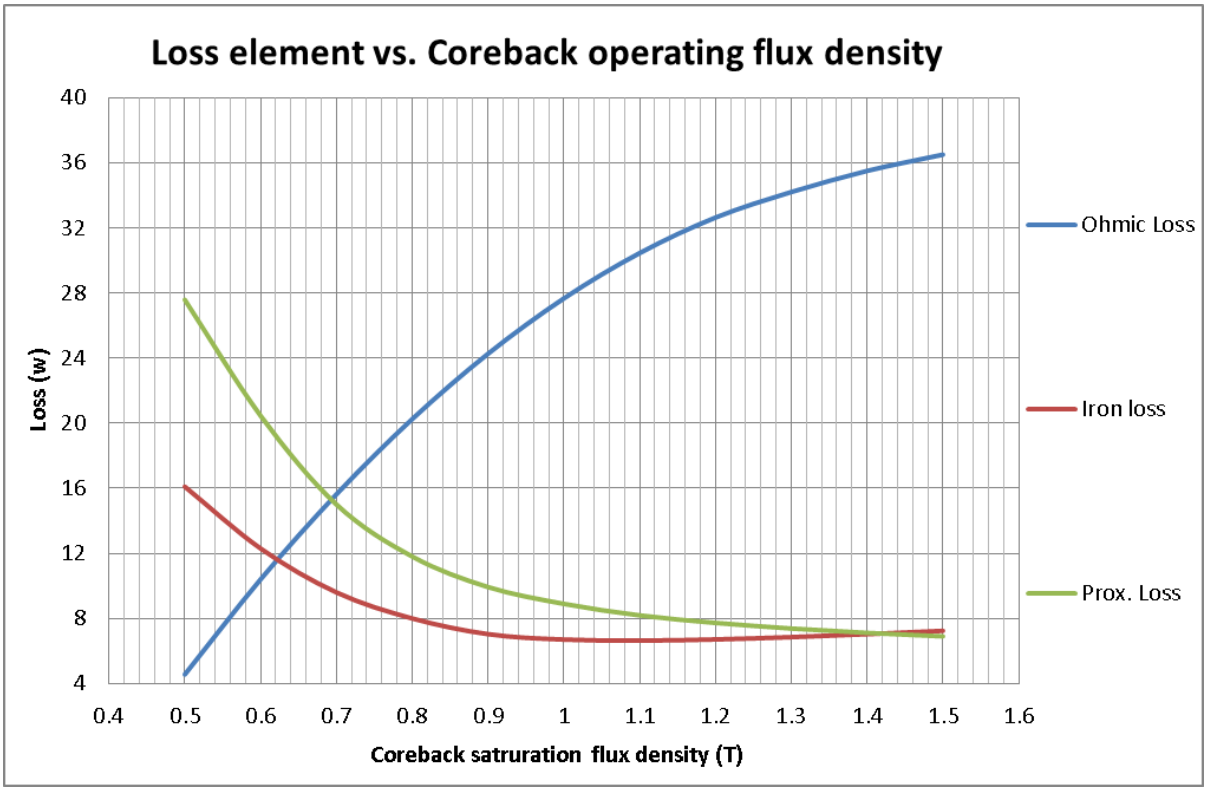

Figure 5-14: The trends of each loss element under varied core-back operating flux density

5.7 Design with varied phase current density limit

Varied current density is investigated in this section. As earlier, only the phase current density is changed, varying from 15A/mm^2 to 25A/mm^2 in 1A/mm^2 steps, while the rest of the design variables including motor overall outer diameter, magnet radial thickness, magnet residual flux density, winding span arc and core-back magnetic flux saturation point are all set to the fixed values as shown in Table 5-7. The required minimum motor axial length, the total number of turns and the wire dimensions are then calculated to generate the required output power. Note that, as the designed motor is placed in the pathway of the flowing air inside the product, the cooling capability of the designed motor is higher compared to the machines with still air cooling. Based upon the nominal product flow ranges of 8L/s to 16L/s, 25A/mm^2 current density is selected as the constraint in this design. The validation of the set current density limit will be discussed in Chapter 8.

	Value	Unit
Motor overall outer diameter	29	mm
Winding span arc	30	Mechanical Degree
Stator magnetic flux operating point	0.8	T
Magnet residual flux density	1.1	T
Magnet radial thickness	4.9	mm
Output torque	0.04297	Nm

Table 5-7: Defined values of fixed five design inputs and targeted output torque

Current density directly affects the induced DC copper loss. Consequently, for fixed cooling conditions, the maximum achievable phase current density is restricted by the motor's thermal limits. Reduced current density can be achieved by either increasing the cross-sectional area of the wire or reducing the injected phase current.

However, the cross-sectional area for phase windings is constrained by the limited winding area within the machine. An increased wire size leads to a reduced number of turns per unit area so that the motor stack length must be increased to maintain the phase back-EMF, which reduces the effect of the increased area upon the winding resistance. Moreover, larger wire

diameter increases the induced proximity loss. Figure 5-15 and Figure 5-16 demonstrates the variation of motor losses with phase current density varying from 15A/mm^2 to 25A/mm^2. Because the proximity loss dominates in the investigated phase current density range, the total motor losses are considerably reduced when increasing the current density. It can be predicted that, with further boost of phase current density, the DC copper loss will become dominant again, and the total motor losses will bounce to a higher value from the minimum loss point.

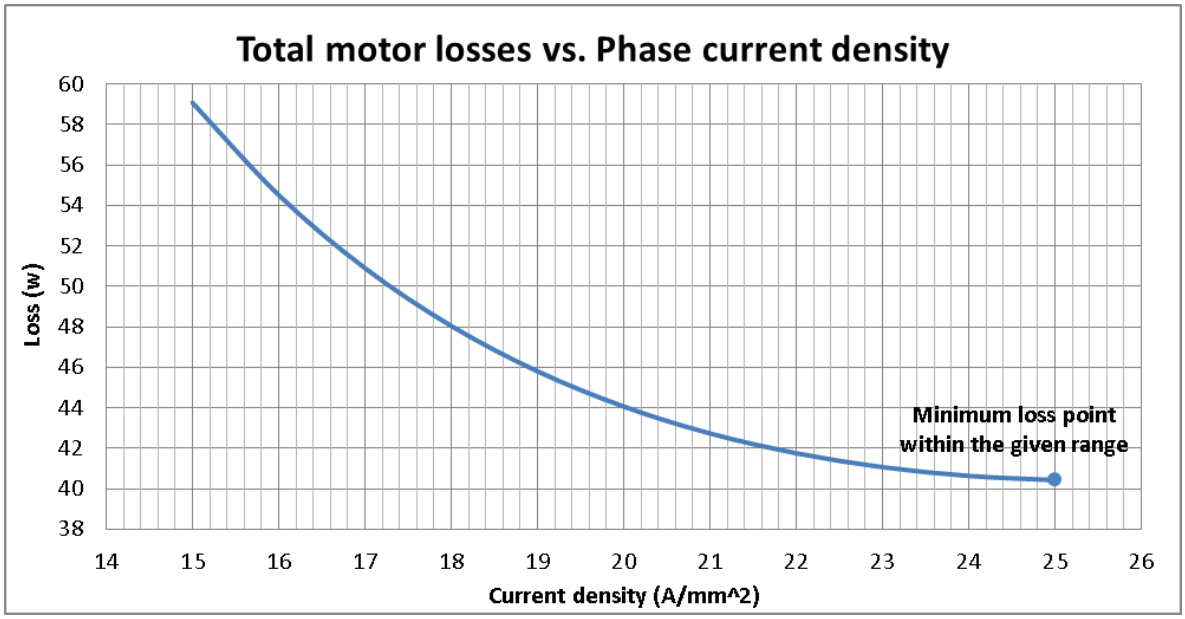

Figure 5-15: The trend of total motor losses under the varied phase current density

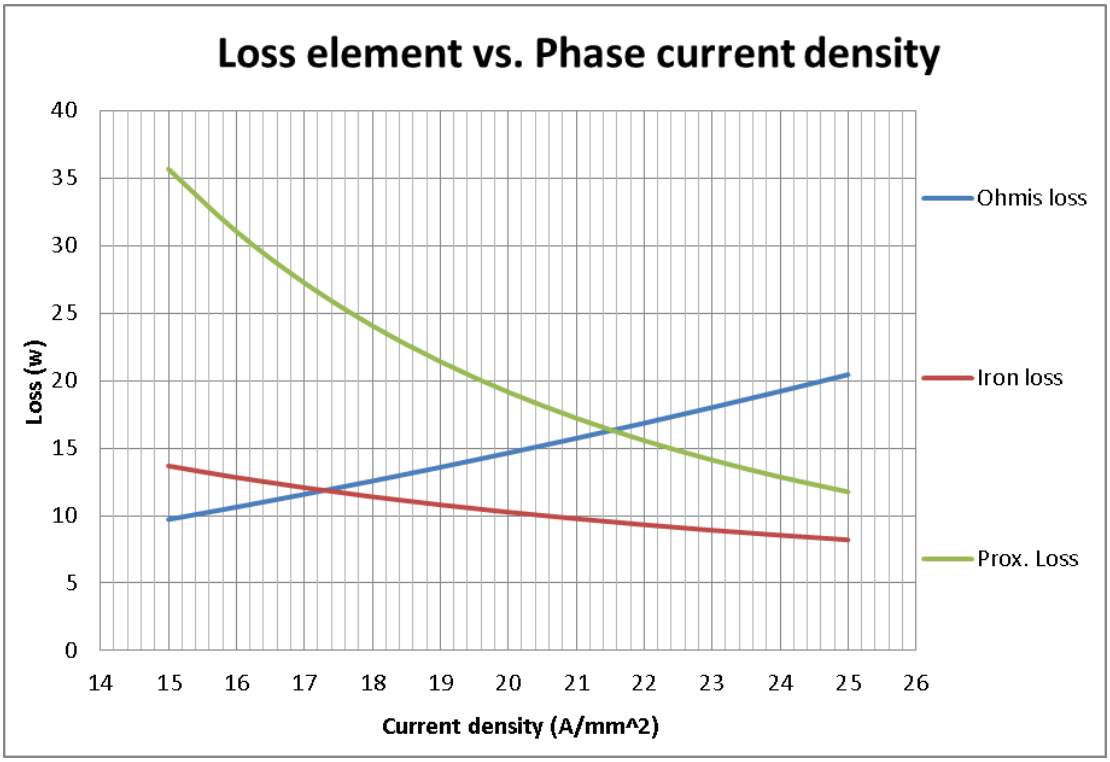

Figure 5-16: The trends of each loss element under varied phase current density

5.8 Summary

To summarise, the sections discussed above have demonstrated trends of the total motor losses as a function of different design variables.

To optimise the design, the motor analytical simulation was carried out globally with all the design inputs varied. To filter the best design, the highest motor efficiency with ±1% tolerance was picked up and regarded as the pass-mark for the family of acceptable designs. Furthermore, all the selected designs were required to satisfy the limits of the motor dimensions, given in Chapter 1.

Br (T)	La(mm)	Lm(mm)	Lw(mm)	Motor η	Cost ($)
0.7	24.9	4.8	2.4	93.867%	3.38
0.8	24.8	4.7	2.3	93.959%	3.34
0.9	24.9	4.5	2.4	94.050%	3.27
1	24.8	4.2	2.8	94.050%	3.64
1.1	24.5	3.9	2.7	94.090%	4.62
1.2	24.6	3.7	2.9	94.077%	4.45
1.3	24.8	3.5	3.2	94.077%	4.29
1.4	24.3	3.4	3.1	94.037%	4.17

Table 5-8: Dimensions for each optimal design using different types of PM

Figure 5-17 below illustrates the contribution of each loss element in the chosen optimal designs with magnets of different residual flux densities, whilst the total motor losses are similar for all designs. The proximity loss increases along with a reduction of Ohmic loss when the residual flux density is changed from 0.7T to 1.4T. These two effects cancel each other out, so the total motor losses are maintained at similar levels. Consequently, sintered magnets are not necessarily better than bonded magnets in this case.

As sintered magnets are over 45% more expensive than bonded ones, it is beneficial for the single phase slot-less design to utilize bonded magnet in the machine to lower down the material cost while still keeping the motor efficiency high.

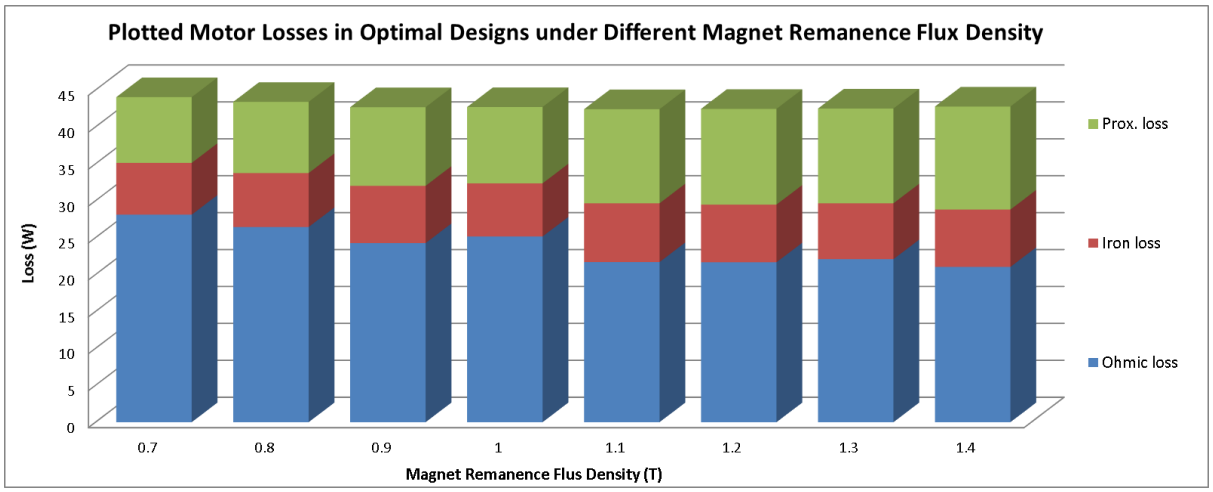

Figure 5-17: The percentages of each loss element in total motor losses in optimal designs under different magnet residual flux density values

Figure 5-18 below is a 2-dimensional drawing of the selected design for the single phase, inner rotor, slot-less stator, permanent magnet motor. It has a 25mm motor overall outer diameter and a 25mm axial length, ignoring the end-winding length. The utilised permanent magnet is a ring shaped bonded magnet of 3.5mm radial thickness, 10.5mm outer diameter and 0.7T residual flux density. The predicted motor electromagnetic efficiency is slightly over 90%, excluding electronics losses in the motor control system and friction losses in the motor bearings. The motor winding span arc is 30 mechanical degree.

On the other hand, the drawbacks of single phase slot-less permanent magnet motor are also obvious. First of all, the available winding area in the machine has not been fully occupied, so that the theoretical maximum power density has not been achieved yet. Secondly, the introduced slot-less stator structure eliminates all cogging torque, but has no saliency in the machine to provide a parking position for the rotor. Accordingly, it is impossible to detect the rotor position during the start-up stage. The direction of rotation becomes unpredictable and cannot be guaranteed in a single phase slot-less motor, even when a Hall sensor is employed.

More importantly, according to the information received from magnet supplier, with the growth of magnet radial thickness, magnetisation of the ring-shape magnets becomes increasingly

challenging. For inner rotor machines, as shown in Figure 5-19, the achievable residual flux density is gradually decreased from the magnet outer surface to the inner surface. The deeper the magnet thickness, the less residual flux density can be attained. Note that the shown model represents only one quarter of the utilised ring shape magnet.

The following Figure 5-20 (the plotted data is obtained from manufacturer) demonstrates the remained magnet residual flux density in percentage along with the growth of magnet thickness. Note that, for the magnets thicker than 3mm, in the regions close to the magnet inner surface, the actual residual flux density becomes almost zero. As a consequence, it is impractical to manufacture the aimed 3.5mm depth ring-shape magnet for the optimal design.

Due to the aforementioned constraints, for low cost, high speed applications, a compromise has to be made in designing a single phase slot-less permanent magnet motor, by using the ring shape magnet thinner than 3mm with reduced motor efficiency (<90%).

To seek for an alternative design with higher competitiveness, in next chapter, a three-phase slot-less structure, surface mounted permanent magnet motor is introduced for investigation. Benefit from the additional two phases, under the conditions of same overall outer diameter and shaft power, the required magnet volume can be reduced in 3-phase design compared to the single phase one, contributing to the reduced motor per unit cost.

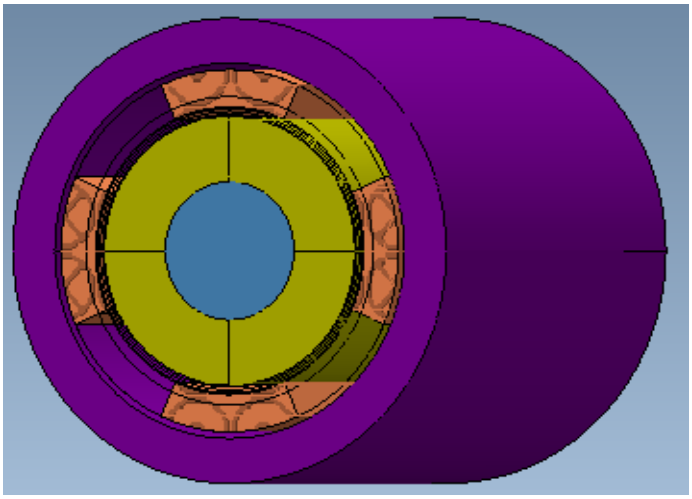

Figure 5-18: The 2-D drawing of the optimal design for single phase permanent magnet motor

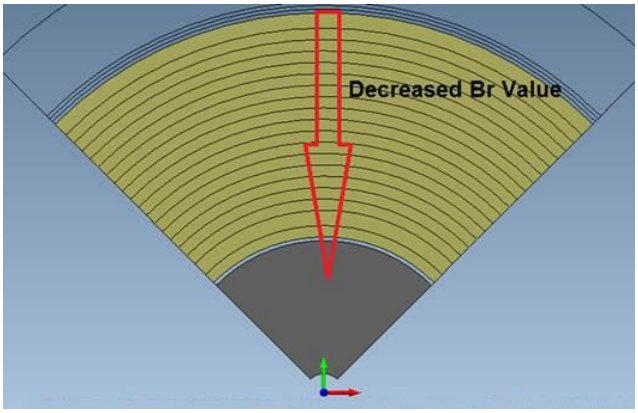

Figure 5-19: Gradually decreased residual flux density from outer surface of magnet to its inner surface

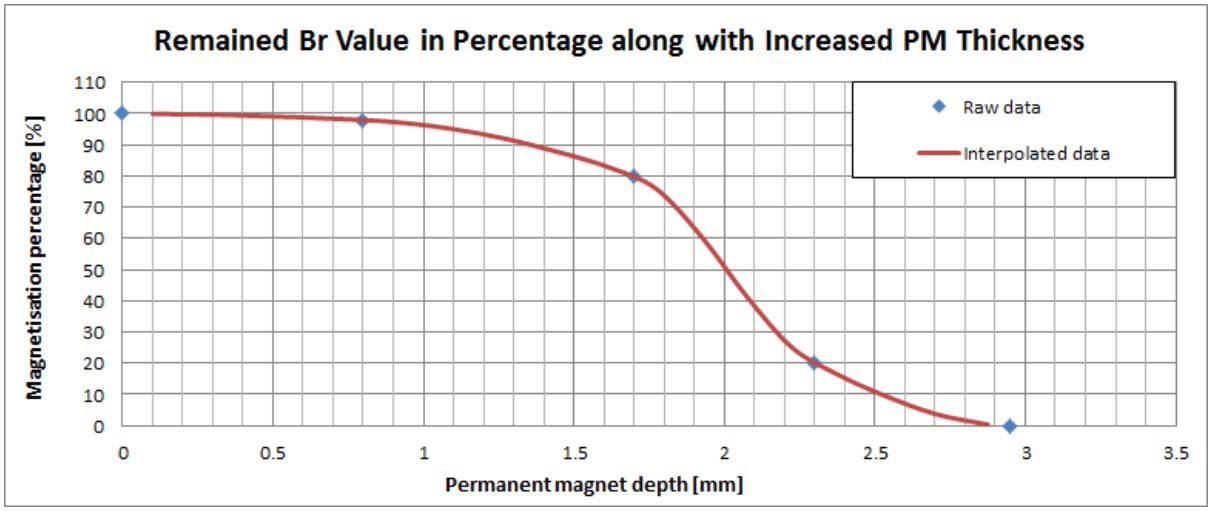

Figure 5-20: Remained magnet residual flux density in percentage along with increased permanent magnet thickness

Chapter 6 : Design of a Three Phase Slot-less Permanent Magnet Motor

6.1 Introduction

This chapter concerns the research and design of an optimised three-phase permanent magnet motor with the slot-less winding structure. The aim of the considered three phase topology is to utilise the complete winding area, in contrast to the single phase motor discussed in Chapter 5. With the introduction of another two motor phases, additional output power can be delivered by the machine with reduced torque ripple.

If the motor power rating is maintained constant, the volume of the permanent magnets, the rotor outer diameter and the motor axial length can be decreased in comparison with the single phase machine, giving comparatively lower motor cost. The dominant contribution to the reduced motor cost arises from the decreased volume of rare-earth permanent magnet materials.

Star-connection and delta-connection of motor phase windings are considered at the beginning of this chapter. Advantages and disadvantages of both connection methods are discussed, leading to a preferred phase connection structure. In addition to traditional winding methods, a toroidal winding approach is introduced and investigated to determine impacts on motor end-winding length, resistive loss and thermal performances. Three different designs of motor housing are demonstrated and analysed to ensure minimised Ohmic loss in the motor housing, adequate air-cooling for the phase coils and sufficient mechanical support for the high-speed rotor.

Afterwards, this chapter illustrates simulated system performances based upon the developed dynamic system simulation tool. The chosen control scheme and resulting motor performance are presented, taking into account manufacturing tolerances of the motor.

6.2 Comparison of star connection and delta connection in three phase motor

Figure 6-1 below demonstrates the circuitry of star and delta connections in a three phase motor. As stated by the figure, star connected three phase machines are more appropriate for high voltage, low current applications whilst delta-connection machines may be utilised for low voltage, high current applications.

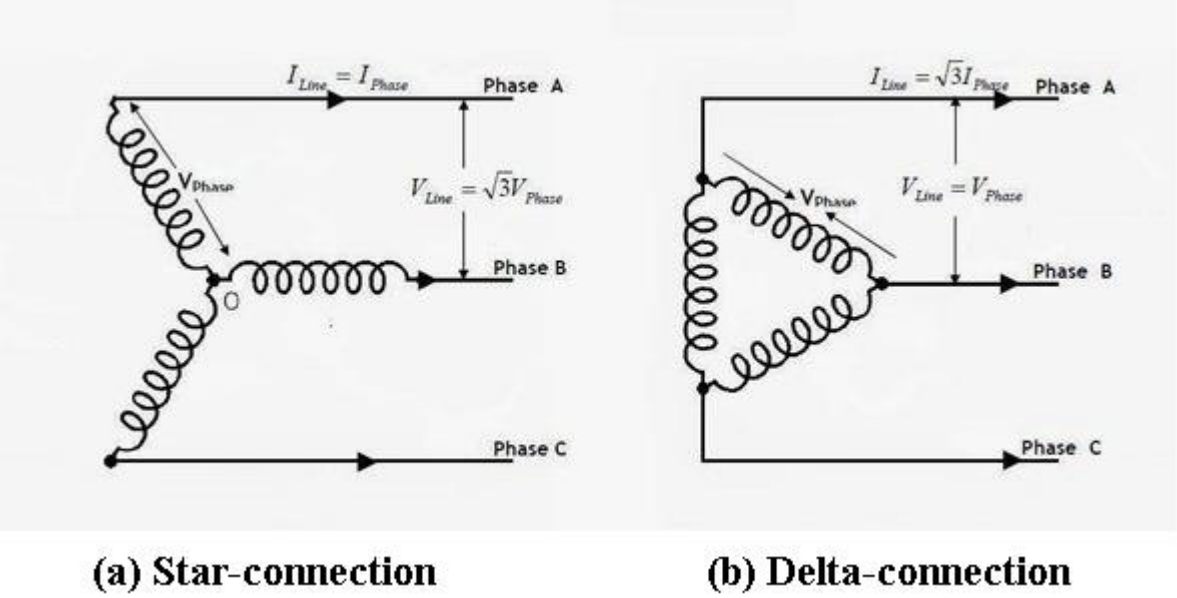

Figure 6-1: (a) Star connected 3-phase motor; (b) Delta connected 3-phase motor

In star-connected motors, there is no current path inside the machine for third harmonic currents. On the contrary, in delta connected motors, a current path is provided inside the machine to allow flow of triplen harmonic currents through the winding coils, although these currents are remained unseen in the input line connections. Consequently, undesirable circulation current can be induced in the phase windings with the delta-connection approach if the effective air-gap magnetic flux linking the motor windings contains a triplen harmonic. This circulation current leads to unwanted additional Ohmic loss in the phase coils, resulting in higher winding temperatures and reduced motor efficiency.

It is known that permanent magnets with different types of magnetisation deliver different patterns of air-gap magnetic flux waveforms. Those permanent magnets with Halbach and

parallel magnetisations feature a sinusoidal shaped air-gap flux waveform, whilst radially magnetised magnets deliver a trapezoidal air-gap magnetic flux. Furthermore, trapezoidal waveforms contain high order harmonics, which can include triplen ones, causing the unwelcome circulation current in the delta connected phase windings. For this reason, three phase designs with delta-connection coils are found not to be the optimal choice when using a magnet with radial magnetisation pattern.

In order to quantitatively investigate the induced circulation current in delta connected three phase permanent magnet motors with Halbach and parallel magnetisation patterns, two 2-dimensional finite element simulation models which have been created, featuring the same dimensions based on the selected design presented in the previous chapter, with the windings modified from single phase to three phase. Figure 6-2 below shows the constructed model in the 2-dimensional finite element simulation, which has 25mm overall outer diameter and 25mm stack length. The simulation is conducted at the motor nominal speed of 150,000rpm, with zero armature current.

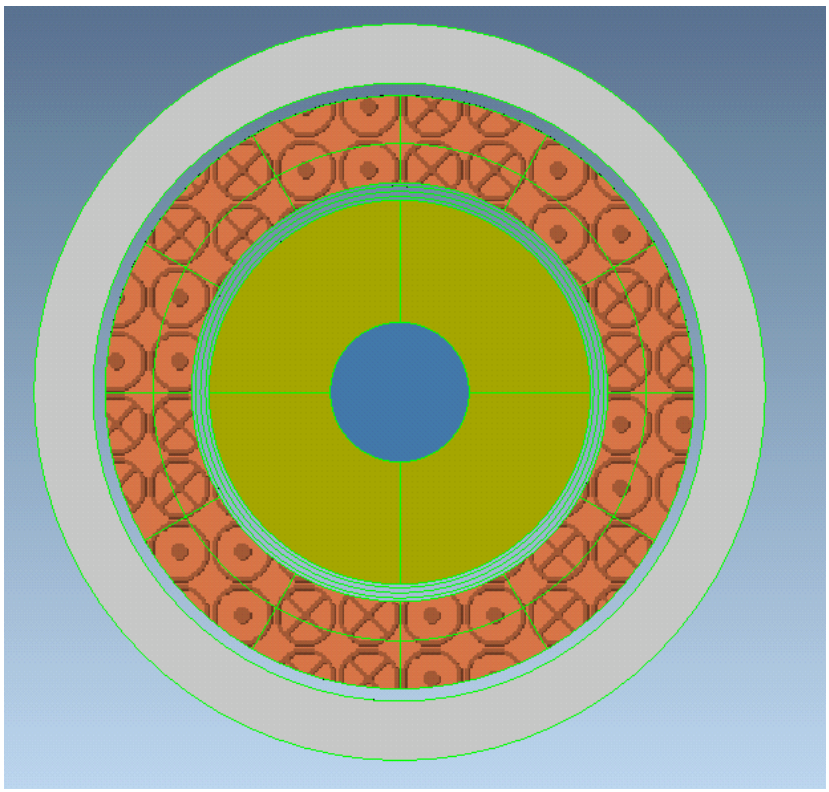

Figure 6-2: The 2-dimensional finite element simulation model for the circulation current analysis in delta-connection three phase motor

Figure 6-3 presents the flux plot of the FE simulated delta-connected three phase motor with a parallel magnetisation pattern. The following Figure 6-4 illustrates the simulated circulation current in the motor windings. It indicates that significant current can be induced inside the closed loop winding circuit due to high order harmonic components in the air-gap magnetic flux. The induced circulation current with 0.655A RMS value is over 16% of the RMS value of the rated current. Figure 6-5 demonstrates the Fast Fourier Transform (FFT) results of the radial air-gap flux density in the radial centre of the winding for the parallel magnetised delta-connection motor. The graph clearly shows that there are third order harmonics of over 5% of the fundamental.

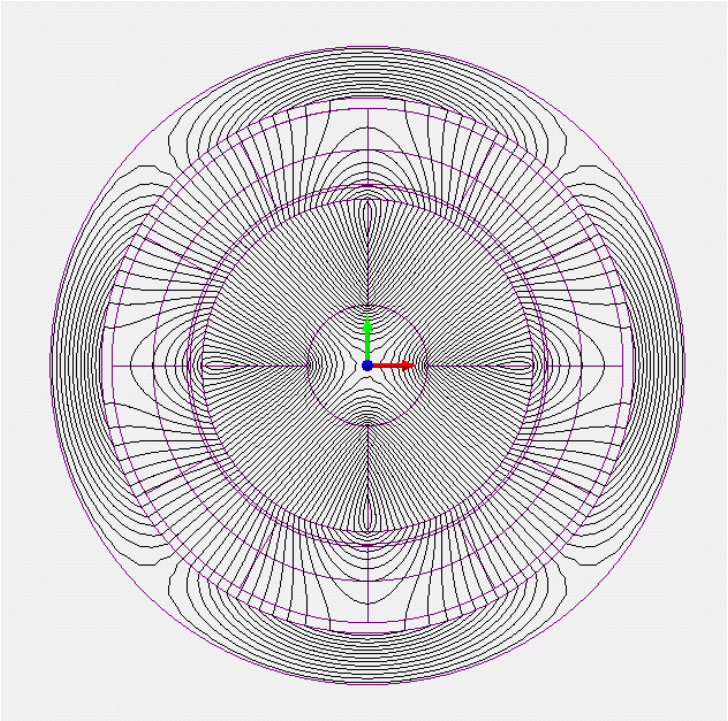

Figure 6-3: The flux plot of the FE simulated delta-connection three phase motor with parallel magnetisation pattern

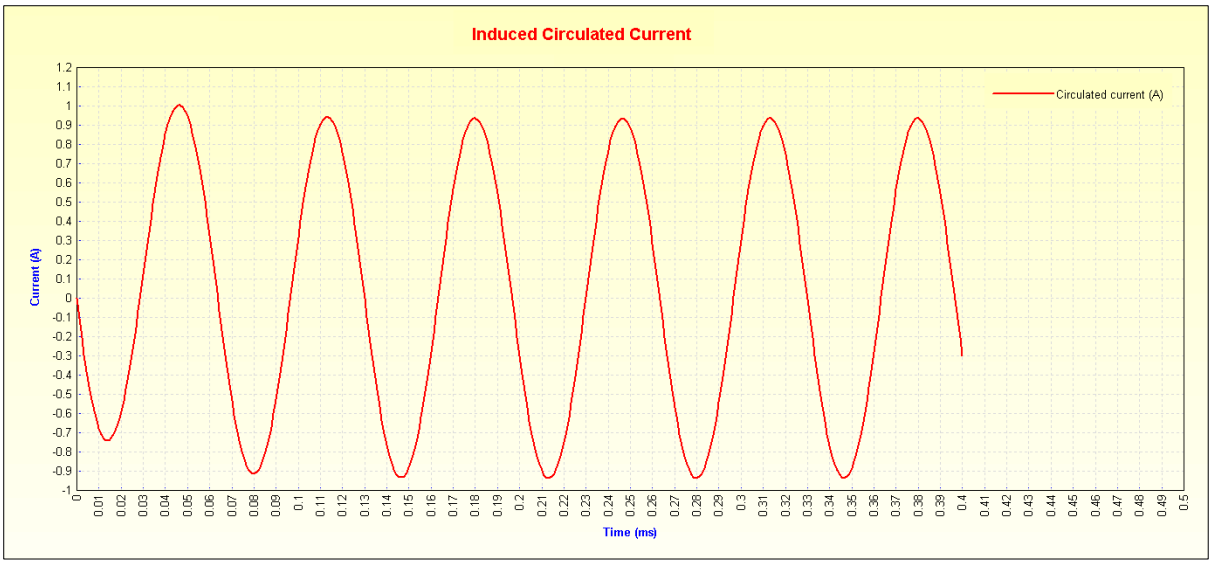

Figure 6-4: The induced circulated current in the delta-connection three phase motor with the parallel magnetised magnets

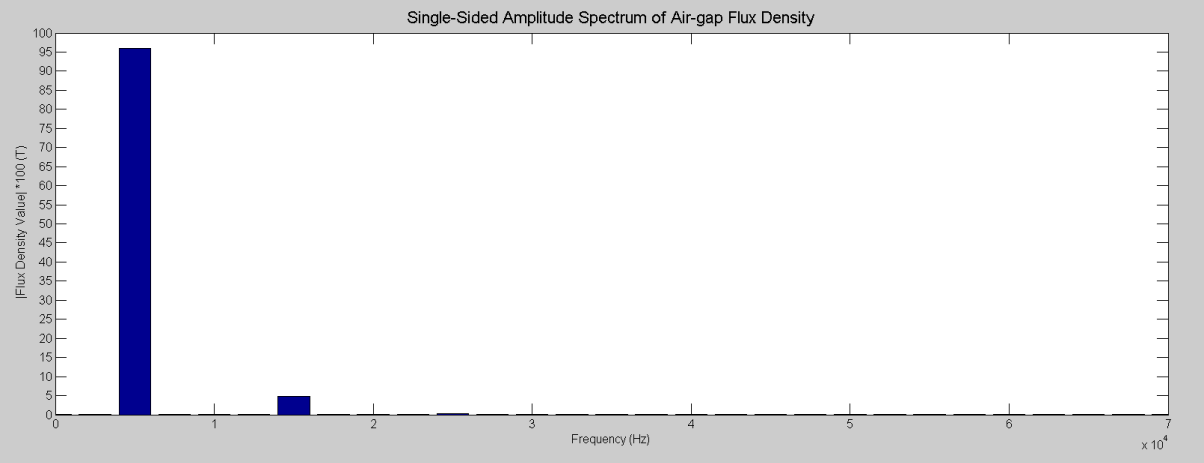

Figure 6-5: The amplitude spectrum of the captured air-gap flux density at the position of the middle of the effective motor air-gap in the parallel magnetised delta connection three phase motor

Figure 6-6 shows a flux plot of the simulated delta-connection motor with a Halbach magnetisation pattern. The following Figure 6-7 demonstrates the induced circulation current in the phase windings. On the basis of the plotted curve, there is no significant circulation current in the coils with a peak of less than 1mA. Similar to Figure 6-5, Figure 6-8 illustrates the FFT results of the captured air-gap flux density in the Halbach magnetised motor. This also indicates that there are no significant triplen harmonics present.

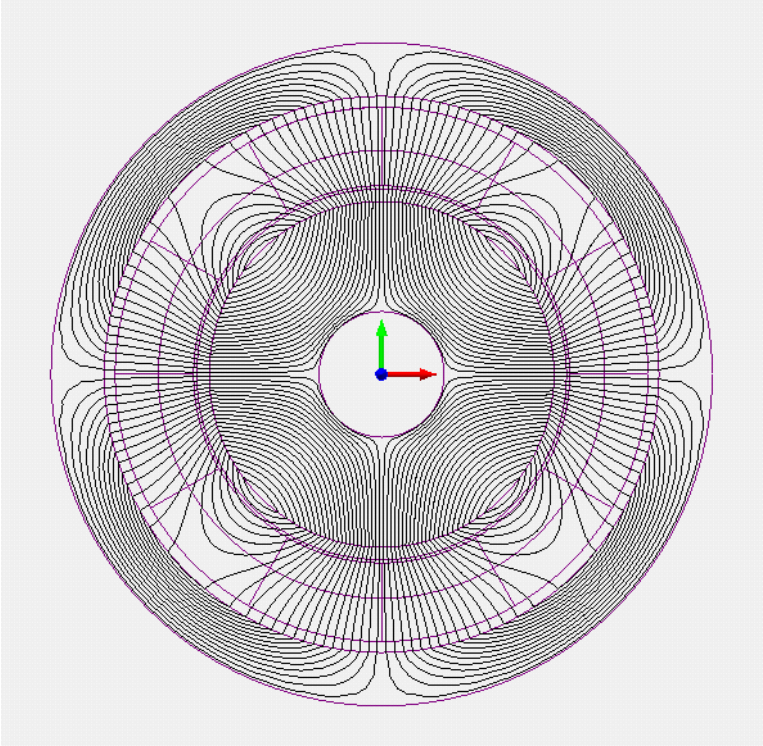

Figure 6-6: The flux plot of the FE simulated delta-connection three phase motor with Halbach magnetisation pattern

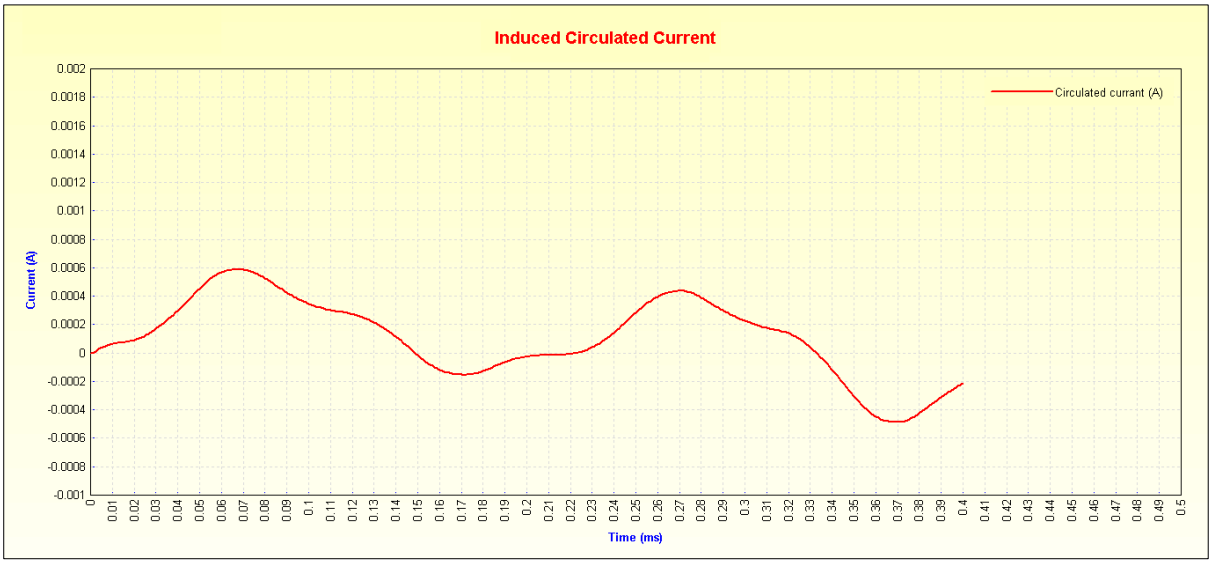

Figure 6-7: The induced circulated current in the delta-connection three phase motor with the Halbach magnetised magnets

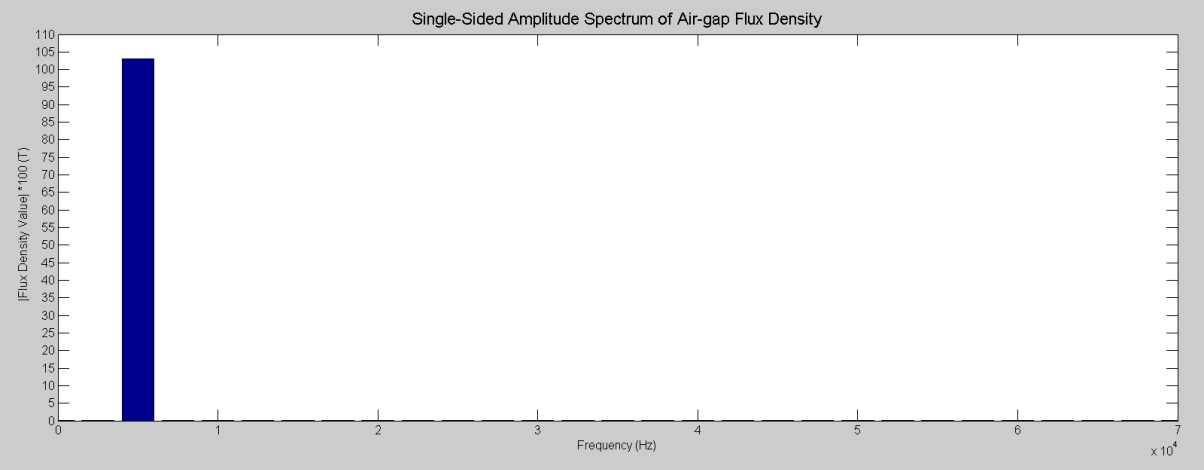

Figure 6-8: The amplitude spectrum of the captured air-gap flux density at the position of the middle of the effective motor air-gap in the Halbach magnetised delta connection three phase motor

On the other hand, Halbach arrays can add additional complexity for mass production. Therefore, it is beneficial to investigate how much the resultant high order harmonics can be minimised with parallel magnetisation pattern. Partially spanned permanent magnets were introduced, as shown in Figure 6-9. As is shown, the original ring-shape magnet is converted into segmented magnets. A series of finite element simulations were carried with the magnet arcs ranging from 120° electrical to 180° electrical. Figure 6-10 demonstrates the simulated circulation current variation with magnet arc. From the graph, it can be seen that the minimum circulation current occurred when the magnet arc was 140° electrical. The following Figure 6-11 illustrates the achieved circulation current in the delta-connection three phase motor with 140° spanned parallel magnetised magnets. The plotted current curve shows minimal circulation current, because there is almost no third order harmonic in the air-gap flux, as shown in Figure 6-12.

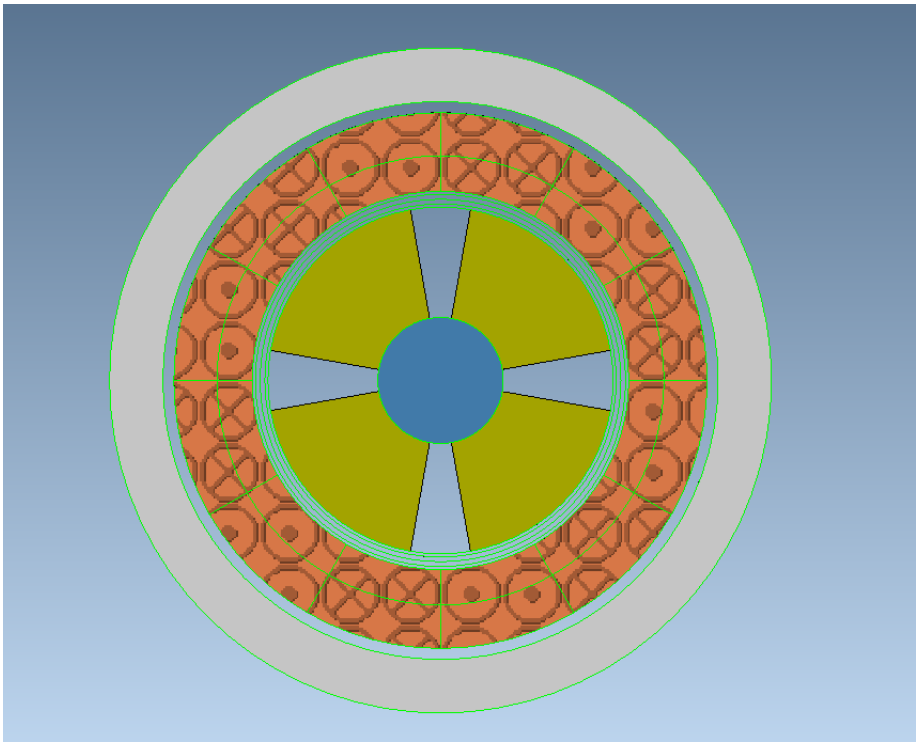

Figure 6-9: The 2-dimensional drawing of a parallel magnetised three phase motor with the partially spanned permanent magnets

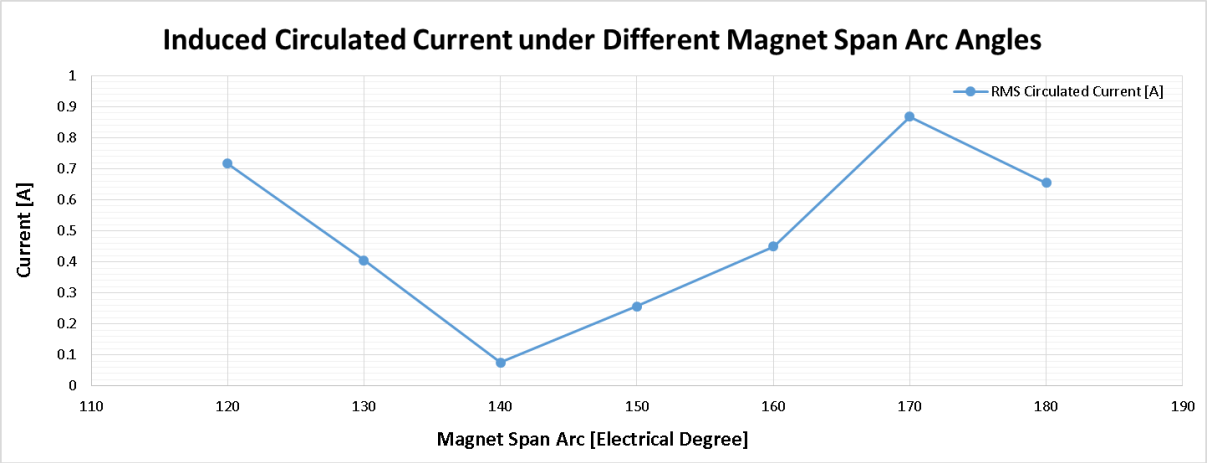

Figure 6-10: The induced circulated current in the parallel magnetised delta connection three phase motor under different magnet span arc angles

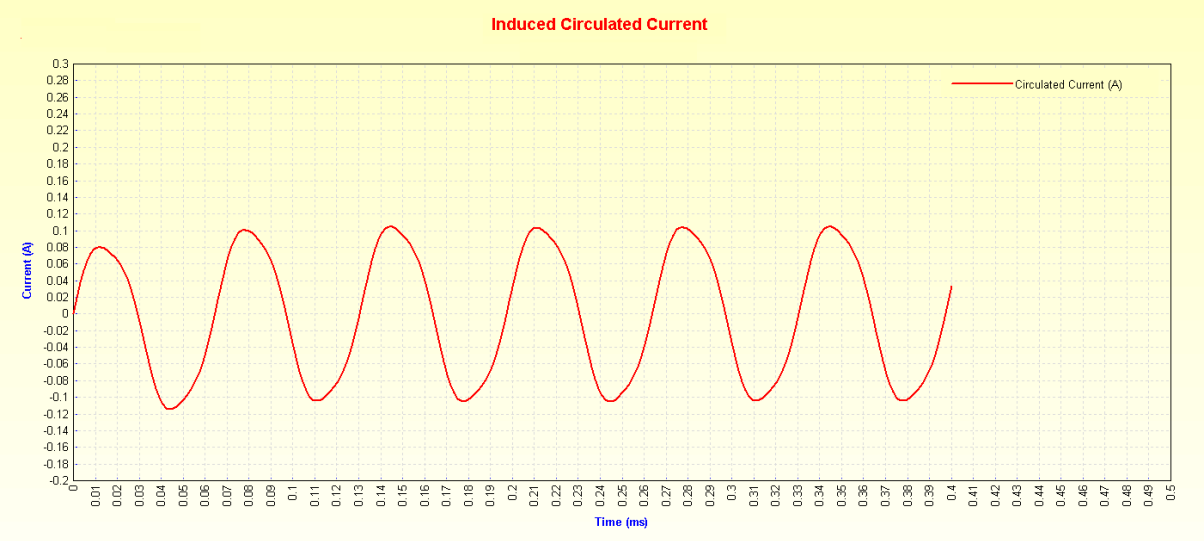

Figure 6-11: The obtained circulated current in the delta-connection three phase motor with 140° spanned Halbach magnetised magnets

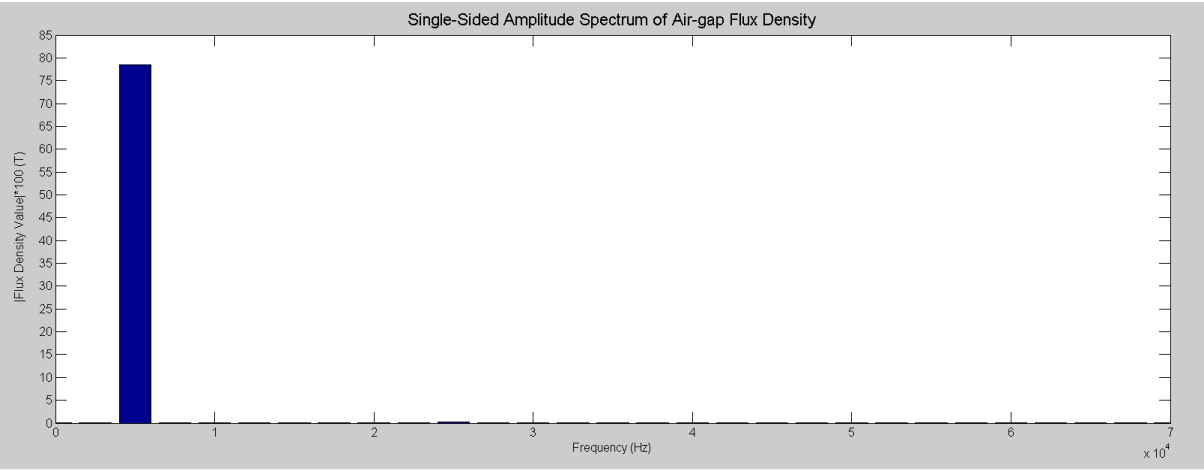

Figure 6-12: The amplitude spectrum of the captured air-gap flux density at the position of the middle of the effective motor air-gap in the 140° spanned parallel magnetised delta-connection three phase motor

To summarise, triplen harmonics can circulate within a delta connected motor windings if there are triplen harmonics present in the induced back-EMF. These harmonics can contribute to significant additional Ohmic loss and therefore should be minimised. Halbach magnetised rotors create a pure sinusoidal flux waveform which has no high order harmonic component. Therefore, they fulfil the requirements to design delta connected three phase motors. For

motors with either parallel or radial magnetisation patterns, the undesirable third order harmonics can be removed through careful design of the selected magnet arc.

Nevertheless, there are two major shortcomings of reduced magnet arcs.

1. Separate segmented magnets are mechanically much weaker than a continuous ring-shape magnet. A rotor sleeve becomes mandatory to resist the centrifugal force generated at high speed operating.

2. The power density of the designed motor is reduced. With reduced magnet arcs, the maximum magnetic loading is inevitably decreased. Based upon the amplitude of the fundamental harmonic shown in Figure 6-5 and Figure 6-12, the peak value of the fundamental of the air-gap magnetic flux drops by over 18%.

Consequently, due to the aforementioned disadvantages, the star-connection method is regarded as more appropriate than the delta-connection approach in this project

6.3 Comparison of normal winding and toroidal winding in three phase motor

This section considers different winding approaches and their effect upon the motor end-windings. Normally, the portion of stator windings which sit outside the stator stack are defined as the end-windings. End-windings deliver the very limited torque and generally only add to the total Ohmic loss in the machine, along with adding volume and mass. Figure 6-13 shows a 3-dimensional three phase motor with normal end-windings. This model has the same dimensions as the single phase design developed in Chapter 5. Because of the air-gap winding, the entire available winding space in the motor is filled with the fully pitched coils. It has to be noted that the minimum axial length of motor end-winding is twice that of the winding radial depth, and the radial depth of the end-winding is about the one third of a coil circumferential length. Undoubtedly, for motors with a short axial length and the large outer diameter, a large proportion of the total winding resistance comes from the motor end-windings, reducing the motor efficiency.

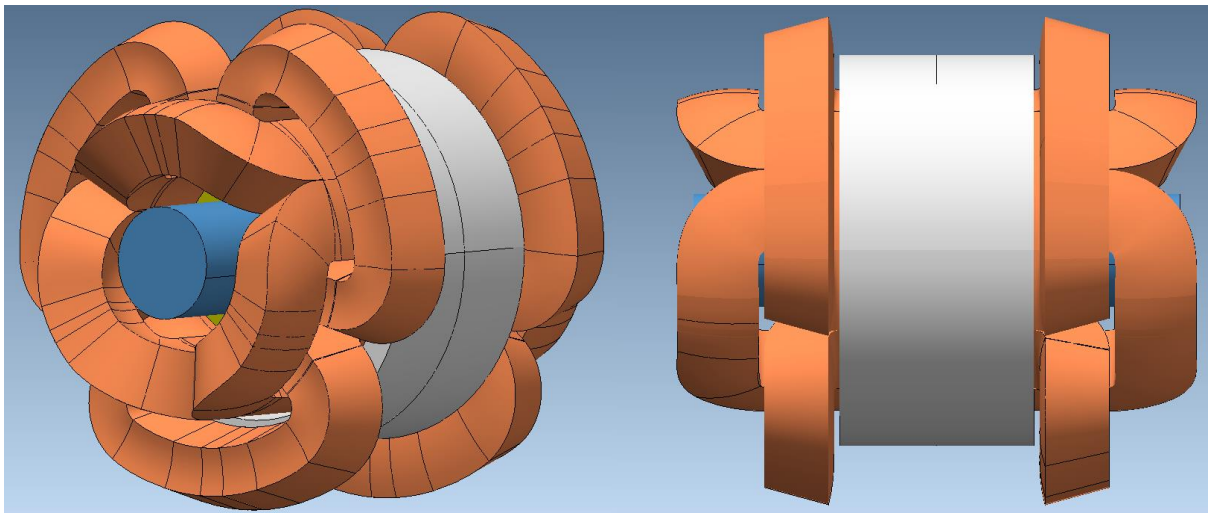

Figure 6-13: The normal and the side views of the 3-dimensional model of the three phasse motor with complete end-windings

Figure 6-14 below demonstrates an alternative toroidal winding approach for a three phase motor. Unlike the normal winding approach, the dominant end-winding length in the toroidal winding machines is in the axial direction. Generally speaking, if the stator axial length is significantly less than its outer diameter, toroidal windings can result in shorter end-windings,

with shorter axial standouts, but give a larger motor overall outer diameter. Also, they require a special winding machine or a more complex stator design to implement a practical coil winding. In this project, the toroidal winding is selected.

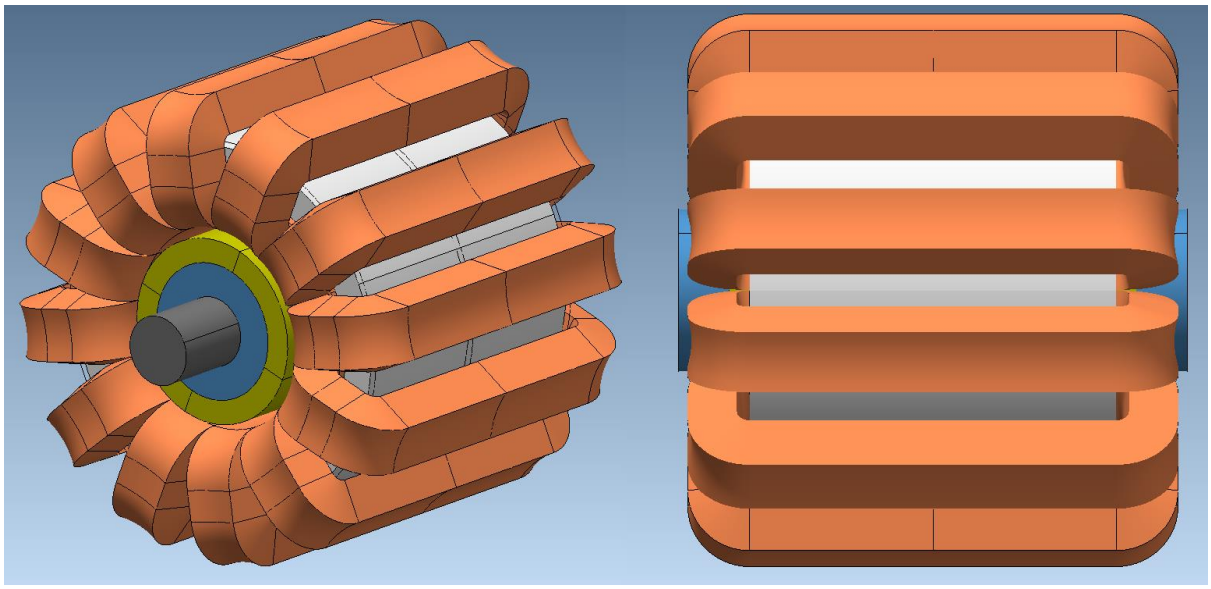

Figure 6-14: The normal and the side views of the 3-dimensional model of the three phase motor with the complete toroidal end-windings.

6.4 Impact of toroidal winding structure on motor housing loss

This section discusses the impact of the toroidal winding structure on the motor housing. In general, a toroidal winding makes it harder for the normal motor casing to provide adequate mechanical support; and there is also increased risk of large induced housing eddy currents and the resultant additional Ohmic loss. This loss is due to the high frequency alternating current flowing through the motor end-winding coils located at the outer surface of the stator. Unlike the active portion of the phase windings, the end-winding coils in a toroidal winding machine are not magnetically screened from the housing. Hence, they generate magnetic fields which link to the motor casing, generating unwanted eddy currents if the housing material is conductive.

Commonly, there are two dominant factors which can influence the amplitude of the induced motor housing loss.

1. The clearance gap between the inner surface of the motor housing and the outer surface of the end-winding coils at the stator outer surface;
2. The radial thickness of the housing frame.

In order to investigate the trend of the induced motor housing loss, a 3-dimensional finite element simulation model has been created, as shown in Figure 6-15. It has to be noted that Figure 6-15 only represents half of the complete motor, so the housing loss will be doubled in the final machine. The aforementioned two housing design factors are regarded as the input variables in the FE simulation model, which are varied from 1mm to 3.5mm in 0.5mm steps.

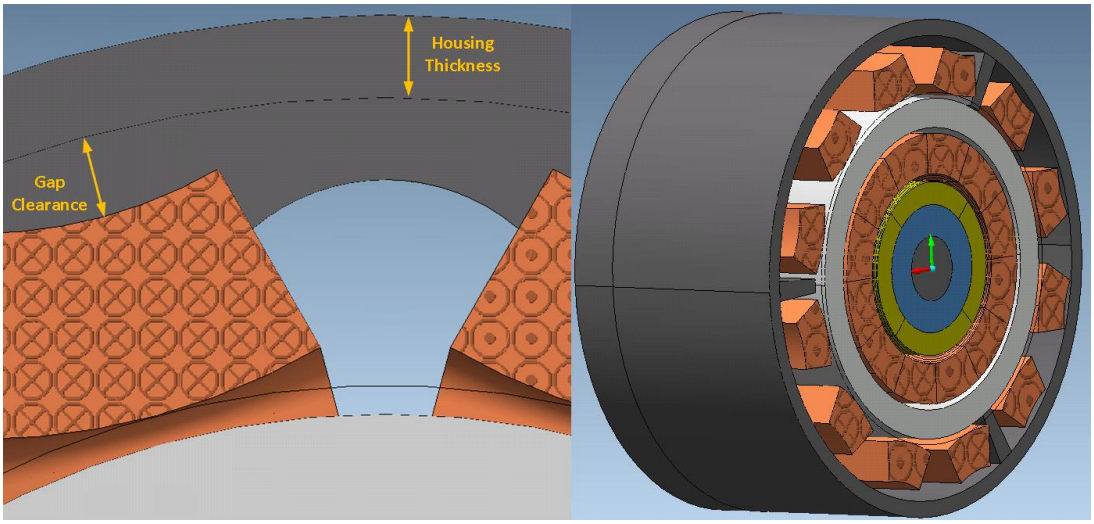

Figure 6-15: The created 3-dimensional finite element simulation model for housing loss investigation

Figure 6-16 below illustrates one example of the induced Ohmic loss in the motor housing frame. The red coloured areas in the diagram represent the regions with the highest loss density while the deep blue parts indicate there is almost no loss generated. The diagram presents that the induced casing loss is periodically distributed in the housing, travelling in circumferential direction during the operation. Most of frame losses are induced in the areas adjacent to the motor end-windings.

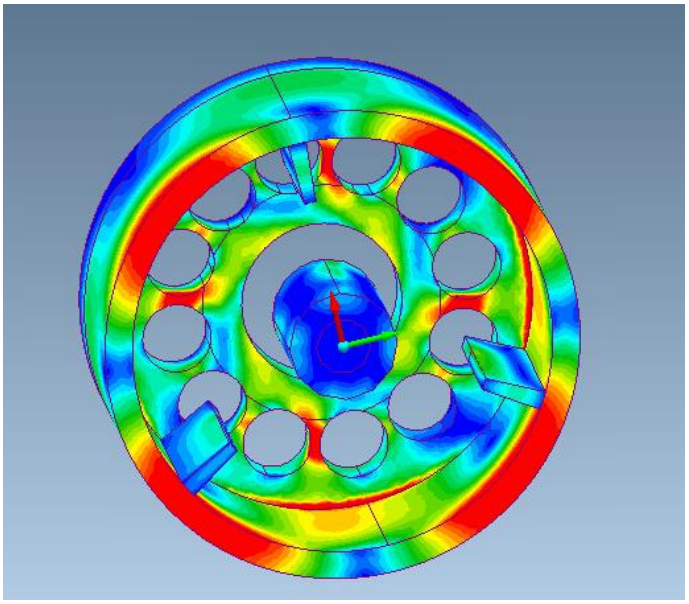

Figure 6-16: The colour shaded graph for the induced Ohmic loss on the motor housing

Figure 6-17 demonstrates the simulated total motor housing loss as a function of the gap clearance and the thicknesses of the housing. It suggests that a thinner housing and a larger clearance gap between the housing and the end-winding coils will minimise the undesirable housing loss. This outcome is due to reduced cross-sectional area for the eddy current loop inside the motor casing and less magnetic flux flowing to the housing.

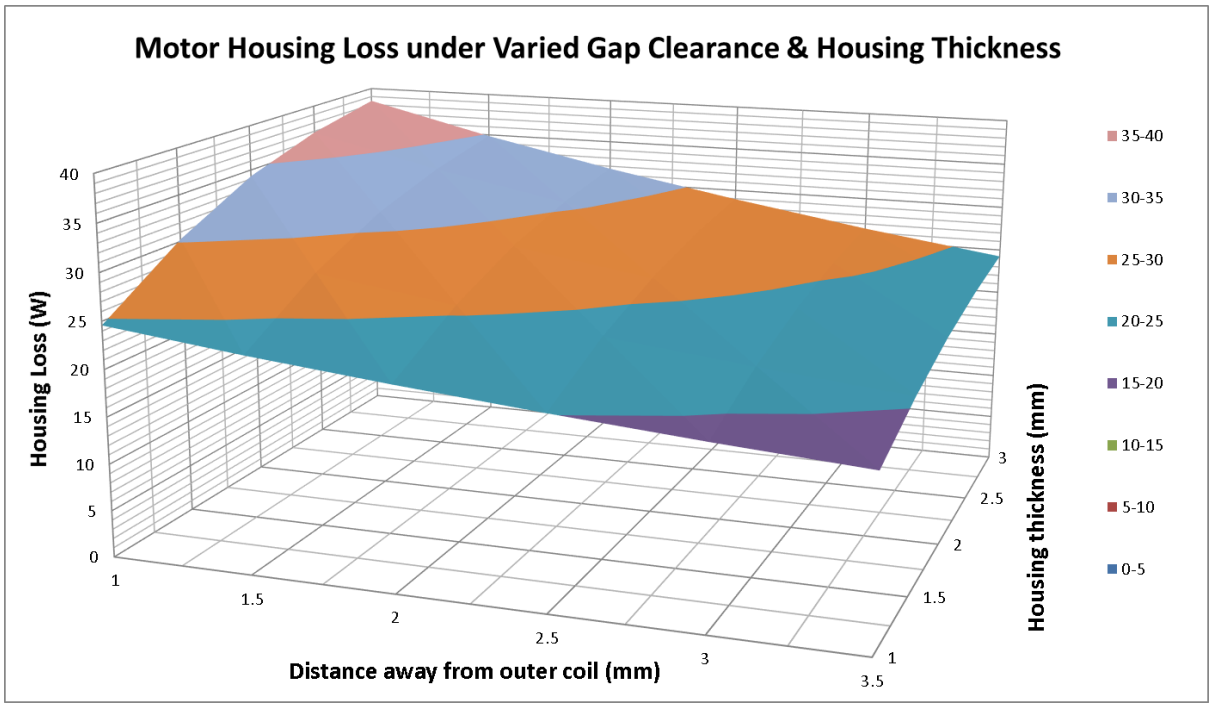

Figure 6-17: Induced motor housing loss under varied gap clearance & thickness of the housing frame

The integral motor housing is split into three different regions in the finite element simulation model to investigate the detailed Ohmic loss distribution, as shown in Figure 6-18. The blue cylinder is the main body of the housing; the housing end cap is in bronze; the dark grey tips on the inner surface of the main body are the supporting teeth. In the conducted finite element simulations, all three components are defined by the same material: cold rolled 1010 stainless steel.

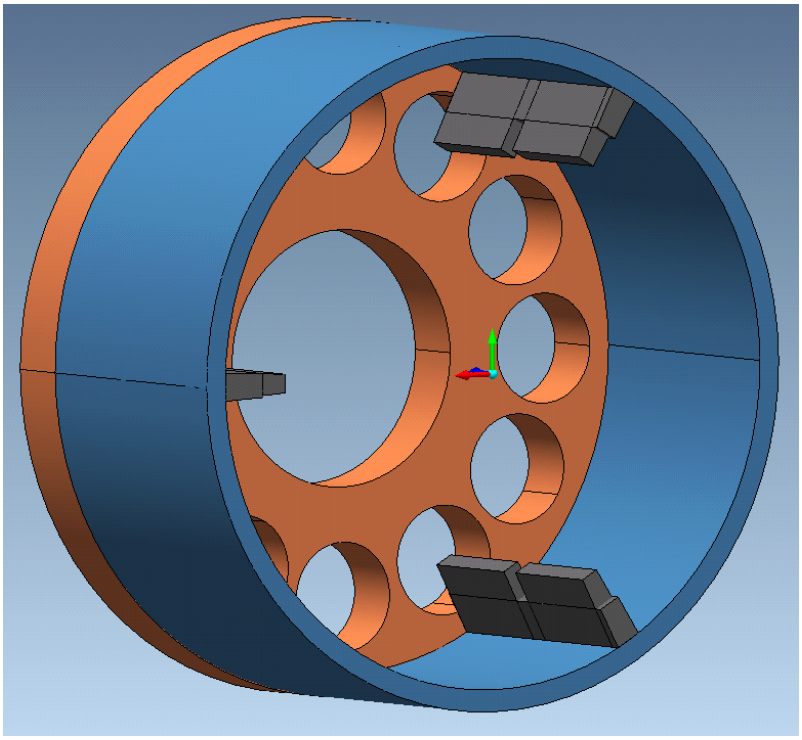

Figure 6-18: The assembled motor housing of three different components: housing main body, housing back cap & housing teeth

Figure 6-19 below illustrates the simulated Ohmic loss in each housing component. In total, there is 11.5W housing loss generated in the simulated model. The plotted curves indicate that the dominant housing loss (over 80% of the total loss) occurs in the main body of the housing while the supporting teeth have less than 0.03W loss per tooth as shown in Figure 6-20. Even if there were twelve teeth selected in the housing design, the total Ohmic loss induced in the supporting teeth is less than 4% of the total housing loss.

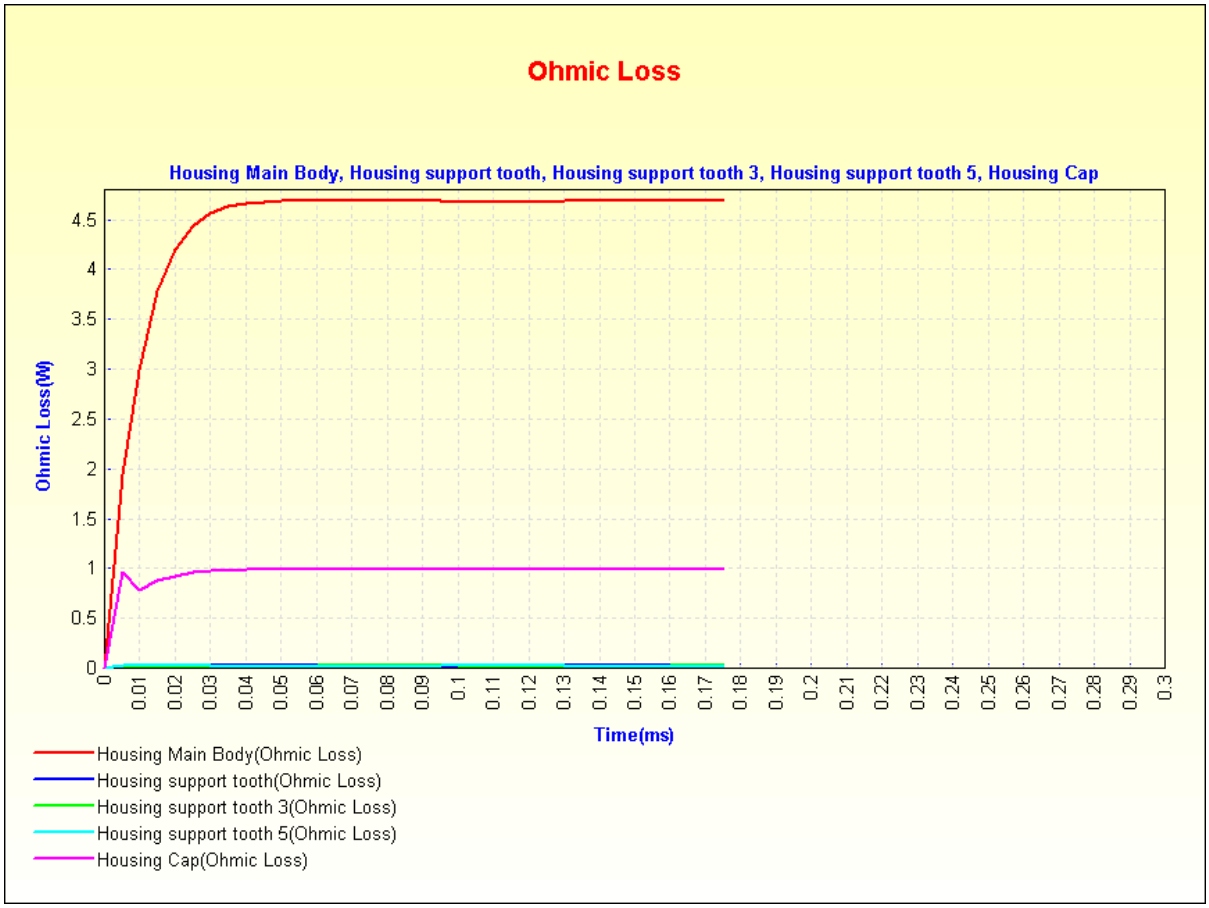

Figure 6-19: Induced housing loss in each housing component

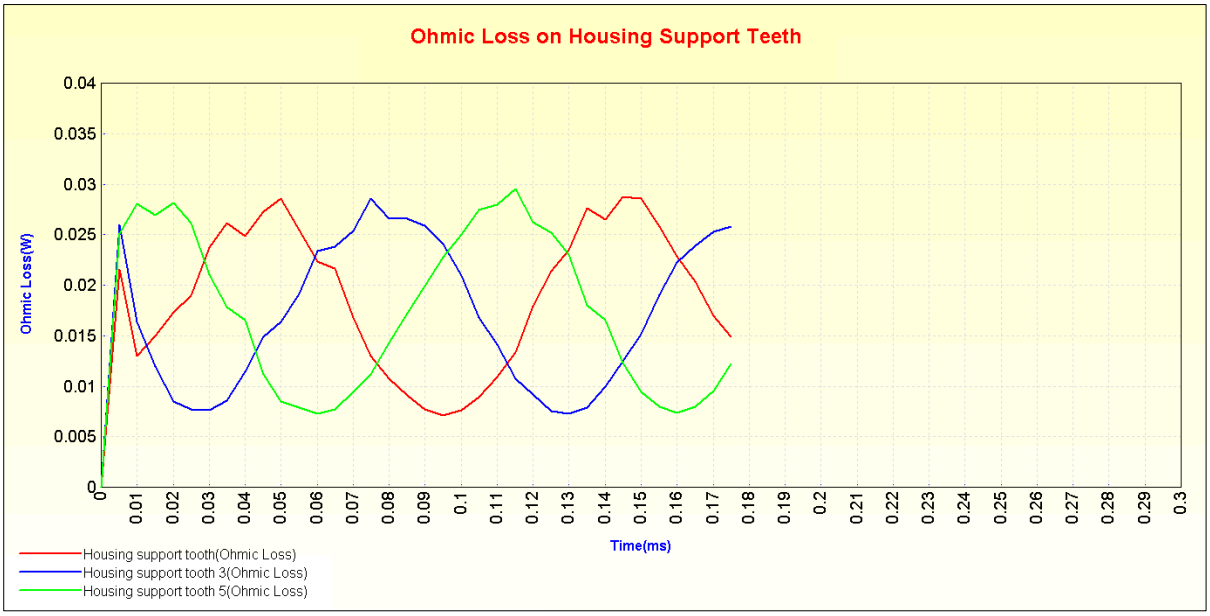

Figure 6-20: The induced Ohmic loss on housing teeth

To summarise, toroidal windings can induce undesirable loss in the motor housing. This is minimised if the housing frame is as thin as possible and placed as far as possible away from the outer surface of the motor end-windings.

6.5 Comparison of three different motor housing designs

Following on the discussions in the previous section, three different motor housing designs have been considered. For design one, the housing is made of nonmagnetic stainless steel and split into two pieces from the middle with a series of supporting teeth on the inner surface of the housing frame. Figure 6-21 presents half of the designed stainless steel housing frame. There are twelve small holes on the housing end-cap to allow the air to be force ventilated through. The advantages of design one can be summarised as follows:

1. It has high mechanical stiffness and can provide the adequate support to both the stator and the bearings;
2. It only requires a straightforward assembly process which is suitable for mass production;
3. It features strong cooling ability due to the high thermal conductivity of the stainless steel.

The disadvantages of method one are as follows:

1. There can be high housing loss induced due to the small clearance between the inner surface of the conductive housing frame and the end-winding coils at the outer surface of the stator;
2. It requires high precision machining to create the supporting teeth due to the limited gap between the two coils on the outer surface of the stator;
3. It is heavy because of the high density of the stainless steel material of the complete motor housing.

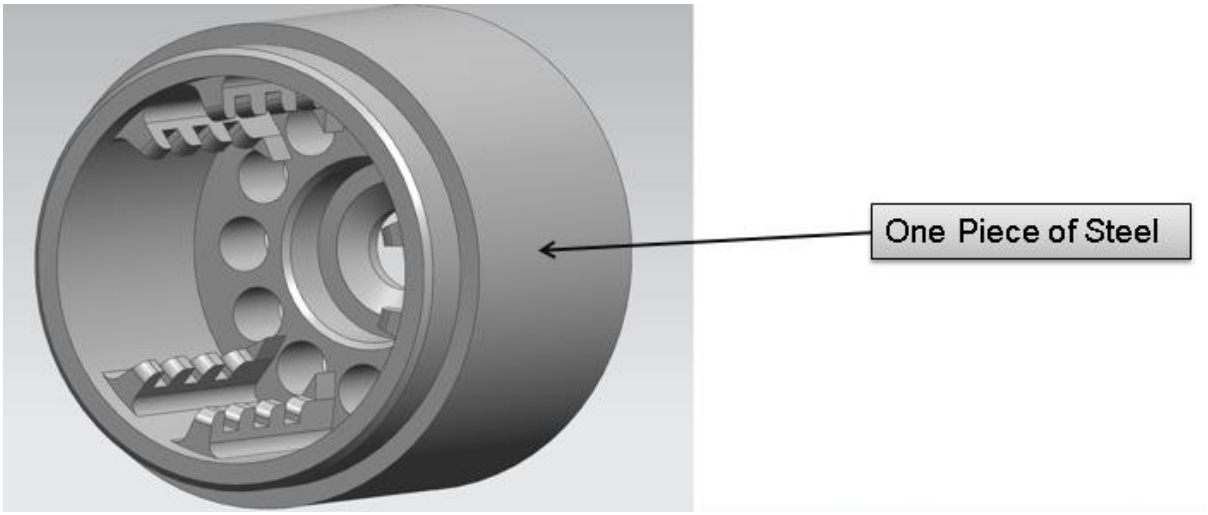

Figure 6-21: The male part of the stainless steel housing frame

In design two, the motor housing consists of two layers which are made of plastic and stainless steel respectively. The inner layer is made by plastic, which can be moulded; while the outer layer is stainless steel, which requires machining tool to produce. Apart from this key difference, the rest of the housing features are identical to the design of method one. The benefits of design two are:

1. It induces comparatively low housing loss as the inner layer of the frame adjacent to the outside end-winding coils is a non-conductive material;
2. The plastic layer can be made via an injection moulding process which can accelerate the manufacturing speed, including the complex supporting teeth.
3. It is comparatively lighter as half of the frame is made of plastic;
4. It is much easier and quicker to machine the ring-shape stainless steel part for the outer layer of the housing frame.

On the other hand, it also has the following shortcomings:

1. The rigidity of the complete motor housing has been reduced owing to the plastic material;
2. An additional assembly procedure and extra assembling tolerances are required to fit the two layers of the housing frame.
3. The plastic inner layer of the motor housing frame features much lower thermal conductivity, reducing the cooling ability compared to design one.

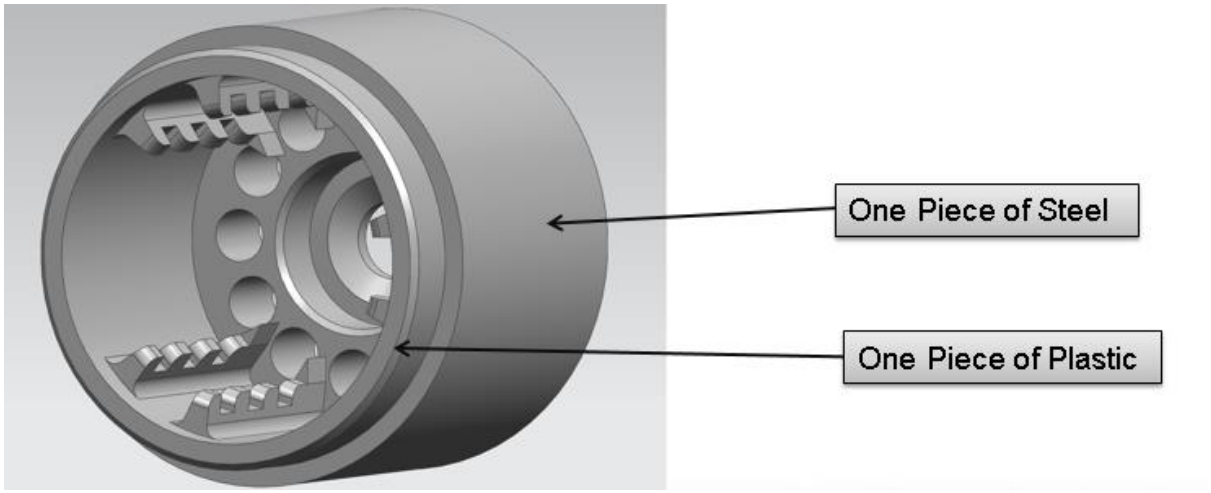

Figure 6-22: The male part of the double layer housing frame: plastic and stainless steel

The third approach to the housing design employs a potted plastic housing with stainless steel end caps. Compared to the previous two housing designs, only the stainless steel end caps are preserved, with twelve air flow tunnels. A cylindrical hollow mould is placed on top of one side of the end caps and the stator is inserted. Plastic particles are then injected into the mould to fulfil the gap between the stator and the inner surface of the mould. When the whole gap has been filled, the mould is removed after the required cure procedure. This method has the following advantages:

1. It can provide excellent support to the stator and the bearings as well as the winding coils;
2. It can minimise the induced housing loss because the plastic particles are non-conductive;
3. There are fewer clearance and tolerance issues concerned.

However, the weaknesses of design three include:

1. The cost of the potted plastic housing is comparatively high due to the cost of the plastic particles and the complex manufacturing procedures;
2. There is no direct cooling to the motor windings as the complete coil outer surfaces are buried inside the plastic which has lower thermal conductivity;
3. The bearing alignment relies on the precision fit of the stainless steel end cap and the plastic housing.

In summary, after considering all the listed pros and cons of each housing design approach, method two was selected. Figure 6-23 below demonstrates a cross-section view of the design including motor and housing. The grey coloured part, A, is the single cylinder shape stainless steel outer housing; the yellow coloured part, B, is the plastic made inner layer housing with 12 teeth supporting the stator outer surface.

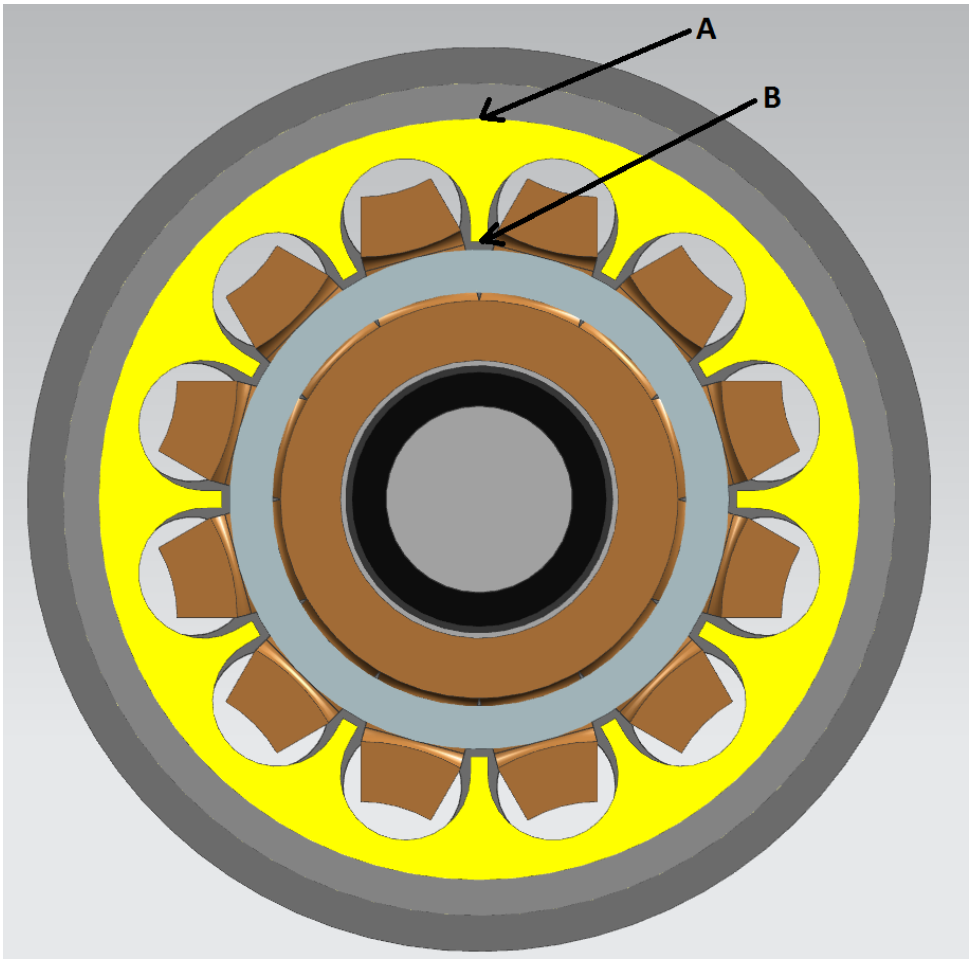

Figure 6-23: The cross-section view of the motor housing design with the toroidal winding motor

6.6 Impact of magnet axial length on motor output power

This section discusses the impact of the axial length of the rotor magnet upon the output torque, motor efficiency and cost, whilst maintaining the active length of the stator and the phase windings constant.

In most cases, the axial length of the rotor magnets is equal to the stack length of the laminated stator. This structure utilises the complete active length of both winding coils and laminated stator to generate the output torque. However, this statement is not 100% correct when analysing via a 3-dimensional model. Figure 6-24 below illustrates an arrow plot of the modelled motor magnetic flux using 3-D finite element simulation of the designed permanent magnet. It has to be noted that the shown model only represents one eighth of the total magnet. Significant flux leakage can be observed at the end-surface of the magnet flowing in the axial direction, as highlighted by the red circle. Figure 6-25 illustrates the air-gap flux density variation along the axial length of the magnet in a design where the stator and the magnet have the same active length. The results are measured at a position 0.5mm away from the magnet outer surface in the 3-dimensional finite element simulation model. The axial lengths of both stator and magnet are 18mm.

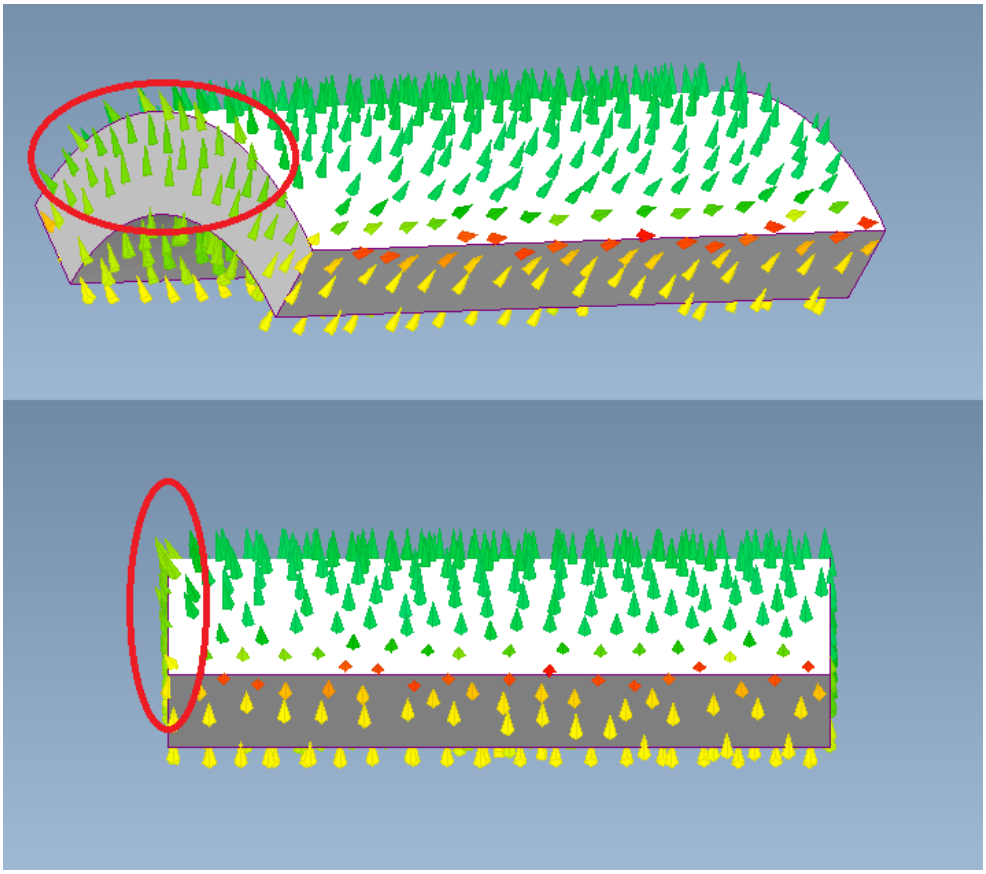

Figure 6-24: Arrow plot of the magnetic flux direction in a 3-dimensional finite element analysis model for the designed permanent manget

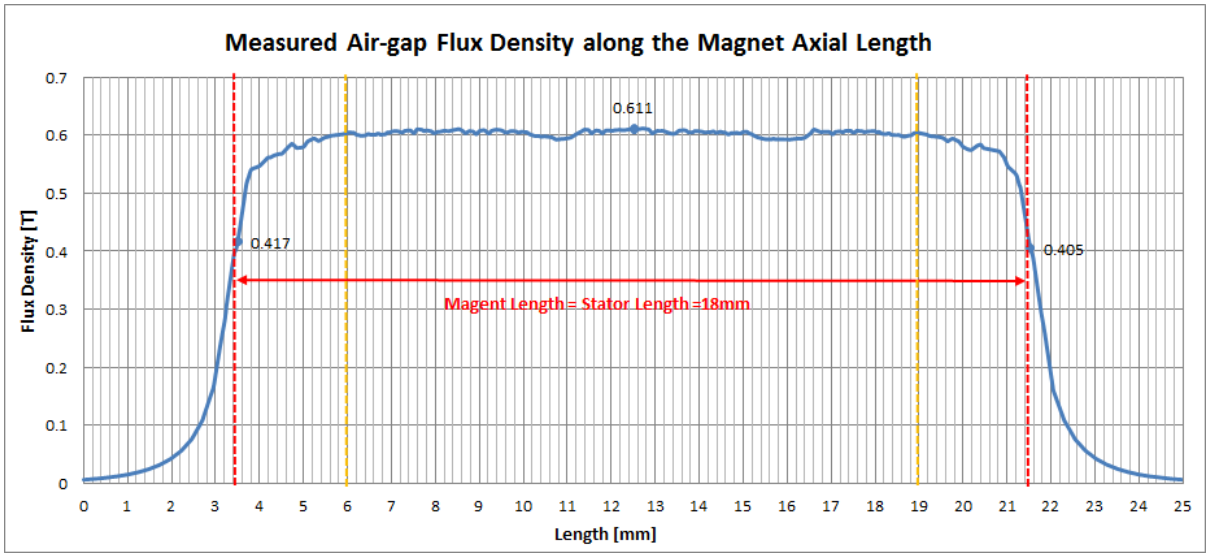

Figure 6-25: Measured air-gap flux density along magnet axial length in the design where both magnet and stator have the same length

Figure 6-25 above shows that the nominal value of the air-gap magnetic flux density is over 0.6T, but this is decreased by over 30% at the axial ends of the permanent magnet. Reduction of the effective air-gap flux density commences about 2.5mm away from the magnet edge, which means that over one fourth of the active length of the winding coils generate reduced back-EMF. This argument is also supported by the fact that the motor output torque achieved in 2-D simulation is 4.5% higher than that in a 3-D simulation.

To compensate for the performance drop due to the above flux leakage, two approaches are considered:

1. To employ an anisotropic permanent magnet.
2. To increase the axial length of the magnet.

Specifically speaking, an anisotropic magnet can only be magnetised in a specific direction, so a relatively stronger magnet can be made as the crystal direction inside the material is unidirectional. Nevertheless, this material feature does not completely eliminate flux leakage in the axial direction even though it is significantly reduced. Consequently, an extended magnet axial length is investigated. Figure 6-26 below illustrates the cross-section view of the toroidal winding slot-less structure permanent magnet motor with an extended magnet axial length. A group of 3-dimensional finite element simulation models have been created with magnet axial lengths varying from 18mm to 24mm in 1mm steps.

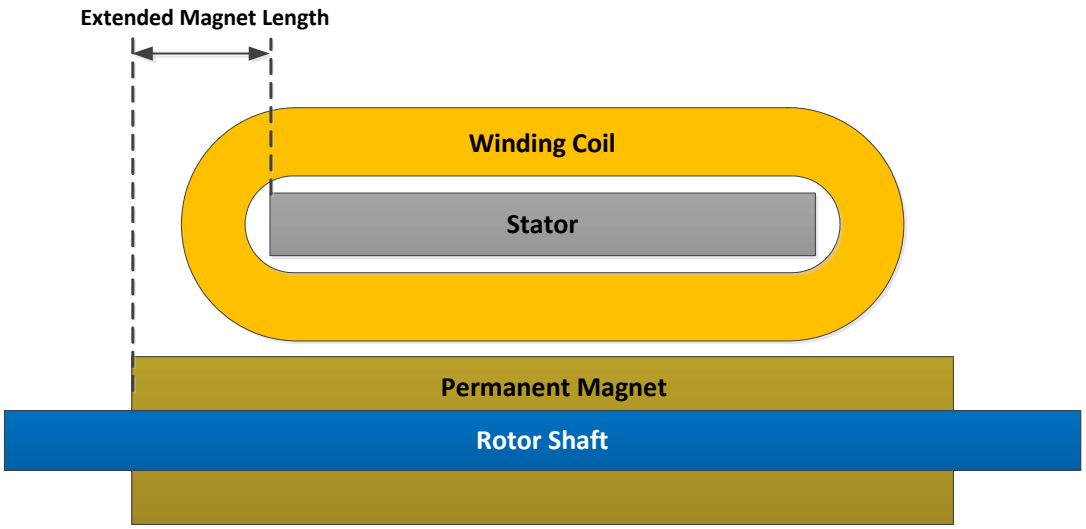

Figure 6-26: The cross-section view of the toroidal winding slot-less structure permanent magnet motor with the extended magnet axial length

Figure 6-27 demonstrates the simulated air-gap flux density variation along the axial length of the magnet with the stator length held constant. As in Figure 6-25, the results are measured at a position 0.5mm away from the magnet outer surface. The graph indicates that the air-gap flux density at the axial ends of the stator becomes increasingly close to the nominal flux density value with growth of the magnet active length. The following Figure 6-28 plots the air-gap flux density at the stator axial edge as a function of magnet length. With the first millimetre of magnet axial length extension, the growth of the air-gap flux density at the stator axial end-surface proves to be most significant. It can contribute to over 85% compensation of the end-surface flux density drop, while the remaining 15% can only be gained with more than a 5mm magnet extension.

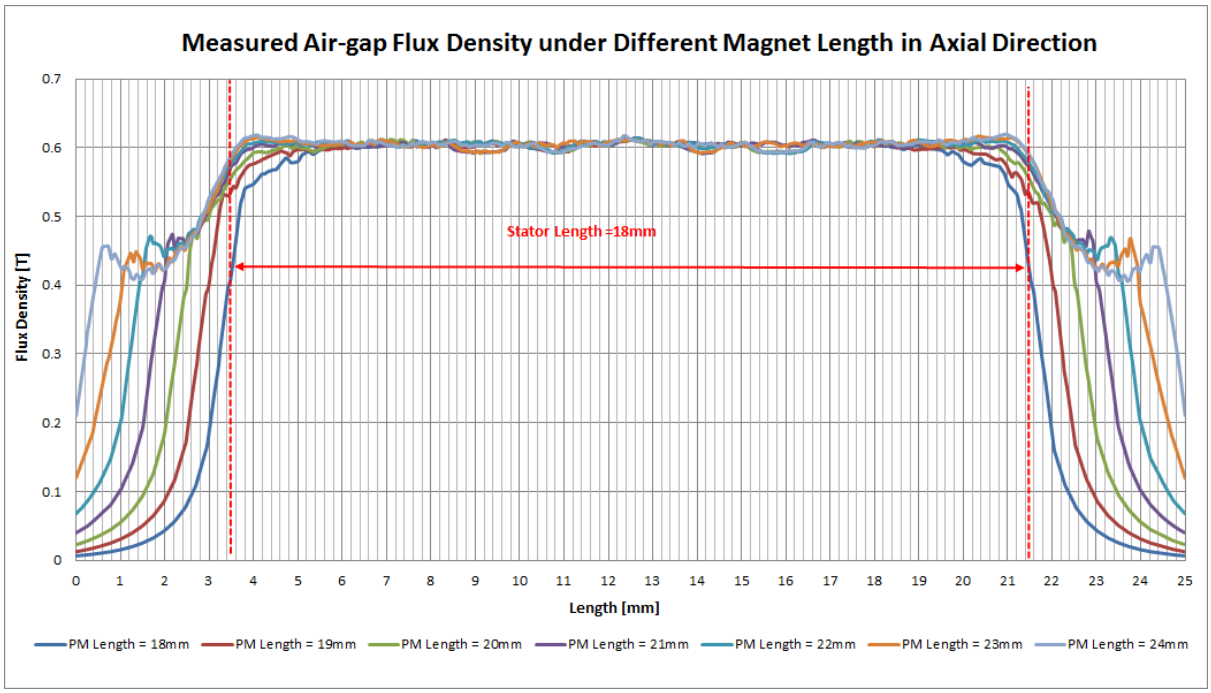

Figure 6-27: Measured air-gap flux density in axial direction under different magnet length but having the same stator length

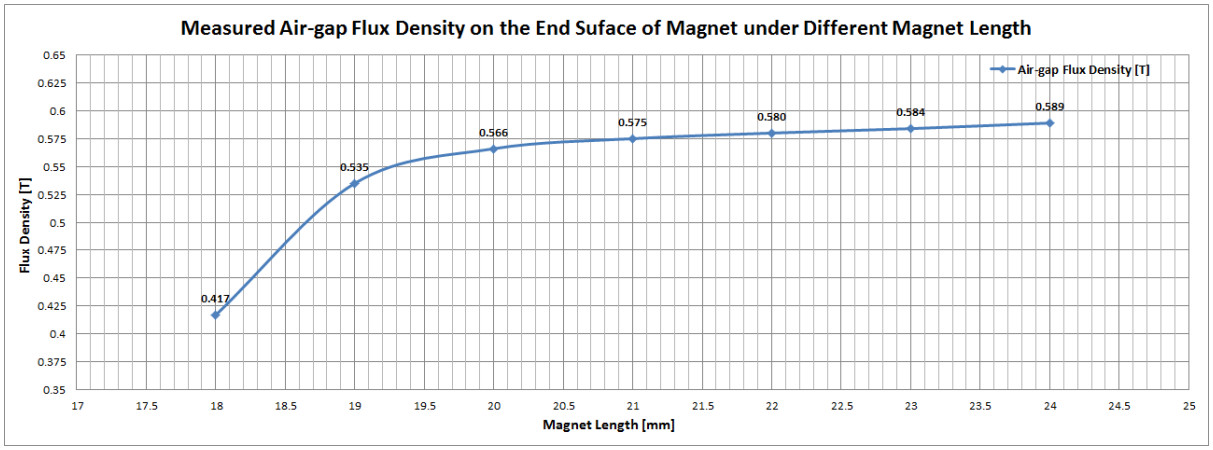

Figure 6-28: Measured air-gap flux density on the end-surface of magnet with different magnet length

Figure 6-29 shows the percentage change in motor output torque as the magnet length is increased beyond the active length of the stator. An increase in length of 2.0mm results in about 10% increased torque capability.

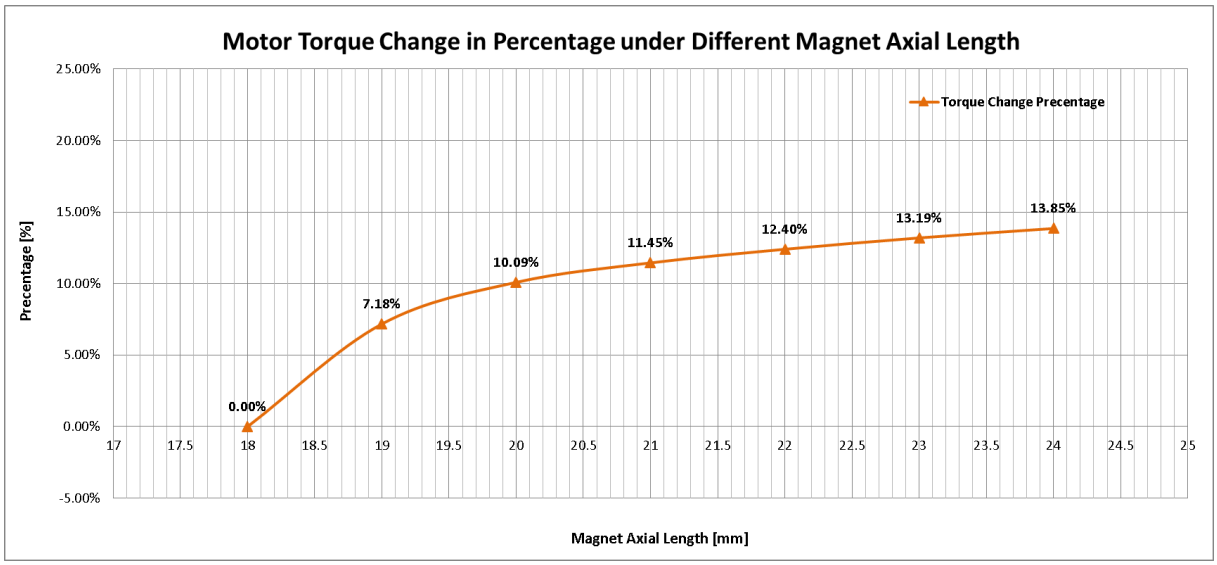

Figure 6-29: Motor torque change in percentage under different magnet axial length

Further, the axially extended permanent magnet can increase the induced back-EMF per turn. Thus, a longer magnet can be utilised in the motor to reduce the required number of turns per phase, whilst still delivering the targeted level of motor output torque. This in turn helps to

lower the winding copper loss and the resultant heat, improving motor efficiency and reducing the winding temperatures.

On the other hand, the extension of magnet axial length has its limits. Figure 6-28 and Figure 6-29 predict that, when the magnet axial length is over 35% longer than the stator stack length, any further growth in magnet axial length will bring very limited further gains on both air-gap flux density at the region of stator axial end-surface and motor output power. Besides, the extension of magnet axial length increases the cost of the utilised motor raw materials. For a magnet with fixed overall outer diameter, the growth of the cost is proportional to the increase of the axial length, which tends to be the dominant cost component in the total motor.

To summarise, after evaluating all the advantages and the disadvantages of the extended magnet axial length discussed above, a 2mm extension of the originally designed permanent magnet is selected.

6.8 Optimal Design of Three Phase Slot-less PM Motor

Similar to the design of single phase slot-less permanent magnet motor, the hybrid simulation approach is utilised to search for the optimal three phase slot-less design, combining the merit of rapid global variable scan with the precise finite element analysis. To filter the best design, the highest motor efficiency with ±1% tolerance was picked up, with the satisfaction of listed motor dimensions and motor specifications given in Chapter 1. Besides, the utilised magnet dimensions are limited, considering the target of minimising the motor per unit cost and the constraint of the maximum achievable magnet radial thickness. As discussed in previous sections, the winding topology is fixed to toroidal winding, and the magnet axial length will be extended to be 2mm longer than stator stack length.

It has to be noted that, due to the high cost and the long-time of building the brand new magnet mould and modifying the current production line of magnet (over £25,000), the most practical solution in this project is to choose the existing magnet mould with the closest dimensions compared to the initial optimal design, and then conduct the re-optimisation based upon the unique magnet sizes.

Figure 6-30 below illustrates a 3-dimensional model of the chosen design. Table 6-1 lists the motor parameters for the selected optimal design. Figure 6-31 gives the magnet open-circuit air-gap flux distribution for the designed 4-pole ring-shape permanent magnet. The most significant achievement for this design is the minimised motor per unit material cost, which is only 1.5 US dollars. This is due to the minimal use of costly rare-earth permanent magnets, and no carbon fibre sleeve on the rotor. All other materials are low cost as well.

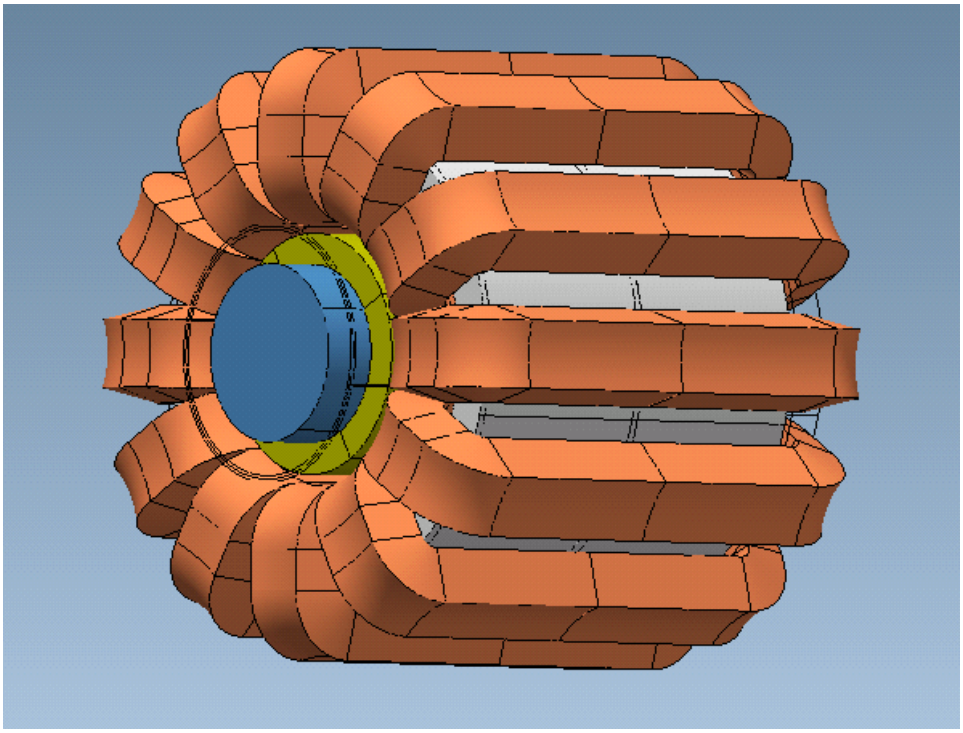

Figure 6-30: 3-dimensional model of the optimal design

Motor Input Power [W]	750
Motor Efficiency [%]	89.95%
Motor Speed [rpm]	150,000
Motor Overall Outer Diameter [mm]	25
Motor overall Length [mm]	22
Stator Core-back Thickness [mm]	1.8
Stator Stack Length [mm]	18
Number of Turns [#]	87
Winding Width [mm]	2.5
Wire Size [mm]	0.331
Phase Current Density [A/mm^2]	26.11
Magnet Thickness [mm]	1.4
Magnet Length [mm]]	20
Magnet Outer Diameter [mm]	10.7
Magnet Inner Diameter [mm]	7.9
Magnet Pole Number [#]	4

Table 6-1: Motor parameters for selected optimal design

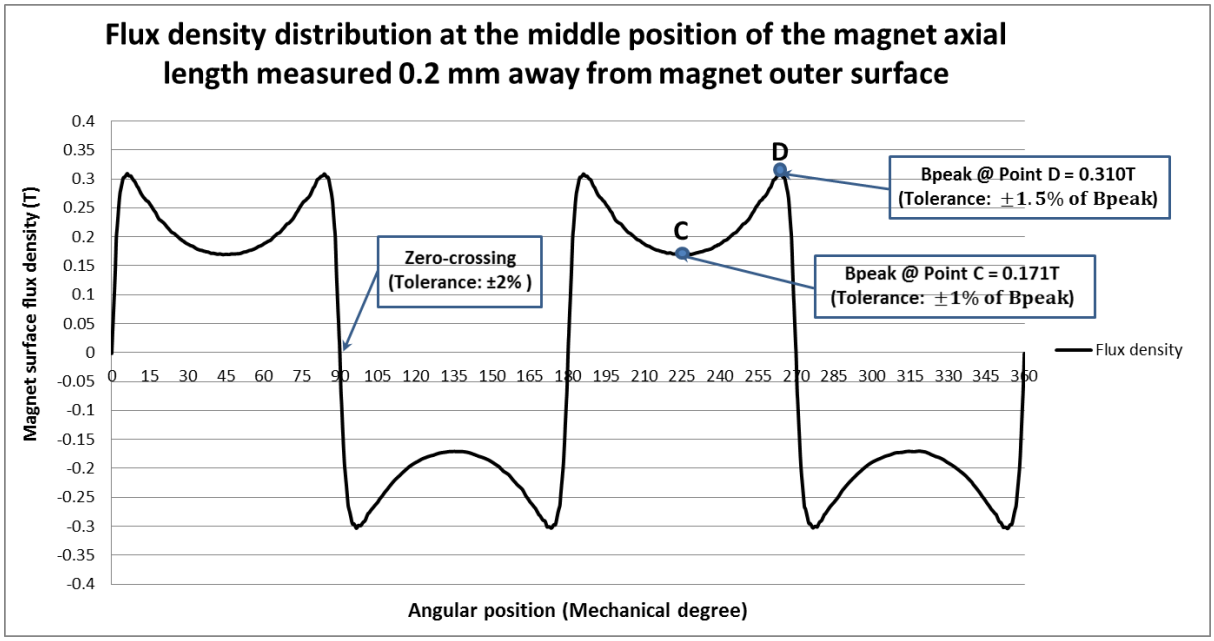

Figure 6-31: Flux density distribution at the middle position of the magnet axial length measured 0.2 mm away from magnet outer surface

6.8 Motor system simulation

Equation 6-1 below shows the general principle of a brushless DC motor operation. The amplitude of the motor back-EMF and the value of phase inductance are two decisive factors, as the interaction between two can significantly impact the selected motor control scheme. With the given back-EMF value due to a fixed motor design, the precise control of motor phase current becomes increasingly challenging in slot-less structure motor owing to the low inductance. The current rate of change, $\frac{di}{dt}$, becomes high, which can lead to both overshoot and high torque ripple issues.

$$V_{terminal} = Back - EMF + I_a * R_a + L_a \frac{di}{dt} \quad (6-1)$$

Therefore, for the selected low inductance slot-less motor design in this project, current hysteresis band control is introduced. During operation, there are two current bands, defined as the current upper and lower limits. Once the measured phase current triggers the higher end limit, the switching devices are then turned off to allow freewheel of the current; when the low end threshold is triggered, terminal voltage is applied across the winding coils to push phase current up.

In this research, a combined Excel-Matlab dynamic system simulation tool is developed to implement motor system simulation. Figure 6-32 demonstrates the Excel Input Datasheet for system validation. Motor and control circuit parameters as well as control schemes can be separately defined on this sheet. The Matlab simulation model can load the spreadsheet information directly to commence the simulation. Figure 6-33 plots an example of simulated motor performance from the carried out dynamic simulation. From the phase current waveforms (highlighted by a black region), the current hysteresis band control can be observed to limit the phase current during operation. The region highlighted in red represents the DC-link voltage, which indicates that there is significant ripple in the DC-link voltage within one electrical cycle. This is because of the too small DC-link capacitance ($10\mu F$) utilised in the simulation. The following Figure 6-34 demonstrates the achieved system simulation results for optimal design with 10% inductance tolerance.

No.	Parameter	Value	Unit		No.	Parameter	Value	Unit
1	No. of simulation electrical cycle	250			2.1	No. of elec. cycle to be saved	200	
					2.2	No. of elec. cycle when speed loop closed	1000	
2	No. of rotor pole pair	2			2.3	Moment of rotor inertia	1.37E-07	kg*m^2
3	Rated speed	150000	rpm					
4	Simulation speed	150000	rpm		2.4	Motor emf factor	1	
5	Electrical frequency	5000	Hz		2.5	Motor inductance factor	1	
6	Electrical cycle	0.2	ms			Motor & control circuit parameters		
7	No. of step per electrical cycle	1800			2.6	Max no. of elec. cycle to be recorded	400	
8	Delta_t	0.111111	us					
9	Delta_electrical degree	0.2	elec.deg		2.7	Top switch on deadtime	1.00E+00	us
					2.8	Bottom switch on deadtime	1.00E+00	us
10	Operation mode	111			2.9	Current control advance angle	20	elec.deg
11	Advanced fire angle for voltage control	0	elec.deg		2.10	Current control peak value	6.95	A
12	PWM frequency Control scheme selection	50	kHz		2.11	Current control hysteresis band width	2.4325	A
13	PWM cycle	20	us					
14	PWM Max duty	100.00%			2.12	Voltage conducting period (operation mode 11)	180	elec.deg
					2.13	Current control free wheel period	5.00E+00	us
15	Input supplier rms voltage	240	Vrms					
16	Input supplier pk voltage	339.36	Vpk		2.14	Fixed DC link	0	
17	Input supplier frequency	50	Hz					
18	Input supplier cycle	20	ms	100	2.15	Battery internal resistance	0.001	Ohm
19	Power electronics operating temperature	90	degC					
20	Motor operating temperature	90	degC					
21	Rectifier bridge model ID	1			2.16	Assumed stator iron loss	2.1	W
22	Power switch model ID	151			2.17	Assumed rotor iron loss	0	W
23	Input inductor inductance	0.25	mH		2.18	Assumed rotor magnet loss	0	W
24	Input inductor resistance	0.35	Ohm		2.19	Assumed mechanical loss	3.5	W
25	DC link capacitor capacitance	4.7	uF		2.20	Assumed other pcb loss	1	W
26	DC link capacitor resistance	0.005	Ohm		3.21	Assumed proximity loss	12	W
27	Over current shunt resistance	0.1	Ohm					

Figure 6-32: Excel Input Datasheet for system validation

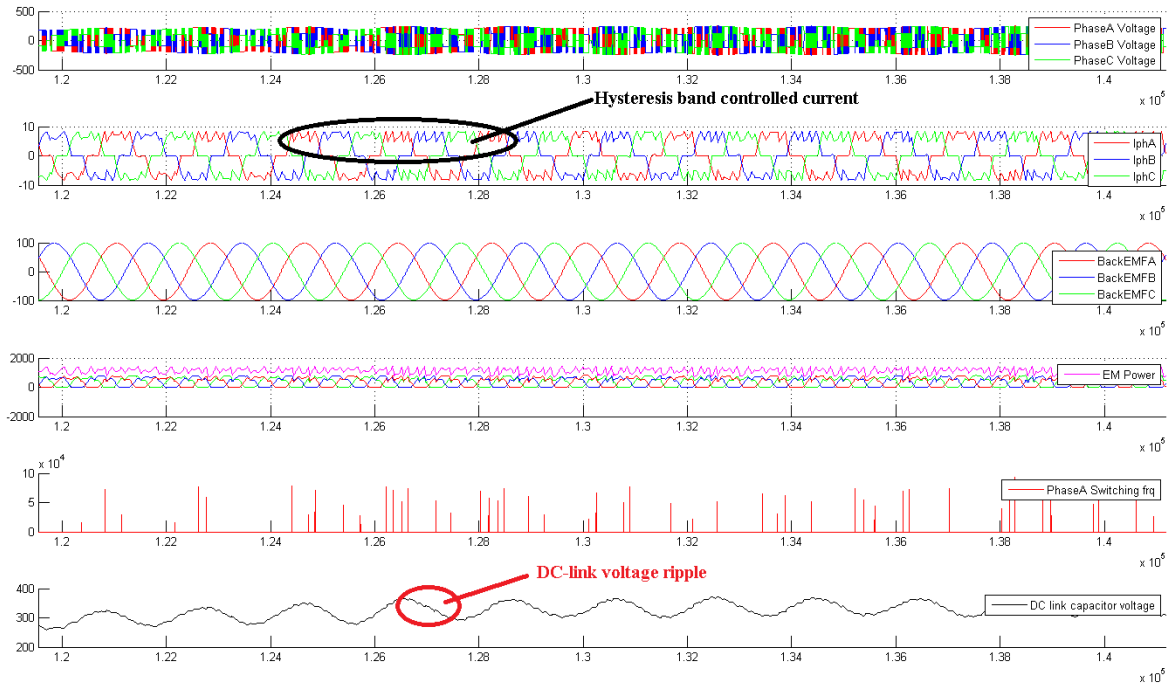

Figure 6-33: Plotted motor system simulation results

magnet temperature	90	oC	(90oC rated)										
Magnet temp coefficient	-0.11	%											
EMF tolerance			10%			Nom.			-10%				
Inductance Tolerance			+10%	Nom.	-10%	+10%	Nom.	-10%	+10%	Nom.	-10%		
Phase Resistance			2.1	2.1	2.1	2.1	2.1	2.1	2.1	2.1	2.1		Ω
Phase Self-Inductance			0.00025	0.000228	0.000205	0.00025	0.000228	0.000205	0.00025	0.000228	0.000205		H
Phase Mutual-Inductance			-9E-05	-8.1E-05	-7.3E-05	-9E-05	-8.1E-05	-7.3E-05	-9E-05	-8.1E-05	-7.3E-05		H
System Input Power			749.39	755.63	768.36	737.34	752.57	761.08	723.07	731.06	741.65		W
Input Power Difference Rate			99.92%	100.75%	102.45%	98.31%	100.34%	101.48%	96.41%	97.47%	98.89%		%
Shaft Output Power			655.41	661.35	671.71	640.25	652.80	659.07	620.60	626.93	635.08		W
System Efficiency			87.46%	87.52%	87.42%	86.83%	86.74%	86.60%	85.83%	85.76%	85.63%		%

Figure 6-34: System simulation results for optimal motor design with ±10% inductance tolerance

On the other hand, the drawback of current hysteresis band control is also obvious. The FET gates switching frequency is extremely high, leading to the high device switching losses. Whilst the defined current hysteresis band is acceptable for trapezoidal current control (BLDC motor), for a permanent magnet synchronous motor (PMSM) with sinusoidal currents, the current band value has to be dynamically changed along with the varying of the sinusoidal current waveform.

Chapter 7 : Built of Prototype Motor

This chapter demonstrates the manufacturing and assembly of the prototype motor, based upon the chosen design.

7.1 Build of rotor

Figure 7-1 displays the hot extruded, ring-shaped, neodymium-iron-boron magnet with a 10.7mm overall outer diameter and a 7.9mm inner diameter. On the outer surfaces of the magnet, there is a 0.2mm thickness coating of nickel powder to protect the magnet from oxygenation. The permanent magnet has been magnetised to have 1.2T residual flux density in a radial magnetisation pattern. The following Figure 7-2 shows the measurement of the magnetic properties of the rare-earth magnet using a gauss meter. The values of the air-gap magnetic flux density produced by the magnet in isolation are measured in the middle of the magnet, 0.2mm away from the magnet outer surface along the magnet circumferential direction. The attained open-circuit air-gap flux density values are then directly compared with the finite-element analysis as shown in Figure 7-3. This comparison is to evaluate the manufacturing tolerance of the effective magnet magnetisation. The graph indicates that there is approximately 2.5% difference in the average air-gap flux density between the measured data and the finite-element simulated results. The biggest difference in amplitude occurs at the regions of the pole edges.

As discussed in Chapter 3, for radially magnetised magnets, there is a large amount of flux leakage between two magnetic poles when a large air-gap exists, especially in those areas adjacent to the magnet outer surface. Owing to the actual manufacturing process, the measured air-gap flux density has smaller amplitude near the pole edges compared to the simulated values. To be specific, the actual magnet is shaped via a hot extrusion process firstly to form the integrated annular shape, and then magnetised separately after moulding. It is magnetised from a fixed starting point on the outer surface of the ring-shape magnet with controlled values of the maximum magnetic flux density, moving along the circumferential direction until reaching back to the original starting point. However, due to the limits of utilised manufacturing

technique, at the regions between two magnetic poles, the achievable amplitude of the peak flux density are restricted to be smaller than the analytically designed values.

In order to eliminate differences between simulated and actual magnets, some parts of the magnet in the regions of the pole edges are removed from the drawn 3-dimensional model in the finite-element simulation. Figure 7-4 demonstrates the revised magnet model in the simulation. The figure shows that there are four sectors removed from the annular shape magnet on the pole edge areas. These regions are 10-degrees wide at the inner radius and 20-degrees at the magnet outer radius. The following Figure 7-5 compares the open-circuit air-gap flux density values from both the actually built magnet and the updated finite-element simulation model in the position of 0.2mm away from the magnet outer surface along the magnet circumferential direction. The amplitudes of the maximum and the minimum as well as the average air-gap flux densities match well, indicating that the update of the finite-element simulation model helps to minimise the error between the simulated and measured results.

Figure 7-1: Produced ring-shape rare-earth permanent magnet

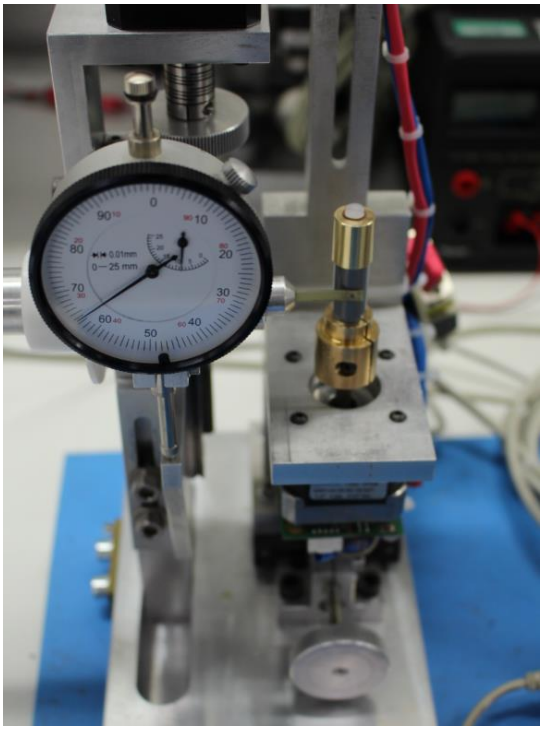

Figure 7-2: Measurement of magnetic properties of produced magnet

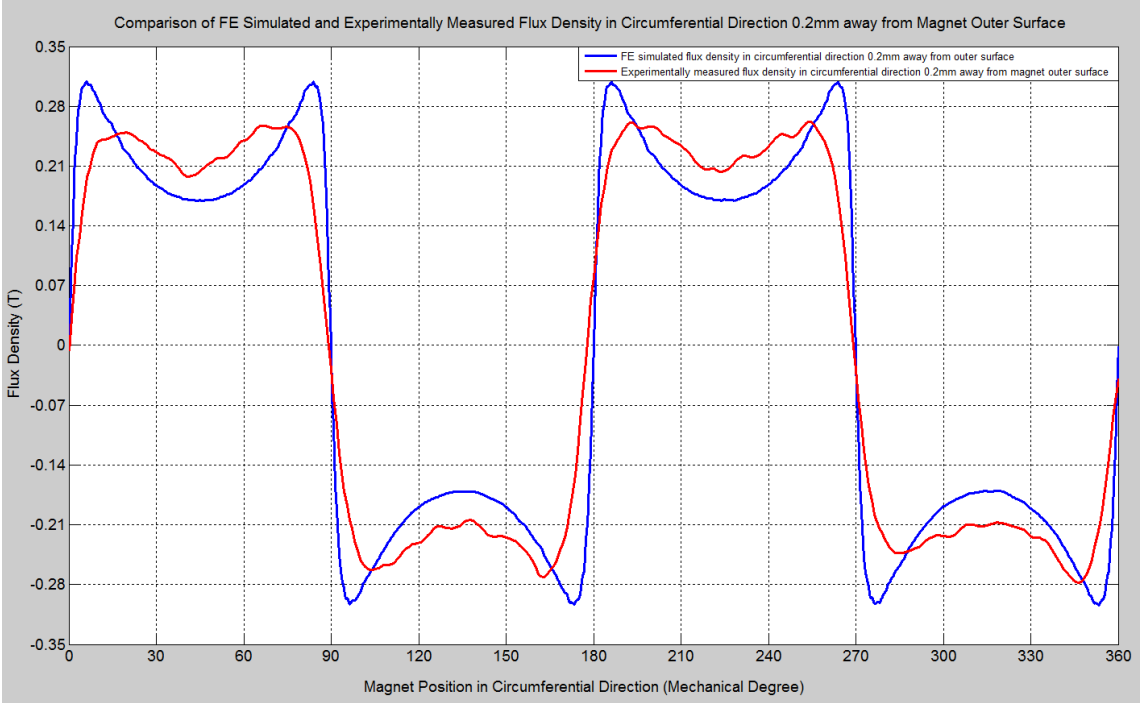

Figure 7-3: Comparison of the FE simulated and the actually measured open-circuit air-gap flux density values at the position of 0.2mm away from magnet outer surface along the circumferential direction

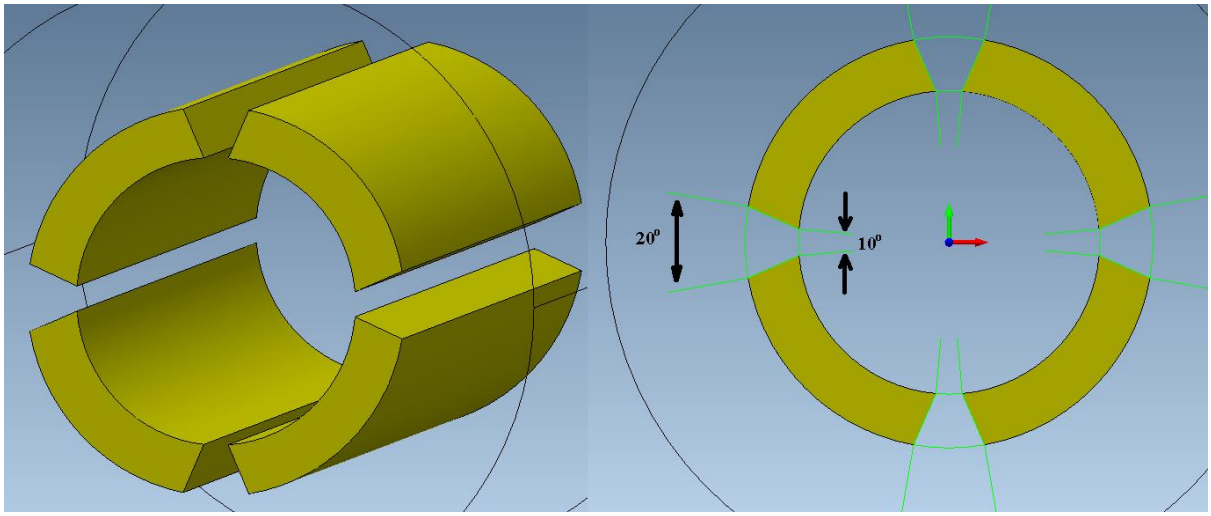

Figure 7-4: The updated 3-D magnet model in FE simulation

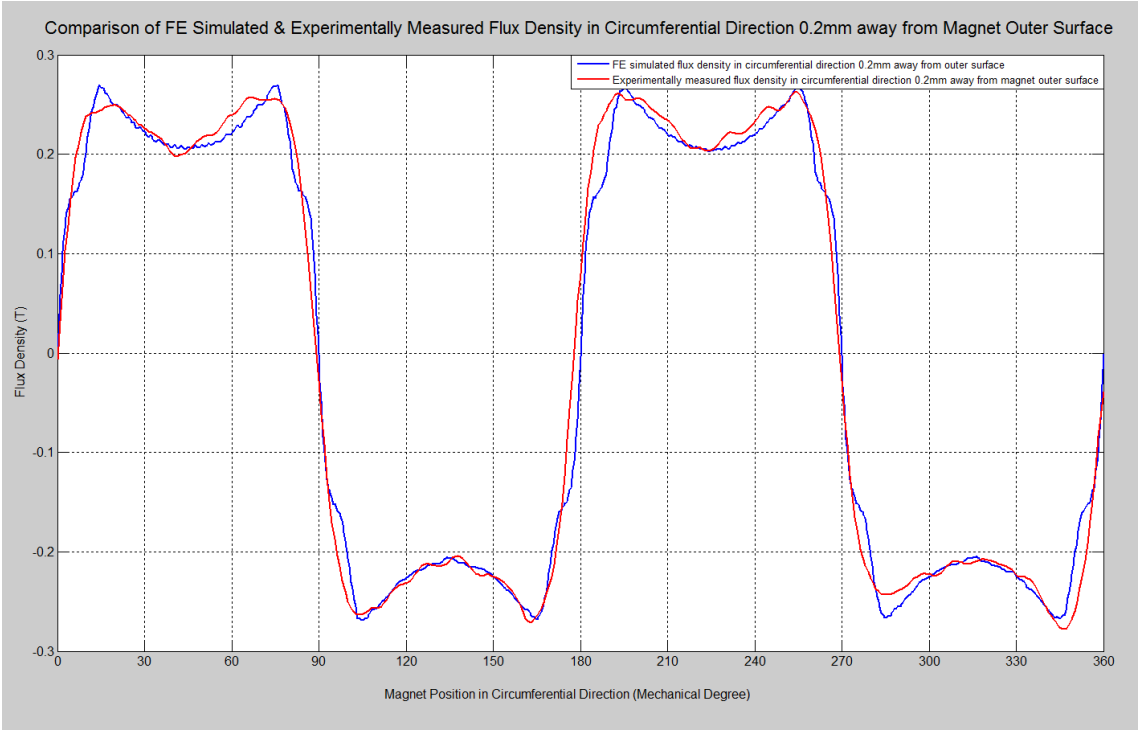

Figure 7-5: Comparison of the open-circuit air-gap flux density values achieved from the updated magnet model in FE simulation and the actually built magnet at the position of 0.2mm away from magnet outer surface along the circumferential direction

Figure 7-6 displays the assembled rotor with the glued ring-shape permanent magnet. Ultraviolet light cured glue was utilised to bond the ring-shape magnet to the stepped cold-rolled steel made shaft, delivering a 0.15mm thickness adhesive layer between the two

components. The following Figure 7-7 illustrates the two machined stainless steel motor housing parts with twelve holes on their axial ends. The purpose of these holes is to allow cooling air to flow through so that the capability of the heat dissipation of the armature coils can be enhanced. Besides, these holes allow the winding terminals to connect to the separate control board.

On each housing part, there is a 13mm wide, 5mm deep slot at the centre of the axial side cap to fit high-speed ball bearing. Figure 7-8 shows that, before the fully assembling of the motor housing, one high-speed bearing is fitted on the female part of the motor steel housing while another one is glued on the shaft of the assembled rotor.

Figure 7-6: Fully assembled rotor

Figure 7-7: Two parts of machined motor outer housing

Figure 7-8: The assembled high-speed bearings

Due to the unavoidable manufacturing tolerances of the hot extruded ring-shape magnet and the machined stepped rotor shaft as well as the glued ball bearing, it is significant to balance the fully assembled rotor to minimise the impact of the generated rotor unbalanced force during high-speed operating. Figure 7-9 below illustrates the assembled prototype rotor in the balancing test. The rotor was held by two parallel placed V-shape plates to keep it level throughout the test. An electrically driven elastic belt was linked to the rotor to drive it from the static state to a speed of 3000 revolutions per minute. Once the rotor reached the required speed, it was significant to maintain the operation for over three minutes to ensure the rotor has reached steady state. During rotation, the transient unbalanced forces induced on each side of the rotor were measured and recorded by the test rig automatically.

In order to reduce the undesirable unbalanced forces, there are two approaches normally selected: one is to remove material from the heavier side; the other is to add additional mass on the lighter side. Figure 7-10 below demonstrates the added extra weight on the rotor shaft to reduce the generated unbalanced forces. The following Figure 7-11 displays the measured values of the induced unbalanced force on each side of the rotor after balancing. The force numbers on the screen, 14.2mg.mm and 13.2mg.mm, indicates that the tested prototype rotor has achieved a high level of balance.

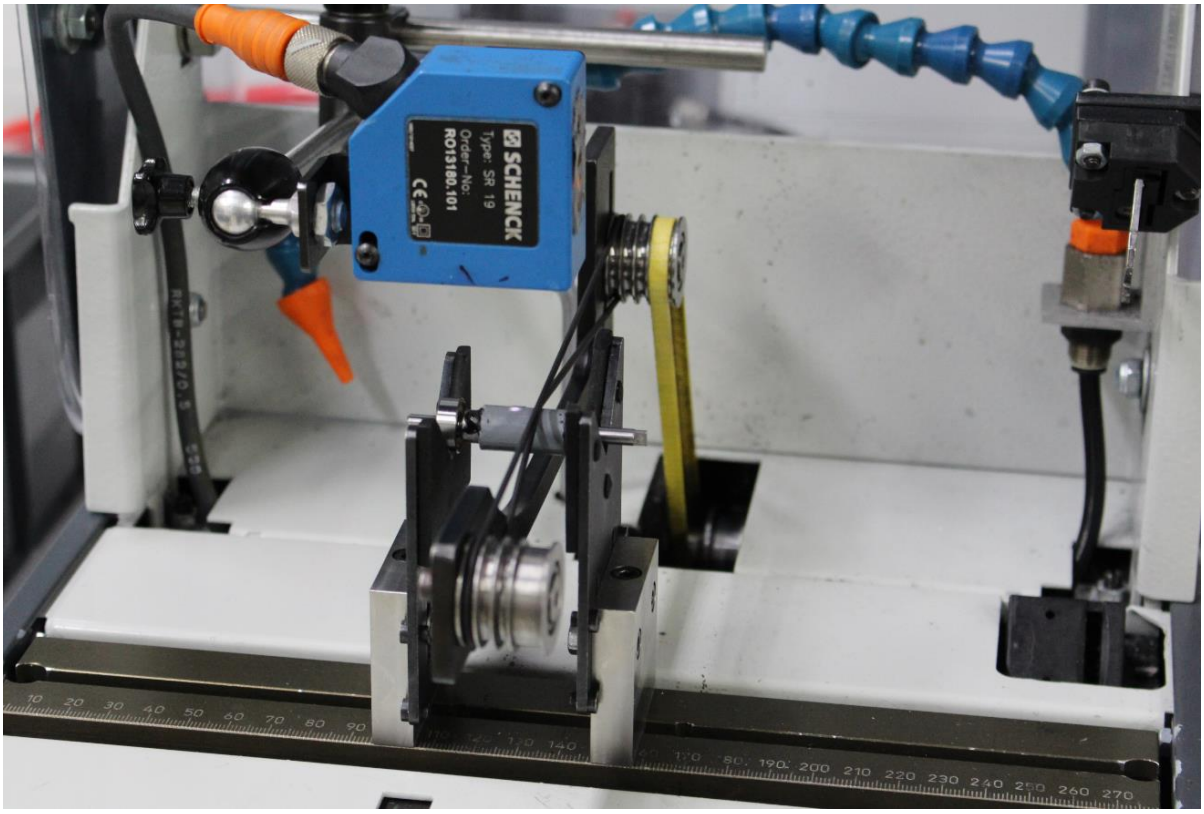

Figure 7-9: Rotor under balancing test

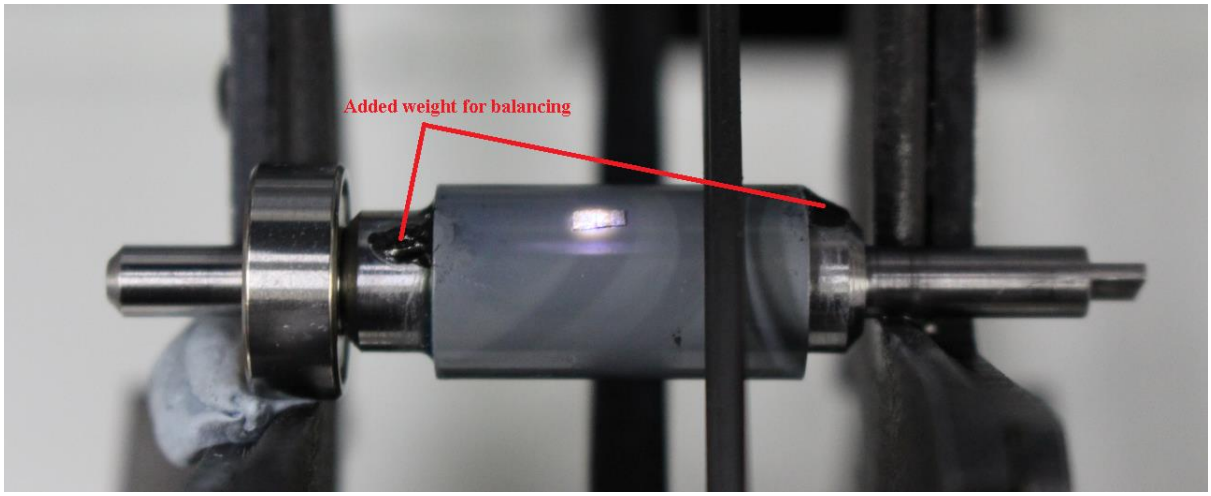

Figure 7-10: Added weight for balancing on the rotor shaft

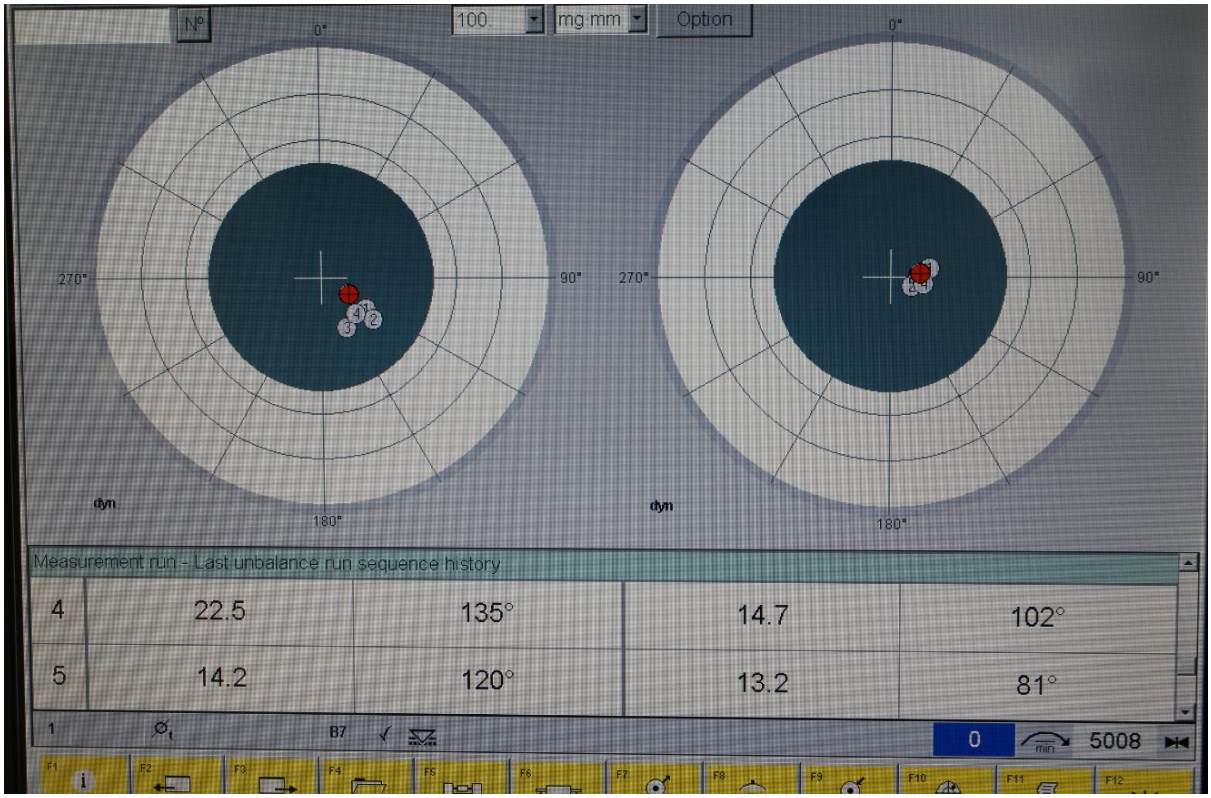

Figure 7-11: Measured unbalanced force after the compensation of unbalancing

7.2 Build of stator

According to the selected design, the wire diameter was set to be 0.28mm, excluding the thickness of enamel layer. To produce a compact coil with a high slot filling factor of over 73% and a rigid construction, an extra layer of polyamide aliphatic bond coating was chosen to give the feature of self-bonding. Consequently, the overall outer diameter of the chosen wire is slightly thicker than the standard wires, at 0.331mm. When heating up the wires to over 170°C, the chemical reaction on the bond coating will firmly stick the wires together to each other. After cooling down the coils, the built coils will become solid, and remain so at temperatures of up to 180°C. As the wire electrical insulation class defined by UL and IEC for the chosen wire is Class F, i.e. 155°C, the wire will always operate in a temperature region where there is no risk of loss of integrity.

Furthermore, as it is difficult and costly to manufacture a traditional toroidal winding especially for a small size motor, a segmental stator is introduced to eliminate the need for expensive toroidal winding equipment. In this research, the original ring-shape slot-less stator is evenly split into two pieces, as shown in Figure 7-12. Regarding the laminated stator, it was made by 0.2mm thickness silicon steel which are glued together first and then wire-cut to the designed shape and dimensions.

Additionally, in order to create electrical insulation between the laminated stator and the toroidal windings, a thin and transparent layer of silicone conformal coating is sprayed on the outer surfaces of the stator and cured for 12 hours in the oven at 120°C to make it solid.

Figure 7-12: Two half-ring shape stator parts

7.3 Build of coil

A winding mould is designed and constructed to help to wind the stator coils independently, and can be heated up to the required curing temperature of over 170°C to activate the wire self-bonding ability. Figure 7-13 shows the individual components of the winding mould while the following Figure 7-14 illustrates the fully assembled mould.

Figure 7-13: Components of the designed winding mould

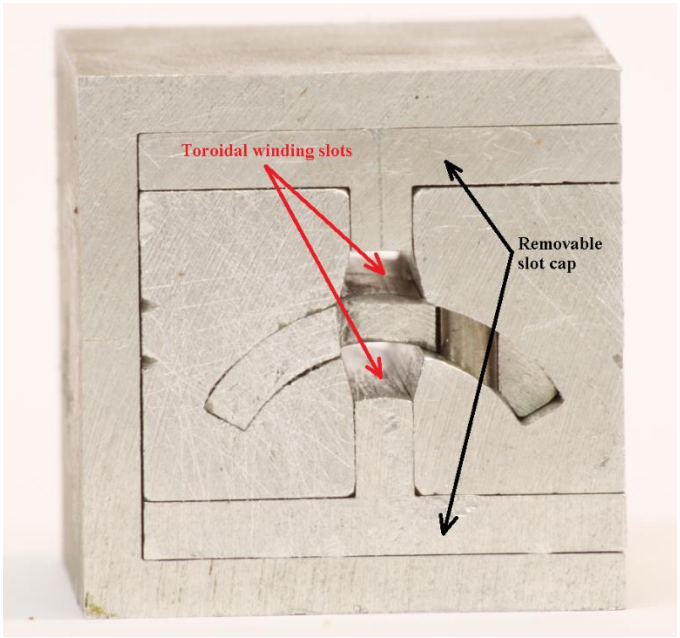

Figure 7-14: Completely assembled winding mould

Figure 7-15 displays one toroidal coil after the curing process. Six identical coils have to slide on the laminated half-ring shape stator to construct half of the fully assembled stator, as shown in Figure 7-16-(a), while Figure 7-16-(b) illustrates the completely assembled stator. The following Figure 7-17-(a) shows the machined plastic supporting cage which provides physical support between the laminated stator and the steel motor housing. This light-weight and non-conductive plastic cage gives both physical support to the stator and increases the gap between the coils and the motor housing to decrease the induced Ohmic loss in the steel made housing. Figure 7-17-(b) illustrates the assembled stator inside the plastic supporting cage.

Figure 7-15: Actually built single toroidal winding coil

(a) Assembled half stator (b) Completely assemebled stator

Figure 7-16: (a) Assembled half stator; (b) Completely assembled stator

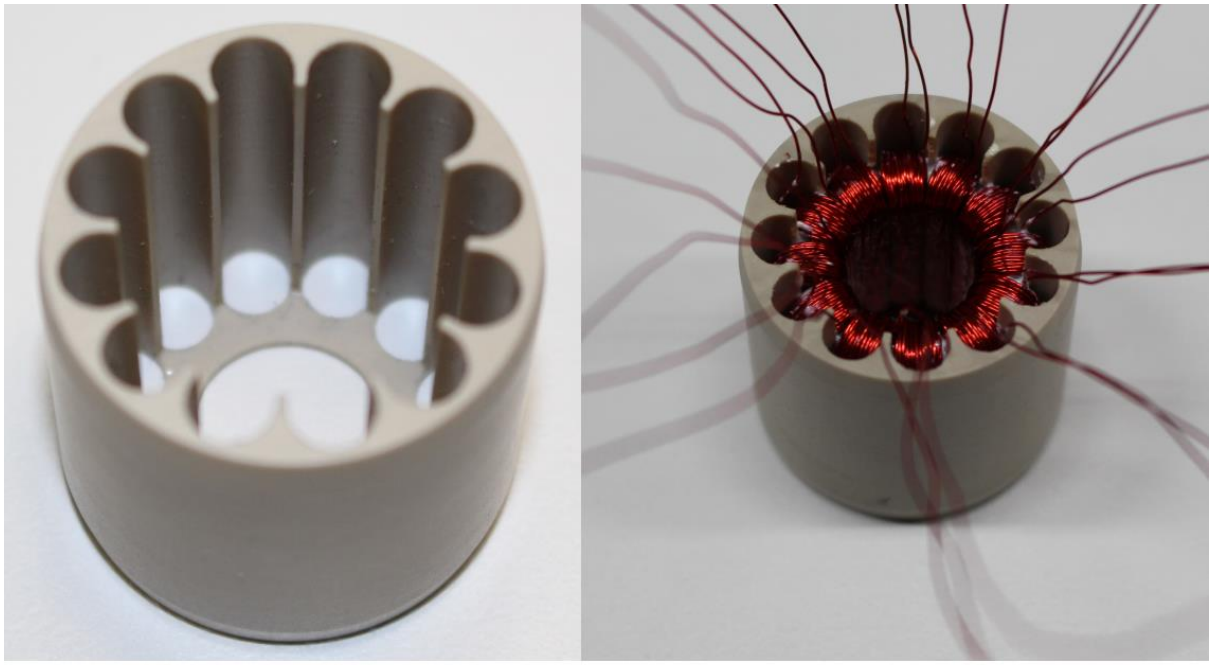

(a) Plastic made stator supporting cage (b) Assembled stator inside the plastic cage

Figure 7-17: (a) Plastic made stator supporting cage; (b) Assembled stator inside the plastic supporting cage

7.4 Motor assembling

At the final step, the plastic supporting cage with the fully assembled stator is inserted into the machined steel motor housing, as shown in Figure 7-18. Winding terminals are individually labelled and put through the corresponding housing holes. The next Figure 7-19 demonstrates the top and the side views of the completely assembled prototype motor.

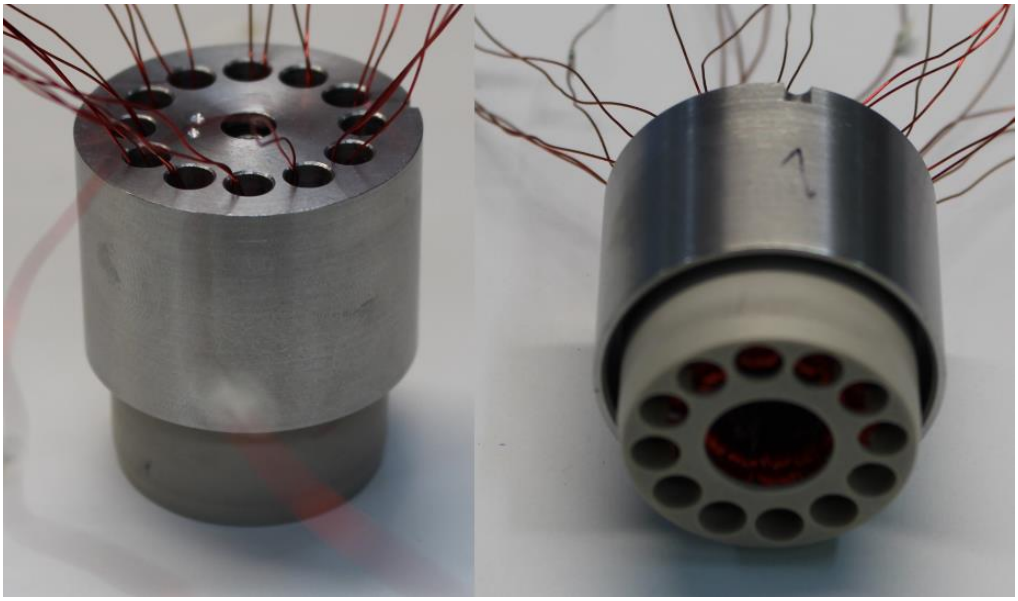

Figure 7-18: Assembled motor housing with the plastic supporting cage

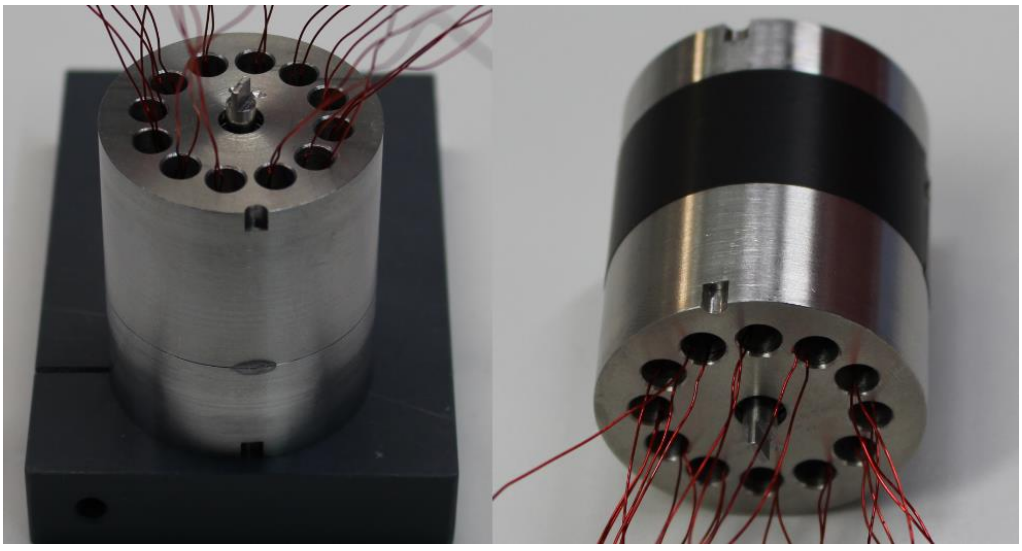

Figure 7-19: Completely assemble prototype motor

7.5 Summary

This chapter has described the complete manufacturing and assembly procedures for the built prototype motor. The manufactured 4-pole, ring shaped permanent magnet features several regions between the magnetic poles that has not been fully magnetised. A finite element simulation can be conducted and achieve very closely matched open-circuit air-gap flux distribution after correcting for this effect in the simulation.

The next chapter will demonstrate the test of the built prototype motor and compare measured and simulated results.

Chapter 8 : Test of Prototype Motor

This chapter systematically demonstrates the achieved practical test results from the fully assembled prototype motor, including measurements of phase resistance and coil inductance, a voltage surge test to verify coil turn-to-turn insulation quality, thermal performance measurement of the built phase windings and validation for the targeted motor electromagnetic characteristics.

8.1 Phase resistance measurement

In order to precisely measure the coil resistance, a high precision milliohm meter was utilised. Before the start of the test, the meter was calibrated under both open-circuit and short-circuit conditions. Based upon theoretical analysis, it predicts a resistance per coil of 1.19Ω. Considering the manufacturing tolerance in the manual coil winding, a ±5% error between simulated and measured values was considered acceptable, when including the end-windings effect upon the total winding resistance.

Table **8-1** gives measured values for each coil, whilst Figure 8-1 illustrates the percentage difference from predicted values. All the twelve coils have a higher resistance than the predicted value, however, the error values is still within the acceptance level of the tolerance at no more than 5%.

Phase A	**#1**	**#2**	**#3**	**#4**
[Ω]	1.235	1.225	1.2495	1.23
Phase B	**#5**	**#6**	**#7**	**#8**
[Ω]	1.235	1.225	1.245	1.23
Phase C	**#9**	**#9**	**#10**	**#12**
[Ω]	1.245	1.2495	1.245	1.22

Table 8-1: The measured resistance values for each motor coil

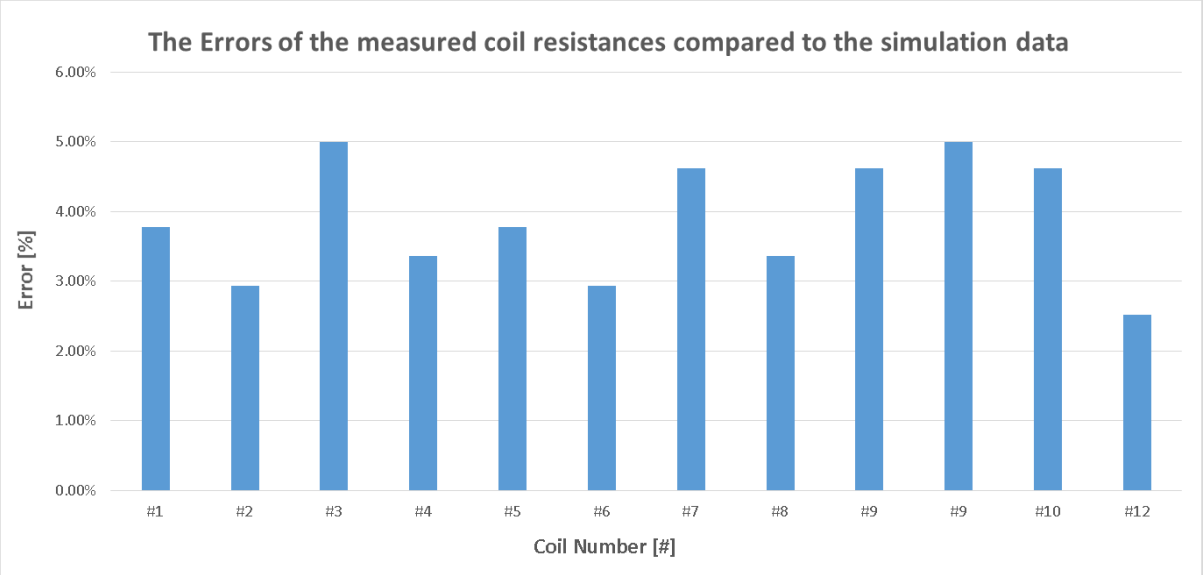

Figure 8-1: The errors of the measured coil resistances compared to the targeted simulation data

8.2 Voltage surge test

Based upon above results, it proves that all the built coils are within the targeted specification with respect to the winding resistance. However, the resistance alone cannot guarantee that there is no insulation damage within a coil. Such damage may only result in the coil breakdown at high voltages and so a voltage surge test was conducted.

The voltage surge test injects a high amplitude voltage pulse for a very short time, creating a potential difference between one turn and the next. Turn-to-turn insulation faults can then be revealed by changes in the capacitance or resistance of the winding. Normally, the surge test system utilises the results from one known healthy coil as a base, and then compares the results of every other coil with this one. With no wire fault, the tested coils should deliver a matching responding waveform.

Figure 8-2 below illustrates the block diagram of the general surge test system. To start a surge test, the main capacitor is charged to a known voltage, and then connected across the tested coil for an extremely short time. As the constructed LCR circuit is purposely designed to be underdamped, oscillation of the coil terminal voltage occurs and will be recorded.

In this work, a Baker Surge Tester is utilised. According to IEEE Std-522-2004[98], as the nominal line voltage of the designed motor is 380V, the amplitude value of the applied voltage surge is set to be 1010V.

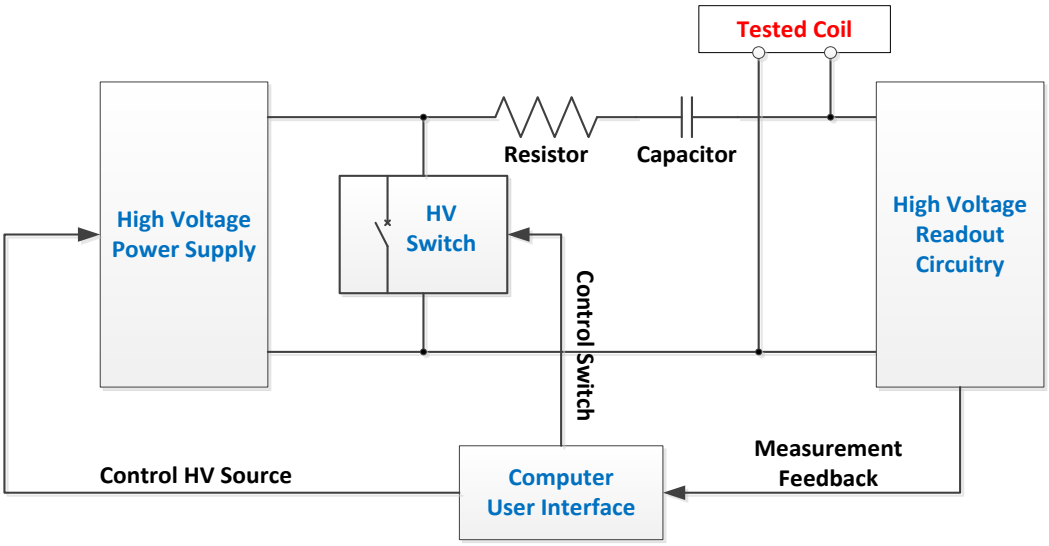

Figure 8-2: The block diagram of the general surge test system

Figure 8-3 illustrates the recorded terminal voltage oscillations for the tested coils in the conducted surge test. The graph shows that most of the built winding coils have a matching voltage response, but there are two coils, highlighted by the red circle, which do not. This outcome indicates that these two coils have a hidden winding failure, despite having the same DC resistance. Both of these winding coils, therefore, have to be replaced.

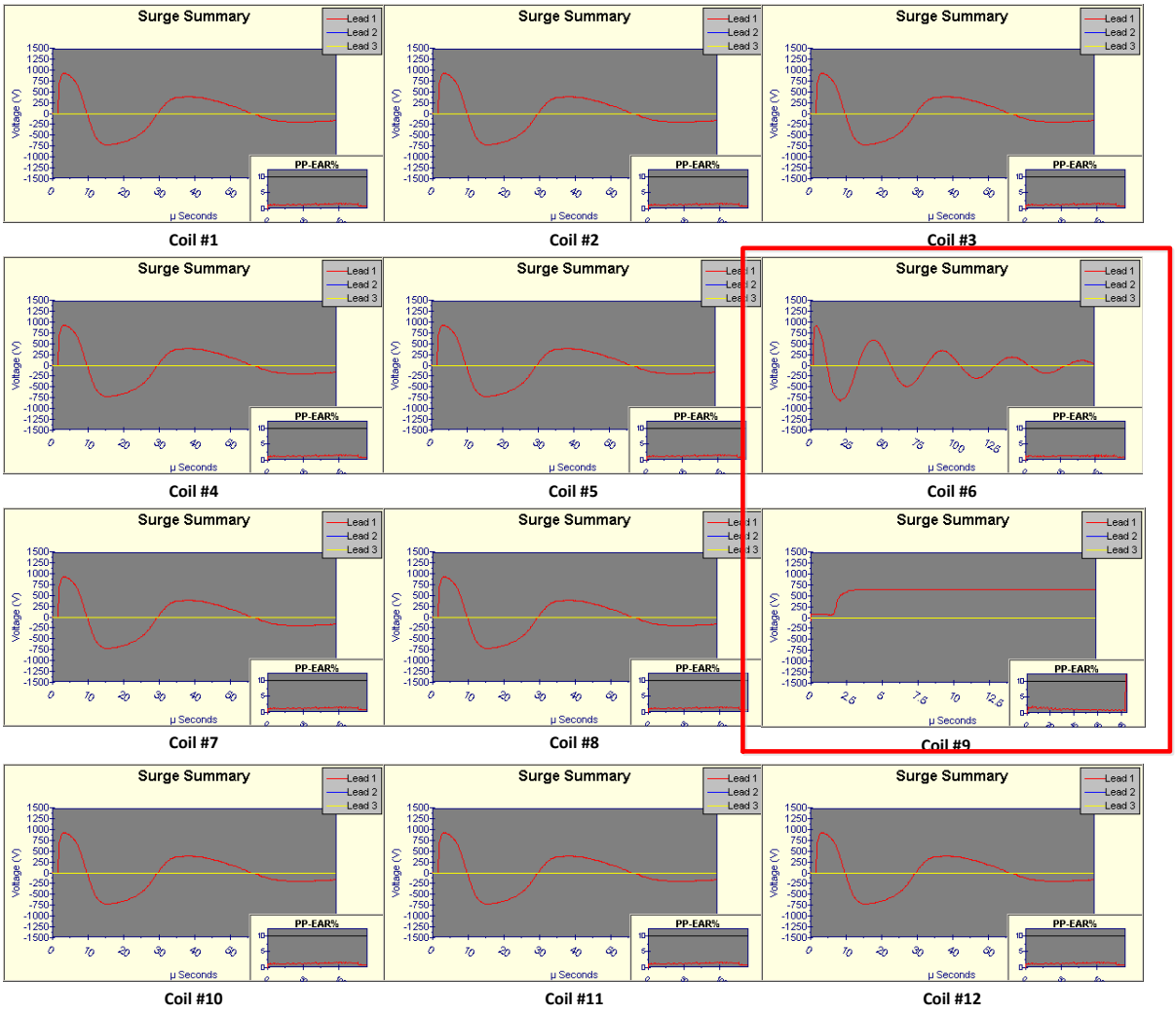

Figure 8-3: The screenshots of the recorded voltage oscillations in the carried out voltage surge test for the built coils

8.3 Coil inductance measurement

Each coil should have the same nominal inductance value which has to be individually measured as a further check of winding integrity. A ±10% variation was considered acceptable in this work.

It has to be noted that, when the rotor is present, the magnetic field of the utilised permanent magnets can influence coil inductance due to saturation effects. Depending upon the position of the rotor with respect to each coil, the rotor can either increase or reduce magnetic saturation. For this reason, the phase inductance measurement was conducted without the permanent magnet assembled in the machine. From a high resolution 3-D finite element simulation, the coil inductance was predicted to be 0.227mH. Magnets were removed by setting them to have zero magnetic coercivity, as shown in Figure 8-4.

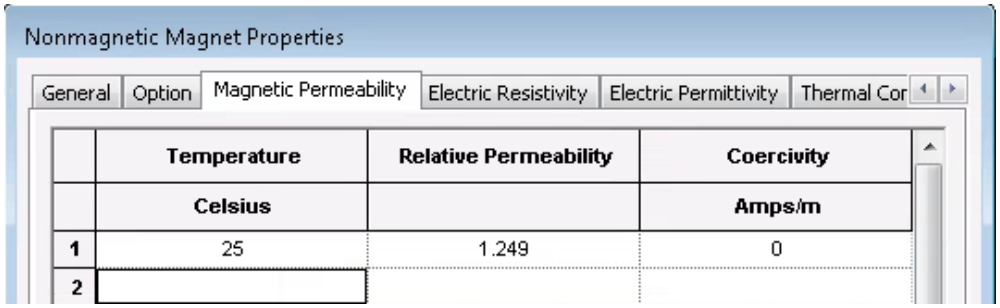

Figure 8-4: The set zero coercivity in the finite element simulation

To implement the measurement of phase inductance, it requires to connect each coil to a voltage pulse generator. The peak value of the applied voltage pulse was adjusted to be capable of delivering over 15A maximum current during the test. A high bandwidth oscilloscope is utilised to measure both the voltage across each coil and the current through it. Figure 8-5 below demonstrates a schematic drawing of the phase inductance measurement rig.

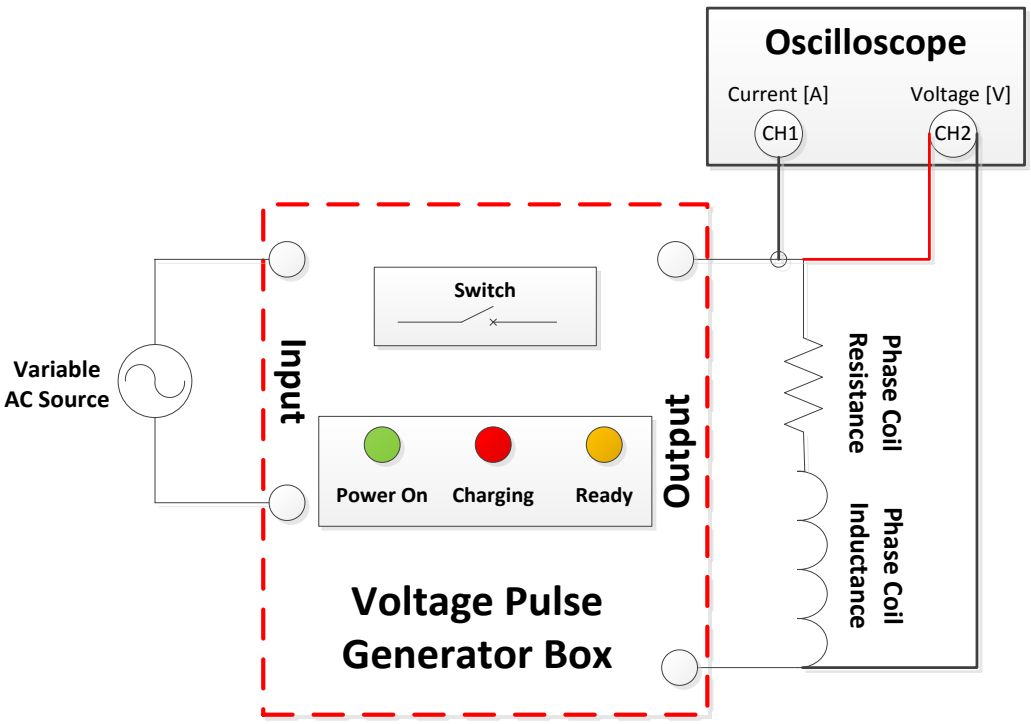

Figure 8-5: The schematic drawing of the connected phase inductance measurement rig

The following Figure 8-6 illustrates an example of the captured voltage and the current waveforms under a given voltage pulse. To ensure the accuracy of oscilloscope measurements, it is compulsory to degauss the current probe and zero-calibrate the voltage probe before the test. Moreover, it has be noted that, the amplitude value of the voltage pulse cannot be excessively high as it can cause magnetic saturation in the stator laminations, leading to inaccurate inductance measurements.

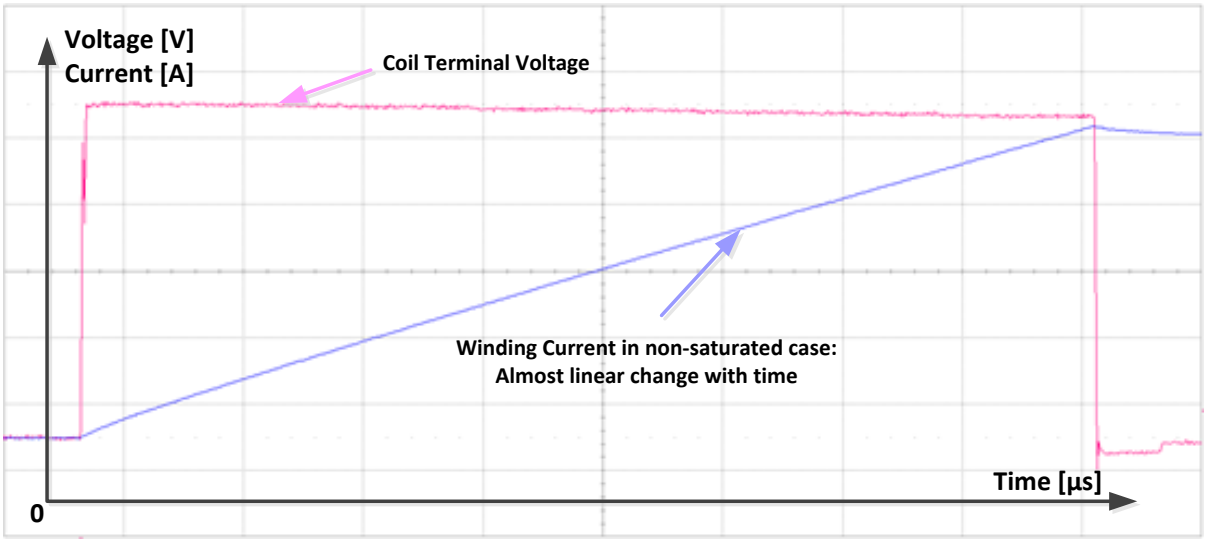

Figure 8-6: An example of the captured voltage and current waveforms after the applied voltage pulse with no magnetic saturation in the stator lamination

Based upon the captured voltage and current waveforms as well as the known resistance value of the coil, the phase inductance can be calculated over the complete period of the measured terminal voltage pulse. The coil inductance is derived from the flux linkage characteristic, as Equation 8-1. The symbol N is the coil number of turns; $\emptyset$ is the created magnetic flux per turn; φ is the coil flux linkage and i is the current flowing through the coil.

$$L_{phase} = N\frac{d\emptyset}{di} = \frac{d\varphi}{di} \qquad (8-1)$$

The coil flux linkage value is obtained using Equation 8-2, in which V is the measured coil terminal voltage, R_{coil} is the effective phase resistance and $i(t)$ is the transient coil current value at the time "t".

$$d\varphi = (V_{coil} - i(t) * R_{coil})dt \qquad (8-2)$$

Figure 8-7 below illustrates the calculated coil flux linkage as a function of the increasing driving current. The graph indicates that the induced coil flux linkage is linearly increased along with the rise of the coil current until it reaches the saturation region.

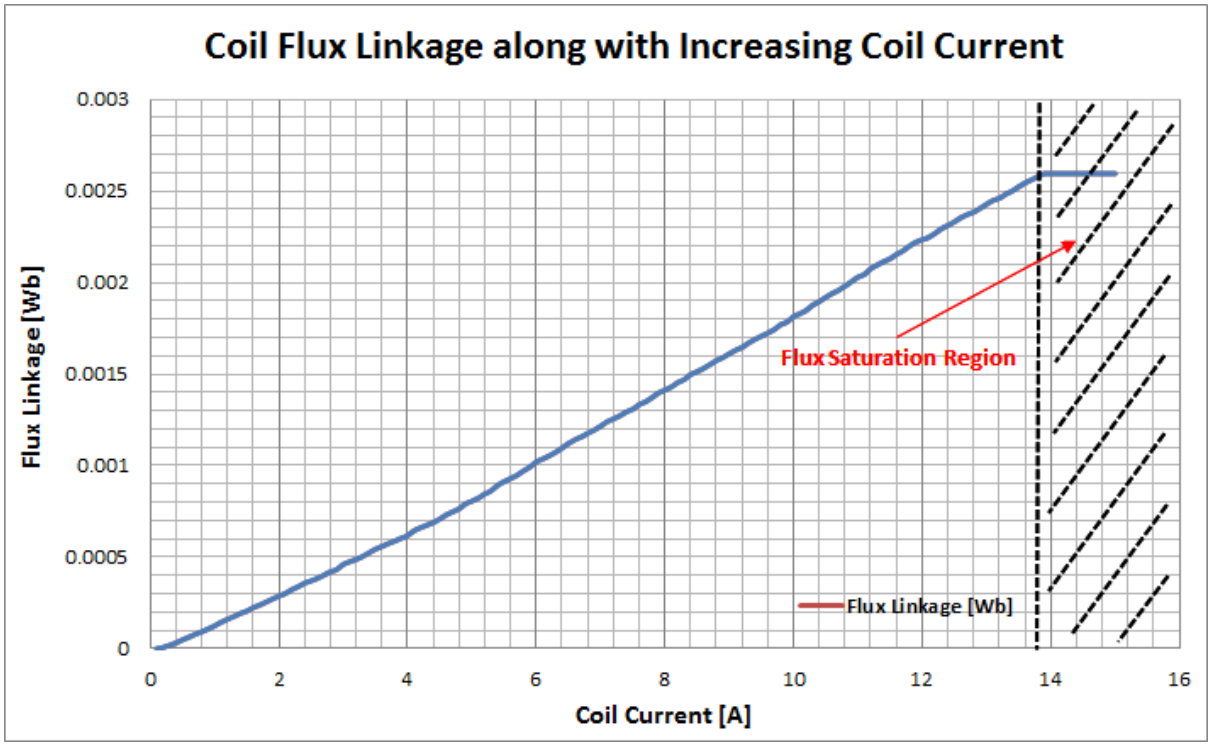

Figure 8-7: Calculated coil flux linkage along with increasing coil current

Based on the plotted coil flux linkage curve, the corresponding coil inductance is obtained. Figure 8-8 illustrates the coil inductance value as a function of coil current. The flux saturation region and the designed nominal operating current region have been highlighted by the black and the green coloured crosslines respectively. The graph proves that there is adequate headroom for the operating current before it reaches the saturation area. The recorded phase inductance value is achieved by the arithmetic mean value of the calculated incremental phase inductance values in the designed nominal operating current range.

Table 8-2 summarises the measured phase inductance for the built prototype. From the table, the actual coil inductances for all three phases are lower than the FE simulation results. This may due to the following three causes.

1. The real phase resistance is higher than that in the ideal finite element simulation;
2. The raw oscilloscope current data is filtered using a 101-point moving average system, which will inevitable produce an element of error.

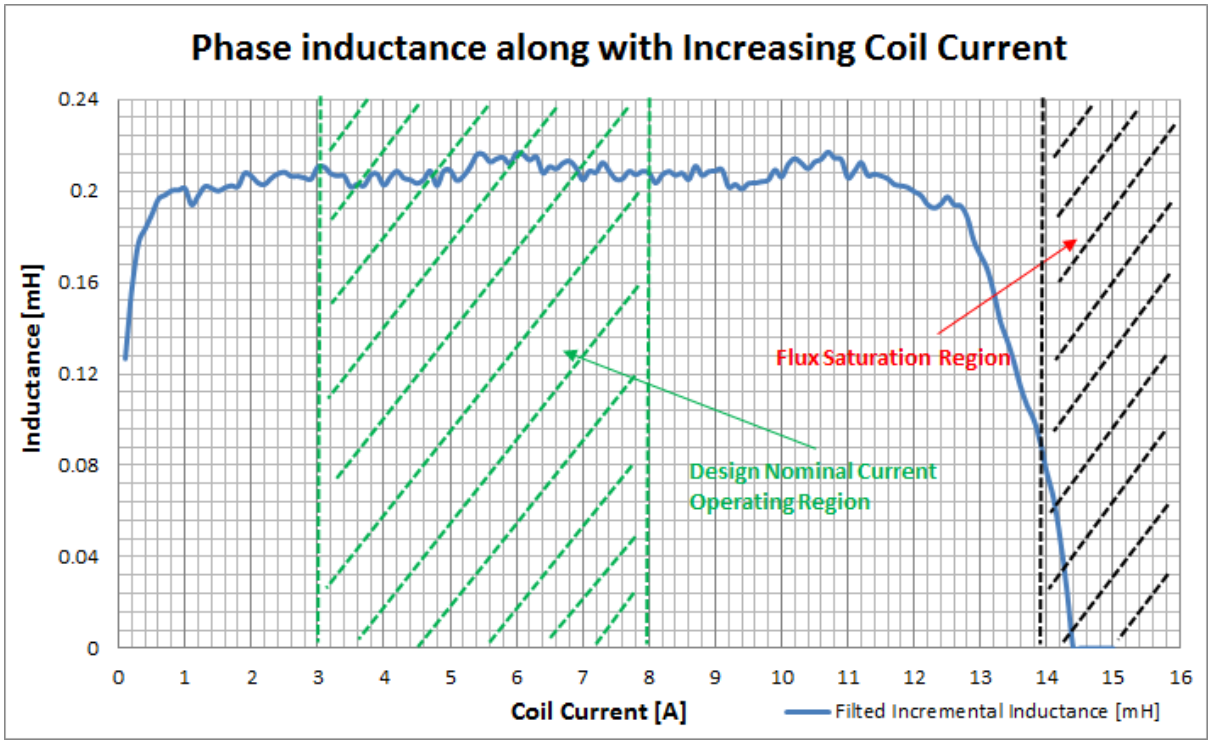

Figure 8-8: The achieved coil inductance along with the increasing coil current

Targeted Phase Inductance [mH]	0.227	Error Band [%}
Measured Phase A Inductance [mH]	0.2087	8.062%
Measured Phase B Inductance [mH]	0.2079	8.414%
Measured Phase C Inductance [mH]	0.2082	8.282%

Table 8-2: The calculated phase inductance value for each phase

8.4 Winding thermal measurement

This section examines the actual winding thermal performance under the different cooling conditions. In domestic applications, both the entire motor and the motor components are required to operate within the thermal limits throughout the operation. For the given electrical loading, different cooling conditions can result in the different motor thermal behaviours due to varied thermal dissipation. For naturally ventilated machines at 25°C ambient temperature, the maximum phase current density is typically less than $10\boldsymbol{A/mm^2}$ for Class F wire. With the designed phase current density value of $25\boldsymbol{A/mm^2}$, it is compulsory to introduce the forced air cooling to ensure that temperature limits are not exceeded. Furthermore, in order to evaluate the thermal impact of both iron loss and proximity loss, the effective current density in the test is boosted to $32\boldsymbol{A/mm^2}$.

Figure 8-9 below illustrates the structure of the assembled rig utilised to test the winding thermal performance. With the support of this rig, the corresponding winding temperatures can be measured when varying the flow rate of the forced cooling air. During this test, the prototype motor windings are powered with DC current to achieve the designed $32\boldsymbol{A/mm^2}$ phase current density. Two thermocouples are glued on the surface of the phase coils to monitor the real-time winding temperature. Furthermore, in order to ensure the forced cooling air only flows through the motor, the whole prototype is enclosed in a plastic tube, as shown in Figure 8-10. The inlet of the tube is connected to an adjustable valve which can control the flow. Also, an electric driven air blower is connected into the system to blow air from an air-box to the prototype motor. A manometer is used to estimate the real-time flow rate.

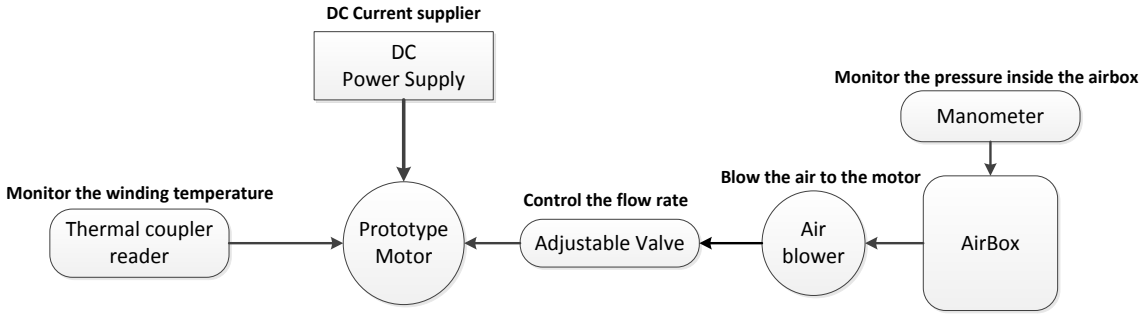

Figure 8-9: The built test rig for the validation test of the winding thermal performance

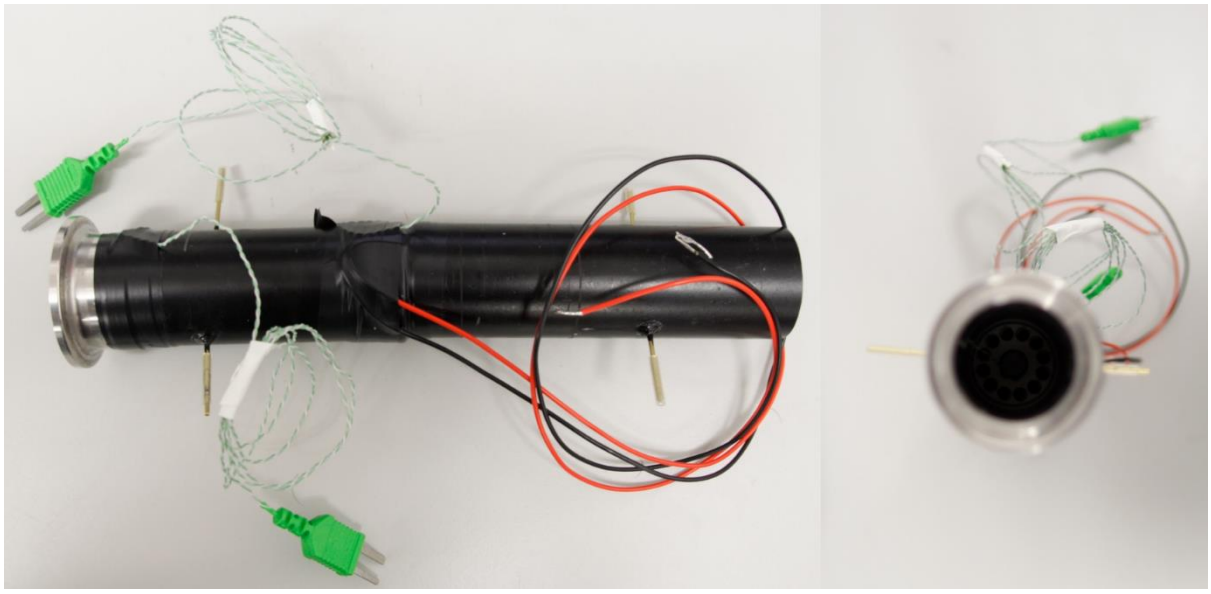

Figure 8-10: The utilised leakage tested tube with the enclosed prototype motor

Table 8-3 below demonstrates the test results of winding thermal performance under the different cooling conditions. The ambient temperature during the test is kept as 23°C with 17% humidity inside the test chamber. The listed air-in pressure is measured at the inlet of the connected air-box. Figure 8-11 below illustrates the positions of utilised thermocouples on the coil and the flow direction of applied cooling air, indicating that T2 is measured at the front end of coil under the direct cooling of air whilst T1 is located at the other end of coil with no direct cooling.

The achieved results show that, the current housing design can provide extremely strong cooling capability to keep motor winding temperature lower than Class B (130°C) in the nominal operational ambient temperature range of 0°C ~ 40°C, even under the lowest flow rate of less than 3 litres per second. Note that the conducted thermal test is imperfect as the utilised thermocouples were attached at the outer surface of coil. The more precise way to measure the winding temperature is either to bury the thermocouple inside the coil or to measure the coil resistance value.

Voltage [Vrms]	Pressure [kPa]	T rise [DegC]		Estimated flow rate (L/s)
	Air-in	T1	T2	
200	-0.112	21.8	21	9.9
200	-0.108	33.5	23.8	9.8
180	-0.0922	34.6	24	9
160	-0.0756	36.8	24.8	8
140	-0.0587	39.9	25.5	7
120	-0.0472	43.8	26.5	6.3
100	-0.033	50.6	28.1	5.2
80	-0.0201	65	31.2	4
60	-0.0088	80	39.2	2.6

Table 8-3: The obtained winding thermal performance under different cooling conditions

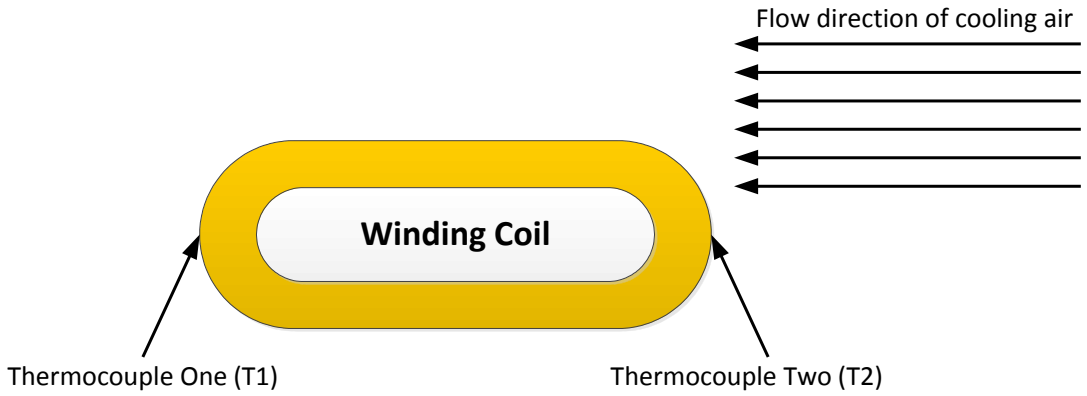

Figure 8-11: The positions of utilised thermocouples on the coil and the flow direction of applied cooling air

8.5 Validation for motor electromagnetic characteristics

8.6.1 Back-EMF measurement

The induced electromagnetic force can only be directly measured when there is no external voltage applied to the winding coils. In this work, the motor is rotated by an external source with open circuited phase coils and the induced back-EMF performance is monitored. Figure 8-12 below shows a schematic drawing of the assembled test rig for the conducted motor back-EMF measurement.

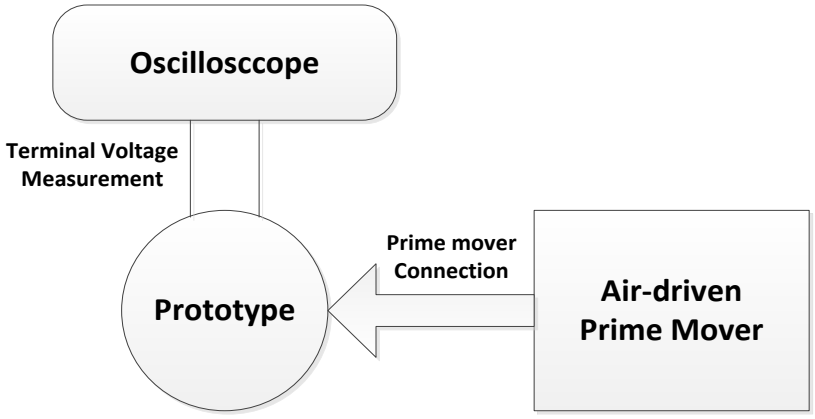

Figure 8-12: The schematic drawing of the assembled test rig

The prototype motor is rotated by an air-driven prime mover and the terminals of the phase coils are connected to a high precision voltage probe and linked back to an oscilloscope. The following Figure 8-13 shows the pneumatic prime mover which can control and provide the varied rotating speed from 10rpm to 200,000rpm by way of adjusting the output air pressure. Figure 8-14 demonstrates the connecting device between the shaft of the prototype and the air-driven spinner in the constructed test rig. Figure 8-15 illustrates the main body of the assembled test rig. The red rectangle shows the stainless steel motor mounting which encloses the motor and housing. The phase coil terminals are brought out through a hole at the bottom of the motor mounting as shown in Figure 8-15.

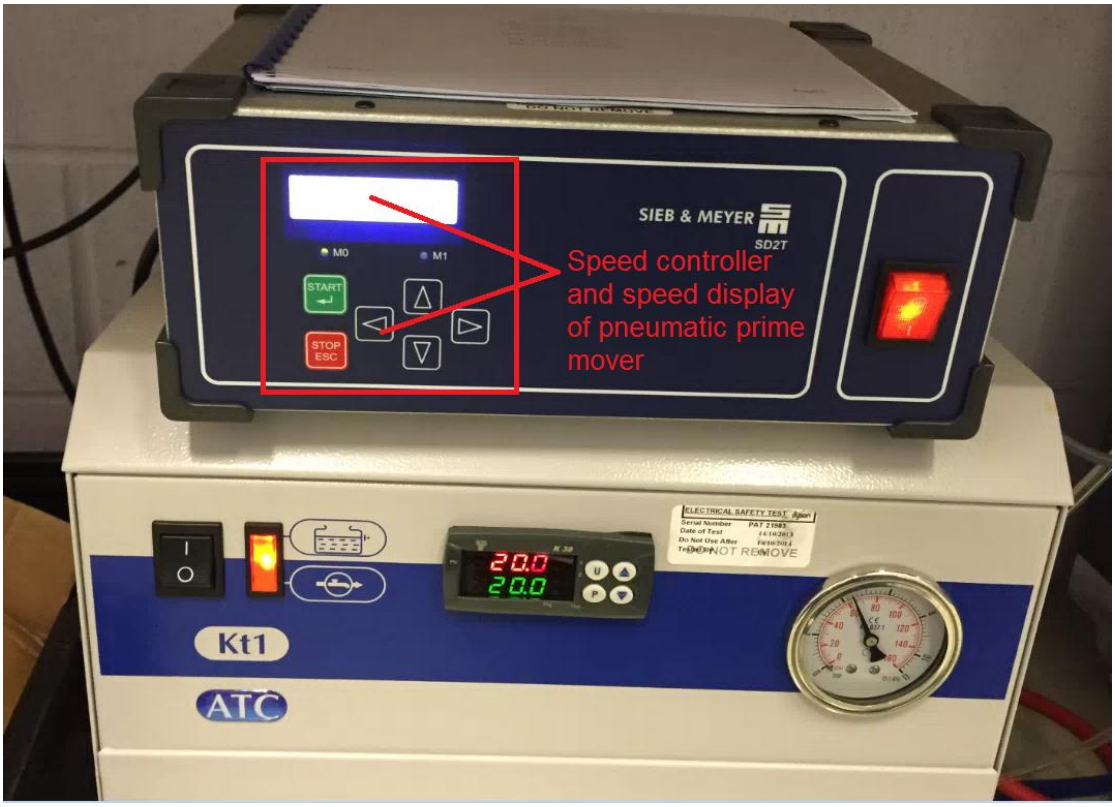

Figure 8-13: The utilised pneumatic prime mover with speed controller & display

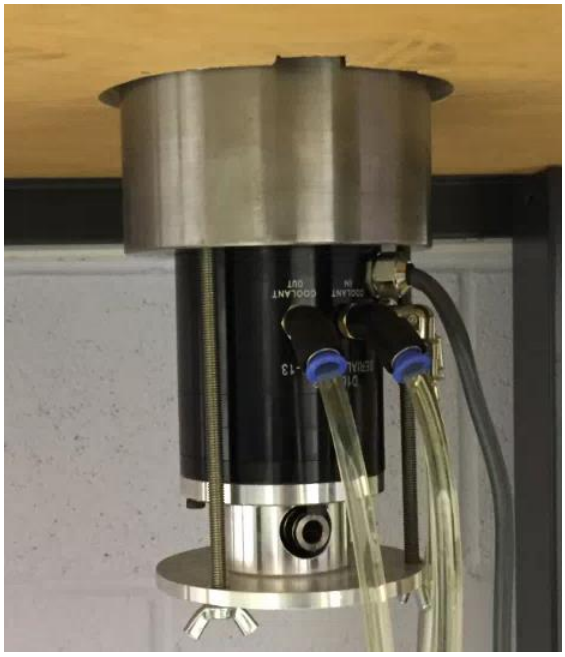

Figure 8-14: The utilised connecting device in the constructed test rig

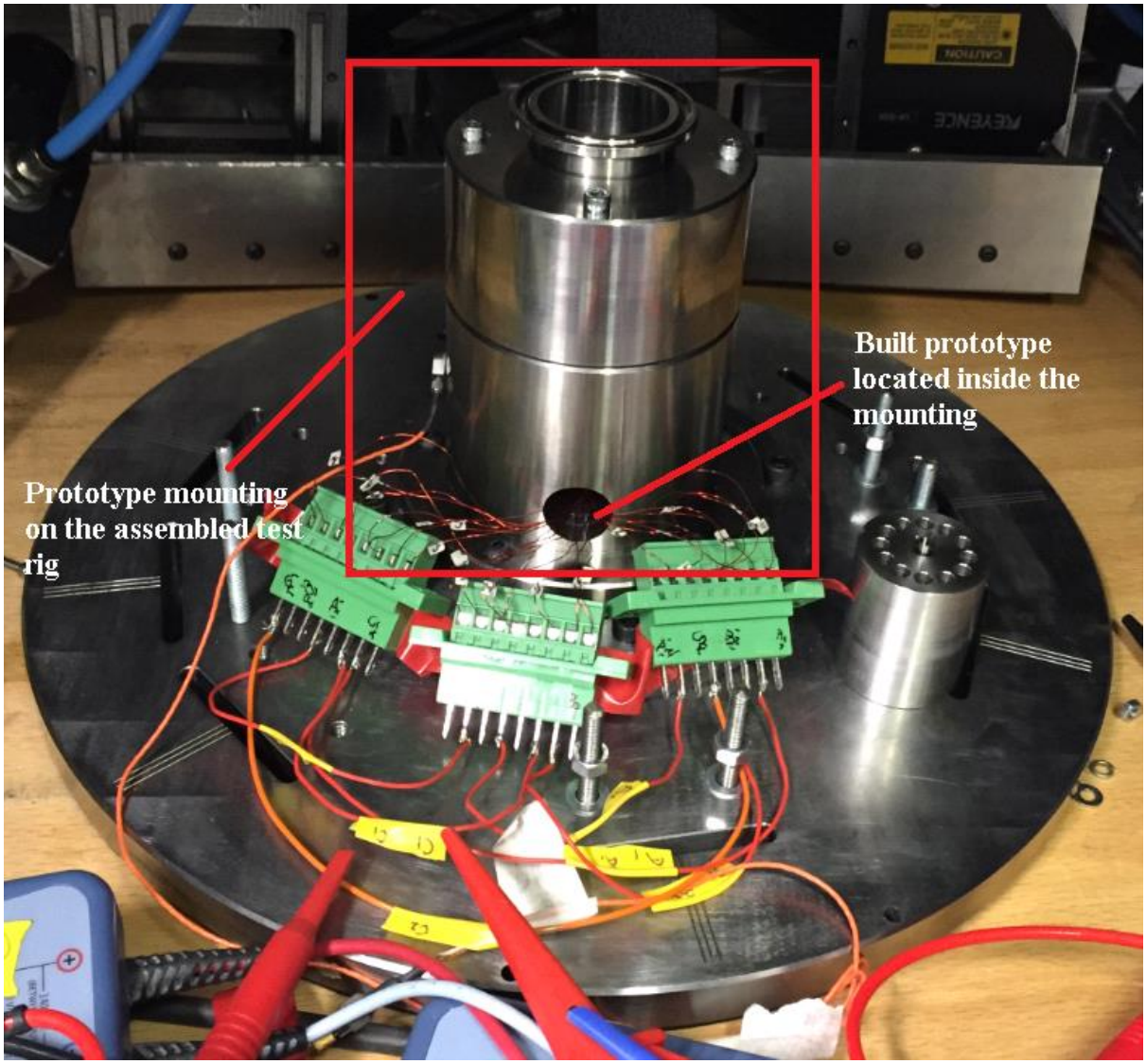

Figure 8-15: The main body of the assembled test rig for the built prototype

The following Figure 8-16 shows a 2-dimensional drawing of the motor with the winding coils labelled. The back-EMFs of all twelve coils are measured separately at a fixed speed of 15,450rpm. The following three pictures: Figure 8-17, Figure 8-18 and Figure 8-19, display the captured back-EMF curves of the tested coils for each phase in the built prototype motor. In Figure 8-17, channel 1 and 3 measured the EMF of coil A1 and A2; channel 2 and 4 measured the EMF of coil A1- and A2-. In Figure 8-18, channel 1 and 3 measured the EMF of coil C1 and C2; channel 2 and 4 measured the EMF of coil C1- and C2-. In Figure 8-19, channel 1 and 3 measured the EMF of coil B1 and B2; channel 2 and 4 measured the EMF of coil B1- and B2-.

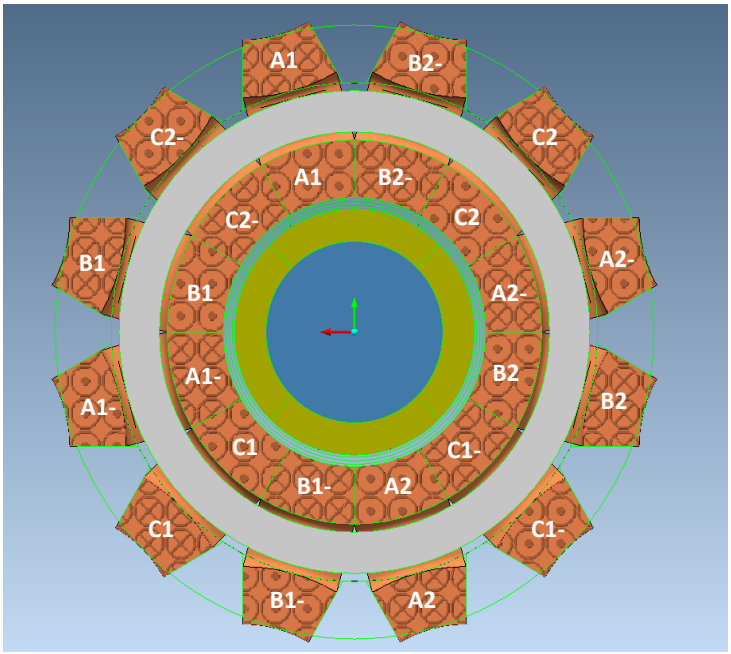

Figure 8-16: A cross-section view of the designed motor with labelled winding coils

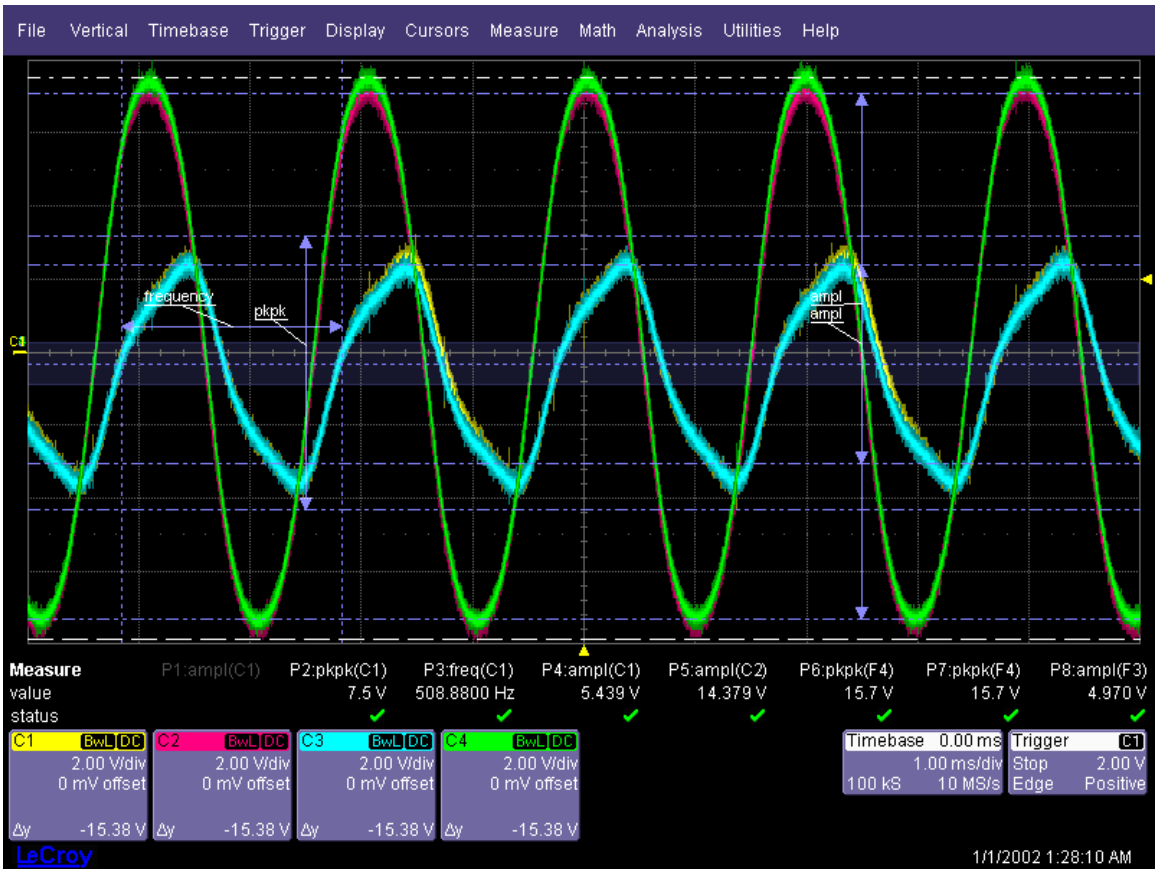

Figure 8-17: The measured back-EMF values of winding coils in phase A

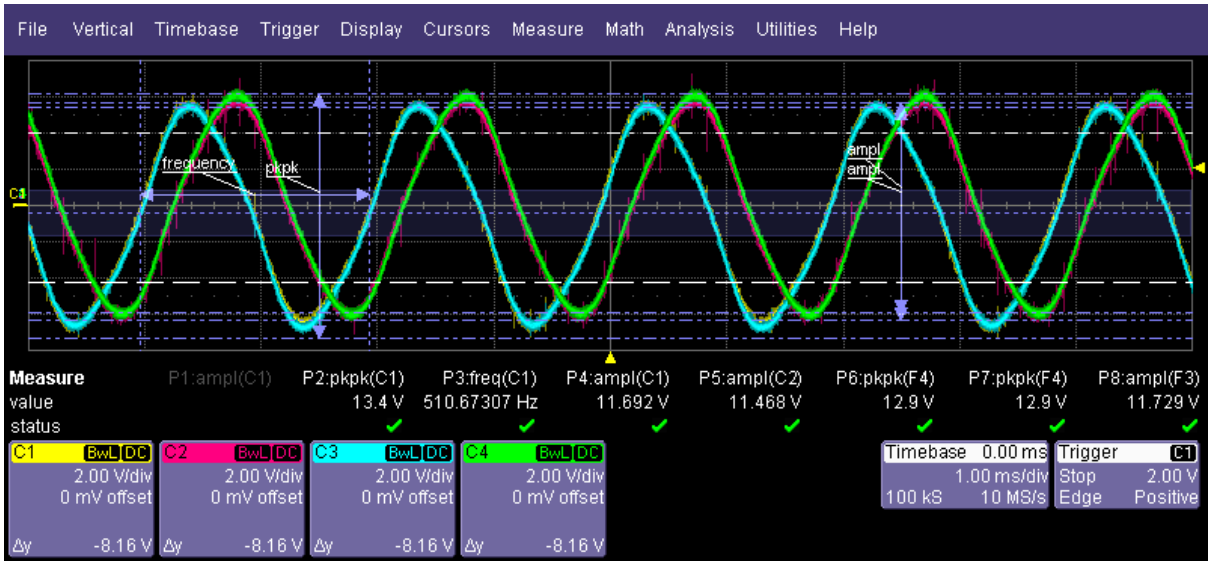

Figure 8-18: The measured back-EMF values of winding coils in phase C

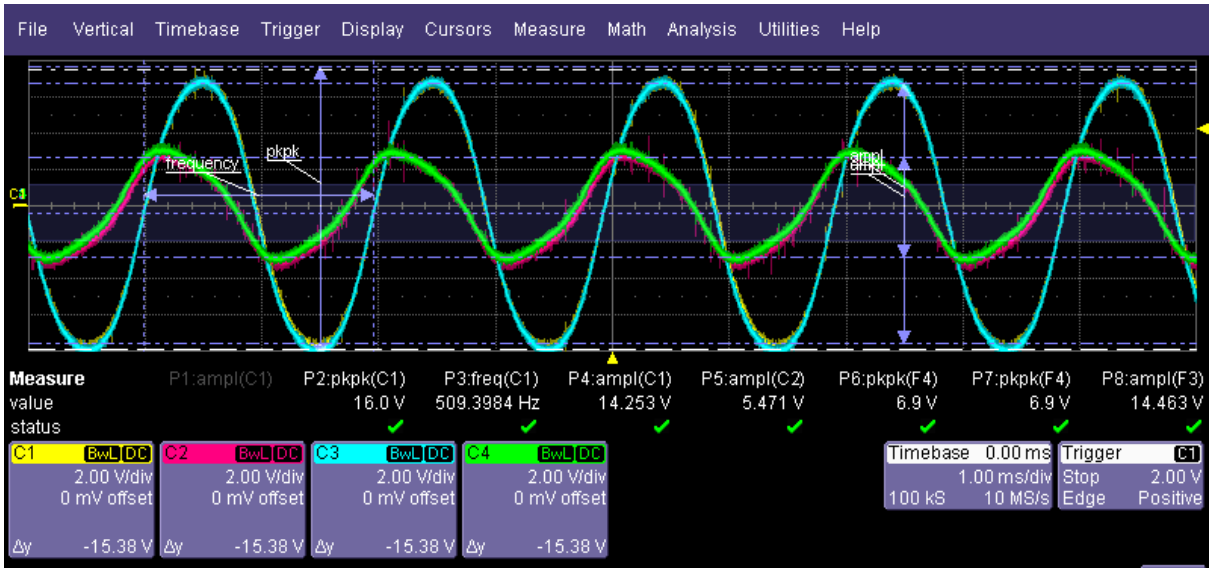

Figure 8-19: The measured back-EMF values of winding coils in phase B

According to the above shown winding terminal voltage curves, it indicates coils located at different positions of the stator have different induced back-EMF waveforms. This outcome should obviously not be the case in a symmetrically designed motor. Hence, it was thought that this imbalance may be caused by the introduced gaps between the two split stator segments, as shown in Figure 8-20 below. The following Figure 8-21 shows an example of how a stator gap was introduced in a 2-dimensional finite element simulation model to test this hypothesis. In

Figure 8-21, the thickness of the introduced gap is defined as 0.02mm with the total length of 2.5 times of core-back radial thickness.

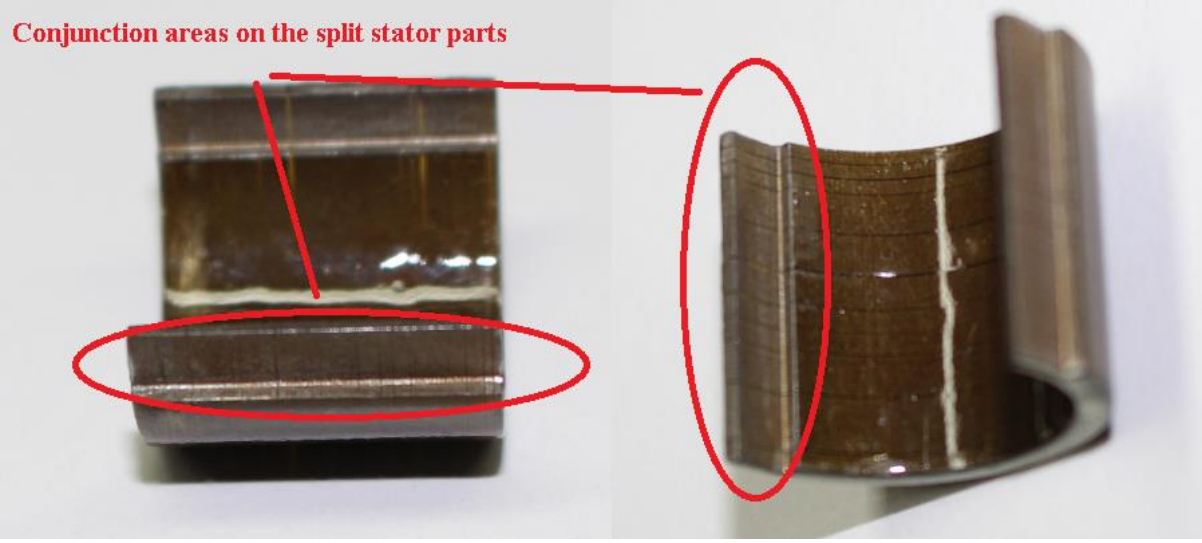

Figure 8-20: Highlighted conjunction areas on the split stator segments

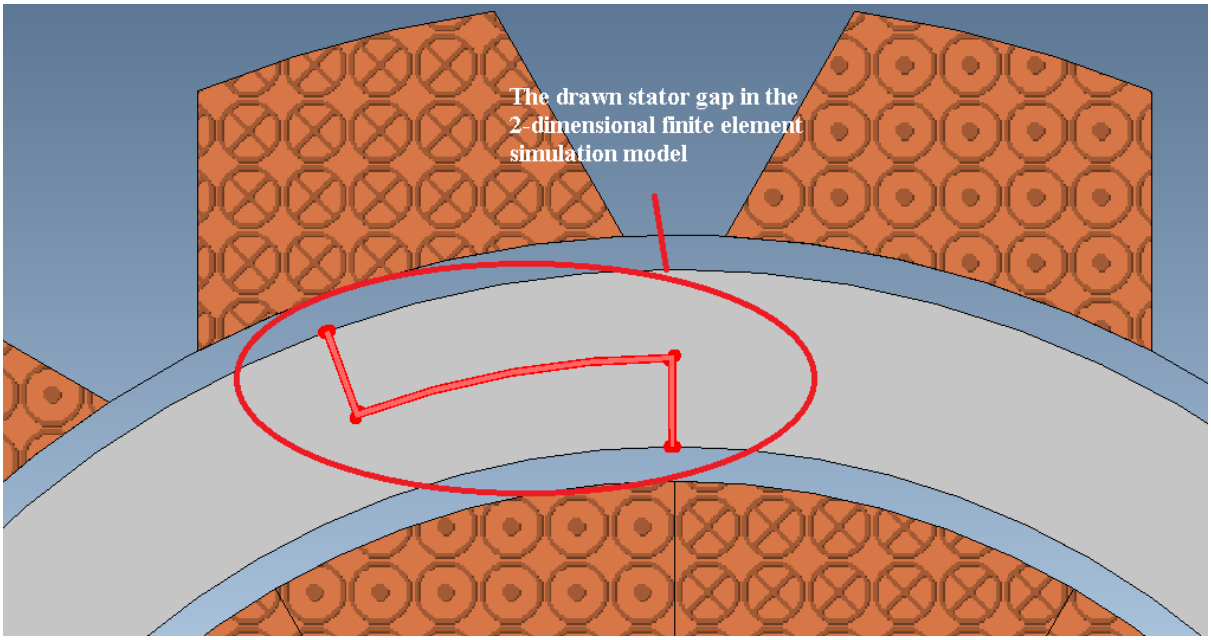

Figure 8-21: The drawn stator gap in the 2-dimensional finite element simulation model

To be specific, the split stator structure was introduced to reduce the manufacturing complexity and has been discussed in Chapter 7. Super glue was utilised to join the two pieces of the half-ring shape stator segments together, creating a small gap in between, and significantly changing the flux flowing pattern round the stator core back.

Figure 8-22 below demonstrates the plotted motor magnetic flux loop in the 2-D finite element simulation model for a single stator 4-pole design. The magnetic flux from a magnet north pole can smoothly flow back to the adjacent south poles on both sides through the effective air-gap and the stator core-back. When the rotor rotates anti-clockwise from the original position by 90°, the flux loop inside the stator laminations will rotate simultaneously and maintain the same 4-pole magnetic flux pattern, as shown in Figure 8-23.

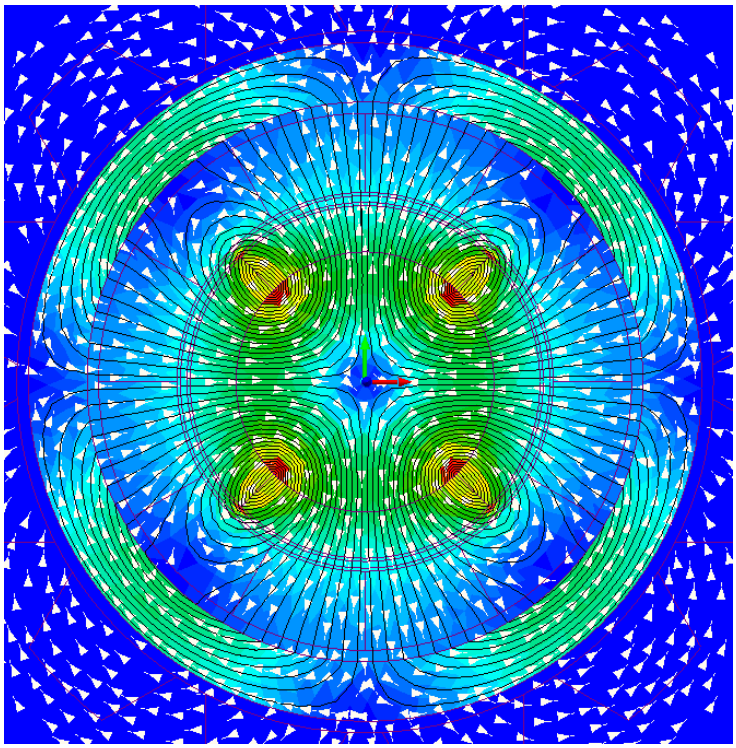

Figure 8-22: The FE simulated magnetic flux loop in single stator 4-pole design

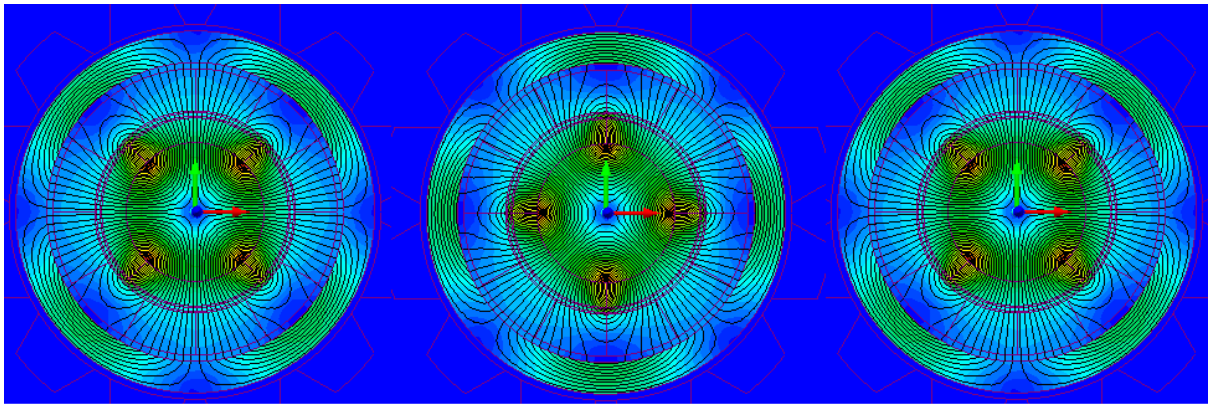

Figure 8-23: The FE simulated flux loop in single stator 4-pole design when magnet rotates from 0° to 90° in mechanical degree.

On the other hand, with the split stator, the motor magnetic flux flowing through the stator core-back is no longer symmetrical. Magnetic flux will generally flow to avoid crossing the gap, as shown in Figure 8-24. For the split stator, the core back flux loop can be essentially similar to that of a 2-pole machine when the magnet pole edge is aligned with the gap. Only a very small portion of the flux crosses this gap because of its higher reluctance. Consequently, there is much less magnetic flux flowing through the coils located at the stator gap regions, resulting in lower induced back-EMFs, whilst higher amplitude back-EMF waveforms are generated on another coils positioned away from the gap.

As the rotor rotates, the virtual location of the magnet pole edge relative to the stator gap continuously changes, along with the actual magnetic flux distribution inside the stator laminations. Figure 8-25 demonstrates the 2-D finite element simulated magnetic flux loop in the split stator 4-pole motor with an anti-clockwise spinning magnet, rotating from its original position by 90 mechanical degree. This illustrates that the effective stator flux pattern is varied depending on the relative location between the magnet pole edge and the stator gap. When the centre of the magnet pole is aligned with the stator gap region, a virtually 4-pole magnetic flux pattern is demonstrated. In order to investigate the impact of the varying stator flux distribution on the induced coil back-EMFs, a series of the 2-D finite element simulations are carried out. The obtained results are utilised to compare with the measured voltage waveforms from the tested prototype.

Figure 8-26 highlights the two winding coils (coil A and coil A- in phase A) in the lower magnetic flux region and the higher magnetic flux region respectively. The following Figure 8-27 illustrates the 2-D FE simulated back-EMF waveforms in the coil A and coil A- in one mechanical cycle of the operation at the designed nominal motor speed. This shows that the coil location in the assembled segmented stator can significantly impact the amplitude and the pattern of the generated coil back-EMFs. Comparing Figure 8-27 to Figure 8-17, there are matched patterns of the voltage waveforms for both winding coils. The unmatched amplitude values are due to the different operating speed in the conducted tests: 15,450rpm in the practical test and 150,000rpm in finite element simulation. Figure 8-28 and Figure 8-29 show the simulated back-EMF waveforms in the winding coils of phase C and phase B respectively. As earlier, both of them deliver the matched curve patterns of the induced coil back-EMFs in comparison with the waveforms shown in Figure 8-18 and Figure 8-19.

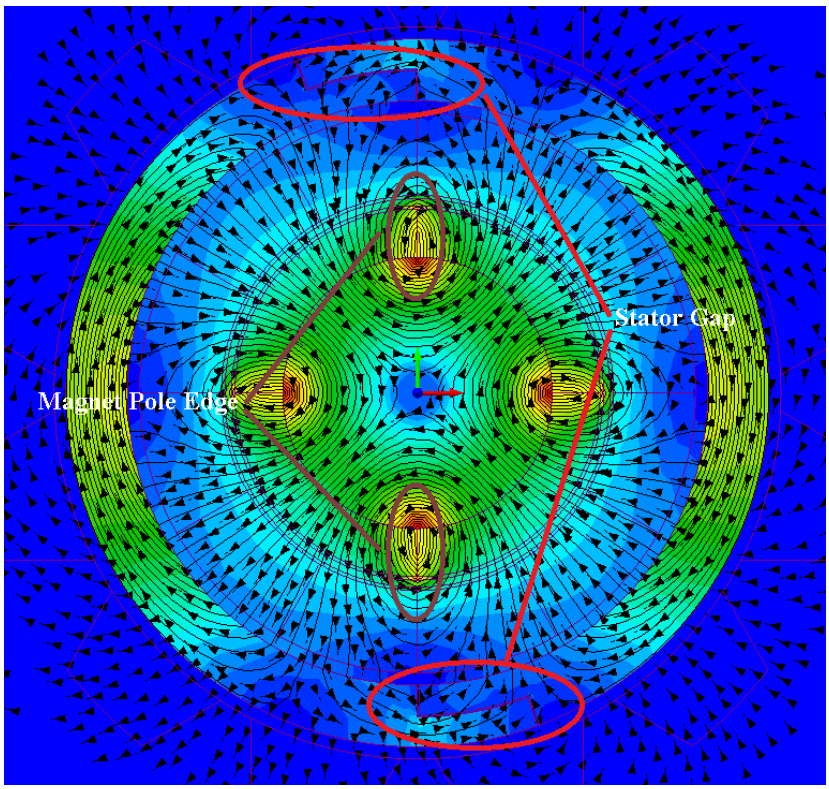

Figure 8-24: The FE simulated magnetic flux loop in split stator 4-pole design

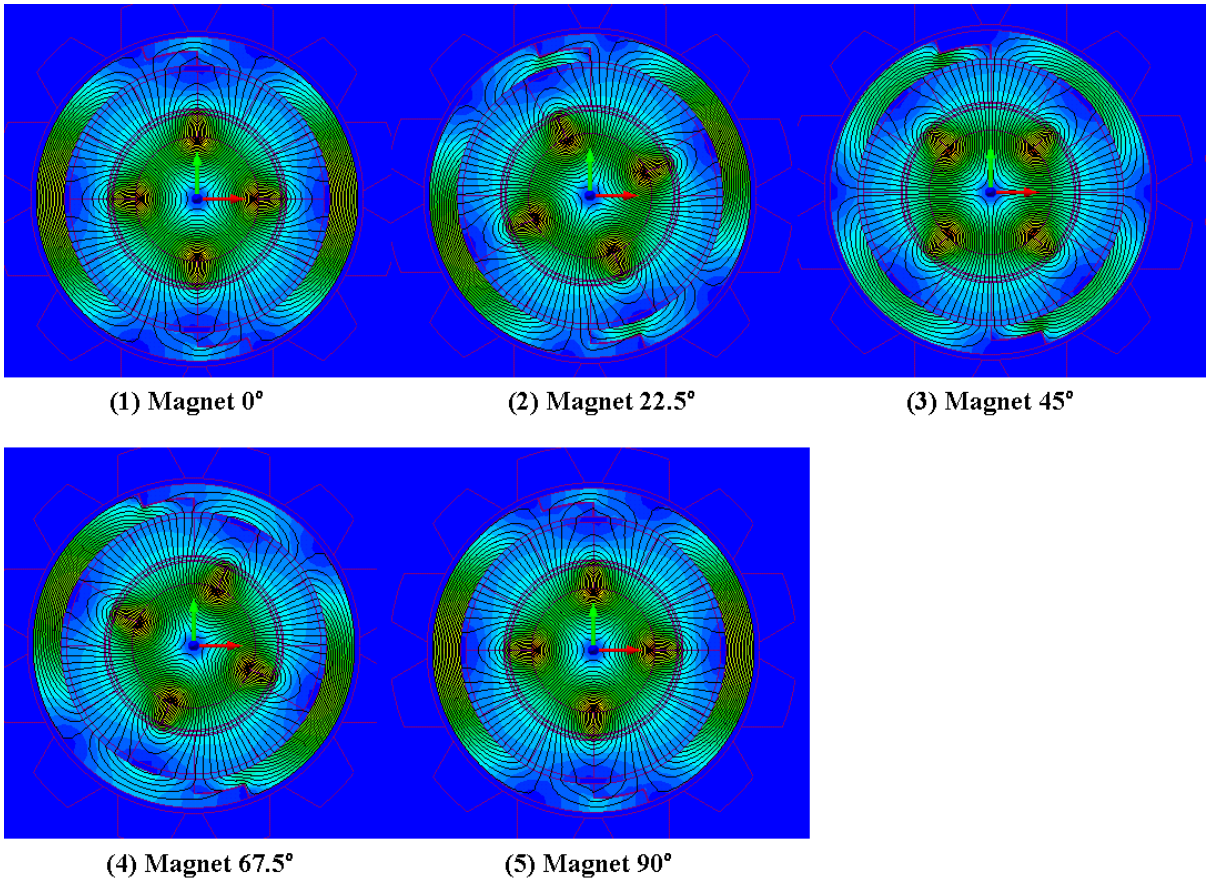

Figure 8-25: The FE simulated flux loop in split stator 4-pole design when magnet rotates from 0° to 90° in mechanical degree

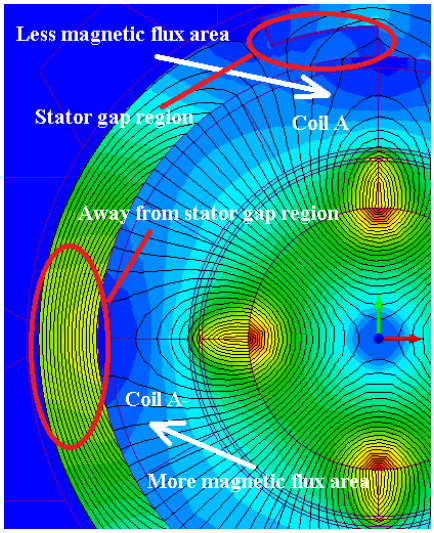

Figure 8-26: Two example coils in the regions of less magnetic flux and more magnetic flux respectively

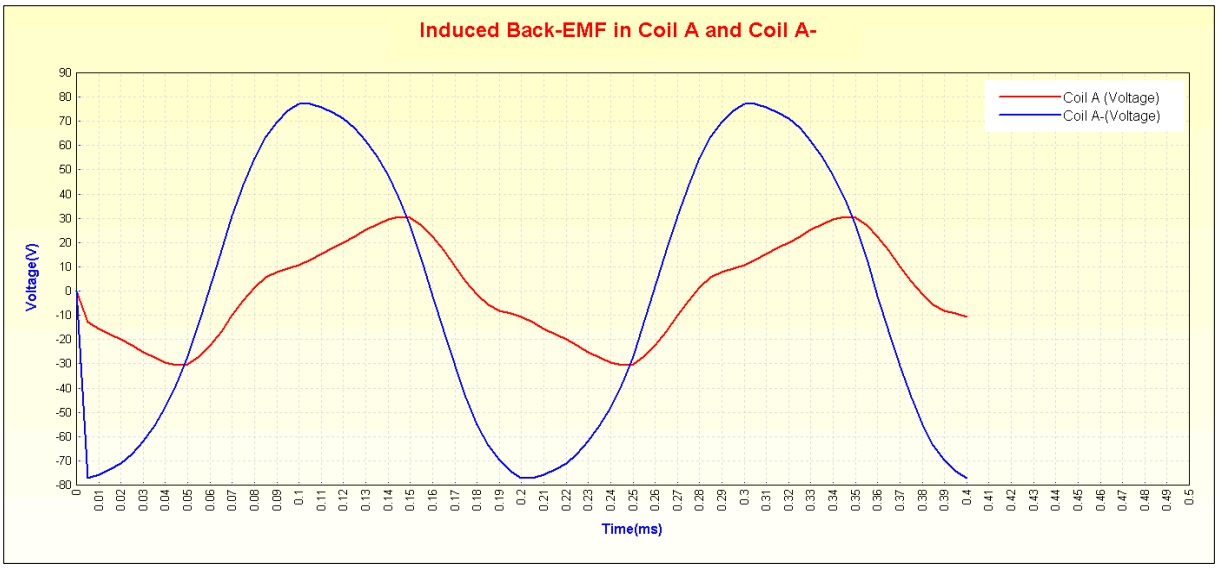

Figure 8-27: The FE simulated back-EMF waveforms in coil A and coil A- (Phase A)

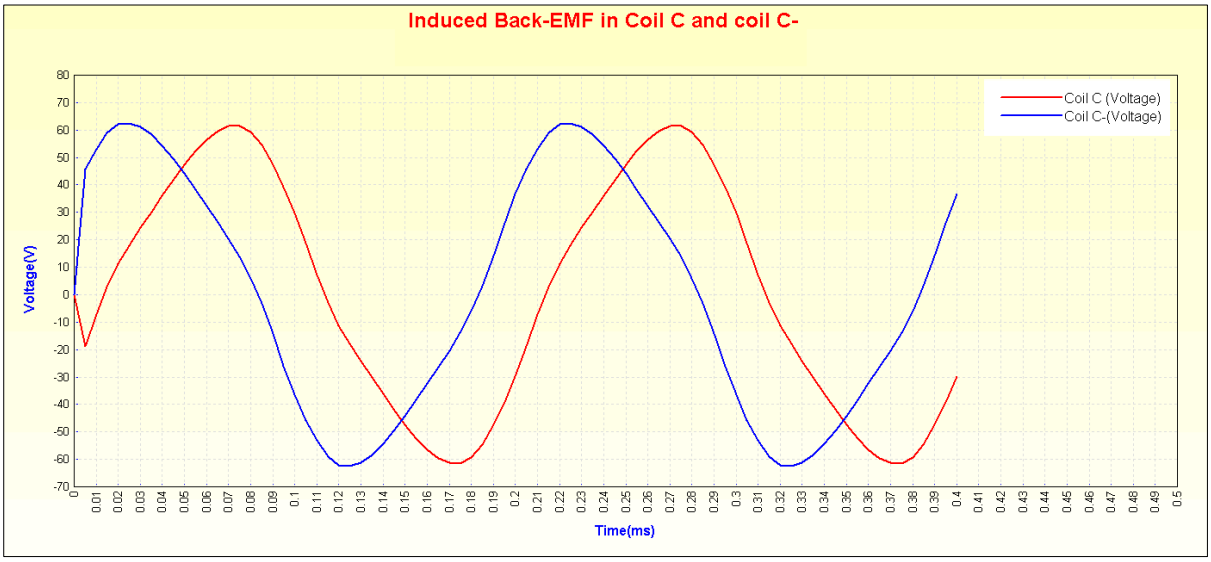

Figure 8-28: The FE simulated back-EMF waveforms in coil C and coil C- (Phase C)

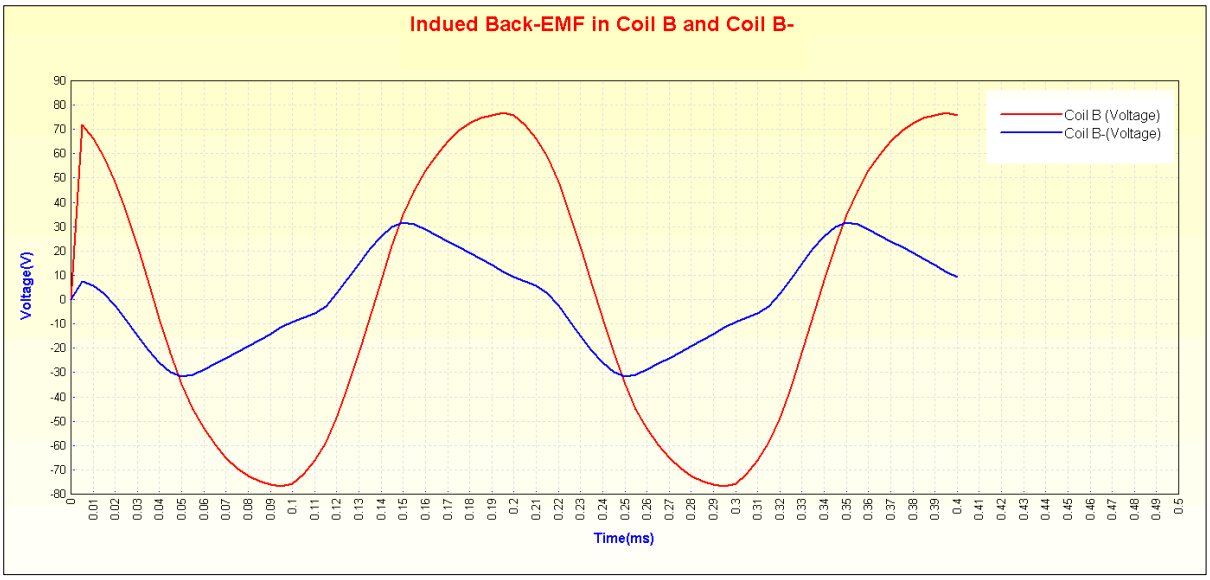

Figure 8-29: The FE simulated back-EMF waveforms in coil B and coil B- (Phase B)

To summarise, the shown FE simulation results indicate that the generated flux linkage is significantly reduced on the coils which are close to the stator gap, while those located at the regions away from the gap feature the enhanced flux linkage value. Therefore, the total induced back-EMF per phase is actually not affected by the introduced stator gaps if all phase coils are series connected. Due to the varied amplitudes and waveforms of induced back-EMF in the individual coils, it is inappropriate to parallel connect all the coils in one phase.

In this project, with the aim of achieving the equal RMS value of induced back-EMFs for each phase, two winding coils in one magnet pole pair are required to be series connected. After finishing the winding connection, the induced back-EMF waveforms per phase is measured by the test rig shown previously (Figure 8-12 and Figure 8-15) at the targeted nominal operating speed of 150,000rpm. Figure 8-30 below shows the captured waveforms of the induced back-EMF per phase for all three phases. The graph proves that, with the series connected winding coils in one magnet pole pair, the measured back-EMF values per phase are identical to each other in magnitude, with the standard 120 electrical degree phase shift between each phase.

Figure 8-31 directly compares the simulated and measured phase back-EMF waveforms for all three phases. The result indicates that both achieved waveforms have the same curve patterns in one complete mechanical cycle, although the peak and the RMS values of the FE simulated back-EMFs for each phase have slightly larger numbers than those in the real prototype test. The theoretical value of the peak back-EMF per phase in the carried out finite element

simulation is about 97.5V; while the captured maximum back-EMF value in the practical test is about 3% lower, at 94.5V. The possible root causes of this voltage difference is discussed below.

1. The actual motor operating speed in the real prototype test is lower than the targeted nominal value of 150,000rpm, at 147,000rpm as shown in Figure 8-30, giving about 2% back-EMF reduction.

2. The ring-shape rare-earth permanent magnet delivers lower open-circuit air-gap flux density in comparison with the ideal case due to the magnetisation process, which gives lower flux density at the magnet pole edges. The details of the actual flux difference between the real magnet and the finite element simulation have been systematically discussed in Chapter 7. With an updated magnet finite element simulation model which includes this effect, the simulated back EMF is approximately 1% lower than the original simulated value.

3. The additional non-magnetic stator gap of the adhesive layer in the built split stator may influence the induced coil back-EMF values depending on the detailed gap thickness and shape. Further investigations of this factor will be demonstrated in the following section.

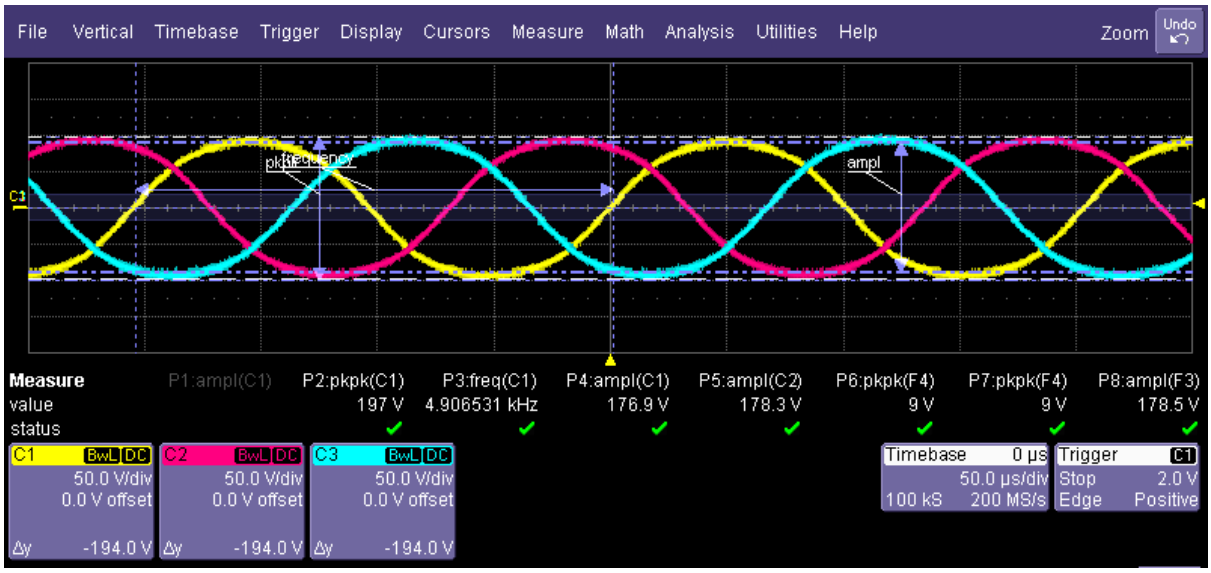

Figure 8-30: The traced back-EMF waveforms for each phase at the targeted nominal speed of 150,000rpm

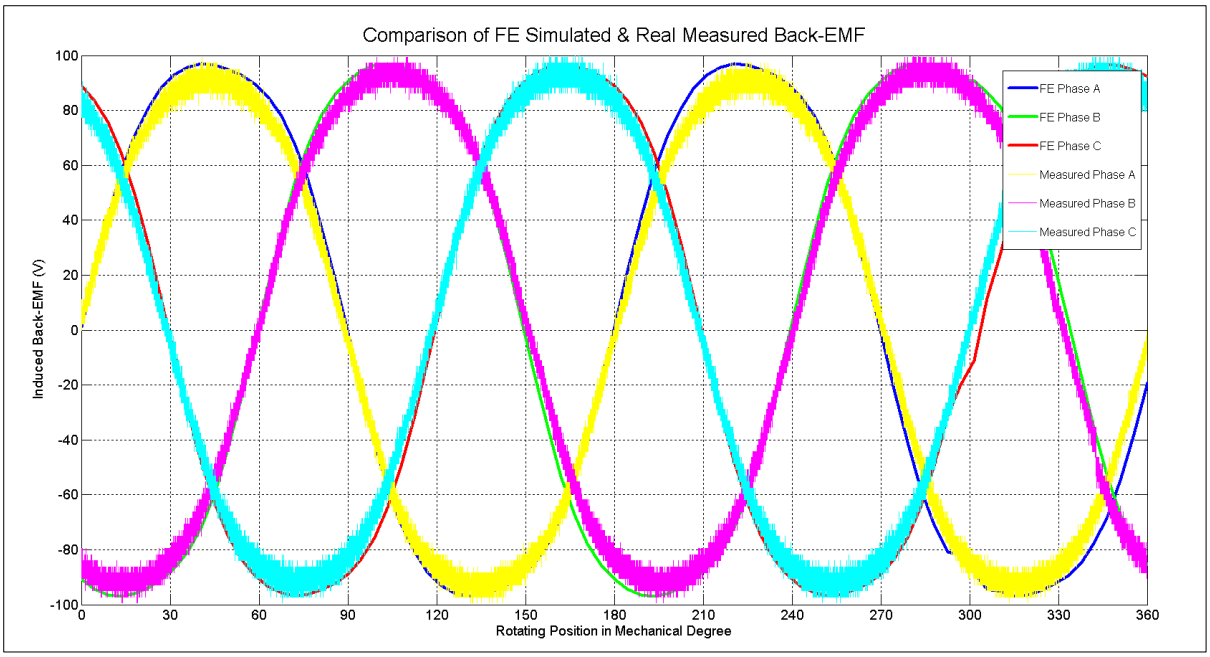

Figure 8-31: The direct comparison of the induced phase back-EMF waveforms for all three phases between the FE simulation and the practical measurement

8.6.2 Impact of varied stator gap on motor phase back-EMF

This section considers the impact of both the length and shape of the introduced stator gap on the induced phase back-EMFs. A series of 2-dimensional finite element simulations were conducted with the varied gap radial thickness from 0.02mm to 0.05mm in 0.005mm steps. The shape of the simulated stator gap in all carried out simulations is maintained the same. The coil A and the coil A- in one magnet pole pair for phase A are utilised as representatives, as the impact of gap thickness on each phase is principally similar.

Figure 8-32 below illustrates the induced back-EMF waveforms in coil A and coil A- under varied gap radial thickness. The graph indicates that, with the growth of the introduced stator gap radial thickness, the peak-to-peak value in coil A is decreased whilst the voltage amplitude in coil A- is increased simultaneously. As it is shown in Figure 8-26, coil A is located close to the stator gap area while coil A- is the farthest coil away from the gap. The thicker stator gap further boosts up the reluctance value in the gap region, forcing the increasingly more magnetic flux to flow away from this area. Therefore, a gradually higher back-EMF value can be induced in coil A- while the opposing trend can be seen in coil A. If the infinite width of stator gap were introduced, there would be very limited back-EMF induced in coil A, resulting in the virtually 2-pole motor been created.

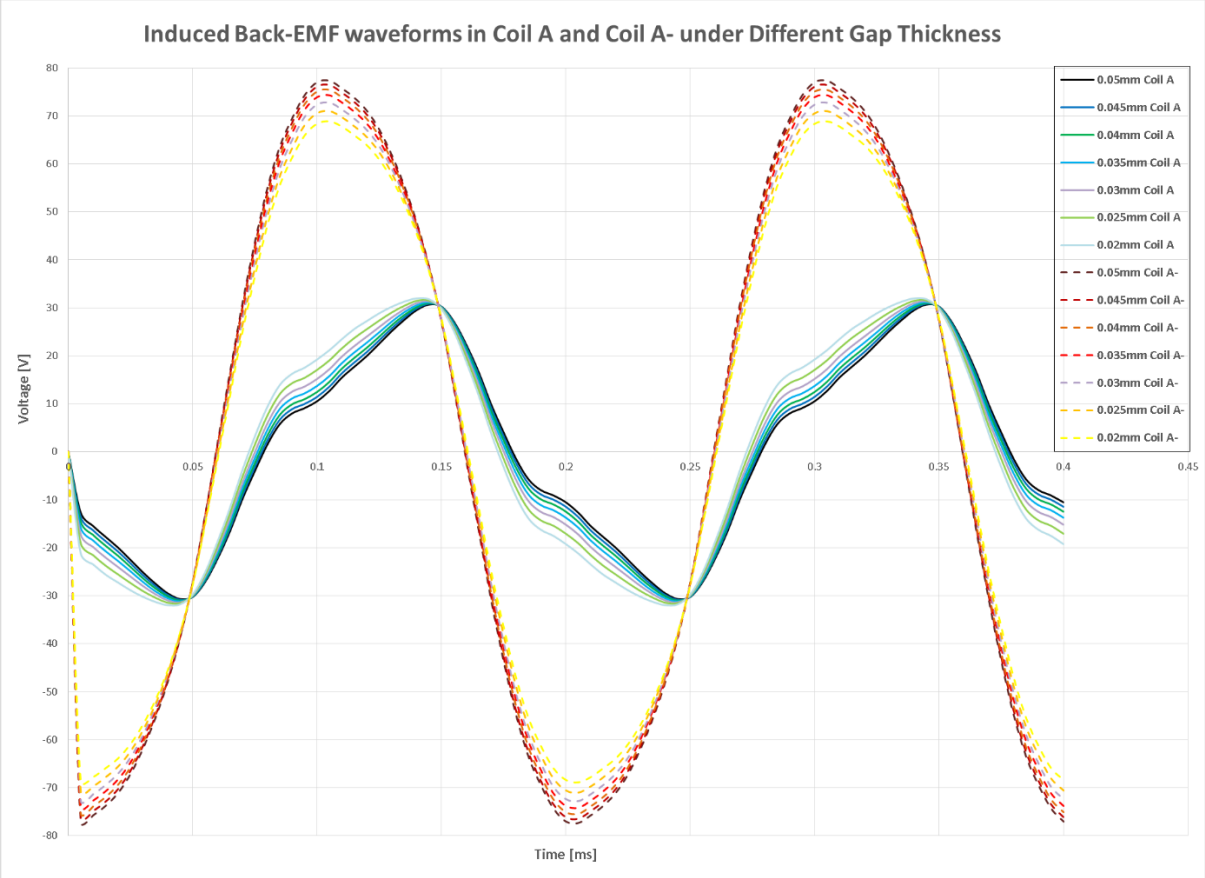

Figure 8-32: Induced back-EMF waveforms in coil A and coil A- under different stator gap thickness

On the other hand, once the two winding coils in one magnet pole pair are series connected, the simulation results indicate that there is no impact on the effective induced phase back-EMF, as shown in Figure 8-33. This outcome is mainly due to the two reasons:

1. The thickness of the stator adhesive layer is small so the effect on the main flux crossing from rotor to stator is negligible; only the core back distribution is affected.

2. The induced back-EMFs in coils away from the introduced stator gap are enhanced.

3. The magnetic flux density in the stator core-back is always under the saturation point. Hence, once entering the core, the flux is free to return to either of its adjacent poles.

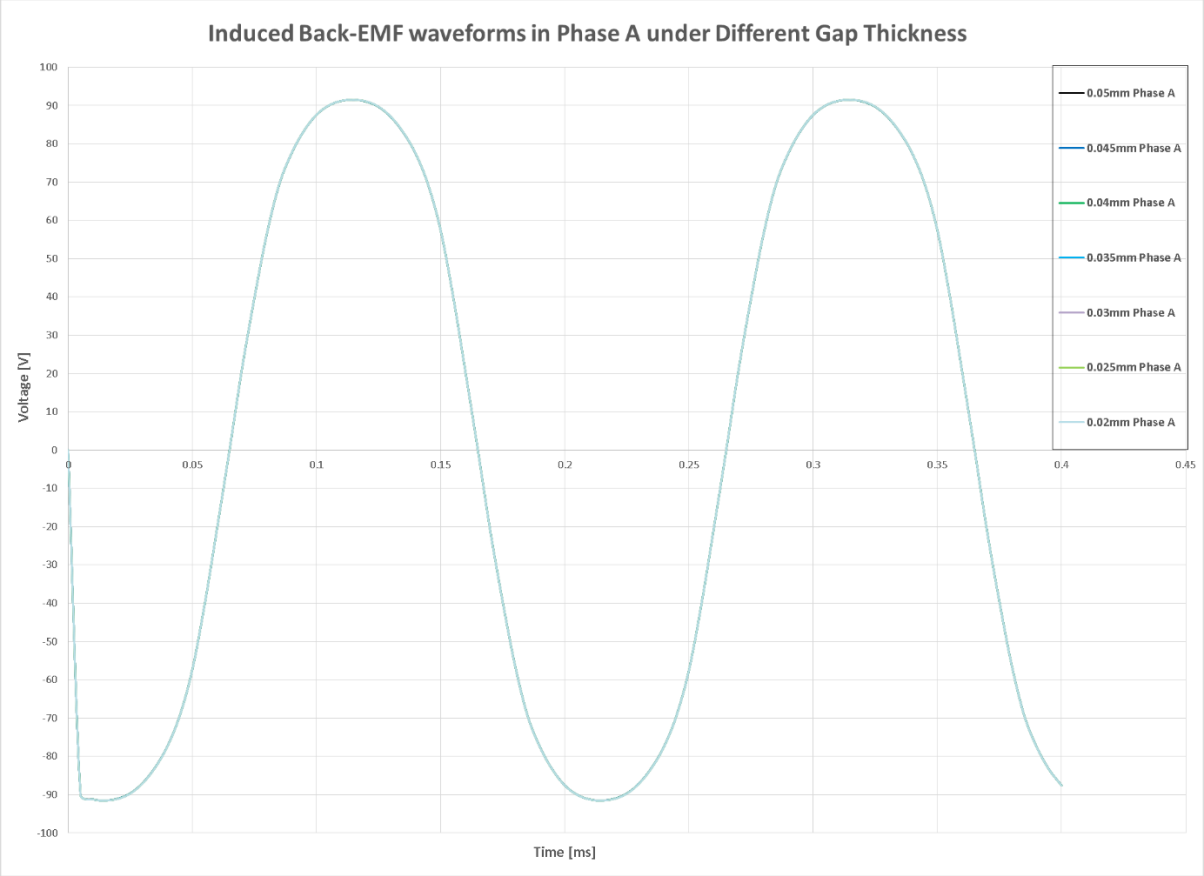

Figure 8-33: Induced back-EMF waveforms in phase A under different stator gap thicknesses

Consequently, the additional non-magnetic stator gap in the built prototype will not influence the induced phase back-EMFs in this work if the coils in one magnet pole pair is series connected. Figure 8-34 demonstrates the simulated back-EMF waveforms in phase A under different stator gap thicknesses including no stator gap case. It shows that, with or without the added stator gap, the resultant impact on the generated back-EMF waveform per phase is insignificant as there is no further flux leakage occurred in the system.

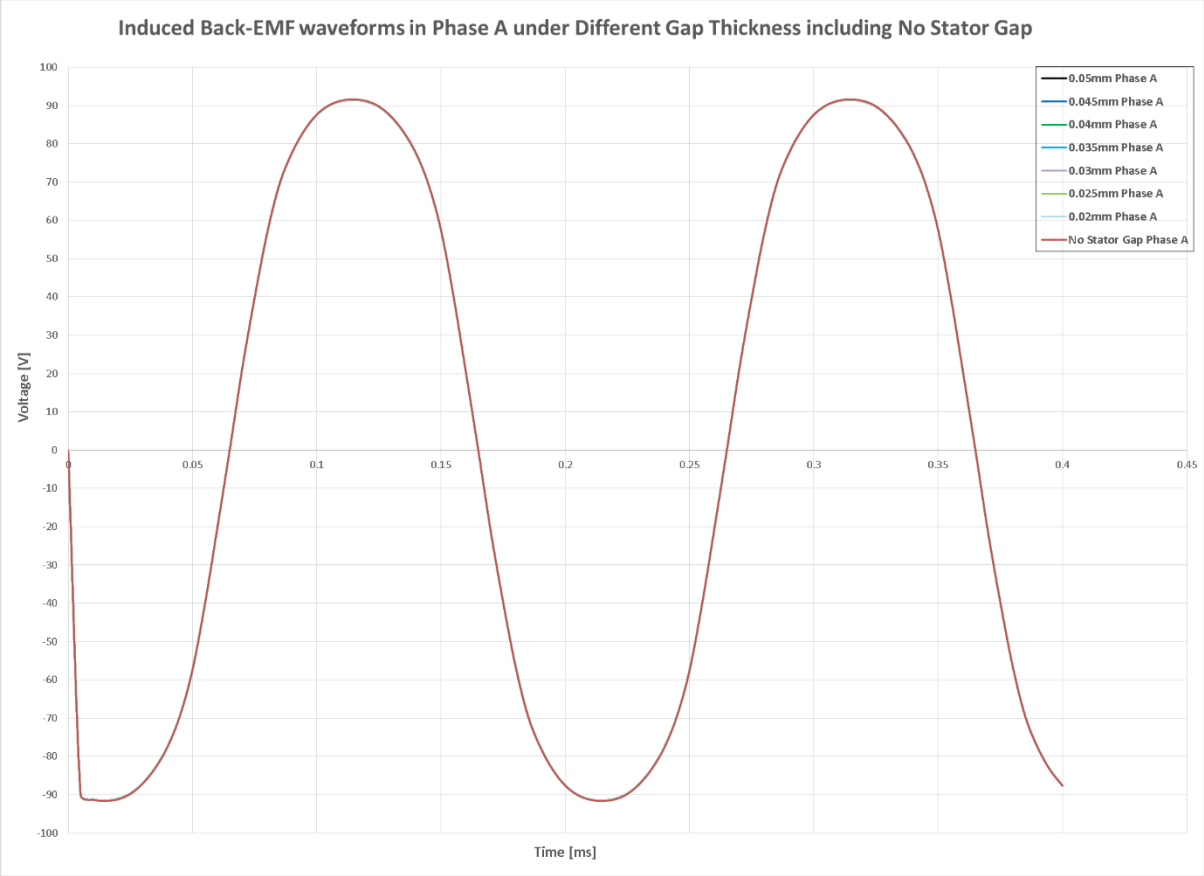

Figure 8-34: Induced back-EMF waveforms in phase A under different stator gap thicknesses including no stator gap

Furthermore, the same conclusion can be received for the induced phase back-EMFs under different shapes of the introduced stator gap. Figure 8-35 below displays different shapes of the introduced stator gap. The following Figure 8-36 shows the achieved phase back-EMF waveforms under the varied shapes of the gap. As it is expected, identical voltage waveforms are plotted for the different cases as there is no extra flux leakage in the slot-less structure, split stator motor.

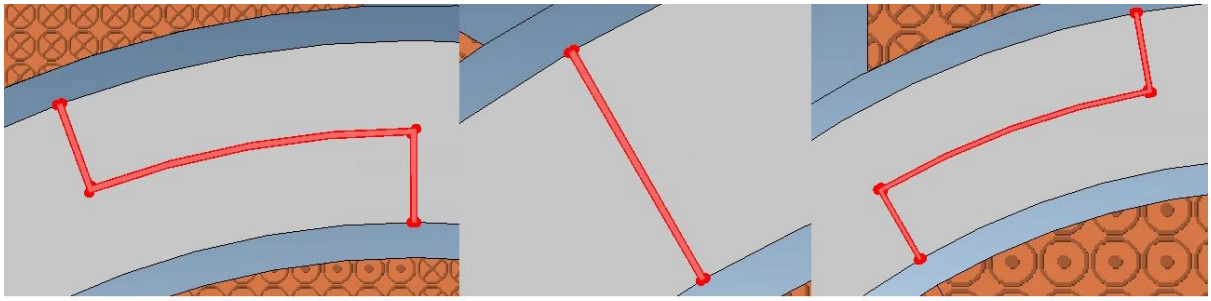

Figure 8-35: The investigated different shapes of the added stator gap

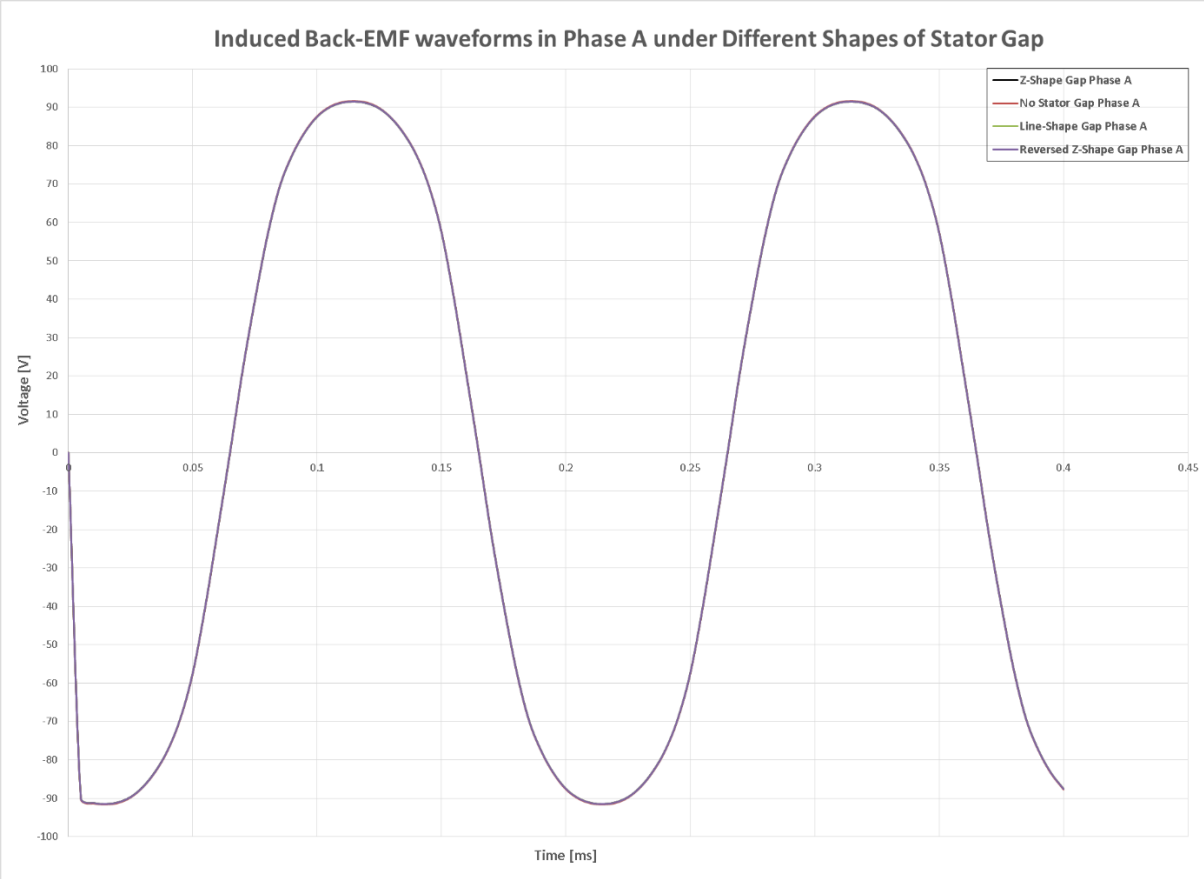

Figure 8-36: Induced back-EMF waveforms in phase A under different shapes of the added stator gap

8.6.3 Impact of segmented stator structure on phase back-EMF

Additionally, with the purpose of generating the equal back-EMF values in each winding coil to permit parallel connected phase coils, a four-part segmented stator was investigated.

Figure 8-37 below demonstrates the conducted finite element simulated magnetic flux distribution in a 4-pole, 4-part segmented, slot-less stator structure design with an anti-clockwise rotating magnet, moving from its original position by 90° mechanically. The graph indicates that, due to the extra two non-magnetic gaps in the assembled stator, the resultant motor flux distribution is similar to a standard 4-pole motor rather than 2-pole machine in a complete electrical cycle. The resultant reluctance values are virtually the same in both directions of the flux paths from the magnet north pole to the adjacent south poles. Figure 8-38 shows the FE simulated back-EMF waveforms in coil A and coil A- in the 4-part segmented, slot-less stator structure design. Both coils have identical voltage waveforms.

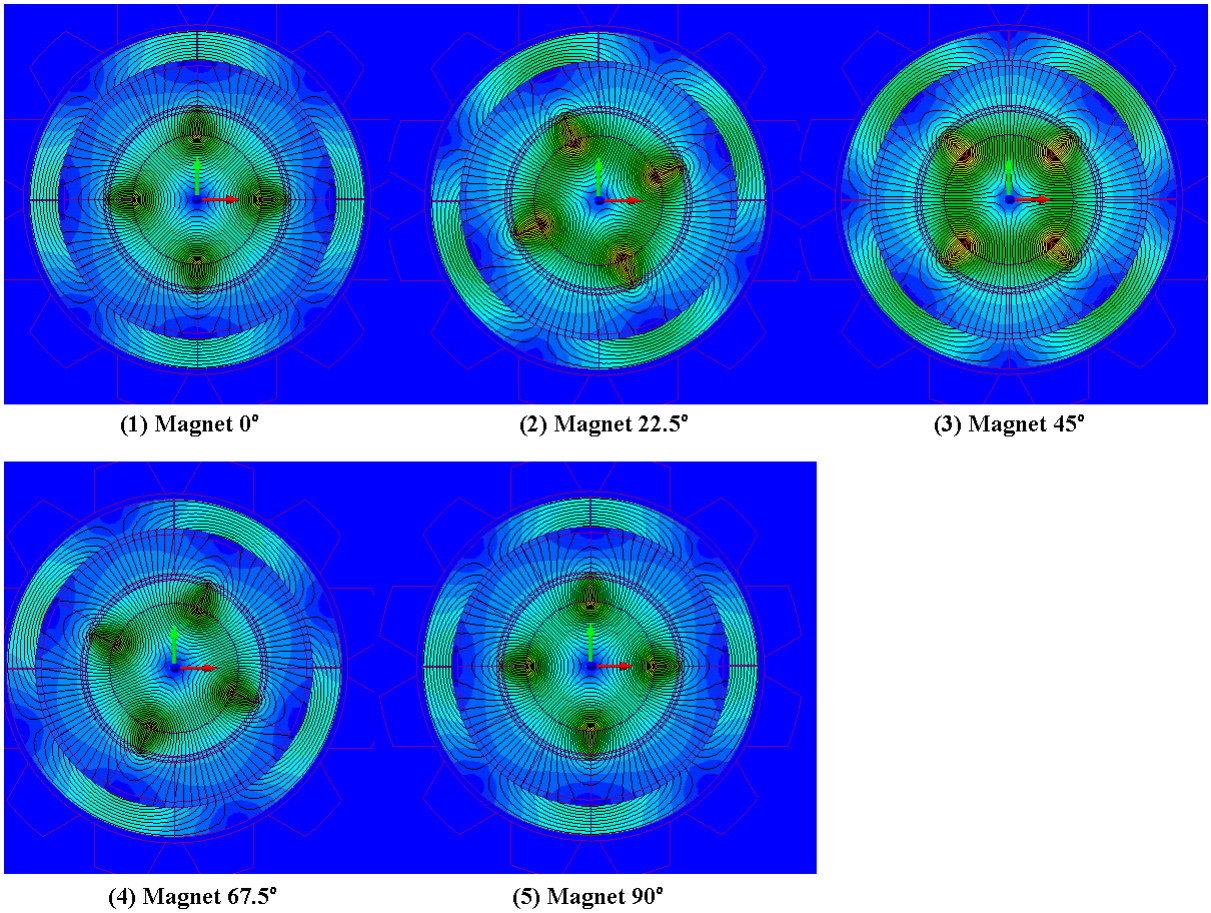

Figure 8-37: The FE simulated flux loop in 4-pole four-part segmented stator design when magnet rotates from 0° to 90° in mechanical degree

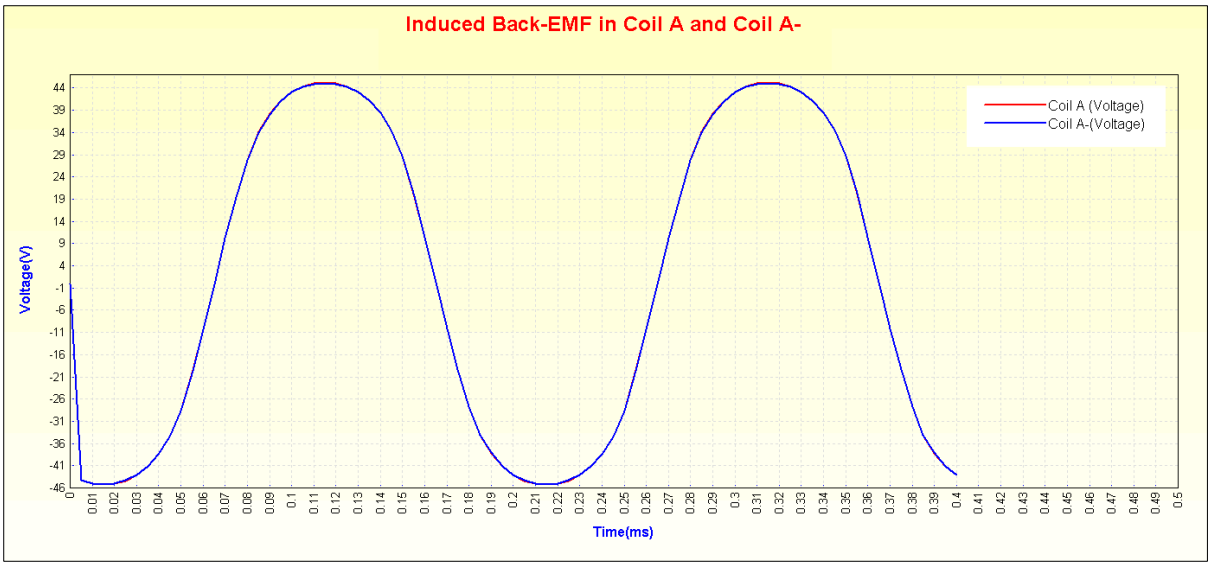

Figure 8-38: The FE simulated back-EMF waveforms in coil A and coil A- in four-part segmented stator design

On the other hand, in comparison with the split stator motor of 2-part segmented stator, the peak-to-peak value of the induced phase back-EMFs is lower in the 4-part segmented stator design. Comparing the motor magnetic flux distribution between Figure 8-25 and Figure 8-37, it indicates that, when the magnet pole edges are aligned with the stator gap regions, there is only a very little portion of the generated magnetic flux flowing through the introduced stator gaps in the split stator motor. In the 4-part segmented stator motor, the whole motor flux is required to go across the introduced gaps. As the reluctance value of the stator gap is significantly higher than the stator laminations, it produces less magnetic flux, leading to the lower amplitude of the induced back-EMFs. Figure 8-39 shows the simulated back-EMF waveforms in phase A for both 2-part and 4-part segmented stator motors. From the graph, it shows that the former can induce 1.2% higher phase back-EMF compared to the latter in the same design. It can claim that, the more number of segmented stator parts, the less phase back-EMF induced.

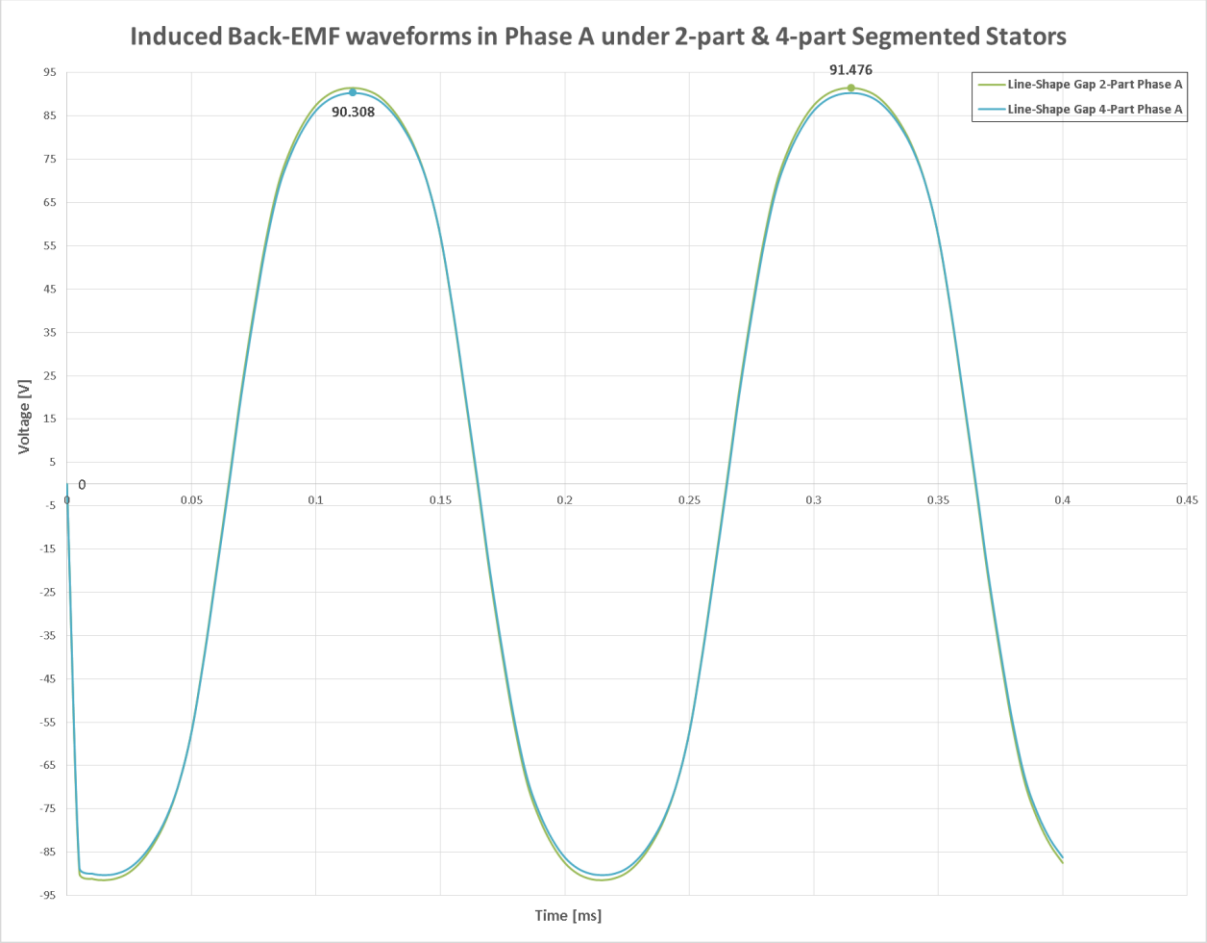

Figure 8-39: Induced back-EMF waveforms in phase A under 2-part and 4-part segmented stators

Chapter 9 : Conclusion and Future Work

9.1 Conclusion

To summarise, the purpose of this research is to create a compact, low weight, high-speed, highly-efficient electric motor which is powered from a mains supply. Compared with existing machines, the motor performance had to be enhanced in at least one of the following aspects, whilst no other aspects should have reduced performance:

- Motor efficiency;
- Motor cost;
- Motor size;
- Motor weight;
- Motor noise;

Before the start of this work, cost implications were considered, excluding such costly motor raw materials as high residual flux density permanent magnets, low loss density amorphous steels, high silicon rate electrical steels, high strength carbon fibre rotor sleeves, etc.

In Chapter 2, a thorough literature review to scan the previous work have been carried out, giving a direct comparison of all potential motor types in the fields of high speed, high efficiency and small size applications. After considering the required nominal operating speed of 150,000rpm and motor power density of 48kW/L, permanent magnet motor is selected as the first choice. However, without changing the fundamental motor type, there has been little research focusing on minimising the motor per unit material cost on high-speed power-dense applications.

In order to balance motor performance and per unit cost, dominant design variables are examined one by one in Chapter 3. As is known, in a permanent magnet motor, the major material cost comes from high residual flux density rare-earth magnets. Reduction of the

utilised magnet volume can contribute to the significantly reduced motor cost. Nevertheless, this means the motor electrical loading has to be maximised at the same time to compensate the power drop. A slot-less stator structure is considered to provide larger potential space for phase winding as well as winding cooling areas. Cogging torque is eliminated, which improves acoustic performance, and also motor iron loss distribution.

Chapter 4 analyses the detailed loss estimation, indicating that only copper loss is dominant in a slot-less stator design, including both AC and DC losses. These two types of losses are both varied with change of wire size and temperature, but featuring the opposite trends. A set of motor loss balancing points are illustrated under the varied ratio of AC loss to DC loss, helping to ensure the optimised wire size. With the slot-less stator structure, asynchronous air-gap harmonics are minimised so that undesirable magnet and shaft eddy current losses both are almost eliminated. The risk of irreversible magnet demagnetisation has also been minimised. Besides, the time harmonics boosted stator iron loss is significantly reduced due to the low inductance and low armature reaction for air-gap windings. The advantages of low stator loss, small dimensions and simple structure enable the use of normal lamination materials in the slot-less design, which are 75% cheaper than low loss density lamination materials.

To remove the expensive rotor sleeve, a ring-shape integral magnet is introduced to replace the traditional segmented magnets. The air-gap flux distribution and flux leakage principles for different magnetised magnets are specifically investigated in a slot-less structure machine, indicting the best choice is a Halbach magnetised magnet. In order to ensure the mechanical stress of the utilised magnet, the ring-shape magnet cannot be oversized, which in turn requires an increase in phase current density, leading to very high density value in the design (over 30A/mm^2).

In order to minimise the resultant high copper losses, the motor end-winding structure is redesigned from a normal fully spanned coil to a toroidal winding coil. This change is based upon the ratio of motor overall diameter to the axial length, delivering the minimised axially end-winding length as well as the minimal total end-winding length. Furthermore, a 3-phase motor is studied to make full use of the complete air-gap winding space compared to single phase design to increase the motor power density and decrease the current density per phase for the same power level.

Simultaneously, the cooling of motor phase windings is still critical as there is no gap between each phase coil, which increases the risk of coil to coil, or turn to turn failure at the elevated temperature. Therefore, a dedicated motor housing is designed to provide individual cooling tunnels for each winding coil with maximised coil convection area. The potential housing eddy current loss due to time varying magnetic fields created by outer layer toroidal windings is precisely evaluated via 3-dimensional finite element analysis. An updated double layer housing design is implemented to minimise the housing loss. With the aim of achieving a cheaper and simpler toroidal winding approach, the split stator structure is raised to allow separately assembled coils and stator.

Based upon the aforementioned investigations, a small-size (25mm OD* 22mm axial length), power–dense (68kW/L), high speed (150,000rpm), high efficiency (89.29%) and extremely cheap ($1.5) motor is carefully designed, optimised, prototype built and tested.

Comparing to the existing similar power–density, similar speed permanent magnet motors, it is true that the chosen slot-less stator structure brings about 2~3% lower motor efficiency, but over 89% motor efficiency is still essentially high. Further, this motor is over 80% cheaper; the utilised magnet amount has been reduced by 60%; the motor weight is less than 100g (Long stainless steel shaft included).

Under the condition of 30A/mm^2 phase current density, it can run without any overheat issue and provide plenty of temperature safe margin under 3L/s air-cooling while the nominal flow rate of target applications ranges from 8L/s to 16L/s. It can run at full designed speed of 150,000rpm with no sign of magnet burst without rotor sleeve. Also, it can generated the designed motor electromagnetic performance, such as phase inductance and back-EMF. Besides, the achieved test results indicate that, for a segmented stator motor, the number of stator segments should equal to the number of magnet poles or else a varied phase back-EMF will be induced in the coils at different stator location. This research demonstrates that a slot-less stator structure motor can be a competitive candidate for low cost, high speed or even ultra-high speed applications.

9.2 Future work

In general, this research has achieved its primary target of designing, optimising, prototyping and testing a high speed, high efficiency, power-dense, mains powered electric motor with the minimised motor per unit cost. The work demonstrated in this thesis is one step toward the implementation of full motor testing. Nevertheless, there are still a few more things can be conducted in the near future to make this research more completed.

1) Mechanical analysis of rotor dynamics:

   There is an unexpected damage spotted on the built prototype of the used pre-load spring as shown in Figure 9-1. It is suspected that this is due to the excessive shaft vibration in axial direction when motor operated in the over speed range (speed > 160,000rpm). A proper mechanical analysis of rotor dynamics contributes to the assessment of rotor vibration force so as to reduce the risk of this type of damage.

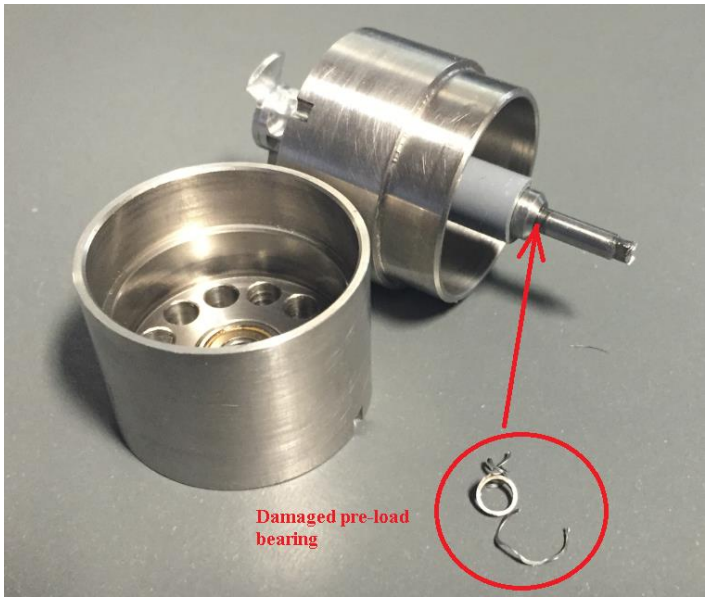

Figure 9-1: Damaged pre-load bearing after disassembling the rig

2) Design of three phase BLDC motor control board with software:

   To drive the built prototype as a motor, the purposely designed motor control board with specific drive software is compulsory. With the support of specifically designed motor drives, motor performance such as motor input power, system efficiency and on load behaviours can be systematically tested. Direct power measurement on board

contributes to the evaluation of actual power electronics losses, for instance, switching loss, conducting loss and shunt resistor Ohmic losses.

3) Proximity loss calculation on load condition

   Proximity loss is calculated only on no load condition in this project. With the real chopped phase current injected, both the armature effect and the high order harmonics bring the non-negligible impact on the effective loss value, especially for slot-less motors. The accurate estimation of motor proximity loss on load condition is beneficial to the more precise analytical evaluation of motor performance.

4) Magnet loss calculation in single phase motor on load condition

   In single phase motor, there is a backwards rotating magnetic field which can induce the undesirable eddy current in rotor magnet, increasing the magnet temperature as well as the risk of demagnetisation. The estimation of the effective magnet loss on load condition contributes to the precise evaluation of magnet properties in motor operation.

Reference

[1] D. Krähenbühl, C. Zwyssig, H. Weser, and J. W. Kolar, "A Miniature, 500000rpm, Electrically Driven Turbocompressor," *Industry Applications, IEEE Transactions on,* vol. 46, pp. 2459-2466, 2010.

[2] C. Zwyssig, M. Duerr, D. Hassler, and J. W. Kolar, "An Ultra-High-Speed, 500000 rpm, 1 kW Electrical Drive System," in *Power Conversion Conference - Nagoya, 2007. PCC '07*, 2007, pp. 1577-1583.

[3] D.-K. Hong, M.-H. Ahn, D.-S. Joo, B.-C. Woo, and D.-h. Koo, "Development of a super high speed motor-generator and controller," *Journal of Applied Physics,* vol. 115, pp. 17E705-17E705-3, 2014.

[4] W. Fengxiang, Z. Ming, Z. Wenpeng, and G. Enlu, "Design features of high speed PM machines," in *Electrical Machines and Systems, 2003. ICEMS 2003. Sixth International Conference on*, 2003, pp. 66-70 vol.1.

[5] H. Do-Kwan, W. Byung-Chul, and K. Dae-Hyun, "Rotordynamics of 120000 r/min 15 kW Ultra High Speed Motor," *Magnetics, IEEE Transactions on,* vol. 45, pp. 2831-2834, 2009.

[6] C. Zwyssig, J. W. Kolar, W. Thaler, and M. Vohrer, "Design of a 100 W, 500000 rpm permanent-magnet generator for mesoscale gas turbines," in *Industry Applications Conference, 2005. Fourtieth IAS Annual Meeting. Conference Record of the 2005*, 2005, pp. 253-260 Vol. 1.

[7] J. Kunz, C. Siwei, D. Yao, J. R. Mayor, R. G. Harley, and T. G. Habetler, "Design of a 750,000 rpm switched reluctance motor for micro machining," in *Energy Conversion Congress and Exposition (ECCE), 2010 IEEE*, 2010, pp. 3986-3992.

[8] P. Imoberdorf, C. Zwyssig, S. D. Round, and J. W. Kolar, "Combined Radial-Axial Magnetic Bearing for a 1 kW, 500,000 rpm Permanent Magnet Machine," in *Applied Power Electronics Conference, APEC 2007 - Twenty Second Annual IEEE*, 2007, pp. 1434-1440.

[9] D. Gerada, A. Mebarki, N. L. Brown, K. J. Bradley, and C. Gerada, "Design Aspects of High-Speed High-Power-Density Laminated-Rotor Induction Machines," *Industrial Electronics, IEEE Transactions on,* vol. 58, pp. 4039-4047, 2011.

[10] L. Papini, C. Gerada, D. Gerada, and A. Mebarki, "High speed solid rotor induction machine: Analysis and performances," in *Electrical Machines and Systems (ICEMS), 2014 17th International Conference on*, 2014, pp. 2759-2765.

[11] D. E. Hesmondhalgh, D. Tipping, and M. Amrani, "Design and construction of a high-speed high-performance direct-drive handpiece," *Electric Power Applications, IEE Proceedings B,* vol. 134, pp. 286-296, 1987.

[12] H. Do-Kwan, W. Byung-Chul, L. Ji-Young, and K. Dae-Hyun, "Ultra High Speed Motor Supported by Air Foil Bearings for Air Blower Cooling Fuel Cells," *Magnetics, IEEE Transactions on,* vol. 48, pp. 871-874, 2012.

[13] T. Yu, F. Wang, J. Wang, and F. Zhang, "Investigation on structure of stator core and winding for high speed PM machines," in *Electrical Machines and Systems, 2005. ICEMS 2005. Proceedings of the Eighth International Conference on*, 2005, pp. 903-906 Vol. 2.

[14] L. Zheng, T. X. Wu, D. Acharya, K. B. Sundaram, J. Vaidya, L. Zhao, L. Zhou, K. Murty, C. H. Ham, N. Arakere, J. Kapat, and L. Chow, "Design of a super-high speed

permanent magnet synchronous motor for cryogenic applications," in *Electric Machines and Drives, 2005 IEEE International Conference on*, 2005, pp. 874-881.

[15] Z. Fengzheng, S. Jianxin, F. Weizhong, and L. Ruiguang, "Study of Retaining Sleeve and Conductive Shield and Their Influence on Rotor Loss in High-Speed PM BLDC Motors," *Magnetics, IEEE Transactions on,* vol. 42, pp. 3398-3400, 2006.

[16] D. Jianning, H. Yunkai, J. Long, G. Baocheng, Z. Tao, L. Heyun, and D. Jiyong, "Development of an air-cooled 150 kW high speed permanent magnet motor with Gramme ring windings for turbo blowers," in *Electrical Machines and Systems (ICEMS), 2014 17th International Conference on*, 2014, pp. 3534-3538.

[17] T. I. Baumgartner, A. Looser, C. Zwyssig, and J. W. Kolar, "Novel high-speed, Lorentz-type, slotless self-bearing motor," in *Energy Conversion Congress and Exposition (ECCE), 2010 IEEE*, 2010, pp. 3971-3977.

[18] L. J. Wu, Z. Q. Zhu, D. Staton, M. Popescu, and D. Hawkins, "Analytical Modeling and Analysis of Open-Circuit Magnet Loss in Surface-Mounted Permanent-Magnet Machines," *Magnetics, IEEE Transactions on,* vol. 48, pp. 1234-1247, 2012.

[19] Z. Q. Zhu, D. Howe, and C. C. Chan, "Improved analytical model for predicting the magnetic field distribution in brushless permanent-magnet machines," *Magnetics, IEEE Transactions on,* vol. 38, pp. 229-238, 2002.

[20] Z. Q. Zhu, K. Ng, N. Schofield, and D. Howe, "Improved analytical modelling of rotor eddy current loss in brushless machines equipped with surface-mounted permanent magnets," *Iee Proceedings-Electric Power Applications,* vol. 151, pp. 641-650, Nov 2004.

[21] D. Fang, "An improved iron loss estimation for permanent magnet brushless machines," *Energy Conversion, IEEE Transactions on,* vol. 14, pp. 1391-1395, 1999.

[22] I. Junaid, J. Qudsia, and K. Byung-Il, "Improved model of the iron loss for the permanent magnet synchronous motors," in *Electrical Machines and Systems (ICEMS), 2010 International Conference on*, 2010, pp. 1246-1251.

[23] Z. X. Fang, Z. Q. Zhu, L. J. Wu, and Z. P. Xia, "Simple and accurate analytical estimation of slotting effect on magnet loss in fractional-slot surface-mounted PM machines," in *Electrical Machines (ICEM), 2012 XXth International Conference on*, 2012, pp. 464-470.

[24] Z. P. Xia, Z. Q. Zhu, and D. Howe, "Analytical magnetic field analysis of Halbach magnetized permanent-magnet machines," *Magnetics, IEEE Transactions on,* vol. 40, pp. 1864-1872, 2004.

[25] K. Atallah, D. Howe, P. H. Mellor, and D. A. Stone, "Rotor loss in permanent-magnet brushless AC machines," *Industry Applications, IEEE Transactions on,* vol. 36, pp. 1612-1618, 2000.

[26] H. Toda, X. Zhenping, W. Jiabin, K. Atallah, and D. Howe, "Rotor eddy-current loss in permanent magnet brushless machines," *Magnetics, IEEE Transactions on,* vol. 40, pp. 2104-2106, 2004.

[27] A. Chebak, P. Viarouge, and J. Cros, "Analytical Model for Design of High-Speed Slotless Brushless Machines with SMC Stators," in *Electric Machines & Drives Conference, 2007. IEMDC '07. IEEE International*, 2007, pp. 159-164.

[28] N. Bianchi, S. Bolognani, and F. Luise, "Analysis and Design of a PM Brushless Motor for High-Speed Operations," *Energy Conversion, IEEE Transactions on,* vol. 20, pp. 629-637, 2005.

[29] W. Xinghua, Z. Xiaocui, Y. Shichao, W. Xiuhe, and Z. Chenghui, "The analysis of high speed slotless permanent magnet brushless DC motor based on soft magnetic ferrite," in *Electrical Machines and Systems (ICEMS), 2010 International Conference on*, 2010, pp. 1061-1064.

[30] Y. Xu and K. Feng, "Analysis on Toothless Permanent Magnet Machine with Halbach Array," in *Power Electronics and Motion Control Conference, 2006. IPEMC 2006. CES/IEEE 5th International*, 2006, pp. 1-5.

[31] Z. Bin, W. Xiuhe, Z. Ran, and M. Xiaolei, "Cogging torque reduction by combining teeth notching and rotor magnets skewing in PM BLDC with concentrated windings," in *Electrical Machines and Systems, 2008. ICEMS 2008. International Conference on*, 2008, pp. 3189-3192.

[32] Z. Q. Zhu, K. Ng, and D. Howe, "Design and analysis of high-speed brushless permanent magnet motors," in *Electrical Machines and Drives, 1997 Eighth International Conference on (Conf. Publ. No. 444)*, 1997, pp. 381-385.

[33] W. Xinghua, Y. Shichao, Z. Xiaocui, W. Xiuhe, and Z. Chenghui, "The rotor topology of slotless permanent-magnet brushless DC motor," in *Electrical Machines and Systems (ICEMS), 2010 International Conference on*, 2010, pp. 1057-1060.

[34] Y. Yubo, W. Xiuhe, L. Xuemei, W. Daohan, and L. Shiyong, "Reducing Cogging Torque in Surface-mounted Permanent Magnet Motors by Teeth Notching," in *Industrial Electronics and Applications, 2007. ICIEA 2007. 2nd IEEE Conference on*, 2007, pp. 265-268.

[35] D. Gerada, A. Mebarki, N. L. Brown, and C. Gerada, "Optimal split ratio for high speed induction machines," in *Energy Conversion Congress and Exposition (ECCE), 2010 IEEE*, 2010, pp. 10-16.

[36] S. Bentouati, Z. Q. Zhu, and D. Howe, "Influence of design parameters on the starting torque of a single-phase PM brushless DC motor," *Magnetics, IEEE Transactions on*, vol. 36, pp. 3533-3536, 2000.

[37] H. Murakami, Y. Honda, Y. Sadanaga, Y. Ikkai, S. Morimoto, and Y. Takeda, "Optimum design of highly efficient magnet assisted reluctance motor," in *Industry Applications Conference, 2001. Thirty-Sixth IAS Annual Meeting. Conference Record of the 2001 IEEE*, 2001, pp. 2296-2301 vol.4.

[38] M. S. Islam, S. Mir, and T. Sebastian, "Issues in reducing the cogging torque of mass-produced permanent-magnet brushless DC motor," *Industry Applications, IEEE Transactions on*, vol. 40, pp. 813-820, 2004.

[39] J. Passenbrunner, D. Andessner, R. Kobler, and W. Amrhein, "Modeling, simulation and design of a claw pole machine using soft magnetic composites," in *Vehicle Power and Propulsion Conference (VPPC), 2011 IEEE*, 2011, pp. 1-6.

[40] L. Morel, H. Fayard, H. Vives Fos, A. Galindo, and G. Abba, "Study of ultra high speed switched reluctance motor drive," in *Industry Applications Conference, 2000. Conference Record of the 2000 IEEE*, 2000, pp. 87-92 vol.1.

[41] A. G. Hofmann, K. A. Kasper, and R. W. De Doncker, "High-speed switched reluctance drives: A promising alternative to power electric vehicles," in *Power Electronics and ECCE Asia (ICPE & ECCE), 2011 IEEE 8th International Conference on*, 2011, pp. 169-175.

[42] J. Klein, "How to develop a low-cost motor controller," *Potentials, IEEE*, vol. 24, pp. 40-43, 2005.

[43] H. K. Samitha Ransara and U. K. Madawala, "Modelling and analysis of a low cost Brushless DC motor drive," in *Industrial Technology (ICIT), 2013 IEEE International Conference on*, 2013, pp. 356-361.

[44] N. Kim, H. A. Toliyat, I. M. Panahi, and K. Min-Huei, "BLDC Motor Control Algorithm for Low-Cost Industrial Applications," in *Applied Power Electronics Conference, APEC 2007 - Twenty Second Annual IEEE*, 2007, pp. 1400-1405.

[45] C. J. Bateman, B. C. Mecrow, A. C. Clothier, P. P. Acarnley, and N. D. Tuftnell, "Sensorless Operation of an Ultra-High-Speed Switched Reluctance Machine," *Industry Applications, IEEE Transactions on*, vol. 46, pp. 2329-2337, 2010.

[46] Y. Shenbo, J. Shi, Y. Jing, and Z. Yonghui, "Calculation of Rotor Critical Speeds from Permanent Magnet Synchronous Machine," in *Electrical and Control Engineering (ICECE), 2010 International Conference on*, 2010, pp. 3439-3442.

[47] R. Mistry, B. Finley, S. Kreitzer, and R. Queen, "Influencing factors on motor vibration & rotor critical speed in design, test and field applications," in *Petroleum and Chemical Industry Technical Conference (PCIC), 2014 IEEE*, 2014, pp. 227-236.

[48] A. C. Smith, "Resonant frequencies in naturally-commutated, converter-fed induction motor drive systems," in *Electrical Machines and Drives, 1995. Seventh International Conference on (Conf. Publ. No. 412)*, 1995, pp. 338-342.

[49] J. D. Ede, Z. Q. Zhu, and D. Howe, "Rotor resonances of high-speed permanent-magnet brushless machines," *Industry Applications, IEEE Transactions on*, vol. 38, pp. 1542-1548, 2002.

[50] Z. Kolondzovski, A. Belahcen, and A. Arkkio, "Comparative thermal analysis of different rotor types for a high-speed permanent-magnet electrical machine," *Electric Power Applications, IET*, vol. 3, pp. 279-288, 2009.

[51] Y.-j. Yang, Y.-p. Liang, and J. Chen, "Thermal field calculation for the rotor of large turbo-generator," in *Strategic Technology (IFOST), 2011 6th International Forum on*, 2011, pp. 584-588.

[52] M. Bahrami, "Natural Convection Heat Transfer," ed: ENSC Simon Fraser University, 2014, pp. 1-7.

[53] M. Bahrami, "Forced Convection Heat Transfer," ed: ENSC Simon Fraser University, 2014, pp. 1-11.

[54] J. J. Wolmarans, M. B. Gerber, H. Polinder, S. W. H. de Haan, J. A. Ferreira, and D. Clarenbach, "A 50kW integrated fault tolerant permanent magnet machine and motor drive," in *Power Electronics Specialists Conference, 2008. PESC 2008. IEEE*, 2008, pp. 345-351.

[55] B. C. Mecrow, A. G. Jack, J. A. Haylock, and J. Coles, "Fault-tolerant permanent magnet machine drives," *Electric Power Applications, IEE Proceedings -*, vol. 143, pp. 437-442, 1996.

[56] B. C. Mecrow, A. G. Jack, D. J. Atkinson, S. Green, G. J. Atkinson, A. King, and B. Green, "Design and testing of a 4 phase fault tolerant permanent magnet machine for an engine fuel pump," in *Electric Machines and Drives Conference, 2003. IEMDC'03. IEEE International*, 2003, pp. 1301-1307 vol.2.

[57] N. Bianchi, S. Bolognani, and M. D. Pre, "Design and Tests of a Fault-Tolerant Five-phase Permanent Magnet Motor," in *Power Electronics Specialists Conference, 2006. PESC '06. 37th IEEE*, 2006, pp. 1-8.

[58] A. M. El-Refaie, "Fault-tolerant permanent magnet machines: a review," *Electric Power Applications, IET*, vol. 5, pp. 59-74, 2011.

[59] C. Qian, L. Guohai, G. Wensheng, and Z. Wenxiang, "A New Fault-Tolerant Permanent-Magnet Machine for Electric Vehicle Applications," *Magnetics, IEEE Transactions on*, vol. 47, pp. 4183-4186, 2011.

[60] W. Holt, "Direct Drive Systems Begins the Build of it Frame 12 Machine," *Texas: Driect Drive Systems*, 2008.

[61] A. Binder and T. Schneider, "High-speed inverter-fed AC drives," in *Electrical Machines and Power Electronics, 2007. ACEMP '07. International Aegean Conference on*, 2007, pp. 9-16.

[62] B. Eberleh and T. Hartkopf, "A high speed induction machine with two-speed transmission as drive for electric vehicles," in *Power Electronics, Electrical Drives, Automation and Motion, 2006. SPEEDAM 2006. International Symposium on*, 2006, pp. 249-254.

[63] M. Larsson, M. Johansson, L. Naslund, and J. Hylander, "Design and evaluation of high-speed induction machine," in *Electric Machines and Drives Conference, 2003. IEMDC'03. IEEE International*, 2003, pp. 77-82 vol.1.

[64] W. L. Soong, G. B. Kliman, R. N. Johnson, R. A. White, and J. E. Miller, "Novel high-speed induction motor for a commercial centrifugal compressor," *Industry Applications, IEEE Transactions on*, vol. 36, pp. 706-713, 2000.

[65] D. Gerada, A. Mebarki, N. L. Brown, Z. He, and C. Gerada, "Design, modelling and testing of a high speed induction machine drive," in *Energy Conversion Congress and Exposition (ECCE), 2012 IEEE*, 2012, pp. 4649-4655.

[66] A. Arkkio, T. Jokinen, and E. Lantto, "Induction and permanent-magnet synchronous machines for high-speed applications," in *Electrical Machines and Systems, 2005. ICEMS 2005. Proceedings of the Eighth International Conference on*, 2005, pp. 871-876 Vol. 2.

[67] J. F. Gieras, "Comparison of high-power high-speed machines: cage induction versus switched reluctance motors," in *Africon, 1999 IEEE*, 1999, pp. 675-678 vol.2.

[68] S. Kachapornkul, P. Somsiri, R. Pupadubsin, N. Nulek, and N. Chayopitak, "Low cost high speed switched reluctance motor drive for supercharger applications," in *Electrical Machines and Systems (ICEMS), 2012 15th International Conference on*, 2012, pp. 1-6.

[69] W. Z. a. B. i. Kwon, "Optimal design of a cost-effective SPM motor to suppress torque pulsations using multi-grade permanent magnets," presented at the Electromagnetic Field Computation (CEFC), 2016 IEEE Conference Miami, FL, USA, 2017.

[70] J. h. C. W. Liu, C. Zhang, Z. q. Cui and X. Wang,, " Ventilation system design and rotor air friction loss of high-speed permanent magnet machines " presented at the 2017 IEEE International Conference on Cybernetics and Intelligent Systems (CIS) and IEEE Conference on Robotics, Automation and Mechatronics (RAM), , Ningbo, 2017.

[71] D. Electrionics. (2014). *Material properties of radially oriented, anisotropic Nd-Fe-B ring magnets (NEOQUENCH-DR).* Available: http://www.daido-electronics.co.jp/english/product/neoquench_dr/material/index.html

[72] D. Electronics. (2014). *Material properties of isotropic polymer bonded Nd-Fe-B magnets (NEOQUENCH-P).* Available: http://www.daido-electronics.co.jp/english/product/neoquench_p/material/index.html

[73] J. Steel. (2015). *Electrical Steel Sheets: JFE G-Core, JFE N-Core.* Available: http://www.jfe-steel.co.jp/en/products/electrical/catalog/f1e-001.pdf

[74] M. A. Rahman, A. Chiba, and T. Fukao, "Super high speed electrical machines - summary," in *Power Engineering Society General Meeting, 2004. IEEE*, 2004, pp. 1272-1275 Vol.2.

[75] L. O. Hultman and A. G. Jack, "Soft magnetic composites-materials and applications," in *Electric Machines and Drives Conference, 2003. IEMDC'03. IEEE International*, 2003, pp. 516-522 vol.1.

[76] G. A. a. N. S. N. Aliyu, "Concentrated winding permanent magnet axial flux motor with soft magnetic composite core for domestic application," presented at the Electro-Technology for National Development (NIGERCON), 2017 IEEE 3rd International Conference Owerri, Nigeria, 2017.

[77] G. L. B. Ma, J. Zhu and Y. Guo, "Design Optimization of a Permanent Magnet Claw Pole Motor With Soft Magnetic Composite Cores," presented at the IEEE Transactions on Magnetics, 2017.

[78] I. Petrov and J. Pyrhonen, "Performance of Low-Cost Permanent Magnet Material in PM Synchronous Machines," *Industrial Electronics, IEEE Transactions on,* vol. 60, pp. 2131-2138, 2013.

[79] M. A. A. Costa, E. R. Braga-Filho, and A. M. N. Lima, "Designing a low cost high performance permanent magnet motor drive system," in *Industrial Electronics Society, IECON 2013 - 39th Annual Conference of the IEEE*, 2013, pp. 2738-2743.

[80] R. K. Gupta and N. Mohan, "A Three-Phase Permanent Magnet Brushless DC Motor for Low-Power Low-Speed Fan Applications - Optimizing Cost and Efficiency," in *Industry Applications Conference, 2007. 42nd IAS Annual Meeting. Conference Record of the 2007 IEEE*, 2007, pp. 846-852.

[81] O. Sung Chul and A. Emadi, "Test and simulation of axial flux-motor characteristics for hybrid electric vehicles," *Vehicular Technology, IEEE Transactions on,* vol. 53, pp. 912-919, 2004.

[82] M. J. K. Jacek F. Gieras，Rong-Jie Wang, *Axial Flux Permanent Magnet Brushless Machines*, Second ed.: Springer Science + Business Media B.V., 2008.

[83] C. Anyuan, R. Nilssen, and A. Nysveen, "Performance Comparisons Among Radial-Flux, Multistage Axial-Flux, and Three-Phase Transverse-Flux PM Machines for Downhole Applications," *Industry Applications, IEEE Transactions on,* vol. 46, pp. 779-789, 2010.

[84] W. C. Young and R. G. Budynas, *Roark's Formulas for Stress and Strain*, Seventh ed. vol. 16: McGraw-Hill, 2002.

[85] M. Nagrial, J. Rizk, and A. Hellany, "Design and performance of permanent magnet slotless machines," in *Electrical Machines, 2008. ICEM 2008. 18th International Conference on*, 2008, pp. 1-5.

[86] N. Bianchi, S. Bolognani, and F. Luise, "High speed drive using a slotless PM motor," in *Power Electronics Specialists Conference, 2004. PESC 04. 2004 IEEE 35th Annual*, 2004, pp. 458-463 Vol.1.

[87] N. Bianchi, S. Bolognani, and F. Luise, "High speed drive using a slotless PM motor," *Power Electronics, IEEE Transactions on,* vol. 21, pp. 1083-1090, 2006.

[88] N. Bianchi, S. Bolognani, and F. Luise, "Potentials and limits of high speed PM motors," in *Industry Applications Conference, 2003. 38th IAS Annual Meeting. Conference Record of the*, 2003, pp. 1918-1925 vol.3.

[89] K. Halbach, "Design of permanent multipole magnets with oriented rare earth cobalt material," *Nuclear Instruments and Methods*, vol. 169, pp. 1-10, 1980.

[90] R. Bjørk, C. R. H. Bahl, A. Smith, and N. Pryds, "Optimization and improvement of Halbach cylinder design," *Journal of Applied Physics*, vol. 104, pp. 013910-013910-9, 2008.

[91] G. Bertotti, "General properties of power losses in soft ferromagnetic materials," *IEEE Transactions on Magnetics,* vol. 24, pp. 621-630, 1988.

[92] K. J. Tseng and S. B. Wee, "Analysis of flux distribution and core losses in interior permanent magnet motor," *IEEE Transactions on Energy Conversion*, vol. 14, pp. 969-975, 1999.

[93] K. Atallah, Z. Q. Zhu, and D. Howe, "An improved method for predicting iron losses in brushless permanent magnet DC drives," *IEEE Transactions on Magnetics*, vol. 28, pp. 2997-2999, 1992.

[94] H. Sano, K. Narita, T. Asanuma, and T. Yamada, "An accurate iron loss evaluation method based on Finite Element Analysis for Permanent Magnet Motors," in *2016 XXII International Conference on Electrical Machines (ICEM)*, 2016, pp. 1284-1289.

[95] F. Chai, P. Liang, Y. Pei, and S. Cheng, "Magnet Shape Optimization of Surface-Mounted Permanent-Magnet Motors to Reduce Harmonic Iron Losses," *IEEE Transactions on Magnetics*, vol. 52, pp. 1-4, 2016.

[96] Z. P. Popovic, B. D., *Introductory Electromagnetics*: Prentice Hall, 2000.

[97] C. R. Sullivan, "Computationally efficient winding loss calculation with multiple windings, arbitrary waveforms, and two-dimensional or three-dimensional field geometry," *Power Electronics, IEEE Transactions on*, vol. 16, pp. 142-150, 2001.

[98] "IEEE Guide for Testing Turn Insulation of Form-Wound Stator Coils for Alternating-Current Electric Machines," *IEEE Std 522-2004 (Revision of IEEE Std 522-1992)*, pp. 0_1-18, 2004.